UNIVERSITAT DE BARCELONA

Estudio eléctrico y topográfico de apéndices bacterianos en la nanoescala

Helena Lozano Caballero

Universitat de Barcelona

Facultad de Física

Departamento de ingeniería electrónica y biomédica

Estudio eléctrico y topográfico de apéndices bacterianos en la nanoescala

Autora:

Helena Lozano Caballero

Programa de Doctorado:

Nanociencias

Línea de investigación:

Nanobiotecnología

Director y tutor de tesis:

Gabriel Gomila Lluch

UNIVERSITAT DE BARCELONA

Barcelona, 2020

"If we knew what it was we were doing, it would not be called research, would it?"

Albert Einstein

Acknowledgments

This Ph.D. thesis is not an individual achievement, but a combined effort from my teachers, friends and family. I would like to thank each one of them individually to show my appreciation.

Firstly, I would like to thank Dr. Gabriel Gomila for all the advice and timely help he has offered me during the Ph.D. I also thank him for being a patient mentor and an excellent scientist. I have learned a lot from our scientific discussions and interactions. I am eternally grateful to be your Ph.D student and thank you for the encouragement and happy attitude that kept me going throughout the Ph.D.

My group at IBEC "Nanobioelec" has been one of the best teams I have worked with. I would like to thank Ruben Millan for being an amazing colleague to work with and for developing the amazing NBE software. I enjoyed a lot testing it. Also, thank you for helping me when I was struggling during my experiments. I would also give him credit for all the discussions we had. Rene had been a wonderful mathematician for the modeling part in my studies and it was a pleasure to collaborate with you. On that order, I would next like to thank Marti Checa, for being a good friend and PhD companion from day one. Our different views and perceptions have hopefully helped both of us to understand the scientific and life stuff better. Ricardo, you are a pleasant person to meet and also a learning experience. Thank you for all our conversations and for helping me in both scientific and non-scientific problems.

I would be doing a big mistake if I do not thank the initial Charlie's angel group, being: Adrica and Martina. Adrica has been a constant support during the final years of my Ph.D and one of the few trusted people I would turn to in case of advice. Thank you for trying to teach me English and writing skills. I would like to thank Martina for her understanding and availability at all times. Lab-life has been easier having you around and I wish you the best to complete your Ph.D. faster. I hope we continue *vermuting.*

Thank you Hari for all our philosophical discussions and for helping me to grow as a human being. I hope you all the best in finishing the Ph.D and the following years.

Up next, the youngest of our team, Larissa and Shubam also deserves a shoutout and I have no doubts in saying that your Ph.D. is in good hands.

I would also like to thank Nuria Blanco for collaborating and teaching me so many things about bacteria. Also, thank you for always work so hard and put my bacteria to grow. I will always remember our times traveling around U.S.A.

I would like to thank El-Naggar group, for hosting Nuria and I during our stay there and for helping in all our doubts. Thank you for helping me in getting the famous *S. oneidensis* nanowires.

The Copenhagen group has been an incredible host during the few months I spent there. I would always thank the wonderful people, right from Lea Rasmussen (my office mate), Christian, Julio, Maria, Dimitri, Daniel, Pascal, Valentina and so on, and especially to my boss there, Edith. The warm reception you have provided me has made my stay exponentially better.

After my support and help from my work friends, it is time to thank the important people in my life. My parents. They have been my pillar of strength and have given me the courage and love to chase what I wanted. They are the best parents I could ever ask for and their advice has made me a better person in every aspect of life. I could never thank them enough for the things they have done, but I would like to keep trying. Marta and Cristina are the two other constants in my life, and it has been an amazing journey with you guys. I am excited about the even better journey ahead with my wonderful sisters in the good times to come.

I would like to thank my partner, César, for the unconditional affection he has showered me through good, normal and bad times. You are the best and I am lucky to have you by my side.

My school friends Maria, Elena, Roser, Andrea deserve a round of applause for making the good times even better. Thank you for sticking around and I wish for better things for all of you. Also, to Albert, Pagan, Jess and Eric, for thinking that I was not working all this time. Also, I would like to thank all the Alcocrew.

In case I have missed someone, please kindly remember that I am eternally grateful to you.

Thank you, everyone, from the bottom of my heart.

Helena Lozano

Table of contents

Summary

Recently, it has been discovered that some bacteria can exchange electrons with non-soluble electron acceptors, such as minerals. In addition, some of these bacteria have the ability to use electrodes as the final electron acceptor. These types of bacteria live in environments where there is a lack of oxygen and develop this behaviour to reduce external sources of metal in order to breathe. The exchange of electrons can be done in three different ways: i) through direct contact by making a short-range electronic transfer, ii) through shuttle molecules or iii) through conducting nanowires that facilitate a long-range electronic transfer, and can be up to several centimeters distance. The existence of these bacteria, and especially their bacterial nanowires, opens the possibility of exploring a high range of applications in the world of bioelectronics due to their biological origin and their unique properties.

Despite the attention generated by these biomaterials, their integration into electronic devices is emerging. This is due to the difficulty in the production and purification of bacterial nanowires and their consequent correct positioning in the electronic device. It is also because their conduction mechanisms are still unclear. In addition, it is not well-known how the environment (in physiological conditions or in dry conditions) in which they are found affects their electrical properties. The uncertainties of these new biomaterials, in part, is due to the lack of techniques capable of characterizing electrical properties at the nanoscale, both in dry and in liquid conditions.

The Atomic Force Microscope (AFM) is a technique that allows the study of various properties (electrical, magnetic, piezoelectric, ...) at the nanoscale in both air and liquid conditions using a nanometric probe. In particular, Scanning Dielectric Microscopy (SDM) allows the study of the polarization properties of a sample. SDM measures the electrostatic force between the probe and the sample and combining it with finite element numerical simulations to extract the interesting parameters of the system (dielectric constant or dimensions of the sample). This polarization properties depend mainly on the geometry and the electrical permittivity of the sample-probe system.

Summary

The main objective of this thesis is the investigation of the polarization properties of electrochemically active bacteria. Specifically, I have studied two types of bacteria, *Shewanella oneidensis* MR-1 and cable bacteria, from the *Desulfobulbaceae* family. With this purpose, I have used the Electrostatic Force Microscopy (EFM) technique combined with finite element simulations to obtain the dielectric constant of bacterial nanowires, which is related to both the dielectric and conductive properties of the sample.

To do this, first, I have developed a method to obtain the dimensions of objects without damaging them, avoiding physical contact, by measuring the electrostatic force. I have tested this technique on silver nanowires and extended it to bacterial flagella. In this way, I have been able to optimize the EFM technique in filamentous biological nanoscale type samples.

Subsequently, I have studied the electrical properties of flagella, one of the *S. oneidensis* MR-1 appendages, and I have compared its properties with *Pseudomonas aeruginosa* PAO1 flagella, a non-electrochemically active bacteria. I have verified that both flagella give similar dielectric constants, being $\varepsilon_{So} = 4.3 \pm 0.6$, for the case of *S. oneidensis*, and $\varepsilon_{Pa} = 4.5 \pm 0.7$, for *P. aeruginosa*. In addition, since flagella are filaments composed of flagellin proteins, these results are similar to the dielectric constant of proteins obtained in other studies (ε~4).

Using the same technique, I have studied the electrical properties of another *S. oneidensis* MR-1 appendage, the outer membrane extensions. These extensions are considered to be involved in the Extracellular Electron Transfer (EET) mechanism. Therefore, they are considered as conductive bacterial nanowires. The conductivity of these nanowires is achieved through an electron hopping mechanism between cytochromes. In this mechanism, the electron is localized and hops along the filament. The measured dielectric constant of these extensions is $\varepsilon_{So} = 3.7 \pm 0.7$, which is a combination of the dielectric constant of lipids (ε~2) and proteins (ε~4). However, taking into account that the electrons are not delocalized at any moment, this result is compatible with the literature.

This same EFM technique to extract the dielectric constant has been used to study the cable bacteria. Cable bacteria is a filamentous bacterium composed of cells interconnected at their ends. Along this filament, there are fibers that are considered responsible for the electron transfer from one extreme of the filament to the other. For this reason, I have studied the electrical properties

of these fibers, obtaining a relatively high dielectric constant $\varepsilon_r = 7 \pm 1$. However, this model does not take into account the conductivity of the fibers. The model that does consider it is the core-shell model where the core conductivity is $\sigma_c = 2000$ S/m. Thus, I have obtained a core of h_c~$10 - 20$ nm for a fiber of h_{fiber}~40 nm.

Subsequently, I have performed EFM measurements in liquid conditions and I have obtained qualitative images of the electrical properties of *S. oneidensis* and their appendages at the nanoscale, in living and rehydrated bacteria. However, their quantification is still under study.

Finally, I have performed a macroscale study of the electrical properties of *S. oneidensis* MR-1 under physiological conditions, and therefore, of living bacteria. To achieve this, I have designed and fabricated a microfluidic system based on a pair of gold electrodes together with a microfluidic channel that allows the medium (and bacteria) flow through it. With this system, I have carried out two-electrode impedance measurements that allow the extraction of the electrical permittivity of the medium with bacteria in it. In this study, I have obtained interesting results, because when bacteria are in anaerobiosis, for frequencies f~$10^2 - 10^3$ Hz, there is an abrupt change in the impedance. Although further experiments are needed to explain this behaviour. This impedance work was performed at the Denmark Technical University (DTU), Copenhagen, Denmark.

Summary

Resumen

Recientemente se ha descubierto que algunas bacterias pueden intercambiar electrones con aceptores de electrones no solubles, como por ejemplo minerales. Además, algunas de estas bacterias tienen la capacidad de utilizar electrodos como aceptor final de electrones. Este tipo de bacterias habitan en ambientes donde hay falta de oxígeno y desarrollan este comportamiento de reducir fuentes externas de metal para así poder respirar. El intercambio de electrones se puede realizar de tres maneras diferentes: i) por contacto directo realizando una transferencia electrónica de corto alcance, ii) utilizando moléculas lanzadera o iii) por nanohilos conductores que facilitan la transferencia electrónica de largo alcance, pudiendo llegar a ser de varios centímetros de distancia. La existencia de estas bacterias, y en especial sus nanohilos bacterianos, abre la posibilidad de explorar una alta gama de aplicaciones en el mundo de la bioelectrónica debido a su origen biológico y sus propiedades únicas.

Sin embargo, a pesar de la atención generada por estos biomateriales, su integración en dispositivos no está muy avanzada. Esto se debe a la dificultad que hay en la producción y en la purificación de los nanohilos bacterianos y su consiguiente posicionamiento en el correspondiente dispositivo electrónico. También se debe a que los mecanismos de conducción de los nanohilos no están todavía muy claros. Además, hay dudas sobre cómo el entorno (en condiciones fisiológicas o bien en condiciones secas) en el que se encuentran afecta a sus propiedades eléctricas. Las incógnitas ante estos nuevos biomateriales, en parte, son debidas a la carencia de técnicas capaces de medir propiedades eléctricas tanto en seco como en líquido en la nanoescala.

El microscopio de fuerzas atómicas (AFM) es una técnica que permite el estudio de diversas propiedades (eléctricas, magnéticas, piezoeléctricas, …) en la nanoescala tanto en aire como en líquido, utilizando una punta nanométrica. En particular, la técnica de microscopía de barrido dieléctrico permite el estudio de las propiedades de polarización de una muestra, midiendo la fuerza electrostática entre la punta y la muestra y combinándolo con simulaciones de elementos numéricos finitos para extraer los parámetros de interés dicha muestra (constante dieléctrica o

dimensiones de la muestra). Estas propiedades de polarización dependen, básicamente, de la geometría y de la permitividad eléctrica del sistema punta-muestra.

En esta tesis he investigado las propiedades de polarización de bacterias electroquímicas y de los materiales biológicos derivados de ellas. En concreto he estudiado dos tipos de bacterias, *Shewanella oneidensis* MR-1 y el *cable bacteria*, de la familia de la *Desulfobulbaceae*. Con este objetivo, he utilizado la técnica de microscopía de fuerzas electrostáticas (EFM) combinada con simulaciones de elementos finitos para obtener la constante dieléctrica de los nanohilos bacterianos.

Para ello, primero he desarrollado una manera de obtener las dimensiones de los objetos sin dañarlos, evitando contacto físico, que consiste en medir las fuerzas electrostáticas. Esta técnica la he probado en nanohilos de plata y en flagelos bacterianos. De esta manera, he podido optimizar la técnica de EFM en muestras de tipo filamento, biológicas y en la nanoescala.

A continuación, he estudiado las propiedas eléctricas de los flagelos, uno de los apéndices de la bacteria *S. oneindensis* MR-1, y he comparado sus propiedades con las propiedades de flagelos provenientes de otras bacterias, la *Pseudomonas aeruginosa* PAO1, una bacteria no electroquímica. Los flagelos son filamentos compuestos de proteínas de flagelina. De esta manera, he comprobado que ambos flagelos dan similares constantes dieléctricas, siendo $\varepsilon_{So} = 4.3 \pm 0.6$, para el caso de *S. oneidensis*, y $\varepsilon_{Pa} = 4.5 \pm 0.7$, para la *P. aeruginosa*. Además, estos resultados son similares a otros valores obtenidos en el estudio de la constante dieléctrica de proteínas (ε_r~4).

De la misma manera, he estudiado las propiedades eléctricas de otro apéndice de la *S. oneidensis*, las extensiones de membrana externa. Se considera que estas extensiones están involucradas en la transferencia extracelular de electrones, y, por lo tanto, son consideradas como nanohilos bacterianos conductores. Estos nanohilos conducen la electricidad mediante mecanismos de salto de electrones entre citocromos. En este mecanismo, el electrón se encuentra localizado en un citocromo concreto y va saltando a lo largo del filamento. La constante dieléctrica medida de estas extensiones es $\varepsilon_{OME} = 3.7 \pm 0.7$, siendo este valor un promedio entre la constante dieléctrica de lípidos (ε_r~2) y proteínas (ε_r~4). Sin embargo, teniendo en cuenta que los electrones no se encuentra deslocalizados en ningún momento, este resultado no contradice otros estudios.

Esta misma técnica de EFM para extraer la constante dieléctrica ha sido utilizada para estudiar el *cable bacteria*. Esta bacteria está compuesta de células interconectadas por sus extremos y forman un filamento. Además, a lo largo de este filamento hay unas fibras que se consideran responsables de la transferencia de electrones de un extremo del filamento al otro. Por este motivo, he estudiado las propiedades eléctricas de estas fibras, obteniendo una constante dieléctrica relativamente alta ($\varepsilon_{fibra} = 7 \pm 1$). Sin embargo, este modelo no tiene en cuenta la conducción de las fibras. El modelo que sí lo considera es el de núcleo-caparazón donde la conductividad del núcleo es $\sigma = 2000$ S/m. Así, he obtenido un núcleo de h_c~$10 - 20$ nm para una fibra de h_{fibra}~40 nm.

A continuación, he realizado medidas de EFM en líquido y he obtenido medidas cualitativas de las propiedades eléctricas de *S. oneidensis* y sus apéndices en la nanoescala, en bacterias vivas y rehidratadas. Sin embargo, su cuantificación aún está en estudio.

Finalmente, he complementado el estudio en la nanoescala de las bacterias en aire mediante medidas de EFM, con el estudio en la macroescala de las propiedades eléctricas de *S. oneidensis* MR-1 en condiciones fisiológicas, y por lo tanto, vivas. Para ello, he fabricado un sistema microfluídico basado en un par de electrodos de oro junto con un canal microfluídico por el que fluye el medio junto con las bacterias. A continuación, he realizado medidas de impedancia a dos electrodos que permiten la extracción de la permitvidad eléctrica del medio que fluye. En estas medidas, he encontrado interesantes resultados, ya que cuando las bacterias se encuentran en anaerobiosis, para frecuencias f~$10^2 - 10^3$ Hz, hay un cambio abrupto en la impedancia. Aunque más experimentos son necesarios para explicar este comportamiento. Este trabajo de impedancias se realizó en la Denmark Technical University (DTU), Copenhaguen, Dinamarca.

1. Introduction and objectives

Recently it has been discovered the capacity of some bacterial species to exchange electrons with electrodes or minerals and to produce nanowires to reach further minerals. They can transport electrons extracellularly to long distances, even up to centimeters [1]. The existence of those bio-nanowires is very interesting for bioelectronic applications due to their unique and fascinating properties [2]. It has been shown that these kinds of bacteria generate electrical currents through the exchange of electrons with external materials [3–5], by means of electrochemical oxidation-reduction processes. Some examples of electrochemically active bacteria are *Shewanella oneidensis* MR-1, *Geobacter sulfurreducens*, or cable bacteria, from the *Desulfobulbaceae* family, which in their natural state, use this ability to reduce metal sources.

Three different mechanisms have been proposed to explain the bacteria electron transport: i) through shuttle molecules, like flavins; ii) through direct contact mediated by c-type cytochromes; or iii) through long-range electron transport, mediated by nanowires which can have different conduction mechanism, like electron hopping or metal-like conductivity, using the c-type cytochromes [6].

In addition, recently, it has been discovered that bacteria from the *Desulfobulbaceae* family can transport electricity by forming live wires with their entire bodies, and extending these nanowires up to centimeter distances [7,8]. Although the electron transport mechanism is still unclear, it has been established that one extreme of the cell is able to oxidize hydrogen sulfide and supply electrons to the other extreme of the wire [1,9].

Despite the attention generated by these new nanomaterials, their integration into electronic devices is still emerging. This is due to the intrinsic difficulties in the production and purification of the bacterial nanowires and their correct positioning in the electronic device. And also, because their conduction mechanisms are still unclear. In addition, it is not well-known how the environment (air or physiological conditions), in which the bacterial nanowire is found, influences its electrical conduction properties [2]. In part, this difficulty is related to the lack of nanometric techniques capable of measuring the electrical properties of nanomaterials in liquid environments.

During recent years, the Nanoscale Bioelectric Characterization Group has developed original methods for the measurement of the nanoscale electrical properties of biological materials based on Scanning Probe Microscopy techniques. In particular, they have developed techniques for the measurement of currents and electrical forces DC [10] and AC [11] at the nanoscale, [12–14] or even measurements at microwave frequencies (GHz) [15]. Specifically, I will highlight the development of quantification procedures for electrical measurements of high relevance for this project thesis [16,17]. These techniques have been applied to a variety of biological systems that include supported biomembranes [13], individual viruses [14] or individual bacterial cells [12]. Likewise, the Research Group has extensive experience in the development of biosensing systems [18] and microfluidic microsystems [19].

In this thesis, we aim to study the polarization of electrochemically active bacteria and their appendages as the polarization plays a key role in the EET mechanisms. The interest also stems out from the increasing interest in using such bacteria as a biosensing platform [2,20,21].

Therefore, I studied the topographical and electrical properties of bacterial appendages at the nanoscale using Atomic Force Microscopy (AFM) techniques, especially Scanning Dielectric Microscopy (SDM) measurements. The SDM is based on the measurement of the electrostatic force using a nanometric probe. The electrostatic force depends mainly on the geometry and dielectric permittivity of the probe-sample system. In particular, I have developed a method to deal with nanowires like structures, which had not been addressed earlier. I have also designed and fabricated microelectronic devices for larger-scale electrical measurements in living bacteria. Thus, I will try to elucidate some unknowns about bacterial nanowires and their conduction mechanism.

This thesis has been organized into eleven chapters. After this **first** chapter of general introduction, the **second** one explains the Extracellular Electron Transfer mechanisms and some examples of bacteria expressing this behaviour. The **third** chapter describes what the dielectric permittivity is and why it is important for this thesis. Finally, the **fourth** chapter closes the theoretical introduction of this thesis with an explanation of the basis of Atomic Force Microscopy and also the main technique used in this thesis, namely Electrostatic Force Microscopy (EFM).

In particular, I describe the use of EFM for the measurements of the dielectric (and conductivity) properties at the nanoscale, which is referred to as Scanning Dielectric Microscopy (SDM).

The experimental part starts at the **fifth** chapter and presents a new methodology to obtain the dimensions of a nanoscale object without damaging the sample, avoiding physical contact, applying the SDM technique. The **sixth** chapter presents the topographical and electrical characterization of one of the *S. oneidensis* appendages, flagella. The **seventh** chapter presents the electrical and topographical characterization of another *S. oneidensis* appendages, namely outer membrane extensions or nanowires. The **eight** chapter presents the electrical characterization of another electrochemically active bacterial cell species, the cable bacteria, from the *Desulfobulbaceae* family. Finally, the **ninth** chapter closes the nanoscale analysis of electrochemically active bacteria and it presents qualitative results of *S. oneidensis* bacteria and their appendages in liquid and living conditions at the nanoscale, using EFM. The **tenth** chapter shows a macroscale analysis of the electrical properties of living *S. oneidensis*. This analysis was performed through impedance measurements. It presents the work performed in the Denmark Technical University, in Copenhagen, which involves the design, fabrication and characterization of an impedance biosensor and two-electrode impedance measurements.

The **eleventh** chapter presents the conclusions and future perspectives of this thesis, which is followed by an appendix and the references.

2. Extracellular Electron Transfer in bacterial cells

This chapter presents a brief introduction about the Extracellular Electron Transfer and different examples in bacterial cells.

2.1.Introduction

Electron transfer (ET) plays an important role in most solid-state electron devices, but it is also an important phenomenon in sustaining life. Electron transfer reactions are fundamental to metabolism for every living cell, whether it is autotrophic or heterotrophic, or it is an obligate or a free-living parasite [22,23]. In order to accomplish respiration, fermentation and photosynthesis, a limited number of strategies are used, but an essential process in all these strategies is electron transfer between or within biomolecules in biomembranes. Indeed, the formation of phosphate bonds in adenosine triphosphate (ATP) is driven by ET reactions that lead to the formation of an electrochemical gradient across the cell or mitochondrial membrane and provides energy. Later, the dissociation of this bond is a universal source of free energy in biology and leads to the conversion of ATP to adenosine diphosphate (ADP) [24]. Usually, ET takes place intracellularly.

During the last decade, bacteria able to exchange electrons with electrodes or minerals, extracellularly, have been found and generate a large interest. In order to understand how they do it, first, we need to know how bacteria capture and process energy. Bacteria grow by catalyzing chemical reactions and harnessing and storing energy in the form of ATP. Electrons are transferred to respiratory enzymes by NADH (reduced form of nicotinamide adenine dinucleotide (NAD)) when bacteria oxidize substrates. These electrons move protons across an internal membrane, while they flow down through the respiratory chain. Subsequently, the protons go back into the cell through the enzyme ATPase, producing ATP. Finally, the electrons are released to a soluble terminal electron acceptor, such as oxygen, nitrate or sulfate. If electrons leave the respiratory

chain at some reduction potential smaller than the one of the oxygen, the bacteria acquire less energy [25].

Normally, soluble electron acceptors are not found in the microbial environment, as in deep ocean waters where no oxygen is found; therefore, microorganisms use non-soluble electron acceptor transferring electrons outside the cell. This process of having the ability to transfer electrons into a natural extracellular electron acceptor is called Extracellular Electron Transfer (EET) [6]. The EET is a rock breathing metabolism.

2.2.Extracellular electron transfer

There is a wide range of microorganisms that can transfer electrons between their cytoplasmic membrane and extracellular electron acceptors, like minerals, through a network of redox and structural proteins. That is, they can exchange electrons with electrodes; they are electrochemically active. Since the microbial cell envelope is neither electrically conductive nor permeable to minerals, microorganisms have developed strategies to have EET [6,26,27].

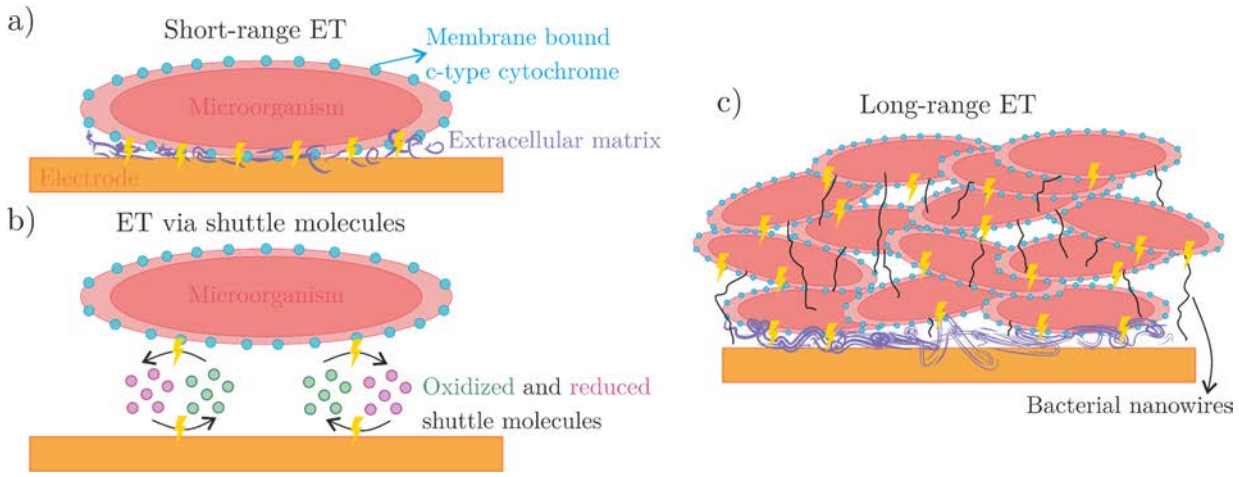

Figure 2.1: Schematic representation of a) short-range electron transfer, b) electron transfer through the oxidation and reduction of shuttle molecules, and c) long-range electron transfer via bacterial nanowires [6].

EET has been studied in microorganisms capable of breathing from insoluble metals, as Fe(III) and Mn(IV), or humic substances too large to enter the cells [28]. In such cases, microorganisms exchange electrons with natural electron acceptors and it is a natural biogeochemical process, such as Fe(III) reduction. However, sometimes they can exchange electrons with electrodes which would be a microbial electricity production. The fact that electrodes are not part of the natural

environment and bacteria can produce electric currents when they exchange electrons with electrodes and are able to consume current to power their respiration makes EET even more exciting and fascinating [27].

There are many microorganisms that can exchange electrons with electrodes when artificial electron shuttles are provided [27], however, EET can happen without the addition of an artificial electron shuttle in three ways (**Figure 2.1**):

- **Short-range direct ET**: mediated via redox-active proteins on the outer cell surface and it requires physical contact between the cell and the electrode. This way of ET can involve membrane-bound electron carriers and conductive appendages called nanowires. Membrane-associated ET is carried out by components of the respiratory chain, and it has been demonstrated that active redox proteins, like c-type cytochromes or iron-sulphur proteins, are located at the outer membrane and act as direct conduits for electron flow to solid-phase electron acceptors [29]. **Figure 2.1a** shows a schematic representation of direct ET, where membrane bounds, as c-type cytochromes, are exposed on the outer surface of the [6,30]. Sometimes, these cytochromes are located close to the electrode surface for direct ET from cytochromes to electrodes [31] and, therefore, function as the electrochemical gate between cells and the electrode surface [6]. Multihaem c-type cytochromes are the major electron carrier proteins used by *Geobacter sulfurreducens* and *Shewanella oneidensis*, the best known electrochemically active bacteria. There is evidence for direct electron transfer to electrodes for several microorganisms [32,33] and some of these bacteria are *Geobacter spp.* [34], *Shewanella spp.* [35], *Desulfobulbus propionicus* [36], *Aeromonas hydrophila* [37] and *Thermincola potens* [38].
- **ET via shuttle molecules**: mediated via soluble electron-shuttle molecules. Electron shuttles or mediators are soluble molecules, that can be reversibly oxidized and reduced, which facilitate ET between microorganisms and electrodes. Oxidized shuttle molecules donate electrons to the electrode. Therefore, these mediators can accept electrons from cellular electron carriers and transfer them to the electrode [27]. **Figure 2.1b** shows this process schematically. The shuttle molecules can be artificial, but also a diversity of gram-negative and gram-positive bacteria can produce them. One example of a

produced shuttle molecule is flavins [39,40]. This mechanism does not require direct contact between the bacteria and the electrode, allowing longer-range electrical interaction. However, the synthesis of them is energetically expensive for the microorganism; therefore, bacteria recycle them many times, so their use is limited to systems with low diffusivity [27]. Some bacteria capable of producing shuttle molecules are *Geothrix fermentans*, which can reduce Fe(III) enclosed in porous alginate beads via shuttle molecules [41], or *Shewanella oneidensis*, which can reduce Fe(III) with which they are not in direct contact [42–44].

- **Long-range ET**: through conductive pilis or nanowires, together with short-range ET mediated by extracellular cytochromes. These conductive nanowires are one of the most captivating microbial structures discovered within the last decade [45,46]. They are pilus-like structures which are conductive thanks to the presence of decaheme surface proteins usually involved in iron reduction [4]. The nanowires allow the ET across the biofilm on electrodes, allowing the contact between the cells and the electrode or between different cells. The log-range electron transfer can be over multiple cell lengths and up to centimeters long [1,7,47]. **Figure 2.1c** shows a schematic illustration of the long-range ET. The combination of conductive nanowires, together with cytochromes, seems to be a general strategy for EET toward Fe(III)-oxides [39]. There is evidence that bacteria like *Shewanella oneidensis* [4,48–51], *Geobacter sulfurreducens* [3,45,46,52,53] or *Desulfobulbaceae spp.* [1,7,54,55] are capable of performing long-range ET.

2.2.1.Outer Membrane Vesicles

Gram-negative and, recently discovered, gram-positive bacteria release membrane vesicles (MVs). MVs were first discovered to come from controlled blebbing of the outer membrane of gram-negative bacteria and, therefore, they are often called Outer Membrane Vesicles (OMVs). These OMVs have sizes between ~40 to 250 nm in diameter and they can have diverse functionalities, from communication among themselves or other microorganisms to traffic of molecules (**Figure 2.2a**) [56,57]. In addition to the OMV, there are other types of MV, like the outer-inner membrane vesicles (OIMV) for gram-negative bacteria which contain cytoplasmic and DNA content and they come from explosive cell lysis and cell budding (**Figure 2.1a**). Or the

explosive outer-membrane vesicle (EOMV), for either gram-negative and gram-positive bacteria, generated through explosive cell lysis and contains cytoplasmic and DNA content (**Figure 2.1a**). For gram-positive bacteria, there is also the cytoplasmic membrane vesicle (CMV) (**Figure 2.1b**) [58].

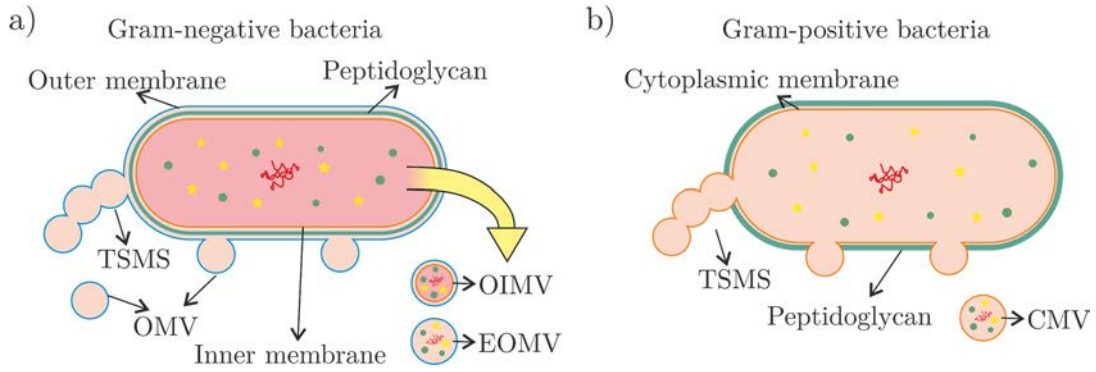

Figure 2.2: a) Schematic representation of the different types of membrane vesicles in gram-negative bacteria and b) gram-positive bacteria.

But the most interesting type of MV, for the present thesis, are the Tube-Shaped Membranous Structures (TSMSs), of which the simplest version is a chain of OMVs [58] (**Figure 2.1a**). The TSMS are tube-like protrusions of the cytoplasmic membrane, that is, a mixture of proteins and lipids and do not contain RNA and chromosomal DNA [58]. *Shewanella oneidensis* MR-1 is a gram-negative bacterium that produces chains of OMV that can elongate and turn into smooth filaments that act as a conduit of electrons between the cell and distant substrates (long-range ET) [49].

2.2.2.Aerobic vs. anaerobic respiration

Oxygen is the best electron acceptor, energetically talking and it is extensively used by a variety of species. When oxygen is used as electron acceptor, the respiration is called aerobic. However, when the electron acceptor is different from oxygen, it is called anaerobic respiration. In some environments, like water sediments at meters beneath the ground, oxygen is limited and bacteria have to find other electrons acceptors, like metal ions. Hence, some organisms, under oxygen-limited conditions, use metal ions to release their respiratory electrons. The group of bacteria that combine metal reduction with cellular respiration is called dissimilatory metal reducing bacteria (DMRBs) [53]. Two of the most known DMRBs bacteria are *Shewanella oneidensis* MR-1 and *Geobacter sulfurreducens*.

However, there are other types of bacteria that are not able to use oxygen as electron acceptor and they are strictly anaerobic. One of the most known bacteria is the cable bacteria from the family of the *Desulfobulbaceae,* which electrically couple sulfide oxidation to oxygen reduction in sulfidic sediments over millimeter to centimeter distances.

2.3.Main types of electrochemically active bacteria

2.3.1.*Geobacter sulfurreducens*

Geobacter sulfurreducens is a rod-shape, gram-negative bacteria able to make direct electrical contact with electrodes via outer-surface c-type cytochromes. It is one of the best known electrochemically active bacteria, and it is a DMRB. It is capable of having long-range electron transport along bacterial nanowire or conductive pili. These pili are 3 – 5 nm in diameter formed by protein filaments that are anchored to the cell envelope and have a metallic-like conductivity [5,26,59], which can be attributed to electron delocalization due to overlapping pi-pi orbitals of aromatic amino acids [3,60,61]. The electron transfer is driven by a wide diversity of c-type cytochromes associated with the inner membrane, the periplasm, and the outer membrane, together with the presence of conductive pili, see **Figure 2.3a** [27]. Some of the c-type cytochromes involved in EET are OmcB, OmcE or OmcS, as can be seen in **Figure 2.3a** [27]. *G. sulfurreducens* is the microorganism that produces the highest currents in pure culture [62] and it has been the first bacteria proposed in studies on current-producing biofilms.

2.3.2.*Shewanella oneidensis* MR-1

Shewanella oneidensis MR-1 is a rod-shape, gram-negative bacteria and DMRB. Therefore, it shows aerobic and anaerobic respiration, so it can grow under a wide range of conditions. *S. oneidensis* is one of the best-known metal-reducing bacteria (together with *G. sulfurreducens*) and it was among the first identified microorganisms capable of using minerals that contain Fe(III), Mn(III) or Mn(IV) as a final electron acceptor.

These bacteria are able to reduce Fe(III) without being in direct contact. This happens thanks to the release of flavins, a kind of shuttle molecule [44]. The role of flavins in promoting ET to electrodes have been widely studied in electrochemical studies [42,43,63,64]. Genetic studies revealed that some of the c-type cytochromes involved in EET are MtrA, MtrB, MtrC, OmcA and CymA, as can be seen in **Figure 2.3b**.

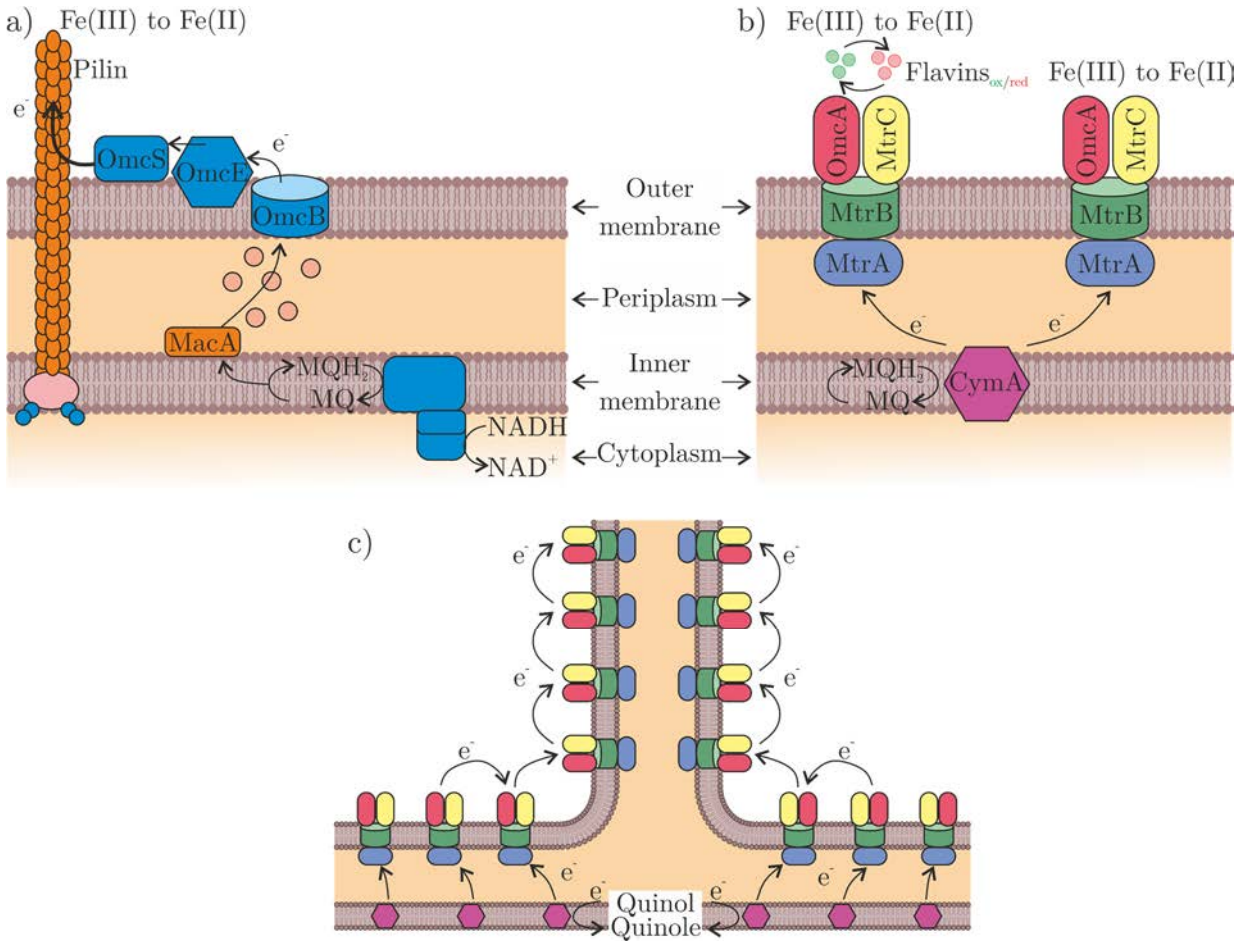

Figure 2.3: a) Representation of the miltiheme c-type cytochromes involved in *Geobacter sulfurreducens* EET [27]. b) Representation of the multiheme c-type cytochromes involved in *Shewanella oneidensis* MR-1 EET. c) Proposed structural model of the *S. oneidensis* nanowires or OMV chains [49].

In addition, *S. oneidensis* MR-1 is able to produce bacteria nanowires to promote long-range ET. These nanowires are extensions of the outer membrane and periplasm, especially the TSMS, rather than a pilin-based structure [49,50]. They are 50 – 100 nm diameter and they can turn into filaments of 10 nm diameter, and they appear under oxygen limitation growth conditions [4]. **Figure 2.3c** shows a structural model of these OMV proposed by El-Naggar *et al.* [49]. The conductivity of the nanowires, that can be up to 1 S/cm, is proposed to be an electron hopping mechanism between cytochromes and they present a p-type tunable electronic behaviour [61,65]. Several studies about the conductivity of *S. oneidensis* nanowires are published; however, all of them are under dry conditions and with non-living bacteria [4,50,66–68]. Due to this, the conductivity of such filaments is still under debate [2,6,45]. However, this could be due to the fact that *S. oneidensis* have several appendages like pili (3 – 5 nm diameter), flagella (8 – 10 nm diameter) and OMV (10 – 100 nm diameter) which could result in the study of them indistinctly

and as responsible of the EET when it is proposed that only the OMV are responsible for the EET [49]. In addition, *S. oneidensis* can grow under several growth conditions but only under a limitation of oxygen (as a final electron acceptor) develop the c-type cytochromes responsible for the EET [4,50]. Also, this conductivity has been tested in dried and chemically fixed nanowires. When the cells are alive, the cytochromes are too far apart, but they can migrate in the membrane to support long-range electron hopping along the filaments. However, it is suggested that when the filaments are dried and fixed, they are substantially shrunk (from > 500 nm in physiological conditions to 10 nm in dry and fixed conditions) and it brings the cytochromes close enough (ca. 1 nm) to facilitate the proposed electron hopping mechanism. These nanowires would significantly increase their attractiveness if they could obtain the same properties eliminating the fixation step, thus eliminating the toxic glutaraldehyde [2].

2.3.3.Cable bacteria of *Desulfobulbaceae*

Marine sediments are anoxic because oxygen is consumed by microorganisms at the surface of the sea. However, even in marine sediments, there is life, as the cable bacteria. Cable bacteria are long, multicellular microorganisms capable of transporting electrons from cell to cell along the longitudinal axis and up to centimeter distances. They are widespread in marine and freshwater sediments. Cable bacteria is a filament that connects oxygen reduction at the surface sediment with sulfide oxidation in the subsurface of those sediments, which can be several centimeters thick, generating electric currents through them [26]. **Figure 2.4a** shows this process schematically.

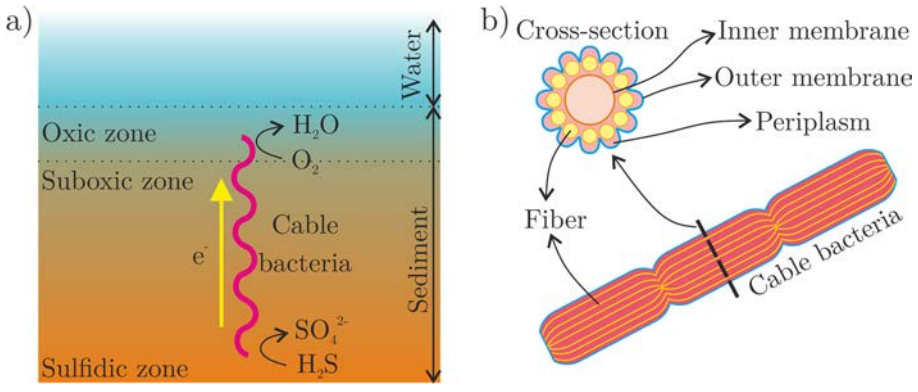

Figure 2.4: a) Schematic representation of the cable bacteria EET. b) Schematic representation of the cable bacteria and a cross-section of it. [9].

Cable bacteria is formed by cells, of an average length of 3 μm, that are joined end to end and form a filament that can be over 10 cm long [1]. Each multicellular filament contains several

unique ridges located between the cytoplasmic and the outer membrane, as shown in **Figure 2.4b**. These ridges are tunnel-like cellular structures that go from one cell to the next and are wrapped up in the gaps between cells, covering the entire filament in the outer membrane. It has been demonstrated that these ridges or periplasmic fibers are ~50 nm diameter, have high conductivity, up to 20 S/cm, and are able to sustain high current densities, up to 1 nA [1], nearly 1000 times more conductive than *S. oneidensis* MR-1 nanowires.

It is hypothesized that the outer membrane function as an insulator to prevent leakage of electrons out of the cell. Consistent with this, EFM measurements and cryo-TEM images showed a higher concentration of ridges in the joint between two cells of the filaments [7,9,69]. Although neither the mechanism of the ET, nor the biological composition of the ridges are known, the best hypothesis for the conductivity of the cable bacteria is an electronic conduction through a multi-step hopping mechanism along their continuous conductive conduits or periplasmic fibers since some studies showed that an ionic conduction could not be possible [1,70].

2.4.Bioapplications

The increasing use of electronic devices is consuming substantial energy and rare resources for material fabrication, together with expansive volumes of toxic waste, which is not sustainable. Therefore, there is the emerging field of bioelectronics which includes the technology developing electronic devices from biological components or mimicking them. These electronics produce little waste and toxic components and are more economical. In addition, since the material comes from living microorganisms, bioelectronics could have the capacity of self-repair and replication. [2,6].

Microorganisms that have EET capabilities have been exploited for various biotechnological applications. These microorganisms have been explored for bioremediation of the environmental contaminants, to produce bioenergy and to produce nanomaterials with novel properties [26]. In addition to all these capabilities, microorganisms offer the possibility of being genetically modifiable to get new electrical connections and provide new functionalities. For example, *G. metallireducens* GS-15 and *S. oneidensis* MR-1 can respire on contaminant water-soluble uranium, U(VI), reducing it to U(IV), insoluble in water and, therefore, immobilizing it [71]. Fe(III)-oxidizing microorganisms can extract copper, gold and other metals from low-grade deposits [72].

Also, protein-based scaffolds, which are very stable, can be used to organize conductive metals at the nanoscale [2].

To move towards green electronics, living microorganisms can be used to build electronic devices, like the naturally conductor *G. sulfurreducens* biofilms that can function as supercapacitors or transistors [73]. Also, E. coli biofilms can be made conductive by exposing the biofilms to gold nanoparticles [74]. Or, *S. oneidensis* MR-1 nanowires present long-range ET based on electron hopping and they might be one possible candidate to substitute the organic semiconductor materials of organic light-emitting diodes (OLEDs), organic solar cells or biosensor. In general, electrically conductive pili or proteins are of great interest in bioelectronics [20,21,75].

3. Dielectric permittivity

Most studies of the conduction properties have been centered on the DC current conduction. In the present thesis, we propose to measure the dielectric constant response of the wires in order to shed further light on their electrical properties. For this reason, this chapter presents a brief introduction to the dielectric permittivity. Also, it will explain its relevance in biology and in the present thesis.

3.1.Dielectric response of materials

Michael Faraday discovered that when the space between the two plates of a condenser was filled with a dielectric material, the capacity increased a factor κ, characteristic of such dielectric material, due to the weakening of the electric field and increased the stored energy. Such factor is related to the electric permittivity as $\kappa = \frac{\varepsilon_r}{\varepsilon_0}$. Although the atoms and molecules are electrically neutral, they are affected by electric fields as they have positive and negative charges and may respond to external fields.

An atom can be considered as a tiny nucleus, positively charged, surrounded by an electronic cloud, negatively charged. In some atoms, this cloud is spherically symmetric and the 'center of charges', coinciding with the positive charges, is located in the center of the molecule or atom. In this case, the atom or molecule has a zero-dipole moment (**Figure 3.1a**). However, when an electric field is applied, the negative and positive charges experience forces in opposite directions and they separate until the attractive force that they exert between them equilibrates the forces due to the external electric field. In this case, the molecule is polarized and it has an electrical dipole (**Figure 3.1b**).

Consequently, one of the most interesting properties of insulator materials is its electric relative permittivity or the dielectric constant (ε_r). It is an intrinsic property of a material that defines how it polarizes when an electric field is applied. When the material polarizes, permanent or induced dipoles reorient under the application of an external electric field, and they generate an additional electric field in the material that screens the external one. The dielectric constant

describes the strength of the electrostatic interaction between two separated charges of the medium.

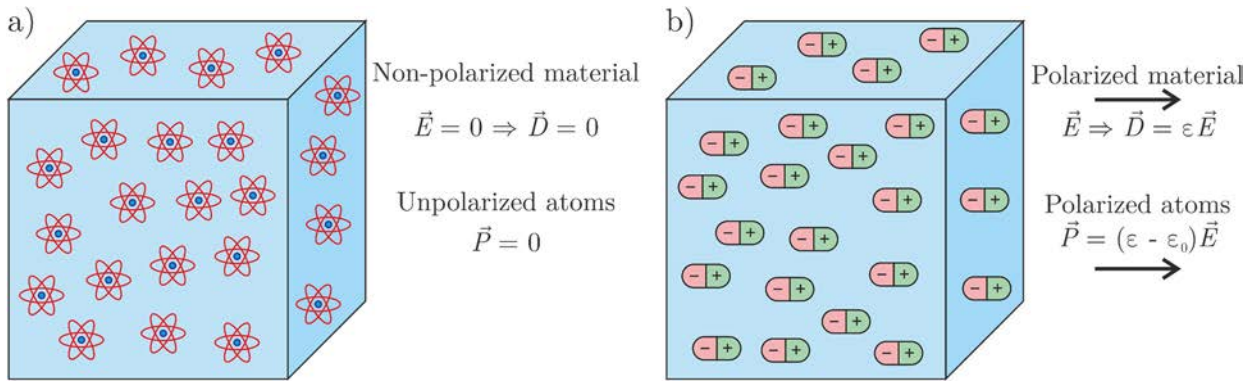

Figure 3.1: a) Schematic representation of a non-polarized material and its dipoles. b) Schematic representation of a polarized material and its dipoles.

The dielectric constant in linear systems is defined as eq. (3.1), where $\vec{D}$ is the electric displacement field, ε_0 is the dielectric constant of the vacuum ($\varepsilon_0 = 8.85 \times 10^{-12\backslash \text{ F/m}}$), $\vec{E}$ the electric field and $\vec{P}$ the polarization.

$$\vec{D} = \varepsilon_0 \varepsilon_r \vec{E} = \varepsilon_0 \vec{E} + \vec{P} \tag{3.1}$$

As can be observed from eq. (3.1), a material with high dielectric constant polarizes more in response to an electric field than a material with lower electrical permittivity; and hence, it screens more the electric field

The dielectric constant depends on the frequency of the electric field applied, showing that the different types of dipoles that form a material have different relaxation times. The frequency dependence of ε_r is frequently represented as a complex number $\varepsilon_r \rightarrow \widehat{\varepsilon_r}(\omega) = \varepsilon' - i\varepsilon''$. The modulus is correlated to the strength of the polarization, and the phase is correlated with the phase difference between the externally applied field and the polarization field, which usually is associated with the losses in the material. Depending on how the dipole is formed, we can distinguish different types of polarization contributions:

- **Electronic polarization**: in the PHz range. The dipole is formed by the electron cloud of the atom that is displaced from its nucleus.
- **Ionic polarization**: in the THz. The dipoles are formed from oppositely charged ions in the material structure.

- **Orientation polarization**: in the GHz. The dipole that reorients is the whole molecule, like water.
- **Interface polarization**: in the kHz. Mobile charges at the interface of different materials form different space charges, like the electric double layer.

As reference values, the electrical permittivity of air is $\varepsilon_{air} = 1$, water is $\varepsilon_{H_2O} = 80$ and the electrical permittivity of a conductive material tends to infinity $\varepsilon_{metal} \to \infty$.

3.2.Importance in biology

One of the main factors governing the electrostatic interaction is the relative permittivity. Therefore it has high relevance in the dielectric behaviour of matter, and its importance spans different fields of science, such as physics, material science, chemistry or biology. Some examples where the dielectric constant is important are: in solar cells to control the efficiency, in radars, in optoelectronic devices or in diverse biological processes like the action potential in a neuronal cell.

In particular, the dielectric properties in biology are of utmost importance. Electrostatic interactions play a central role in many diverse biological processes. In order to understand these interactions, their nature and strength, first, an understanding of the physicochemical properties of molecules in aqueous solutions is necessary. During the last few years, there have been several studies to understand the effect of the solvent on the solute properties since they are needed to understand major biological problems such as protein folding or structure-based drug design. To understand the properties of an aqueous solution, models of the solute, the solvent and the interaction between them are required [76,77]. But in all of these models, the dielectric constant is a parameter that must be known.

In cell membrane biophysics, the dielectric properties are of key importance. The cell membrane is a lipidic bilayer whose structure is formed by two sheets of phospholipids, glycolipids and proteins that maintain the equilibrium between the interior and the exterior of the cell. It regulates the entry and exit of substances to the cell. Trapped in the membrane, there are several proteins and other biomolecules, like ionic pumps or ionic channels, with several biological and structural functionalities. These biomolecules can change the physical structure of the membrane, allowing the flow of ions through it, thus, changing the conductance of the membrane. When the ionic channels open, a flow of ions through the membrane is allowed; therefore, it acts as a conductor.

However, when the ionic channels close, the membrane behaves as an insulator, maintaining different ionic concentrations between the intracellular and the extracellular components. The partitioning of ions in the cell membrane is dictated by Born's energy, which depends on the difference between the dielectric constant of the membrane and that of the water. The low dielectric constant gives almost negligible ionic concentration in the cell membrane from where its insulating nature (**Figure 3.2c**).

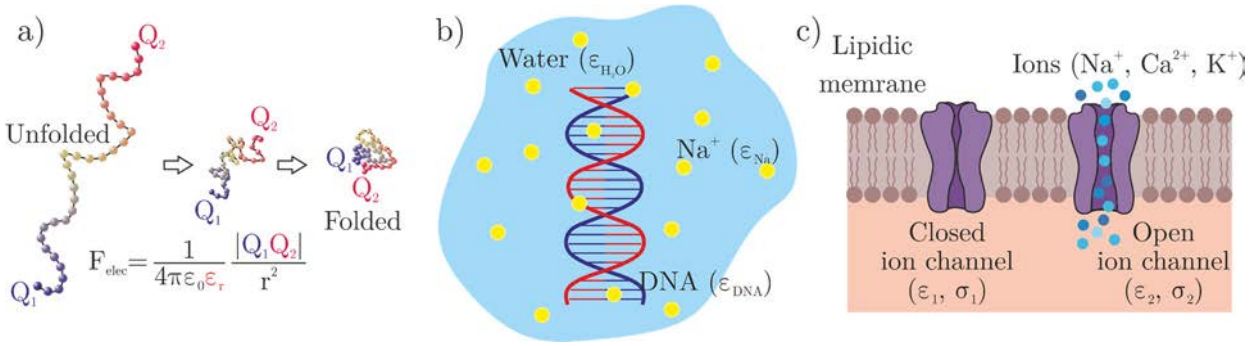

Figure 3.2: a) Schematic representation of the protein folding interaction. b) Schematic representation of the protein-ion carrier interaction. c) Schematic representation of a lipidic membrane and a closed and open ion channel.

In addition, the human genome encodes tens of thousands of different proteins, which perform a vast range of biological functions. Several carry electrons or small metabolites, such as oxygen or carbon dioxide. Others are enzymes. Others develop mechanical scaffolds within the cell or function as motors. Others channel electrons through membranes and produce a flow of protons in the opposite direction. A significant and important group is involved in the transport and processing of information. This includes proteins that bind to DNA in response to chemical signals and activate or block the expression of groups of genes. Again, the electrostatic effect plays a key role in determining these protein interactions since many of these functions are driven or directed by electrostatic interactions. Thus, the function of most proteins requires recognition and binding of other molecules [78]. As said, the dielectric constant determines the degree by which electric fields are screened by the protein microscopic electric dipoles. As such, it has a strong effect in charge-charge and charge-dipole interactions in the proteins, and hence, in the electrostatic energy contribution in protein folding (**Figure 3.2a**), and protein-protein, protein-DNA, protein-charged ligand interactions or DNA-ion interaction (**Figure 3.2b**) [79].

3.3.How does one measure the dielectric constant?

The electrical permittivity can be measured in many ways in the bulk macroscopic form of the material. One technique used is **impedance measurements.** They are used to resolve processes of electrical polarization according to the relaxation frequencies or time constant of the material. In this technique, the material under study is placed between two electrodes and the impedance is measured. For the case of proteins, a solution with proteins or dry crystal powders is prepared. However, with this technique, the obtained electrical permittivity reflects both the dielectric properties of the sample (for example proteins) as well as those of the sample-solvent (for example protein-solvent) interface [80], which is a relative electrical permittivity that combines the sample and the medium dielectric constant. On the other side, measurements performed on dry crystal powders only partially reflect the structure and dynamics of proteins in physiological conditions [78]. As a result, until today, there is a large uncertainty on the specific value of the dielectric constant of, proteins, which have values spanning a relatively wide range; usually, it is ε_r~$2-5$, but also includes larger values, such as $\varepsilon_r = 8$ or $\varepsilon_r = 20$ [81]. Although, the most used value is ε_r~4, which is believed to account for electronic polarization and small backbone fluctuations, although direct supporting experimental evidence is scarce.

There are **computer simulations** where the effective electrical permittivity of materials is calculated, from molecular dynamics simulations and from first principles. However, there is a lack of experimental studies validating the conclusions [78,81–83].

Also, it can be measured by **reflecting radiation** techniques. In this technique microwaves or radiofrequency radiation are directed onto the surface at a right angle, then a portion of the energy is reflected from the surface. The quantity of radiation reflected is dependent mainly on the dielectric constant [84–86]. Or measuring the electromagnetic resonating modes, using the **dielectric resonator** technique where the resonant frequency of the dielectric material when an electromagnetic field is applied is measured [87,88]. However, this technique is suitable only for low loss materials and low dielectric constant otherwise, a problem with impedance matching could occur.

The permittivity is not constant with the frequency of the field applied, but it also depends on humidity, temperature or the position in the medium (among other parameters). Usually, it is

measured and defined at the macroscale, but in several cases, it should be studied at the nanoscale. An example of it is the recent discovery where nano-confined water has different polarization properties than the bulk water [89]. Other examples include determining the dielectric constant of biological molecules, like proteins or DNA, which have a microscopic nature. Some techniques able to characterize the dielectric properties at the nanoscale are now available, based on optical or scanning probe microscopies.

Fluorescent spectroscopy techniques use fluorescent probes that measure the polarizability of certain functional samples have been developed [90,91]. The main disadvantage of these techniques is the impossibility of obtaining quantitative results; only qualitative measurements are feasible. This is because there is a lack of comprehensive theoretical expressions to quantify the data and because the measurements have important crosstalk effects and are not only sensitive to the polarization, but also to stress and other physical magnitudes.

Another technique to measure the dielectric constant at the nanoscale is the **Electrostatic Force Microscopy (EFM) technique**. One of the advantages of this non-invasive technique is the ability to work under air, vacuum or liquid environments. The EFM allows us to map the intrinsic dielectric properties at the nanoscale through label-free measurements. However, it is time-consuming and it is difficult to obtain quantitative results. The EFM technique is the one used in this thesis in order to characterize the electrical permittivity of different samples; therefore, it is explained in detail in Chapter 4.

Some values of biological molecules or structures measured at the nanoscale, locally in air or humid conditions and through the EFM technique are shown in **Figure 3.3**. In this figure, we can observe that the dielectric constant of lipids is ε_{lipid}~2, measured on DOPC patches ($\varepsilon_{DOPC} = 1.9 \pm 0.3$) and cholesterol crystals ($\varepsilon_{chol} = 2.1 \pm 0.3$) [13]. The one of proteins is $\varepsilon_{protein}$~4, measured in a T7 bacteriophage virus capsid ($\varepsilon_{capsid} = 3.5 \pm 0.5$) [14] and on a virus tail ($\varepsilon_{tail} = 3.4 \pm 0.4$) [92], on a submicrometric monolayer patch of bacteriorhodopsin ($\varepsilon_{BR} = 3.3 \pm 0.3$) [13] and on bacterial polar flagella ($\varepsilon_{flag} = 4.4 \pm 0.7$) [93]. The DNA has an electrical permittivity of $\varepsilon_{DNA} = 8.5 \pm 1.4$, measured on a T7 bacteriophage DNA and it is mainly due to its sugar-phosphate backbone bonds [92]. Also, the electrical permittivity of a virus $\varepsilon_{virus} = 6.3 \pm 0.4$ was measured on a T7 bacteriophage [14]. Finally, the electrical permittivity of a full bacteria has

been differentiated from gram-positive and gram-negative bacteria and in dry (ε_{bact}~$3-5$) or humidity (ε_{gram-}~$6-7$, ε_{gram+}~$18-19$) demonstrating a significant contribution of moisture, which has a bigger effect on gram-positive bacteria due to the thicker and more hydrophilic envelope [12].

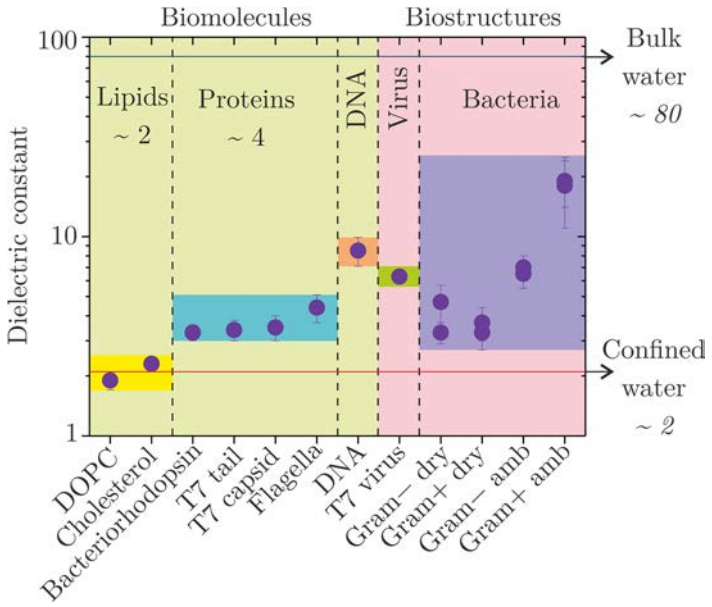

Figure 3.3: Values of the relative dielectric constant of several supramolecular biological micro/nanostructures measured by Electrostatic Force Microscopy. Data from [12–14,92,93].

In this thesis, we aim to study the polarization of electrochemically active bacteria and their appendages as the polarization plays a key role in the EET mechanisms. The interest also stems out from the increasing interest in using such bacteria as a biosensing platform [2,20,21].

4. Scanning Dielectric Microscopy

This chapter presents a brief introduction about Scanning Dielectric Microscopy, the main technique used in this thesis. Also, a brief introduction to Atomic Force Microscopy will be explained. At the end of this chapter, the novel methodology for the dielectric constant quantification used in this thesis is explained, showing some experimental results.

4.1.Scanning Probes Microscopies

The local probe microscopies technologies started in 1981 with the invention of the Scanning Tunneling Microscope (STM) by G. Binnig *et al.* [94]. For the first time, surface microscopy using tunneling current was developed and topographic pictures of surfaces on an atomic scale were obtained in vacuum conditions. For this discovery, G. Binning and H. Roher won the Nobel prize in 1986. However, this technique was only valid for conductive samples. To overcome this problem, the same year (1986), G. Binning *et al.* [95] invented the Atomic Force Microscopy (AFM), a technique capable of measuring forces as small as 10^{-18} Newtons. This technique combined the principles of STM and the stylus profilometer and had the advantage that it did not damage the sample and it could measure the surface of insulator samples. Between 1987 and 1991, different modes of AFM were invented (dynamic AFM in Amplitude Modulation (AM) mode [96] and dynamic AFM in Frequency Modulation (FM) mode [97]). Finally, after different discoveries, the true atomic resolution with AFM arrived in 1995 by Franz J. Giessibl, who reached atomic resolution of the Silicon (111)-(7x7) surface by AFM [98].

Scanning probe microscopy covers several related technologies for imaging and measuring surfaces on a fine scale, down to the level of molecules and groups of atoms with atomic resolution. It can scan surfaces from microns to nanometers height. SPM technologies are based on the interaction between a sharp tip (probe) (typically 3 – 50 nm radius of curvature) and a sample

surface. The tip is on a cantilever whose stiffness is characterized by the equivalent spring constant which can go from 0.01 N/m to 100 N/m. When the tip moves in proximity to the investigated object, forces of interaction between the tip and the surface influence the movement of the cantilever. Later, this movement is passed to a feedback system. In these systems, the probe scans the sample like a deaf person reads braille with a finger. SPM instruments are composed of three parts: the probe, the scanner and the controller.

The **probe** senses the sample surface. It is placed close to the sample surface (on the nanometer level) with the help of a piezo actuator and a feedback system. So, it can feel short-range forces with the surface. This interaction depends on local physicochemical material properties, probe-sample distance and probe type. Depending on the SPM technique, very different types of probes can be found, although most of them follow the structure of a needle-like shape with a very sharp apex.

The **scanner** is responsible for the precise movement and positioning of the sample and the probe. It is composed of three piezoelectric actuators that move the sample in X, Y and Z directions with sub-nanometric precision. Therefore, the location (X, Y) of either the probe or the sample and the probe sample distance (Z) are controlled very accurately (down to atomic level).

The **controller** is responsible for the scanner movement and the recording of the probe-sample interaction. These movements are in the lateral direction (X, Y), usually performed at constant rates. Since it is typically a line by line image acquisition, one direction (e.g., X) is performed faster than the other direction (e.g., Y). The vertical direction (Z) is of special interest in these systems since it is normally dominated by a feedback control system that tries to maintain constant the desired probe-sample interaction. Thus, the displacement in Z length of the scanner, which, together with the (X, Y) position of the tip, form the image of the sample surface properties.

The SPM techniques have been mostly used as characterization techniques, where different properties of the samples are obtained depending on the feedback used. The three most common scanning probe techniques are: AFM that measures the interaction force between the tip and surface; STM that measures a weak electrical current (tunneling current) flowing between the conductive tip and the conductive sample; and Near-Field Scanning Optical Microscopy (NSOM)

that scans a tiny light source very close to the sample. In this thesis, we will mainly focus on the AFM, which has been used to acquire topographical images of the sample, and especially on the Electrostatic Force Microscopy (EFM) technique to obtain the electrostatic forces and characterize, electrically, the samples. These methods are further explained in the following sections.

4.2.Atomic Force Microscopy

As said before, in 1986, Binning *et al.* [95] invented the AFM which overcome the limitation of the STM, which only can measure conductive samples. Therefore, it offered more versatility to researchers to address the nanoscale level.

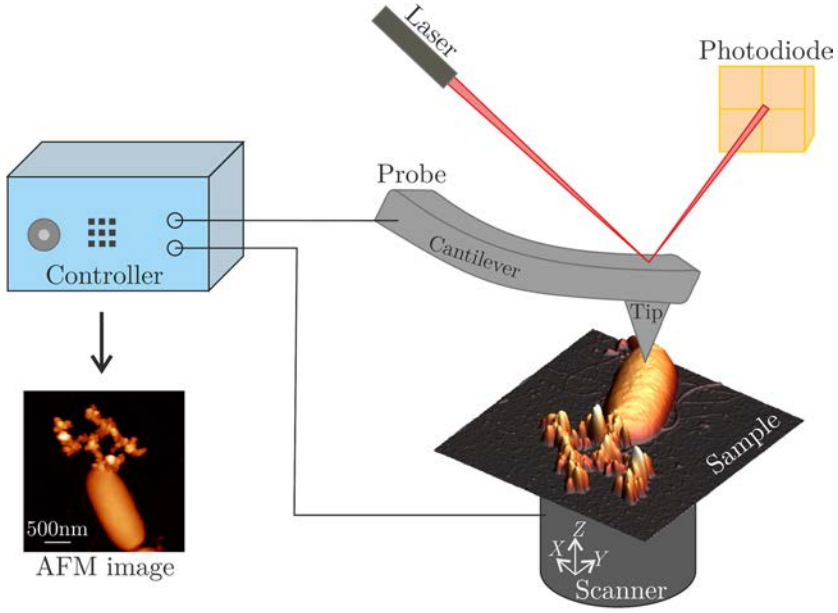

Figure 4.1: Schematic illustration of an AFM setup

The AFM is based on a small cantilever (hundreds of μm long, tens of μm wide and few μm thick), with a sharp tip at its end whose apex is in the nanometer range. The cantilever deflection provides a measure of the interaction force with the sample and it is measured while the tip scans it. The deflection is measured with a laser that reflects on the cantilever and hits in a four-quadrant photodiode, as it is shown in **Figure 4.1**.

The force detected by the AFM is in the range of pN and it is limited by the thermal noise of the system or the vibrations of the environment. The AFM can work under a wide range of conditions, such as liquid, air or vacuum conditions, and can study, not only conductive samples

but also insulating ones. The use of forces can also be used to detect physical and physicochemical properties. The good force resolution (~pN) and the good spatial resolution allow the study of capillary forces [99], Van der Waals forces [100] or chemical affinity [101], among others. In addition, the tip can be functionalized allowing the study of ligand-receptor interactions [102], cell surface interactions [103] or protein folding [101], among others. Finally, properties such as the Young modulus, the dielectric constant or magnetic properties at the nanoscale can be measured [104,105], as an example. As a drawback, the AFM is a slow technique and during the experiment, the tip or the sample can get damaged if not carefully controlled.

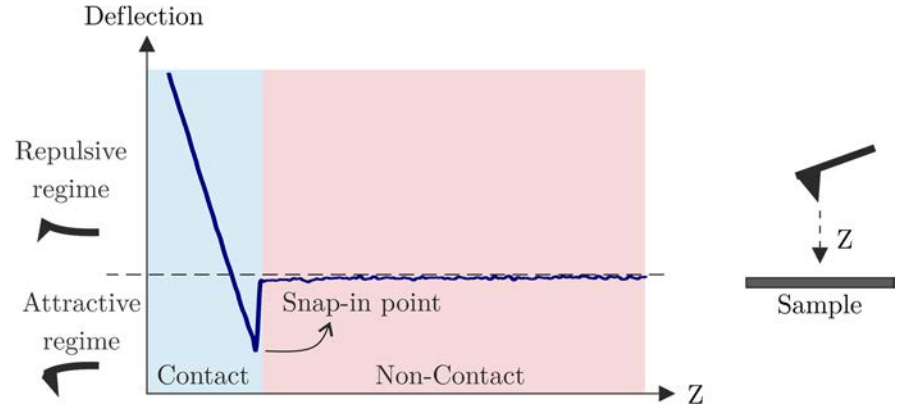

Figure 4.2: Schematic illustration of the AFM force regimes as a function of piezo displacement (Z).

The main use of the AFM is to acquire topographic images thanks to the good spatial resolution, which can go down to the atomic level. The probe-sample interaction depends on the relative position of the probe with respect to the sample, as shown in **Figure 4.2**, which shows the cantilever deflection as a function of the piezo displacement. At long distances, the probe and the sample do not interact, and no deflection is observed. When the probe approaches towards the sample, short-range Van der Waals forces (< 10 nm) start to be relevant and bends the probe towards the sample (negative deflection) until instability occurs and brings the tip in contact with the sample (snap-in point). As the piezo continues to expand, the repulsive force increases until it balances the downward bending of the probe (zero-deflection state). Finally, while the piezo continues expanding, and the probe pushes towards the sample, the repulsive force bends the probe upwards (positive deflection). Depending on the region in which the probe-sample interaction is established, the imaging technique can be classified into three different modes:

- **Contact mode**: The tip and the sample are in constant contact. The probe-sample interaction is in the repulsive regime and positive deflection (**Figure 4.2**). In this mode, the feedback control, to maintain the force constant, is made over the deflection of the cantilever. The desired deflection setpoint is a zero-deflection point, where no force is applied, and it is the less aggressive point. However, this is not possible due to the instability of the system, and so, a low force is applied to the sample. Since this mode maintains the tip in constant physical contact with the sample, the sample or the tip can get damaged while scanning. For this reason, usually soft cantilevers ($k < 1$ N/m) and low scan velocities are used.
- **Dynamic mode**: The tip and the sample are in intermittent contact (**Figure 4.2**). This mode can also be called tapping mode or AC mode. The cantilever mechanically oscillates close to its resonant frequency to obtain maximum oscillation, thanks to a piezoelectric actuator attached to the probe holder. In this mode, the feedback control is made over the oscillation amplitude, which will decrease as the probe gets close enough to the sample to contact with it in the bottom part of the oscillation. The oscillation amplitude is recorded through a lock-in amplifier which filters out the contribution from frequencies that are not the exciting frequency. In addition, the lock-in amplifier reads the dephasing between the excited oscillation and the measured one, information that can complement the topography image giving some material composition or adhesion information. Dynamic mode is less aggressive than the contact mode since the probe-sample interaction time reduces; therefore, the possibility to modify the sample and/or the probe decreases. In addition, shear forces exerted by the tip on the sample while performing the image are drastically reduced.
- **Non-contact mode**: The tip and the sample are not in physical contact. The probe-sample interaction is in the attractive non-contact regime (**Figure 4.2**). The cantilever oscillates (at small amplitudes, < 10 nm) at its resonance frequency very close to the sample (~10 nm). The attraction force produces a decrease in the resonance frequency of the cantilever as the probe-sample distance decreases. In this mode, the feedback control is made over the resonance frequency, which detects the shift in frequency (or amplitude) and affects the vertical displacement of the scanner to maintain the desired

resonance frequency. The main disadvantage is that it is difficult to maintain good feedback since the probe hovers over the sample, and either the probe nor the sample suffer modifications, being especially challenging in topographically tall samples.

In addition to topographic imaging modes, there are a number of modes and techniques to measure physical material properties, such as Magnetic Force Microscopy (MFM) [106,107] for magnetic properties, Piezoelectric Force Microscopy (PFM) [108–110] for piezoelectric properties, Kelvin Probe Force Microscopy (KPFM) [111,112] or Electrical Force Microscopy (EFM) [92,113–116] for electrical properties, among others. In this thesis, I will use EFM for the characterization of electrically active bacteria. Therefore, this technique will be explained in detail in the following section.

4.3.Electrostatic Force Microscopy

Electrostatic Force Microscopy (EFM) is an AFM technique where electrostatic forces are measured. It is a two-pass technique where, in the first pass, the topographical image is acquired using conventional AFM imaging. In the second pass, the tip is lifted until a certain height, a voltage is applied between the tip and the sample and the electrostatic force (between the tip and the sample) is measured. In this technique, conductive tips and substrates are needed, and often, physical models are required in order to quantify the data and convert it into physical magnitudes (e.g., dielectric constant).

The most basic EFM mode is DC-EFM in which a dc voltage (V_{dc}) is applied to the tip, which would cause a static bending of the cantilever. In this technique, the dielectric properties of the sample can be extracted if the surface potential (V_{sp}) is known (eq.(4.4)), although at high DC-voltages the error induced by not knowing the V_{sp} is negligible. In addition, the sensitivity is limited by the thermal and electronic noise, giving a poor signal to noise ratio [117].

In this thesis we are going to use a dynamic scheme, AC-EFM, in which an ac voltage (V_{ac}) is applied to the tip, eq. (4.1).

$$V_t = V_{\mathrm{dc}} + V_{\mathrm{ac}}\cos(\omega t) \tag{4.1}$$

where ω is the frequency of the ac voltage applied between the tip and the sample. As known, the capacity of a condenser depends on the geometry of the metals conforming it and on the dielectric

constant between the metals. In our case, since we consider that the dielectric material is homogeneous, isotropic and the geometry is maintained constant, the capacity only depends on the tip sample-distance and the dielectric constant, $C(z, \varepsilon_r)$. Considering that the energy, E, of a condenser is:

$$E = \frac{CV^2}{2} \tag{4.2}$$

where $C = C(z, \varepsilon_r)$ and $V = V(t)$. Making the derivative of eq. (4.2) respect to z we obtain the force acting on the plates, given by eq. (4.3).

$$F = \frac{\partial E}{\partial z} = \frac{1}{2}\frac{\partial C}{\partial z}(V(t) - V_{sp})^2 \tag{4.3}$$

If we take into account $V(t)$ in eq. (4.1) and that $\cos^2(\phi) = \frac{1}{2} + \frac{1}{2}\cos(2\phi)$, we obtain three different contributions to the force, one in dc (eq. (4.4)), another in the first harmonic (ω) (eq. (4.5)) and the last one at the second harmonic (2ω) (eq. (4.6)),

$$F_{dc} = \frac{1}{2}\frac{\partial C}{\partial z}\left((V_{dc} - V_{sp})^2 + \frac{V_{ac}^2}{2}\right) \tag{4.4}$$

$$F_{\omega} = \frac{\partial C}{\partial z}(V_{dc} - V_{sp})V_{ac}\cos(\omega t) \tag{4.5}$$

$$F_{2\omega} = \frac{1}{4}\frac{\partial C}{\partial z}V_{ac}^2\cos(2\omega t) \tag{4.6}$$

As we can infer from these equations (eq. (4.4), eq. (4.5) and eq. (4.6)), the forces of the two first harmonics, F_{dc} and F_{ω}, provide mixed information about the dielectric properties of the sample, by including a dependence on the capacitance gradient ($\partial C/\partial z$), and the surface potential, V_{sp}. However, the second harmonic, $F_{2\omega}$, only includes the derivative of the capacitance, which only contains contribution from the dielectric properties of the sample. Therefore, in this thesis, we are going to use the AC-EFM technique and focus on the detection of the 2ω mode. For simplification, hereon, we will refer to it simply EFM).

The EFM measurements can be performed in Frequency Modulation (FM-EFM) or in Amplitude Modulation (AM-EFM) depending on the detection system. In the FM-EFM, the frequency shift is detected since electrostatic forces lead to a slight modification of the cantilever spring constant. Meanwhile, in AM-EFM, the electrical oscillation amplitude of the cantilever is measured. FM-EFM has , spatial resolution theoretically; however, the setup implementation is

more complex [14,118]. For this reason, we are going to use AM-EFM. (For simplification, hereon it is going to be mentioned as only EFM).

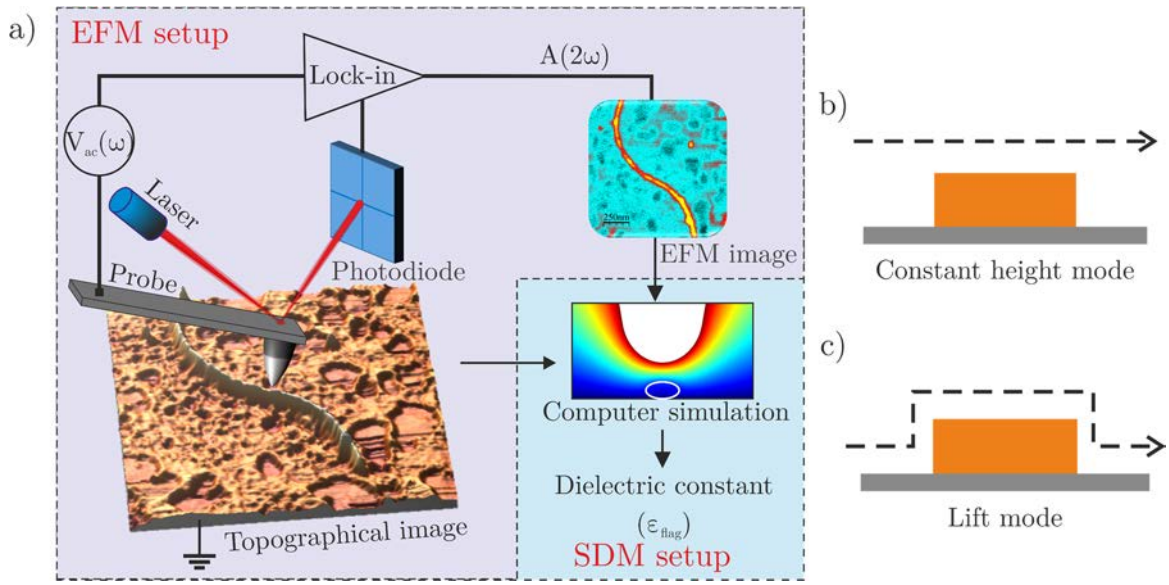

Figure 4.3: a) Schematic representation of the EFM (in purple) and the SDM (in blue) setup. b) Schematic representation of the constant height mode and c) of the lift mode.

As mentioned before, the EFM is a two-pass AFM technique (purple zone of **Figure 4.3a**). The first pass works like the standard AFM, a topographical image is acquired in tapping or constant mode with the electrical oscillation switched off. Then, the tip is lifted until a certain height, a voltage is applied, by a lock-in amplifier, between the tip and the sample (V_{ac}) and the electrostatic force at the second harmonic ($A_{2\omega}$) in off-feedback mode, recorded by the photodiode, is measured using the lock-in amplifier. There are two different modes depending on how the tip performs the second pass and flies over the sample:

- **Constant height mode**: in the second pass of this mode, the tip hovers parallel to the metallic substrate at a given **tip-substrate** distance. This mode does not have a topographical crosstalk effect [119], but still, it does not show the intrinsic polarization properties of the sample since they also depend on sample geometry. The higher contrast is usually obtained from the highest point of the sample since the tip passes closer to it. This method is not suitable for high non-planar samples because the tip could easily crash with the sample or fly too far from it (**Figure 4.3b**).
- **Lift mode**: in the second pass of this mode, the tip hovers parallel to the sample at a given **tip-sample** distance. This mode allows us to approach closer to the sample and obtain

maximum contrast from the entire sample. However, the fact that the tip moves up and down during the electrical pass introduces topographic crosstalk artifact that can mask the intrinsic properties of the sample [15,119] (**Figure 4.3c**).

An experimental aspect to consider is to determine which frequency of V_{ac} is suitable for the experiments. As explained in the supplementary information of ref. [120], the spectra of $A_{2\omega}$ as a function of frequency is not flat since it is strongly convoluted by the mechanical spectra of the cantilever. Although we will find higher signal if we choose the electrical frequency, ω_{elec}, close or at the mechanical resonance frequency, $\omega_{r,mech}$, it is better to choose it well below that frequency ($\omega_{r,mech}$), where the spectra of $A_{2\omega}$vs. f is flat. In this way, we will avoid contributions from the mechanical response of the cantilever.

The photodiode of the AFM system coupled to the lock-in detector is used to obtain oscillation amplitude and phase at the second harmonic ($A_{2\omega}$). The amplitude, $A_{2\omega}$, can be related to the force of eq. (4.6), $F_{2\omega}$, via eq. (4.7), using Hooke's law ($F_{2\omega} = kA_{2\omega}$) [14].

$$\frac{\partial C}{\partial z} = \frac{2\sqrt{2}}{V_{\mathrm{ac}}^2}\frac{k(A_{2\omega}[V] - OffsetLockin)}{mG} \tag{4.7}$$

where V_{ac} is the RMS voltage amplitude ($V_{pictopic} = \sqrt{2}V_{RMS}$), G is the lock-in gain, k the equivalent spring constant, m the optical lever sensitivity (in [V/m]) and $OffsetLockin$ is the zero correction of the lock-in.

4.4.Scanning Dielectric Microscopy

EFM images are strongly dependent on the tip and sample geometries; therefore, they give qualitative information about the dielectric properties under study. Scanning Dielectric Microscopy (SDM) combines the EFM measurements with computer simulations to obtain quantitative information about the measurements. **Figure 4.3a** shows a schematic representation of the SDM setup, stressing with the blue square the differentiation from the EFM setup. This quantification is not easy and different aspects must be considered [114].

In the EFM measurements, the tip geometry plays an important role. The force measured is related to the capacitance gradient ($\partial C/\partial z$) of the full probe-sample system. However, each part

of the system, apex, cone and cantilever, can have different contributions and dependencies with the tip-sample distance and the dielectric constant of the sample.

$$\frac{\partial C_{tot}(z,\varepsilon_r)}{\partial z} = \frac{\partial C_{apex}}{\partial z} + \frac{\partial C_{cone}}{\partial z} + \frac{\partial C_{cantilever}}{\partial z}$$

The variation of the cantilever contribution is negligible as compared to the cone and apex for the nanometric displacements of the probe [121]. Therefore $\frac{\partial C_{cantilever}}{\partial z}$ can be considered as a background offset in the measurements. Analytical expressions for the case of the apex and cone contributions are scarcely available. They are only available for two cases: a probe interacting with a plane metallic surface [122] or a probe interacting with a very thin ($h < 50-100$ nm) dielectric film [123]. Both cases can be described by the analytical expressions of eq. (4.8) and eq. (4.9).

$$\frac{\partial C_{apex}}{\partial z}(z,\varepsilon_r) = 2\pi\varepsilon_0 \frac{R^2(1-\sin\theta\}}{\left(z+\frac{h}{\varepsilon_r}\right)\left(z+\frac{h}{\varepsilon_r}+R(1-\sin\theta)\right)} \tag{4.8}$$

$$\frac{\partial C_{cone}}{\partial z}(z,\varepsilon_r) = \frac{2\pi\varepsilon_0}{\ln\left[\tan\left(\frac{\theta}{2}\right)\right]^2}\left[\ln\left(\frac{H}{z+\frac{h}{\varepsilon_r}+R(1-\sin\theta)}\right) - 1 + \frac{R\frac{\cos^2\theta}{\sin\theta}}{z+\frac{h}{\varepsilon_r}+R(1-\sin\theta)}\right] \tag{4.9}$$

where ε_0 is the electrical permittivity of the vacuum, ε_r is the relative electrical permittivity of the sample, R the tip radius, θ the cone angle, h the thickness of the sample and H the cone height. For the case of a plane metallic surface, $h = 0$ in eq. (4.8) and eq. (4.9).

Due to the lack of accurate expression for the capacitance gradient of the system, finite element numerical simulations are most often needed to quantify EFM measurements [12,14].

4.4.1.Quantitative analysis of EFM measurements

The quantification process to obtain the dielectric properties consists of two parts: tip-sample system geometry calibration and dielectric constant extraction [114]. The tip-sample system geometry calibration consists of obtaining a geometrical model as realistic as possible since the same experimental signal, quantified with different geometrical models, will lead to a different intrinsic dielectric constant of the sample. In order to do so, first, one characterizes the tip geometry, that is, the tip radius and the cone angle since the commercial specifications are not very accurate and sometimes the values can differ from the specified ones.

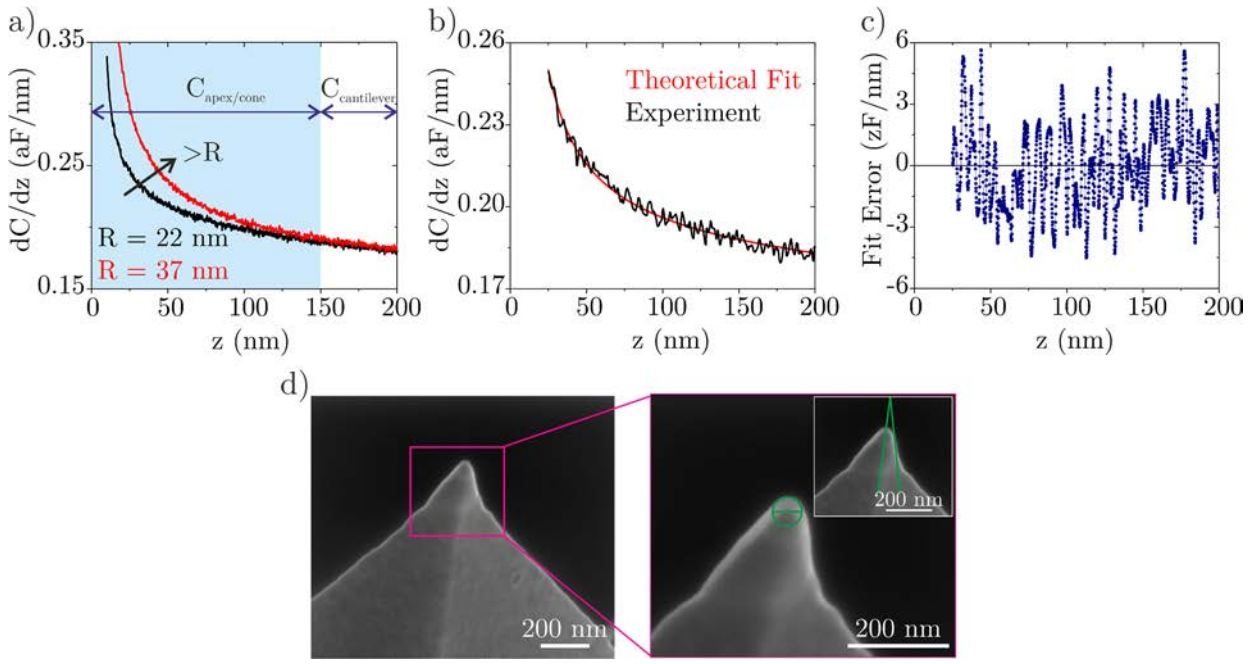

Figure 4.4: a) Example of two capacitance gradient approach curve on a bare metallic part of the sample with different tip geometries. b) Theoretical fitting (red line) to one of the experimental electrical approach curves already calibrated (in capacitance gradient units) (black line). c) Error of the electrical approach curve fitting, giving a mean = 0.3 zF/nm and a standard deviation = 2.1 zF/nm. d) SEM images of the tip of (b).

For the **tip geometry characterization** [17], one acquires an EFM approach curve on a bare metallic part of the sample. **Figure 4.4a** presents two approach curves obtained with different tip radius, and it shows that the approach curves are sensitive to the tip radius. Later, one simulates, via finite element numerical calculations, approach curves with different tip radius and cone angle. Finally, one compares experimental and simulation approach curves to fit the best tip radius and cone angle parameters (**Figure 4.4b**). We verified that determining the tip geometry from EFM measurements shows similar results than alternative methods based on SEM imaging, the use of tip reconstruction methods, or the use of calibration samples [124–129]. This can be observed in **Figure 4.4b**, **Figure 4.4c** and **Figure 4.4d** where the tip geometry, for one of the tips used in this thesis, obtained through the EFM calibration gives $R_{EFM} = 33 \pm 1$ nm and $\theta_{EFM} = 11 \pm 1$ and the dimensions obtained through SEM images are $R_{SEM} = 29 \pm 3$ nm and $\theta_{SEM} = 12.5 \pm 2.3$.

Once the tip geometry is known, the **sample geometry** has to be obtained. The simplest way of obtaining the sample geometry is to consider that it has a simple geometrical shape; for example, a bacterium can be simplified as an ellipsoid and a flagellum as a cylinder. Subsequently, the

equivalent dimensions are obtained [93,130]. However, for heterogeneous samples, it is not possible to obtain a simplified geometry, and another strategy should be performed. One strategy is to use a topographic reconstruction strategy, where the AFM topographic image is imported into the simulated geometry [120]. In this method, a local sample geometry of $n \times m$ pixels and centered in the point of interest is obtained by selecting and area of the measured topography of $N \times M$ pixels. Subsequently, the local geometrical model is built by assigning the measured height at the center of the pixel and interpolating linearly between consecutive pixels. Therefore, a smooth surface is obtained, being efficient and adequate for the subsequent meshing and finite numerical calculation. The local sample geometric models are assumed to have a uniform dielectric constant, and the remaining part of the simulation, which are not included in the local geometrical model, is set to zero height and ground. This model ensures locality, the consideration of geometric effects and it can be handle computationally [120]. In all cases, the tip deconvolution has to be taken into account, although for big geometries, as can be a bacterium (~ 80 nm), the error induced, due to not considering it, is negligible [16,120].

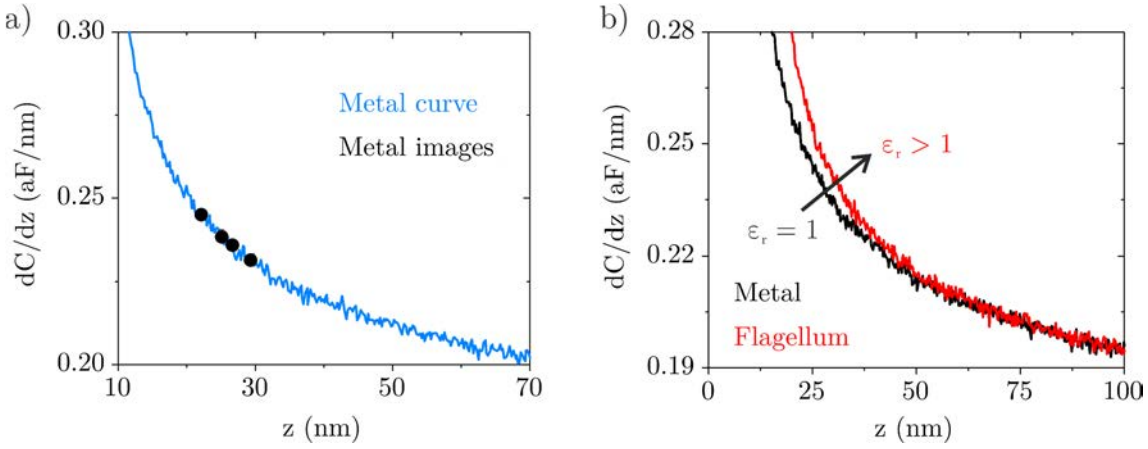

Figure 4.5: a) Capacitance gradient approach curves over a metallic substrate (blue line) and the values of the capacitance gradient on the substrate (black dots). The calibration curve is also used to set the tip-sample distance of the EFM images by comparing images and curve values. b) Capacitance gradient approach curve over a metallic part of the sample and $\varepsilon_r = 1$ (black line) and over a flagellum (red line) with $\varepsilon_r > 1$.

In the quantitative analysis, the **tip-sample distance** needs to be accurately determined. When evaluating an approach curve, the tip-sample contact point ($z_{CH} = 0$ nm) has to be defined. The contact point, or the snap-in point, is obtained from the deflection curve (experimentally, the deflection and the electrical curve are taken simultaneously). However, when we evaluate an electrical image, it must be compared with electrical approach curves measured at selected points

of the sample. To do so, the value on a bare metallic part of the electrical EFM image is compared with the electrical approach curve over the metallic part of the sample; when the value of the electrical image overlap the approach curve, the tip-substrate distance is obtained (**Figure 4.5a**) [14,93].

The second part of the quantification of the dielectric properties consists of the **electrical permittivity extraction**. Once the system geometry is known, a realistic geometric model is built in a finite element numerical simulator. Then, the capacitance gradient on the tip is simulated for a sweep in values of the dielectric constant ($\varepsilon_r = 1 - 1000$). Finally, the simulated values are compared with the experimental ones and the electrical permittivity is determined. **Figure 4.5b** shows two electrical approach curves for two different electrical permittivities.

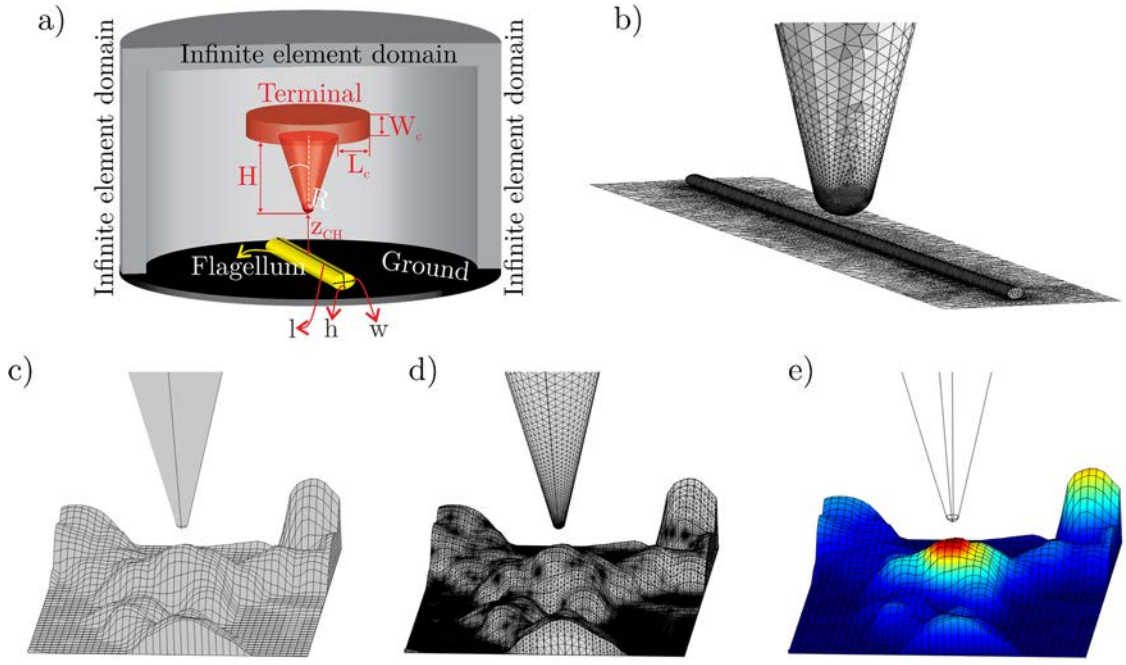

Figure 4.6: a) Schematic representation of the simulated geometry of the model to calculate the theoretical electric force acting on the tip. b) Image of a real meshing of the model. c) Model, d) meshing and e) calculated voltage of a topographic *S. oneidensis* OME reconstruction model.

In order to perform the finite numerical simulations, in this thesis, we use COMSOL Multiphysics®. The tip geometry is usually built as a truncated cone of half-angle θ and cone height H terminating in a tangent hemisphere of radius R. A disc of thickness W_c and with a radius that oversees the cone base by an amount L_c is located onto the cone base, and it models local cantilever effects, as can be seen in **Figure 4.6**. Nonlocal cantilever contributions have been

considered through a phenomenological capacitance gradient offset contribution term [15,130]. In addition, **Figure 4.6c**, **Figure 4.6d** and **Figure 4.6e** show the model, the mesh and the calculated electric voltage, respectively, of a topographic reconstruction *S. oneidensis* OME model. This is a novel technique used in this thesis.

For the physics module, the electrostatic or the electric currents (if we introduce conductivity to the sample model) module is used. Later, the electrostatic force acting on the tip is determined by solving Poisson's equation with an applied voltage V on the tip. The surface of the tip is set to terminal, setting the sample to ground and establishing the top and side boundaries of the geometrical model to zero charge. The infinite element function is used on the top and side boundaries to get rid of finite size effects of the simulation domain. Then, the Maxwell stress tensor is integrated on the tip surface to obtain the capacitance gradient (dC/dz) [114]. In addition, custom codes written in Matlab® (The Mathworks®) linked with COMSOL Multiphysics® have been used.

4.4.2.Trends

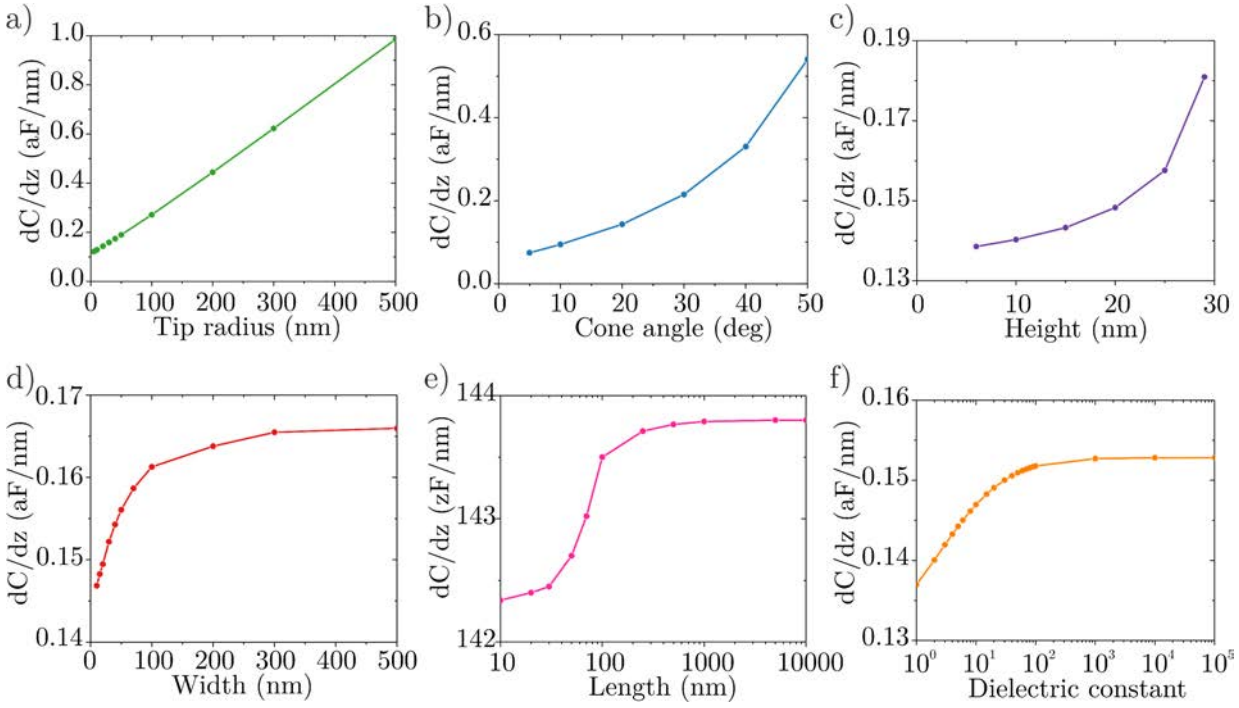

Figure 4.7: Trend of the capacitance gradient when changing the a) tip radius, b) cone angle, c) nanowire width, d) nanowire height, e) nanowire length and f) dielectric constant.

In order to have an idea of the influence of the system dimension in the capacitance gradient (dC/dz), simulations with a sweep in the tip radius, cone angle, dielectric permittivity, nanowire

length, height and width have been done. The results are shown in **Figure 4.7**. As observed, dC/dz depends linearly with the tip radius, R (**Figure 4.7a**), and quadratically with the cone angle, θ (**Figure 4.7b**). Regarding the nanowire dimensions, dC/dz increases when the height, h, is increased (**Figure 4.7c**), however, this trend is constrained to the tip-sample distance, since the wire cannot be higher than the tip-substrate distance, z, or the tip would crash. Moreover, dC/dz increases rapidly when the nanowire width is increased, w (**Figure 4.7d**) until it saturates to the thin film response. As will be explained further (Chapter 6), dC/dz increases when the nanowire length increases until it saturates (**Figure 4.7e**). The point of saturation indicates the portion of sample probed by the tip. Finally, dC/dz increases when the dielectric constant, ε_r, increases (**Figure 4.7f**) until it arrives at the metallic behaviour. Finally, dC/dz decreases as the tip-substrate distance increases (**Figure 4.4** and **Figure 4.5**). In order to do these simulations, one parameter is varied while the others are fixed to: $R = 20$ nm, $\theta = 20°$, $h = 15$ nm, $w = 15$ nm, $l = 4000$ nm, $z = 30$ nm and $\varepsilon_r = 4$.

5. Sizing single nanoscale objects from polarization forces

This chapter reproduces almost literally the article: Sizing single nanoscale objects from polarization forces, Scientific reports, ***9****, 2019, by H. Lozano, R. Millan-Solsona, R. Fábregas and G. Gomila* [131]*. My contribution to this paper was the realization of all the measurements (from sample preparation to image acquisition) and data analysis using a custom-written Matlab code developed by R. Millan-Solsona. The 3D modelling was performed by R. Fábregas and R. Millan-Solsona. The manuscript was written by me in collaboration with my supervisor G. Gomila and the other authors.*

In this thesis, I will study mostly the properties of nanowire type samples, and the size of the object under study is very important. For this reason, in this chapter, I present a methodology to obtain the dimensions of a sample which is poorly adhered to the substrate or can be easily damaged. Also, this chapter is used to validate the technique in nanowire type samples.

This method is based, first, on the measurement of the nano-objects electrical polarization, rather than on the measurement of its topography. And, second, in the extraction of the physical dimensions from the electric polarization using EFM, by using a specifically designed multiparameter quantification algorithm. The proposed method is similar to the quantification of a single-parameter (dielectric constant) of SDM (Section 4.4.1), but in this case, the dielectric constant is assumed to be a known value and the width and the height (multi-parameter) are unknown. The proposed EFM method, based on the measurement of long-range polarization forces, can be applied without contacting the sample at any moment. Hence, it is fully compatible with poorly adhered or soft nanoscale objects. In this chapter, we first validated the method with silver nanowires, and, as an application, we considered the case of a macromolecular protein complex (bacterial polar flagella), as an example of a fragile and low polarizable sample.

5.1.Introduction

Determining the physical dimensions (width and height) of manufactured and natural nanoscale objects, such as nanoparticles, nanowires, nanotubes, nanofibers, macromolecular protein complexes, viruses, liposomes, nanodroplets, etc. is very important in many areas of science and technology, such as nanocatalysis [132], nanofiltering [133], and nanomedicine and nanotoxicology [134–137]. There exist several characterization techniques to determine the dimensions of nano-objects [138,139]. Examples include ensemble techniques, such as Dynamic Light Scattering [140] or Nanoparticle Tracking Analysis [141], and single nanoscale object techniques such as TEM [142] and AFM [143]. Among single nano-object sizing techniques, AFM [95] is one of the more used and versatile ones since it can address the three spatial dimensions of the nano-objects, it can be applied to nano-objects of any material type (metallic and insulating, organic and inorganic), and it can be used in any environmental condition (air, liquid, vacuum) [144–147]. AFM can determine the height of the nano-objects on a substrate with nanometric precision in a relatively straightforward way. Concerning the width, AFM can provide a good estimation of it, although some post-processing of the data is necessary to account for tip dilation effect and other factors [148]. Tip dilation effects are due to the finite size of the measuring tip, and they tend to broaden the measured topography. To subtract these effects, geometric deconvolution methods combined with tip geometry calibration methods have been developed [124–129,149], whose accuracy varies largely depending on the nature, geometry and size of the nano-objects and of the measuring probes. In general, the width is determined by AFM with a smaller accuracy and reproducibility than the height.

Despite its wide use, sizing single nanoscale object by AFM faces difficulties for the case of poorly adhered or soft nano-objects. For poorly adhered nano-objects, the AFM tip can induce lateral displacements of the object during the image acquisition, which can further broaden the measured topography [150,151]. Moreover, for soft samples, the lateral and vertical forces exerted by the tip on the nano-object during the image acquisition can deform the sample, and, subsequently, can impact on the measured topography [152,153]. Therefore, sizing poorly adhered or soft samples still constitutes a challenge for AFM.

5.2.Materials and methods

5.2.1.Silver nanowires sample preparation

We used commercial ~ 50 nm diameter silver nanowires A50, research grade from Novarials. The sample contains 0.5 g of AgNWs suspended in 50 ml of isopropanol (IPA) for a final concentration of 10 mg/ml. We diluted the AgNWs in IPA 20 times, and we put one drop over the substrate used for the measurements. The substrates used are custom made AFM/EFM/SEM finder grids (see below and **Figure 5.1**), TEM grids (**Figure 5.2**) and Highly Oriented Pyrolytic Graphite (HOPG).

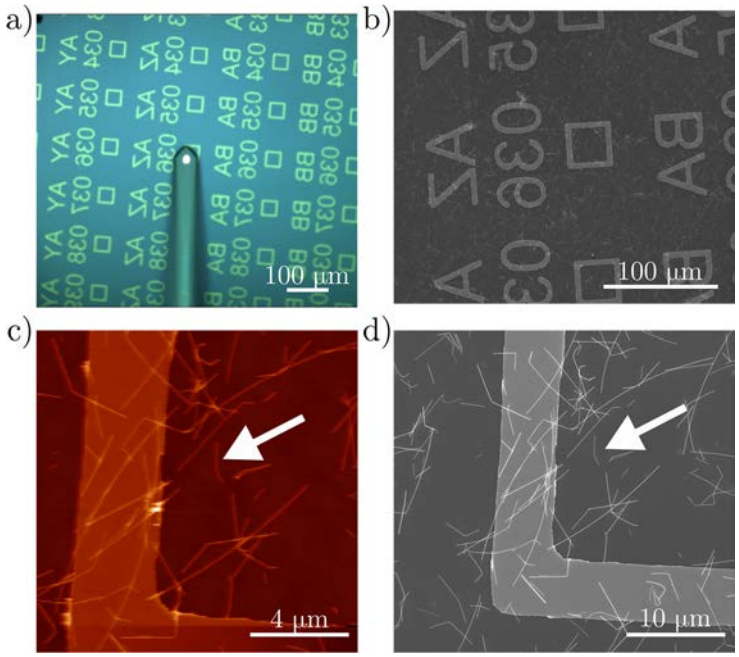

Figure 5.1: a) Optical microscopy image and b) SEM image of the AFM/EFM/SEM custom finder grid. c) AFM topography image and d) SEM image pointing towards the same AgNW.

5.2.2.AFM/EFM/SEM custom finder grid

To analyze the same nanowire in AFM, EFM and SEM imaging, we fabricated a custom-made finder grid in the Nanotechnology Platform of IBEC, Spain. The grid has been fabricated on a highly doped silicon wafer (76.2 mm diameter, Boron p-doped, orientation <100> and resistivity $0.001 - 0.005\ \Omega$cm, from UniversityWafer, Inc). It consists of $\sim 200 \times 200$ labelled $50 \times 50\ \mu m^2$ square areas delimited by a gold square stripe 5 µm wide and 50 nm thick, plus 10 nm of Cr adhesion layer. Each square is labelled with gold microfabricated letters and numbers (from AA1 to ZZ200) of an approximate size of $50 \times 50\ \mu m^2$ easily identifiable with the integrated optical camera of the AFM or with the SEM. The grid, being fabricated on a highly doped (conductive)

support, facilitates both AFM and EFM imaging, as well as, SEM imaging. It allows to study the same part of the sample by all these different techniques, as can be seen in **Figure 5.1**.

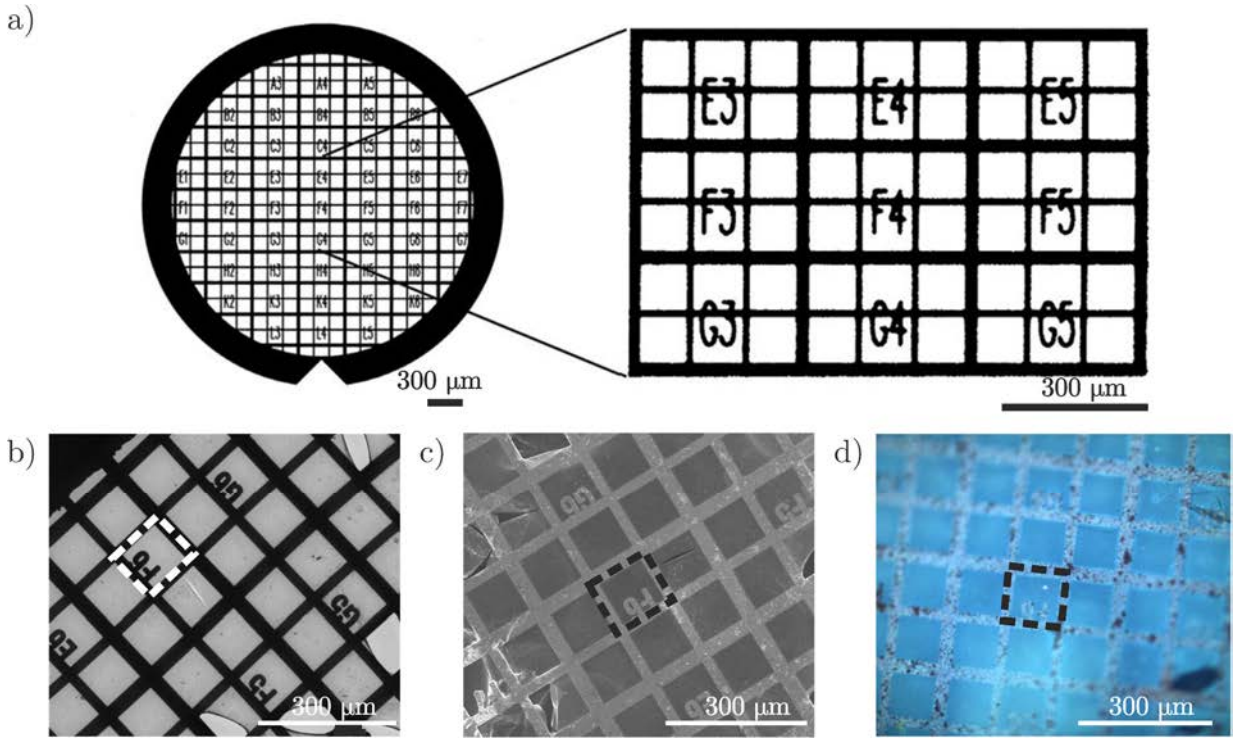

Figure 5.2: a) Image of the TEM grid and a zoom-in of one part of the grid. b) TEM, c) SEM and d) Optical Microscopy images of the finder TEM grid, with one of the cells used in the experiments highlighted by a dashed line. The optical microscopy image has been obtained with the camera integrated into the AFM and which is used to position the tip in the selected area.

5.2.3.Transmission Electron Microscopy imaging and width determination

TEM images have been obtained with a Jeol J1010 80 kV TEM, from the Scientific Services of the University of Barcelona (Spain). We used a 200 mesh and 3.06 mm diameter commercial copper TEM finder grid (Monocomp), covered with a formvar layer and 7 nm of carbon (see **Figure 5.2a**). The finder grid allowed the study of the same AgNW with TEM, SEM and EFM (**Figure 5.2b**, **Figure 5.2c** and **Figure 5.2d**). To determine the nanowire width we acquired images of $1.8 \times 1.3\,\mu m^2$ for the ensemble analysis of the sample and of $1.3 \times 1.0\,\mu m^2$ for the individual measurements, both with 1376×1032 pixels. The width of the nanowires was obtained by using the software Fiji by Image J. For each nanowire, five different measurements have been done, from where the mean and the standard deviation were obtained, as can be observed in **Figure 5.3a**.

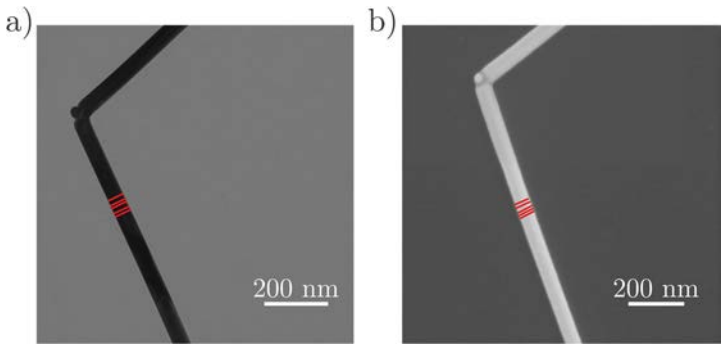

Figure 5.3: a) TEM and b) SEM image of the same AgNW showing the five profiles taken for the width quantification.

5.2.4.Scanning Electron Microscopy imaging and width determination

We used a Nova NanoSEM FEI SEM using the detector LVD from the Nanotechnology platform of the Institute of Bioengineering of Catalonia (IBEC), Spain. Images have been obtained by applying a voltage of 5 kV, a current of 56 pA and a working distance of 6.5 mm. SEM images have been performed on AgNW samples prepared on both the TEM and the AFM/EFM/SEM custom made finder grids. To determine the nanowire width we acquired images of $2.5 \times 2.2\ \mu m^2$ ($2048 \times 1886\ pixels$). The widths of the AgNWs have been determined in the same way as the TEM images (described above), as can be observed in **Figure 5.3b**.

5.2.5.Atomic Force Microscopy imaging and height determination

We used a Cypher S AFM from Oxford Technologies (former Asylum Research). Topographic AFM images of 1024×1024 pixels ($6.4 \times 6.4\ \mu m^2$) have been obtained at 0.5 Hz per line in intermittent contact mode by using conductive PtSi-CONT probes (Nanosensors) with a spring constant $k \sim 0.2$ N/m (determined by the provider according to the probe dimensions), resonance frequency $f_r \sim 13$ kHz, nominal tip radius $R \sim 20$ nm and half cone angle $\theta \sim 11.5°$. AFM images have been obtained on samples prepared on the different substrates (TEM and AFM/EFM/SEM finder grids and HOPG). To determine the nanowire height, we acquired images of $0.5 \times 0.5\ \mu m^2$ (256×256 pixels). For each nanowire, five different determinations have been done from consecutive topographic profiles, from where the mean and the standard deviation of the measurements were obtained. Images were processed in both Gwyddion and WSxM [154] (Nanotec Electrónica S.L.).

5.2.6.Tip geometry calibration

The tip geometry was determined from EFM approach curves measured on a bare part of the metallic substrate, as detailed in Section 4.4.1 or ref. [14][17]. The following tip parameters were set to their nominal values in the tip geometry calibration: cone height $H = 12.5\,\mu m$, local cantilever $L_c = 3\,\mu m$ and cantilever thickness $W_c = 3\,\mu m$.

5.2.7.Tip deconvolution and width determination from AFM imaging

The deconvoluted width of the AgNWs and of the bacterial flagella has been obtained from the topographic AFM images by means of a semi-automatic analytical tip deconvolution model. From the AFM topographic images, we obtained a cross-section profile by using the Gwyddion free software. Then, through a Matlab script, the profile in the x-axis was centered and moved to $h = 0\,nm$ from the substrate region. Then, the Full Width at Half Maximum (FWHM) and the height (maximum point of the profile) were determined. To calculate the FWHM of the profile, the script adjusts a polynomic function of second order. To obtain the deconvoluted width, the script solves eq. (5.1) and eq. (5.2). This procedure was repeated for five nearby profiles. The mean and standard deviation corresponds to the AFM width and error, respectively.

$$p_y \leq y_0$$
$$\begin{cases} \dfrac{(w-x_0)^2}{a^2} + \dfrac{y_0^2}{b^2} = 1 \\ y_0 = p_y + (x_0 - p_x)\tan\left(\dfrac{\pi}{2} - \theta\right) \\ \tan\left(\dfrac{\pi}{2} - \theta\right) = \dfrac{b^2}{a^2}\dfrac{(w-x_0)}{y_0} \end{cases} \tag{5.1}$$

$$p_y > y_0$$
$$\begin{cases} \dfrac{(w-x_0)^2}{a^2} + \dfrac{y_0^2}{b^2} = 1 \\ x_0^2 + (y_0 - R)^2 = R^2 \\ \dfrac{x_0}{(y_0 - R)} = \dfrac{b^2}{a^2}\dfrac{(w-x_0)}{y_0} \end{cases} \tag{5.2}$$

where (x_0, y_0) is the point at which the tip contacts the ellipse when the tip is at the half-height point; a, b are the semiaxes of the ellipse; $w = \text{FWHM}/2$ is the distance between the center of the ellipse and the center of the tip; R and θ are the radius and the half cone angle of the tip, respectively and $p_x = R\cos(\theta)$ and $p_y = R - R\sin(\theta)$. R and θ are known from the tip calibration, while the $a = h/2$ where h is the height of the sample, known from the topographic profile. Thus,

the unknown parameters are b, x_0 and y_0. This procedure was repeated for five nearby profiles and the mean and standard deviation corresponds to the AFM width and error, respectively

5.2.8.Electrostatic Force Microscopy imaging

EFM images have been obtained with the AFM system and probes described above. We recorded the 2ω harmonic of the probe oscillation amplitude, $A_{2\omega}$, by using the system internal lock-ins in the two-pass SNAP mode, the Cypher built-in line by line constant height mode, check Section 4.3 for more information. EFM data were obtained with a voltage amplitude $V_{\mathrm{ac}} = 5$ V at a frequency $f = 2$ kHz (well below the mechanical resonance peak of the probe, see Section 4.3). EFM measurements have been performed on the AFM/EFM/SEM finder grid. EFM data were reported in terms of the capacitance gradient, which is related to the 2ω oscillation amplitude by eq. (4.7).

Typical values of the parameters of eq. (4.7) are $m \sim 1$ mV/nm, $A_{2\omega,\mathrm{offset}} \sim 0.1$ mV, $G = 1$, $V_{\mathrm{ac}} \sim 3$ V, $k \sim 0.15$ N/m and $A_{2\omega} \sim 10 - 20$ mV. The capacitance gradient instrumental noise was in the range 1– 2 zF/nm depending on the probe used and recording parameters. EFM measurements were performed in controlled dry air conditions (RH $< 1\%$) maintained by N_2 flow.

5.2.9.Finite element numerical calculations

We used finite element numerical calculations to simulate theoretical EFM capacitance gradient profiles and approach curves for the tip nanowire system. The geometrical model and theoretical approach are the same as those detailed in ref. [93], adapted to the dimensions of the AgNWs and tips used in the present work. Further explanation can be found in Section 4.4.1.

5.2.10.Flagella sample preparation and AFM and EFM flagella imaging

For these experiments, we used *Shewanella oneidensis* MR-1 (ATCC 700550) cultivated first overnight at 30°C in Luria–Bertani (LB) (Scharlab) broth under aerobic conditions. Then, bacteria were resuspended in minimal AB medium [155] supplemented with 100 mM fumarate and 20 mM lactate during two days under anaerobic conditions at 30°C in Hungate tubes. We also used *Pseudomonas aeruginosa* PAO1 (ATCC 15692) grown overnight in LB medium at 37°C under aerobic conditions. The samples for EFM inspection are prepared by taking a drop of the culture solutions, depositing it onto a freshly cleaved HOPG and leaving it to rest for 10 min to promote the adhesion of bacteria on the substrate. Afterward, the drop sample is rinsed two

times, first with PBS and second with mili-Q water to remove any poorly adhered cells or any residual from the sample. Finally, we left the sample to dry under ambient conditions. The HOPG substrate was attached to a 1.5 cm diameter magnet using a carbon double side stick, which was connected to the electrical ground of the atomic force microscope by a small wire.

5.3.Results and discussion

5.3.1.Characterization of the dimensions of the silver nanowire test sample by conventional AFM, TEM and SEM imaging

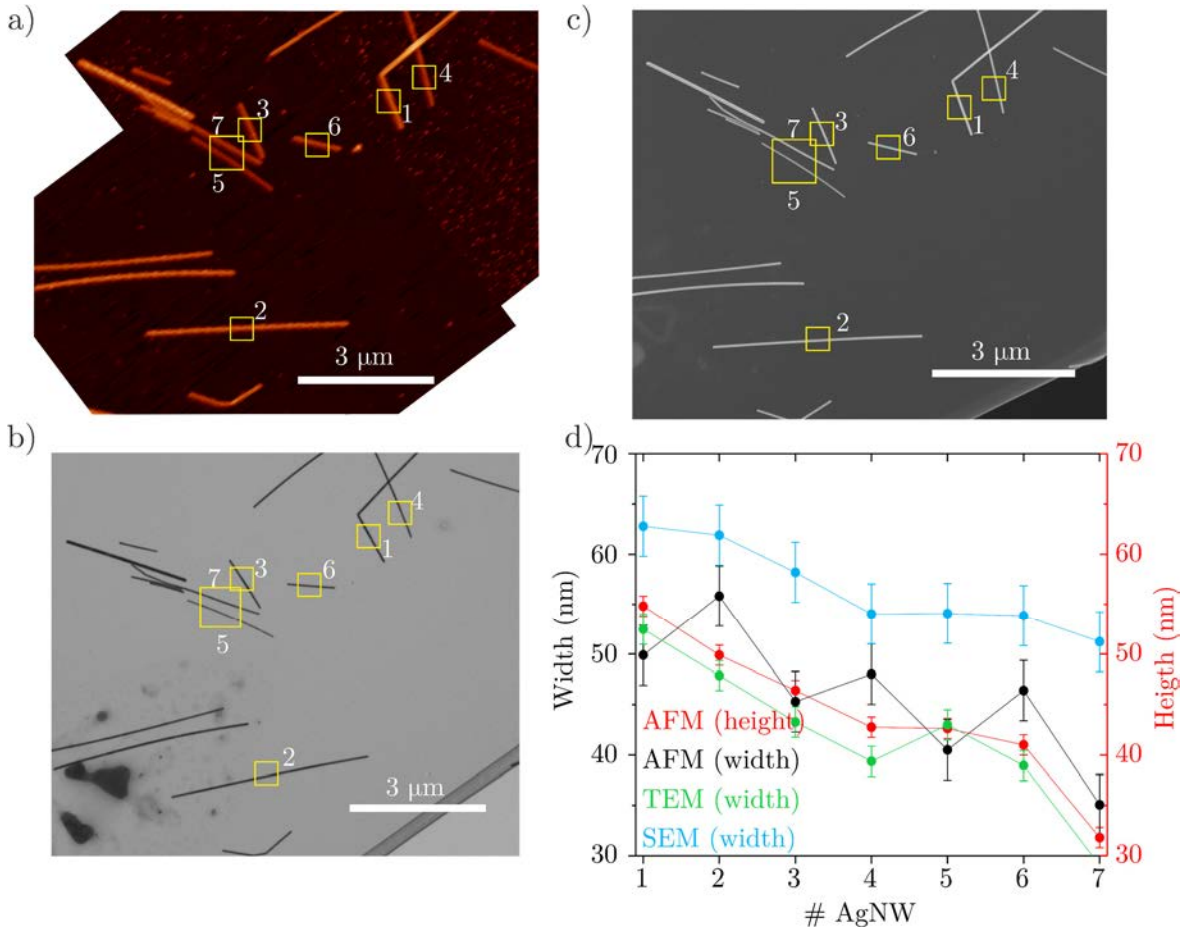

Figure 5.4: a) AFM, b) TEM and c) SEM images of the same set of AgNWs deposited on a TEM finder grid. The seven numbered AgNWs are those analyzed explicitly. d) SEM (blue symbols, left axis) width, TEM width (green symbols, left axis), height (red symbols, right axis) and (deconvoluted) width (black symbols, left axis), of the numbered NWs obtained from zoom-ins AFM images in (a).

To extract the dimensions of the test sample that we used ($\sim$ 50 nm diameter silver nanowires, AgNWs), we first analyzed it using the conventional techniques, namely, AFM, TEM and SEM.

Once we obtained the values of the dimensions, we tested our new method based on EFM to extract the same dimensions on the sample and validate our analysis.

Figure 5.4a, **Figure 5.4b** and **Figure 5.4c** show, respectively, AFM, TEM and SEM images of a given set of AgNWs deposited on a TEM finder grid (**Figure 5.2**). **Figure 5.4d** shows the heights and (deconvoluted) widths obtained from the AFM images (red and black symbols, respectively), as well as, the widths measured from TEM (green symbols) and SEM (blue symbols) images. For greater accuracy, in all cases, the physical dimensions were obtained from zoom-in images taken on each individual nanowire. One of these AgNW is shown in **Figure 5.3**. The error bars in the measured heights and widths represent the standard deviation of five consecutive profiles in the images. The AFM tip geometry used for this analysis is apex radius $R = 31 \pm 2$ nm and half cone angle $\theta = 25 \pm 1°$. These values were obtained from an EFM approach curve (Section 4.4).

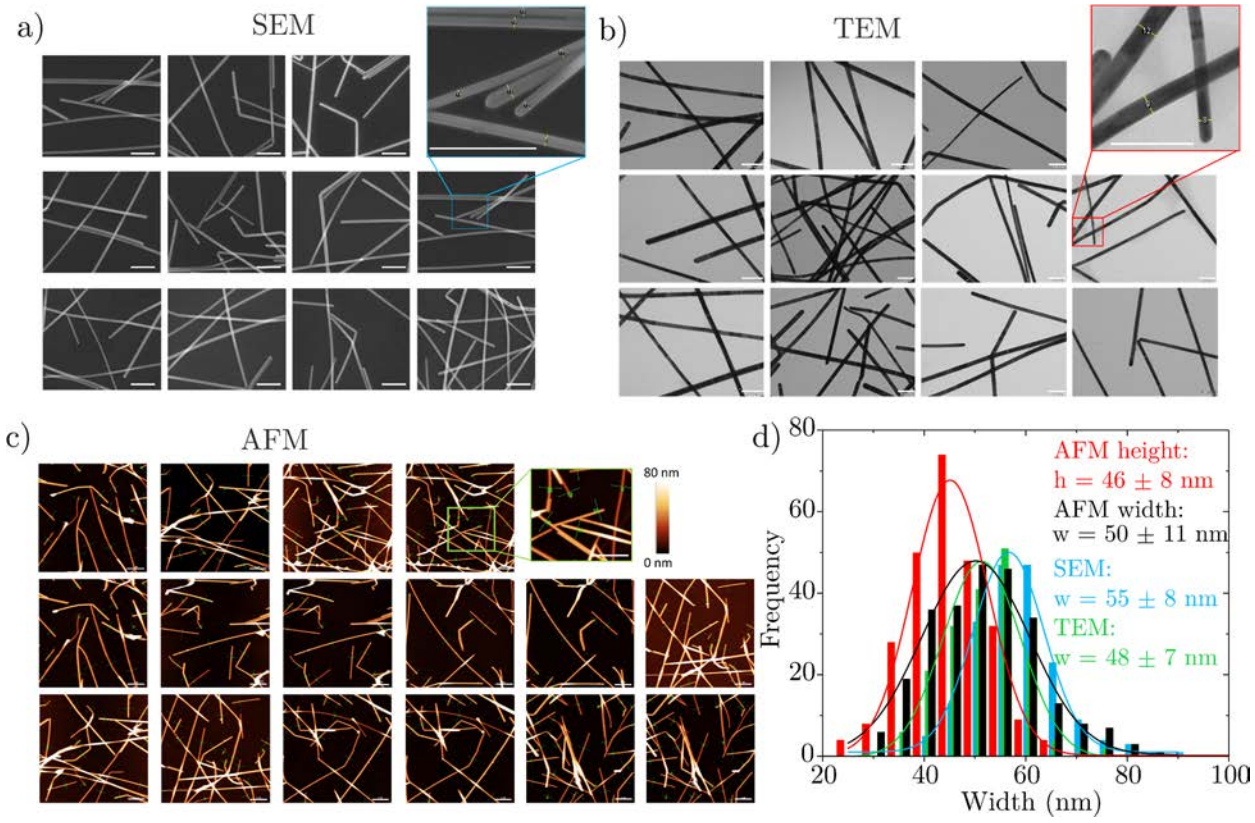

Figure 5.5: a) SEM, b) TEM and c) AFM images of different populations of AgNWs. The images correspond to different regions and samples (TEM images are taken on TEM grids, while the SEM and AFM images on HOPG). The scale bars are: 500 nm in (a), 200 nm in (b) and 1 µm in (c). d) Histogram representation of a population analysis of the AgNWs dimensions by different techniques: (red bars) AFM height, (black bars) (deconvoluted) AFM width, (green

bars) TEM widths, (blue bars) SEM widths. The lines represent Gaussian fits to the different distributions.

The (deconvoluted) widths obtained from topographic AFM imaging closely follow the widths determined by TEM, within the experimental error (± 5 nm). Instead, the SEM widths tend to be systematically overestimated ~ 10 nm, as has been reported earlier [146]. Finally, the heights obtained from the topographic AFM images are very close to the widths measured by TEM, with just a slightly systematic underestimation (~ 1–3 nm). This fact is consistent with an almost circular geometry of the AgNWs. These results show that AFM topographic imaging combined with the tip deconvolution process implemented here and explained in Section 5.2.7, offers an accurate description of the dimensions of the AgNWs, and so, it can be used as a good reference method to validate the proposed EFM method.

Technique	2N	Mean (nm)	Standard deviation (nm)	Maximum (nm)	Minimum (nm)
TEM	182	48	7	72	31
SEM	182	55	8	86	36
AFM height	268	46	8	73	25
AFM width	268	50	11	81	19

Table 5.1: Summary of the data obtained from the images in **Figure 5.5**.

This conclusion has been confirmed from a population analysis of the nanowire sample, whose SEM, TEM and AFM images are shown in **Figure 5.5a**, **Figure 5.5b** and **Figure 5.5c**. The histograms of the statistical distribution of the measurements of the width from the SEM, TEM and (deconvoluted) AFM images and height from the AFM images are shown in **Figure 5.5d**. In addition, the values of the statistical analysis are summarized in **Table 5.1**. The height and width values show approximately a Gaussian distribution with mean values: $h_{\mathrm{AFM}} = 46 \pm 8$nm, $w_{\mathrm{AFM}} = 50 \pm 11$nm ($N_{\mathrm{AFM}} = 134$), $w_{\mathrm{TEM}} = 48 \pm 7$nm ($N_{\mathrm{TEM}} = 91$) and $w_{\mathrm{SEM}} = 55 \pm 8$nm ($N_{\mathrm{SEM}} = 91$), corresponding, respectively, to the AFM heights (red bars), AFM (deconvoluted) widths (black bars), TEM widths (green bars) and SEM widths (blue bars). The errors here represent the standard deviation within the population of nanowires obtained from the Gaussian fit to the data. Each nanowire has been measured twice (in different points) to reduce the error of the measurement. Again, the (deconvoluted) AFM and TEM widths give similar results, while the

SEM widths tend to be systematically overestimated ~ 7 nm. Additionally, the AFM height is very close, just slightly smaller to the AFM or TEM widths, confirming (again) the almost circular nature of the nanowires. The tip geometry for the AFM deconvolution analysis is $R = 33 \pm 1$ nm and $\theta = 11 \pm 1°$.

5.3.2.Sizing single silver nanowires from electric polarization forces

The proposed method consists of measuring the electric polarization of single nano-objects by EFM, and then use a multiparameter quantification algorithm to obtain the dimensions of the nano-object that best reproduces the measured electric polarization (by assuming a known dielectric constant of the object, further explained in Section 5.3.4). The dependence of the electric polarization of an object on its shape and size is a well-known property of polarizable materials [16,156]. The quantification algorithm to extract the physical dimensions of the nano-object from the measured polarization forces is inspired in the method developed earlier to measure the dielectric constant of nanoscale objects [114] but generalized to the much more complex situation of multiple parameter extraction (here the width and the height). We have analyzed, theoretically, a similar quantification algorithm in the context of EFM tomographic reconstruction [157], but it has not been implemented in practice, yet.

The complete procedure is described in **Figure 5.6** (for details on the EFM measurements and numerical calculations see Section 5.2 and Section 4.4.1). The EFM measurements have been performed on a custom-made AFM/EFM/SEM finder grid, which enables also performing AFM and SEM measurements for validation purposes (see Section 5.2 and **Figure 5.1**). We first calibrate the tip geometry from an EFM capacitance gradient approach curve measured on a bare part of the substrate, as explained in Section 4.4.1 (**Figure 5.6a**). In the present example, we obtain a tip radius $R = 42 \pm 1$ nm, a half cone angle $\theta = 23 \pm 2^{o}$, and a capacitance gradient offset $C'_{\text{offset}} = 112 \pm 2$ zF/nm. Then, we localize the nano-object of interest from a conventional AFM image (not shown) and acquire a calibrated constant height EFM image (**Figure 5.6b**). From the EFM image, we extract a capacitance gradient cross-section profile, which can be eventually averaged with nearby profiles to reduce the instrumental noise (**Figure 5.6c**).

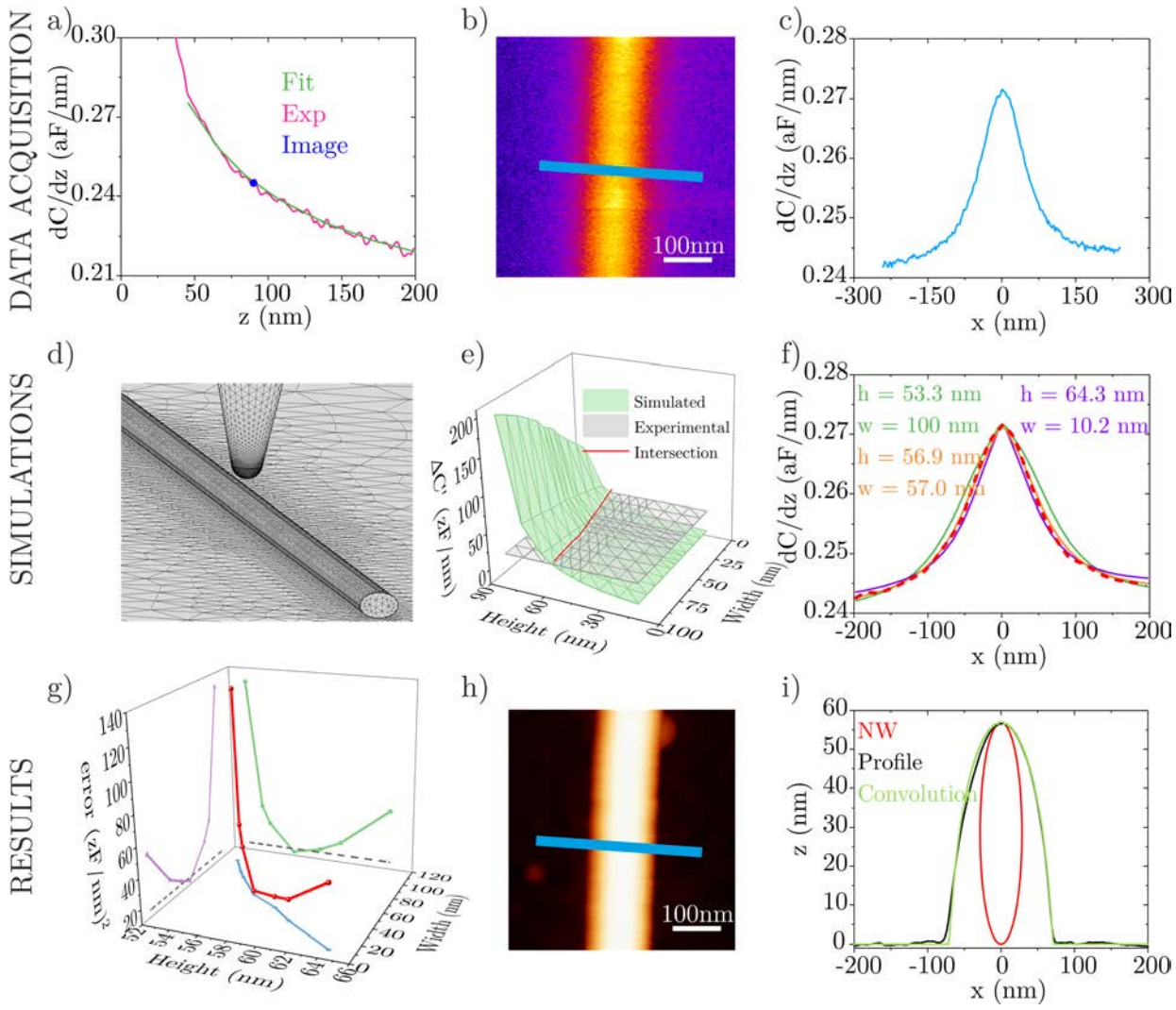

Figure 5.6: a) Capacitance gradient EFM approach curve on a bare part of the metallic substrate (red line). Least square fitting of the theoretical model to determine the tip geometry (green line). Value on the substrate of the EFM image (blue circle) in (b) used to determine the tip-sample distance of the EFM image. b) Capacitance gradient EFM image measured in constant height mode on a single nanowire. c) Capacitance gradient cross-section profile along the line in (b). d) Geometrical tip-nanowire model used for the numerical calculations. e) Calculated maximum capacitance gradient EFM contrast as a function of the width and height of the nanowire (green surface). Experimental capacitance gradient contrast obtained from (c) (gray plane). f) Numerically calculated capacitance gradient profiles corresponding to the couples of height/width values that provide the experimental contrast (continuous lines), compared to the experimental profile (dashed red line). g) Cumulative quadrative error, R^2, of the calculated profiles as a function of the height and width, giving a contrast equal to the experimental one (red symbols). Projections of the main curve on the lateral planes of the width and height (purple and green symbols). The position of the minimum gives the dimensions of the AgNW that best fit the experimental profile. The dashed lines represent the noise error floor for R^2. h) AFM image of the same AgNW shown in (b). i) Deconvolution of the AFM profile.

A geometrical model is then built to describe theoretically the electric polarization of the nanoscale object and the electric force acting on the tip (**Figure 5.6d**). In the present case, the

model consists of the tip, with the calibrated geometric parameters, and the nanowire, which is assumed to have an ellipsoid cross-section with variable height and width. For simplicity, we consider nanowires longer than $\sim 1\,\mu$m, for which finite length effects can be neglected (further details in Chapter 6). The dielectric constant of the nanowire is assumed to be known; in this case, we assume a metallic nature for the AgNW, which can be modeled by a very large value of the relative dielectric constant, e.g., $\varepsilon_r = 10^6$). The tip-sample distance in the model is set with the help of the EFM approach curve, used to calibrate the tip geometry (**Figure 5.6a**), by using the value measured on a bare metallic part of the EFM image (**Figure 5.6b**) (blue circle in **Figure 5.6a**, giving here $z_{CH} = 87 \pm 2$ nm with respect to the substrate). The theoretical model is, then, numerically solved and used to calculate all possible EFM capacitance gradient values at the center of the nanowire (maximum contrast) for different combinations of height and width of the nanowire (here we swept the width between 10 nm and 100 nm and the height between 10 nm and 60 nm). The calculated maximum capacitance gradient contrast as a function of the width and height of the nanowire is shown in **Figure 5.6e** (green surface). The intersection of this surface of possible EFM contrast values with the experimental measured EFM contrast (here $\Delta C' = 28 \pm 1$ zF/nm, see **Figure 5.6c**) determines the set of height/width couples compatible with the maximum measured contrast (red line in **Figure 5.6e**). For each couple of possible height/width values, full capacitance gradient profiles are calculated and compared with the experimental one (**Figure 5.6f**). For greater accuracy, in the calculations of the profiles, we account for the small tilting of the sample and bending of the cantilever when passing above the nanowire as shows in **Figure 5.7**. For each calculated EFM profile we determine the cumulative quadratic error R^2 with respect to the experimental EFM profile. By performing this calculation for all possible height/width couples, and plotting R^2 against these variables, we observe the presence of a minimum in R^2 for one of the height/width couples (see **Figure 5.6g**). These couple of values represent the solution wanted, since for them, the calculated EFM profile shows the minimum error with respect to the experimental one. In the present example, we obtained $h_{\mathrm{EFM}} = 58 \pm 1$ nm and $w_{\mathrm{EFM}} = 55 \pm 9$ nm. The error in the width and the height of the AgNW has been estimated by setting a noise floor to R^2 determined by the experimental noise (dashed lines in **Figure 5.6g**). We essentially assume that a calculated EFM profile can be distinguished from the experimental one if it exists a cumulative quadratic error larger than $R^2_{det} = (3/2\delta C')^2 n$,

where $\delta C'$ is the experimental noise of the measured profile, and n the number of points of the calculated profile. The minimum value of R^2 is roughly $R^2_{min} = (\delta C')^2 n$. In the present case, the instrumental noise is $\delta C' = 0.5$ zF/nm and the number of calculated points per profile $n = 36$, from where $R^2_{det} = 17$ (zF/nm)^2 (dashed lines in **Figure 5.6g**).

We remark that the physical dimensions obtained in the previous analysis have been determined exclusively from information obtained from the electric polarization measurements, with no input coming from the sample topography. This result shows that it is possible to extract the physical dimension of a nanoscale object only using the electric polarization measurements, assuming a known dielectric constant of the object.

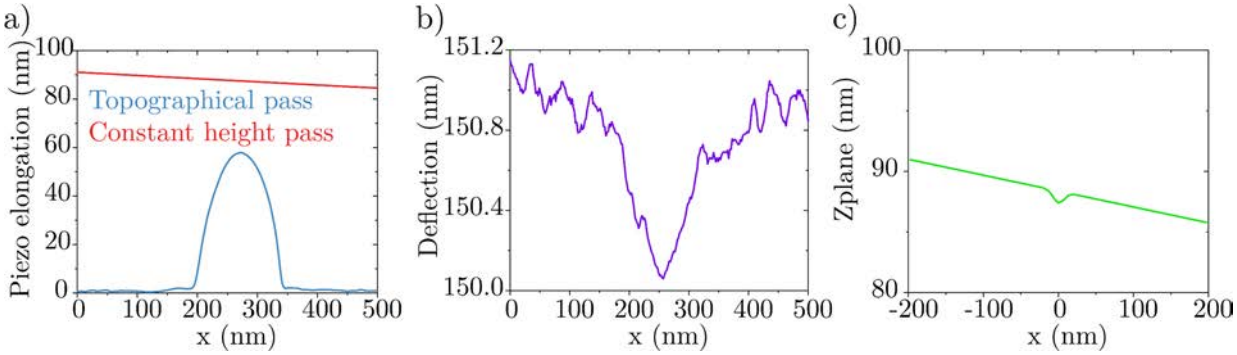

Figure 5.7: a) Piezo elongation in the AFM topographic pass (blue line) and in the EFM constant height pass (red line). b) Cantilever deflection profile acquired simultaneously to a constant height EFM profile. c) Tip-substrate distance used in the simulations.

The results obtained from the EFM method can be compared with the ones obtained from conventional AFM imaging on the same nanowire. For the specific AgNW analyzed in **Figure 5.6**, the corresponding topographic AFM image is shown in **Figure 5.6h**. The tip deconvolution analysis of this AFM image (**Figure 5.6h**) gives $w_{\mathrm{AFM}} = 57 \pm 2$ nm and $h_{\mathrm{AFM}} = 59.0 \pm 0.5$ nm. These values are almost identical (within the experimental error) to the ones derived from the EFM method ($h_{\mathrm{EFM}} = 58 \pm 1$ nm and $w_{\mathrm{EFM}} = 55 \pm 9$ nm). We specially highlight the excellent agreement between the heights obtained by the two methods, given the relatively small uncertainty. For the widths, the agreement is also good, although the uncertainty in the EFM method is larger than in the AFM method (see Section 5.3.4). We have also taken a SEM image of the same AgNW analyzed in **Figure 5.6** (not shown), thanks to the use of the custom-made AFM/EFM/SEM finder grid. We have obtained a width $w_{\mathrm{SEM}} = 67 \pm 2$ nm, consistent with the

values obtained by AFM and EFM above, also considering the systematic ~7 – 10 nm broadening effect of SEM images described before.

Similar conclusions have been obtained from different nanowires analyzed, whose sizes span the full range of sizes present in the sample (see **Figure 5.8** and Section 5.5.1).

We conclude that, by measuring the electric polarization of nanoscale objects of known dielectric constant, one can obtain its physical dimensions with an accuracy similar to the one obtained from conventional AFM topographic imaging, especially on what concerns the height. The main advantage of the proposed method is that the dimensions of the nano-objects are obtained from images that are acquired in non-contact mode (constant height EFM). Hence, it is expected to provide more reliable values for the case of soft or poorly adhered samples.

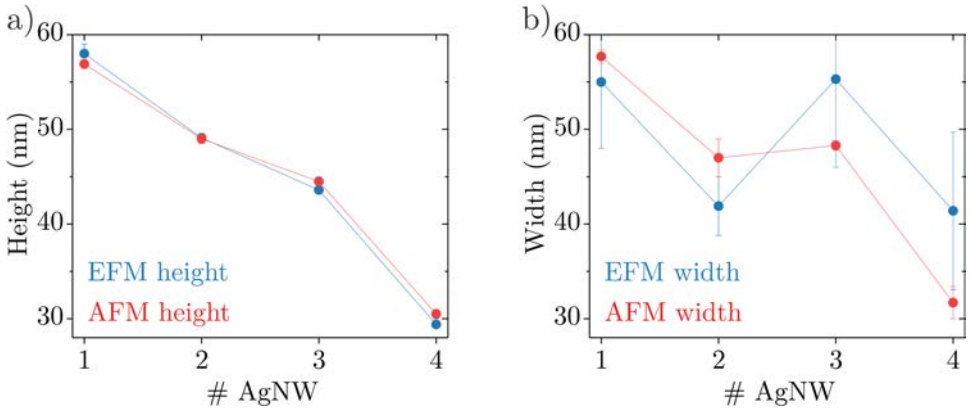

Figure 5.8: a) Heights and b) widths obtained on four different AgNWs with dimensions spanning the full range of sizes present in the AgNWs sample with the EFM method (red symbols) and with the conventional AFM topographic method (blue symbols).

5.3.3. Application to polar bacterial flagella

As an example of application to a fragile sample, we considered the case of bacterial polar flagella. Bacterial polar flagella are long thin (~10 – 20 nm diameter) whip like appendages that bacteria use to move towards the nutrients. They are composed of 11 flagellin protein monomers twisting every ~5 nm [158]. In this section, we will determine dimensions of two different bacterial species, *Pseudomonas aeruginosa* PAO1 and *Shewanella oneidensis* MR-1, taking as a dielectric constant, a typical dielectric constant value for proteins (ε_r~3 – 5). In Chapter 6, we will determine the dielectric properties of these flagella. However, to perform this analysis, we need to determine the physical dimensions of the bacterial flagella; although in Chapter 6, we will determine the dimensions using conventional AFM topographic analysis. Polar bacterial flagella

are macromolecular protein complexes which are soft and poorly adhered to the substrate. Therefore, the AFM topographic images, even after tip deconvolution, might not represent the actual geometry of the flagella due to sample deformations by the tip or to small displacements caused during AFM imaging. In order to assess this possibility, we will obtain the dimensions of polar flagella from the electrical measurements. To this end, we assume a known dielectric constant for the flagella ($\sim 3-5$ typical of proteins [13,92]), for a later determination of the corresponding width and height compatible with the EFM measurements. This example will serve to illustrate the particularities of the method when applied to low polarization nano-objects.

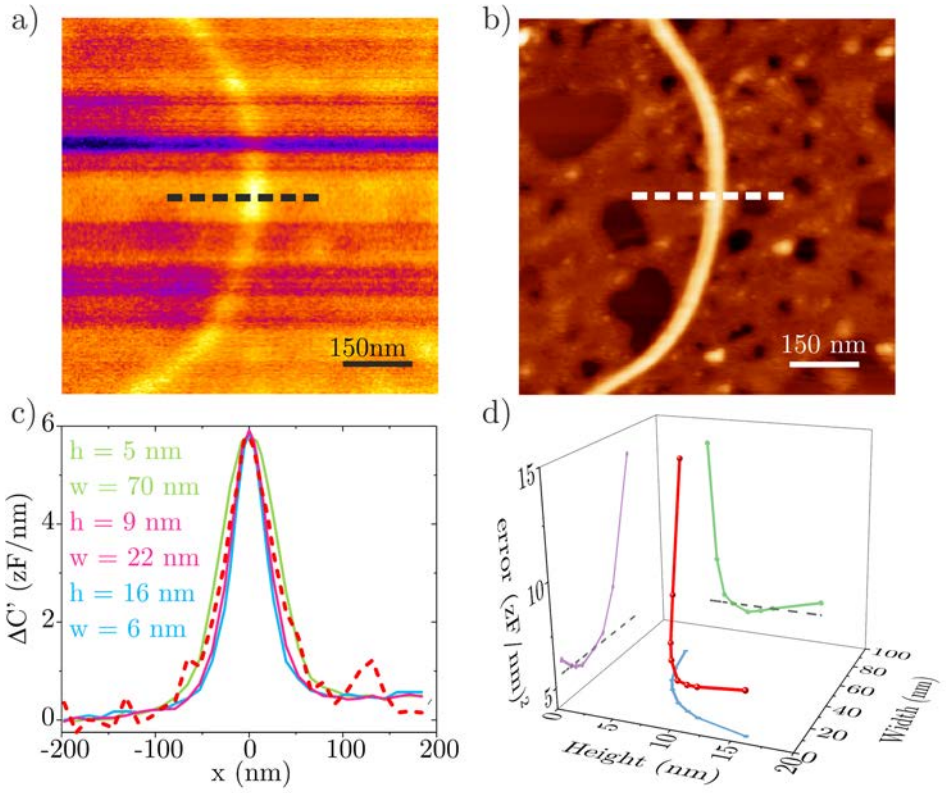

Figure 5.9: a) EFM image in constant height mode of a bacterial flagellum acquired at a tip substrate distance $z_{CH} = 26.4 \pm 0.5$nm. b) Topographical AFM image. c) Experimental profile along the dashed line in (a) (dashed line) and simulated profiles with different height/width (continuous lines). d) Cumulative square error R^2 of the different theoretical profiles with respect to the experimental profile as a function of w and h.

Figure 5.9 shows the analysis for one bacterial flagellum of *S. oneidensis* MR-1. In the EFM image (**Figure 5.9a**), we observe that different lines show slightly different contrast values. These differences do not correspond to a change in the geometry of the flagellum or to a variation of its dielectric constant. The differences correspond to slightly different imaging tip-substrate distances, due to the presence of some residues on the substrate. These residues introduce small variations

in the reference distance taken at the beginning of each line during the constant height EFM imaging mode [93].

An EFM approach curve has been acquired on a bare part of the substrate (not shown) to calibrate the tip radius and set the EFM imaging distance, giving $z_{\mathrm{CH}} = 27 \pm 1$ nm, $R = 24 \pm 1$ nm and $\theta = 11 \pm 1°$. By assuming a dielectric constant $\varepsilon_r = 4$ for the flagellum and applying the procedure described before, we have determined the possible couples of height/width values compatible with the measured dielectric contrast. For each of these couples, we simulated the corresponding EFM profiles (**Figure 5.9c**), from where we calculated the cumulative quadratic error R^2 with respect to the experimental profile (red dashed line in **Figure 5.9c**). In the calculus of the profiles, we considered the presence of a ~2 nm thin layer of residues on the substrate [93]. A plot of R^2 with respect to the possible widths and heights (**Figure 5.9d**) reveals again the presence of a minimum, which corresponds to the physical dimensions of the flagella that best fits the measured EFM profiles. In the present case, we obtain a height $h_{\mathrm{EFM}} = 9 \pm 2$ nm and a width $w_{\mathrm{EFM}} = 22 \pm 10$ nm. These physical dimensions are completely realistic for a bacterial flagellum on a substrate [158] and are similar to the dimensions obtained directly from a gentle topographic AFM image acquired in tapping mode on the same flagellum (**Figure 5.9b**), which gives a height $h_{\mathrm{AFM}} = 9.5 \pm 0.5$ nm and a width $w_{\mathrm{AFM}} = 23 \pm 2$ nm. Similar good agreement results have been obtained by analyzing additional flagella or additional cross-section profiles (for more detailed data, see Section 5.5.2). These results show that the proposed EFM method can be successfully applied to objects of small size, fragile and low polarizable with no need of information coming from its topography.

5.3.4.Discussion

We have shown that the physical dimensions of single nanoscale objects of known dielectric constant can be determined, with good accuracy, from the measurement of its electrical polarization, using EFM measurements combined with a specifically designed quantification multiparameter extraction algorithm. We have shown that the obtained values, for the width and the height of the nano-objects, are comparable to those obtained from AFM topographic imaging. With this method, we have obtained just a slightly larger uncertainty in the dimensions, especially on what concerns the width. We have shown that the proposed EFM method, being based in a

non-contact imaging mode, can be applied to soft and poorly adhered samples, where conventional AFM imaging can face some difficulties.

In the EFM method proposed, the height is obtained with better accuracy than the width. This fact is due to the higher sensitivity of the electric polarization force acting on the EFM probe on the height of the nanoscale object than on its width. We illustrate it in **Figure 5.10a**, where we show EFM capacitance gradient profiles calculated at a tip-substrate distance $z = 72$ nm for a circular metallic NW of width and height 50 nm (red line), and for the same NW but with widths (left) and heights (right) varied by $\pm$ 4 nm (dashed lines). In order to perform these simulations, the following parameters were taken: tip radius $R = 31$ nm, cone angle $\theta = 25°$ and NW length $l = 4000$ nm.

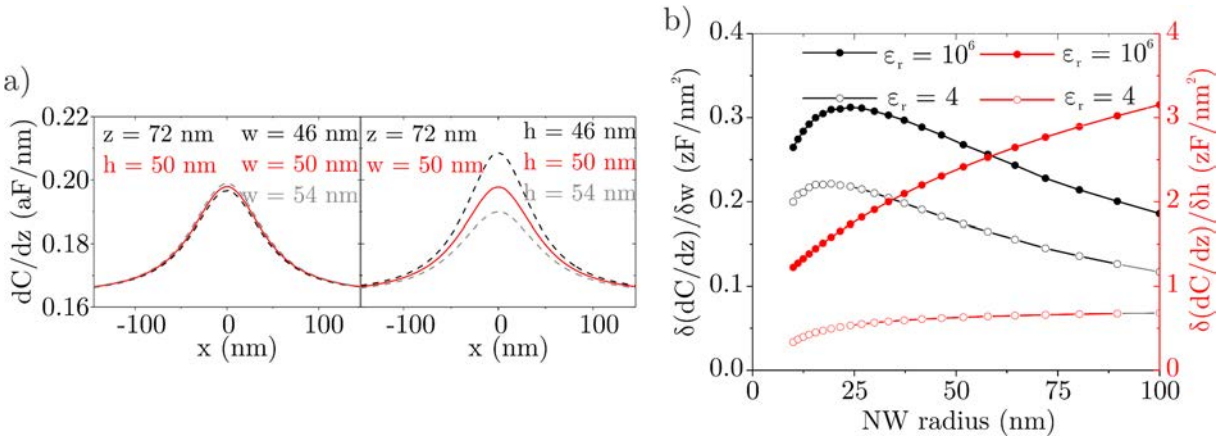

Figure 5.10: a) Calculated EFM capacitance gradient profiles for a metallic circular NW of height and width $h = w = 50$ nm at a tip-NW distance $z = 22$ nm (red solid line), and for widths (left panel) and heights (right panel) varying $\pm$ 4 nm (dashed lines). b) Calculated sensitivity of the EFM capacitance gradient contrast to variations of the width (black symbols, left axis) and of the height (red symbols, right axis) of a circular NW as a function of the NW radius. Solid symbols correspond to $\varepsilon_r \gg 1$ and empty symbols to $\varepsilon_r = 4$.

It is apparent that the variation in the EFM contrast is much larger when the height is varied than when the width is varied. **Figure 5.10b** shows this fact in terms of the sensitivity to variations in the width (black symbols, left axis) and height (red symbols, right axis) as a function of the NW radius, for the case of a metallic (solid symbols) and low polarizable ($\varepsilon_r = 4$) (empty symbols) circular NWs. We see that the sensitivity to the height is nearly one order of magnitude larger than to the width. Therefore, higher accuracy can be achieved when determining the height. Furthermore, the sensitivity in both, height and width, is lower for low polarizable NWs, from where the accuracy achievable in these cases would be lower, as we can see by comparing the

accuracies for the cases of the metallic AgNWs and for the bacterial flagella. Finally, we note that the sensitivity to the height decreases by reducing the size of the NW, due to a reduction in the signal to noise ratio. Instead, the sensitivity to the width increases as the width increases up to roughly the tip radius, after which it starts decreasing smoothly. These considerations are important in order to select the appropriate tip radius for a given fixed size of the nano-object to be analyzed.

On the other hand, the accuracy with which the physical dimensions can be determined also depends on the noise of the EFM measurements, as we mentioned before (dashed lines in **Figure 5.6g**). In the present work, the experimental noise of a single EFM profile measured on the AgNWs was $\sim 1-2$ zF/nm, which we reduced to ~ 0.5 zF/nm by averaging five consecutive profiles. Experimentally it has been shown that a noise level down to just ~ 0.1 zF/nm can be achieved [14]. Since the uncertainty scales almost proportionally to the experimental noise, we expect that the uncertainty of the extracted physical dimensions can still be further reduced. This reduction will, at some point, be overcome by the appearance of other sources of uncertainty, such as those related to the tip geometry calibration or the determination of the tip-sample distance. In any case, it is expected that the accuracy achievable with the EFM method under optimal conditions will be close to the one achievable by conventional AFM topographic imaging.

One obvious drawback of the proposed EFM method is the need to know the dielectric constant of the nano-object a priori. It has been investigated the possibility to overcome this limitation by considering a multiparametric extraction algorithm that included the dielectric constant of the nano-object as an additional unknown parameter (together with the nano-object dimensions). In such study, R. Fábregas, *et al.* [157] concluded that, from the mathematical point of view, an algorithm could be solved and provides a unique solution. However, for its practical implementation, it needs a noise floor well below ~ 0.1 zF/nm, which is very difficult to attain in practice. Therefore, even if theoretically is possible, the experimental implementation of this more general approach will need to wait until significant instrumental noise improvements can be attained.

Finally, it was mention that the method developed is sensitive to the cross-section shape of the nanowire object only in an effective manner. Indeed, it was shown that due to tip convolution

effects, the shape of the cross-section of the object (e.g., circular, square, pentagon, hexagon, etc.) could not be directly inferred, since all of them show a rounded shape. But, in all cases, the cross-section profiles can be interpreted in terms of a nanowire with an elliptical shape, where the height is close (within $\sim$ 1 nm) to the actual height of the nanoscale object, and the width represents an effective value, the larger, the further the shape departs from an actual ellipsoidal shape (check the Supplementary Information of ref. [131] for more detailed information, especially Figs. S17 and Table S2).

5.4.Conclusions

In this chapter, we have proposed a method to size single nanoscale objects based on the measurement of its electrical polarization by using Electrostatic Force Microscopy measurements combined with a multiparameter quantification extraction algorithm. We have validated the method for the case of $\sim$ 50 nm diameter silver nanowires and obtained values for the width and height comparable to those obtained from (deconvoluted) AFM topographic imaging and TEM imaging, with just a slightly smaller accuracy. As an application of the method to a fragile and low polarizable nano-object, we have considered the case of a macromolecular protein complex (bacterial polar flagella) ~10 nm in diameter, providing, again, a good agreement with AFM topographic data. The main advantage of the proposed method is that it can be applied to soft and poorly adhered samples, as it is based on the measurement of the long-range electric polarization forces, which does not require contact with the sample at any moment. This fact opens interesting possibilities in the determination of the physical dimensions of nano-objects made of soft materials like biological materials, polymers, gels, biomolecules, liquids, etc., for which an accurate determination has remained elusive for SPM methods until now.

5.5.Appendix

5.5.1.Additional AgNWs analyzed with the EFM method

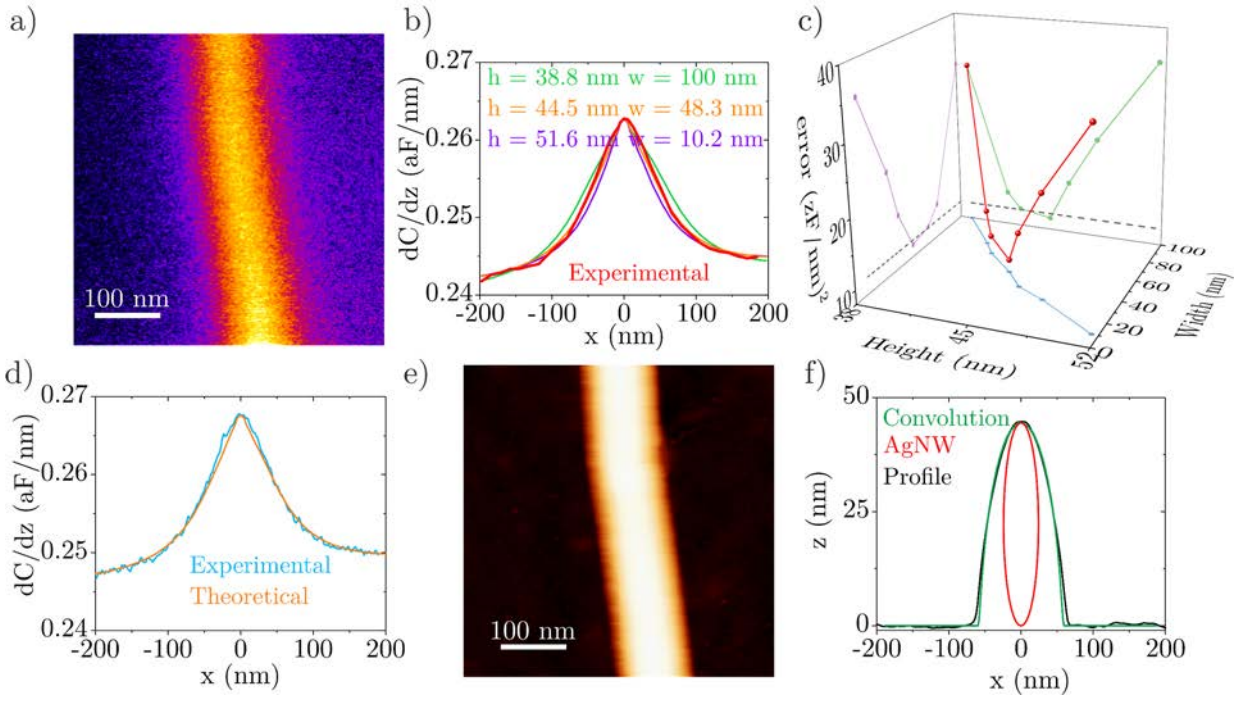

Figure 5.11: a) Constant height EFM image of AgNW #2 corresponding to **Figure 5.8** of the main paper. The imaging distance has been set to $z_{CH} = 77.5$ nm by using an EFM capacitance gradient approach curve (not shown). With the same curve, the tip geometry has been determined giving $R = 35 \pm 1$ nm, $\theta = 24 \pm 1°$, $offset = 105 \pm 2$ zF/nm. b) Calculated EFM cross-section profiles for some width/height couples that give the experimentally measured contrast. c) Cumulative error square of the calculated profiles with respect to the experimental profile as a function of the width and height. From the position of the minimum, we obtain $w_{EFM} = 55 \pm 10$ nm and $h_{EFM} = 43 \pm 1$ nm. d) Comparison of the selected EFM theoretical profile with the experimental one. e) AFM image of the same AgNW. f) Fitted convoluted AFM topographic profile to the experimental one giving $w_{AFM} = 48 \pm 1$nm and height $h_{AFM} = 44 \pm 1$ nm. From a SEM image (not shown) we obtained $w_{SEM} = 55 \pm 2$ nm.

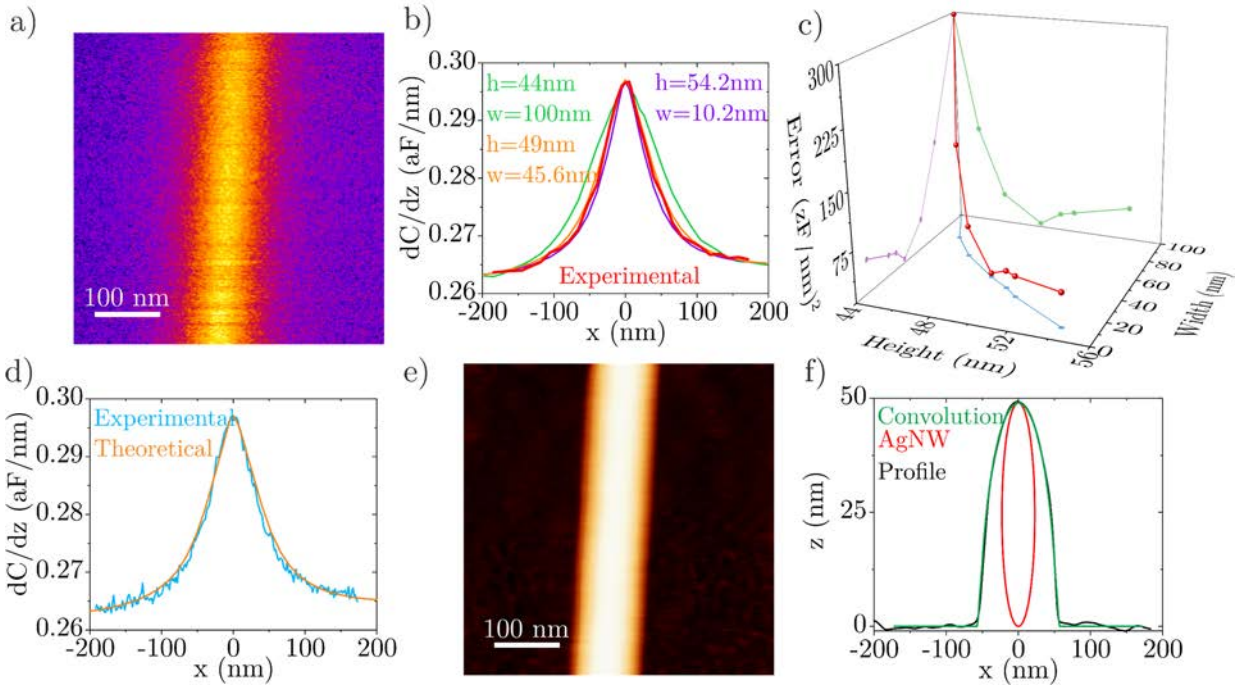

Figure 5.12: a) Constant height EFM image of AgNW #3 corresponding to **Figure 5.8** of the main paper. The imaging distance has been set to $z_{CH} = 70$ nm by using an EFM capacitance gradient approach curve (not shown). With the same approach curve the tip geometry has been determined giving $R = 31 \pm 2$ nm, $\theta = 25 \pm 1°$ and $offset = 112 \pm 2$ zF/nm. b) Calculated EFM cross-section profiles for some couples of width/height that give the experimentally measured contrast. c) Cumulative error square of the calculated profiles with respect to the experimental profile as a function of the width and height. From the position of the minimum, we obtain $w_{EFM} = 42 \pm 3$ nm and $h_{EFM} = 49 \pm 1$ nm. d) Comparison of the selected EFM theoretical profile with the experimental one. e) AFM image of the same AgNW. f) Fitted convoluted AFM topographic profile to the experimental one giving $w_{AFM} = 46 \pm 2$ nm and height $h_{AFM} = 49.0 \pm 0.5$ nm. From a SEM image (not shown) we obtained $w_{SEM} = 65 \pm 2$ nm.

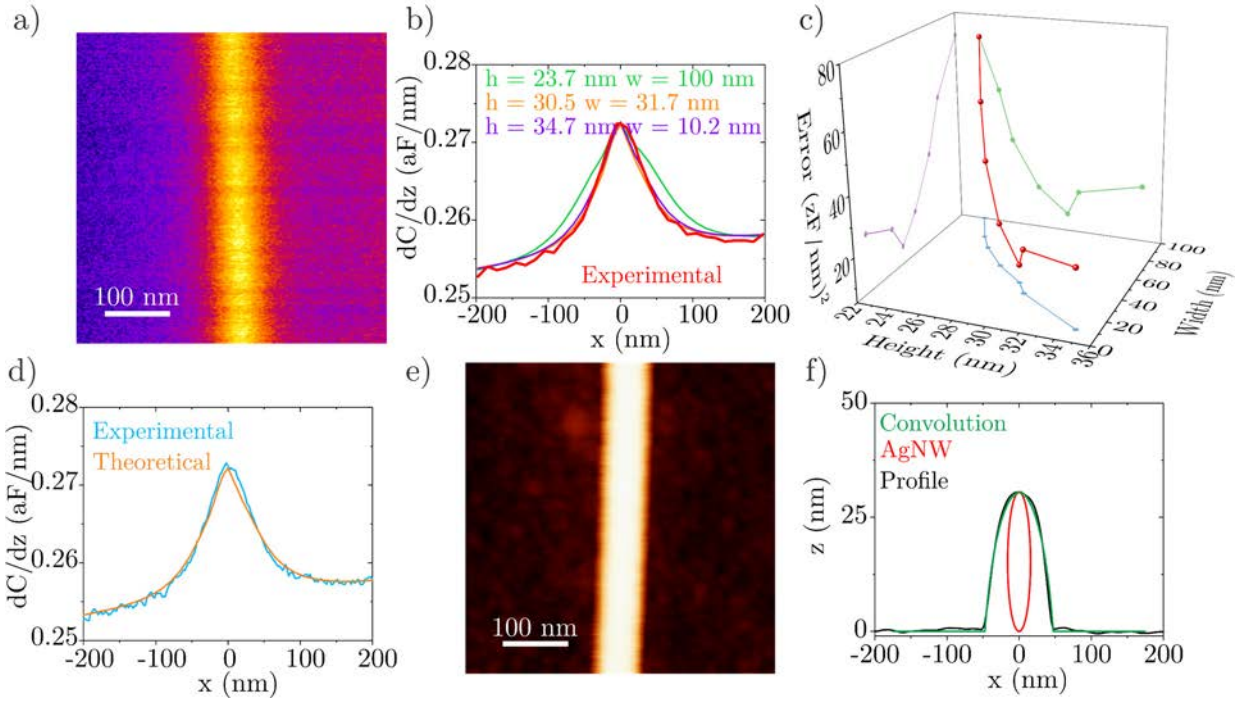

Figure 5.13: a) Constant height EFM image of AgNW #4 corresponding to **Figure 5.8** of the main paper. The imaging distance has been set to $z_{CH} = 60$ nm by using an EFM capacitance gradient approach curve (not shown). With the same curve, the tip geometry has been determined giving $R = 36 \pm 1$ nm, $\theta = 25 \pm 1°$, $offset = 99 \pm 2$ zF/nm. b) Calculated EFM cross-section profiles for couples of width/height that give the experimentally measured contrast. c) Cumulative error square of the calculated EFM profiles with respect to the experimental profile as a function of the width and height. From the position of the minimum, we obtain $w_{EFM} = 41 \pm 8$ nm and $h_{EFM} = 29 \pm 1$ nm. d) Comparison of the selected EFM theoretical profile with the experimental one. e) AFM image of the same AgNW. f) Fitted convoluted AFM topographic profile to the experimental one giving $w_{AFM} = 32 \pm 2$ nm and height $h_{AFM} = 30.5 \pm 0.5$ nm.

5.5.2.Additional flagella analyzed with the EFM method.

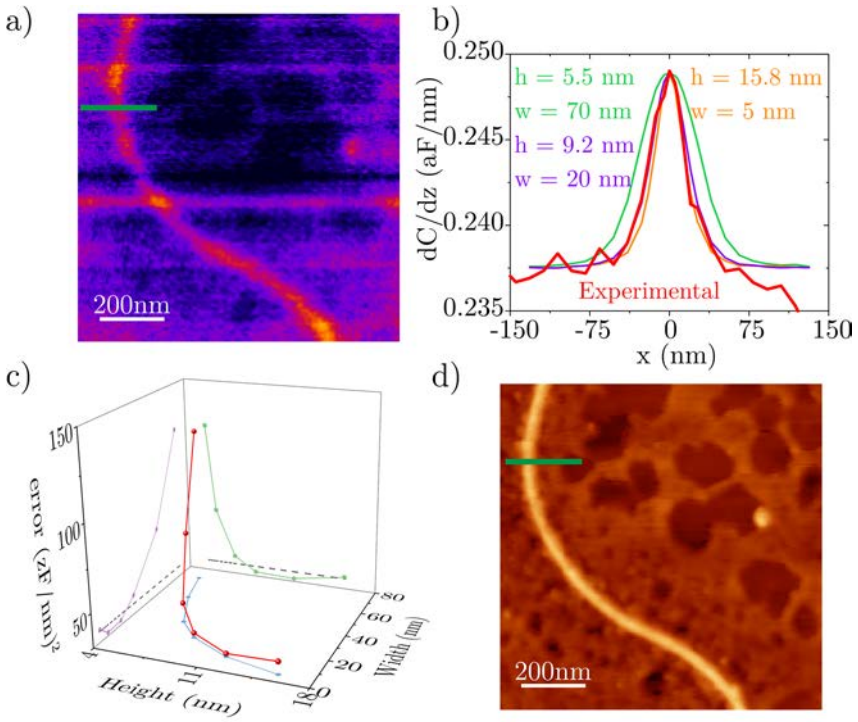

Figure 5.14: a) Constant height EFM image of a *S. oneidensis* flagellum. The imaging distance was set to $z_{CH} = 21$ nm by using an EFM capacitance gradient approach curve (not shown). With the same curve, the tip geometry was determined, giving $R = 24 \pm 1$ nm, $\theta = 11 \pm 1°$ and $offset = 118 \pm 1$ zF/nm. b) Calculated EFM cross-section profiles for couples of width/height that give the experimentally measured contrast. c) Cumulative error square of the calculated EFM profiles with respect to the experimental profile as a function of the width and height. From the position of the minimum, we obtain $w_{EFM} = 15 \pm 9$ nm and $h_{EFM} = 12 \pm 3$ nm. d) AFM image of the same flagellum. From the analysis of the image, we obtain $w_{AFM} = 18 \pm 2$ nm and $h_{AFM} = 11 \pm 1$ nm.

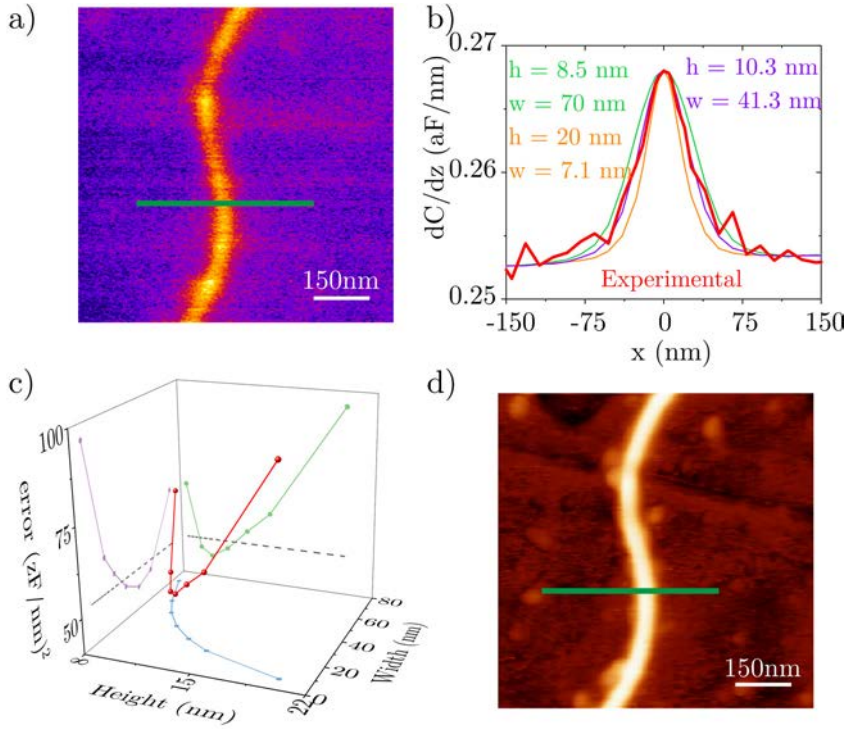

Figure 5.15: a) Constant height EFM image of the *P. aeruginosa* flagellum. The imaging distance was set to $z_{CH} = 25$ nm by using an EFM capacitance gradient approach curve (not shown). With the same curve the tip geometry was determined, giving $R = 30 \pm 1$ nm, $\theta = 11 \pm 1°$ and $offset = 128 \pm 2$ zF/nm. b) Calculated EFM cross-section profiles for couples of width/height that give the experimentally measured contrast. c) Cumulative error square of the calculated EFM profiles with respect to the experimental profile as a function of the width and height. From the position of the minimum, we obtain $w_{EFM} = 41 \pm 13$ nm and $h_{EFM} = 11 \pm 2$ nm. d) AFM image of the same flagellum. From the analysis of the image, we obtain $w_{AFM} = 35 \pm 2$ nm and $h_{AFM} = 13 \pm 1$ nm.

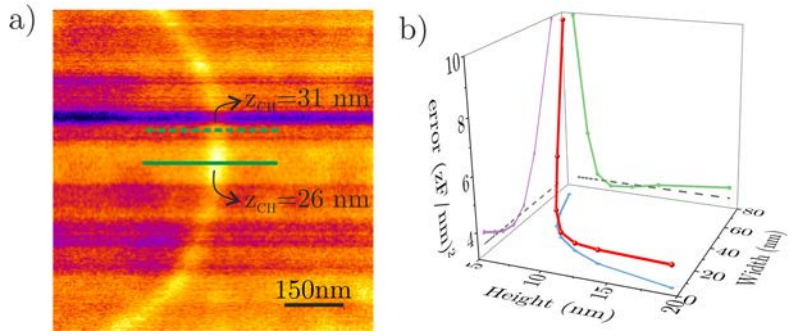

Figure 5.16: a) Additional cross-section line (dashed line) of **Figure 5.9** corresponding to a tip-sample distance of $z_{CH} = 31$ nm. (b) Cumulative square error R^2 of the different theoretical profiles with respect to the experimental profile as a function of w and h. The position of the minimum gives the physical dimensions of the flagellum: $h_{EFM} = 10 \pm 2$ nm and $w_{EFM} = 24 \pm 8$ nm. These values agree with the ones reported in **Figure 5.9** and obtained from the capacitance gradient profile corresponding to the solid line at a tip sample distance of $z_{CH} = 26$ nm ($h_{EFM} = 9 \pm 2$ nm and $w_{EFM} = 22 \pm 10$ nm).

6. Dielectric constant of flagellin proteins measured by SDM

This chapter reproduces almost literally the article: Dielectric constant of flagellin proteins measured by scanning dielectric microscopy, Nanoscale, ***10****, 2018, by H. Lozano, R. Fabregas, N. Blanco-Cabra, R. Millan-Solsona, E. Torrents, L. Fumagalli and G. Gomila* [93]*. My contribution to this paper was the realization of all the measurements (from sample preparation to image acquisition) and data analysis using a custom-written Matlab code developed by R. Millan-Solsona. The 3D modelling was performed by R. Fábregas and R. Millan-Solsona. N. Blanco-Cabra helped with the bacteria growth and E. Torrents supervised the biological aspects. The manuscript was written by me in collaboration with my supervisor G. Gomila and the other authors.*

In this chapter, I studied one of the *S. oneidensis* appendages, that is, flagella. Flagella are not supposed to be involved in the EET but they have been studied to consider the results as a reference dielectric sample for further studies on conductive bacterial nanowires.

As said before, in this chapter, we extend the applicability of SDM to macromolecular protein complexes forming sub-10 nm diameter nanoscale filamentous structures (and, in general, any 3D geometry) in a controlled environment. This chapter, by dealing with low polarizable sub-10 nm nanofilaments, goes well beyond earlier studies on the conducting (rather than dielectric) properties of organic and inorganic nanofilament structures, such as DNA [159], carbon nanotubes [115,159,160], or semiconductor nanowires [161]. Filamentous macromolecular protein complexes include important protein systems like actin or myosin filaments, microtubules, intermediate filaments, amyloid fibers or bacterial polar flagella, which is the specific case considered in the present work. These systems are fundamental in the biology of cells and, in some cases, play a central role in important diseases [162].

6.1.Introduction

The electric polarizability of proteins, represented in mean field theories by the relative dielectric constant [76,77], has long been recognized as a key parameter in determining the structure of the protein and their electrostatic interactions with charged biomolecules and ligands [78,163–165]. The dielectric constant determines the degree by which electric fields are screened by the protein microscopic electric dipoles themselves. As such, it has a strong effect in charge-charge and charge-dipole interactions in, and between, proteins, and hence, in the electrostatic energy contribution to protein folding, protein-protein, protein-DNA and protein-charged ligand interactions [79].

As we have described in Chapter 4, Scanning Dielectric Microscopy (SDM) is a technique able to access the dielectric constant of small scale macromolecular biological systems in a controlled environment [14,92]. The method has already enabled determining the dielectric constant of proteins in empty virus capsids and in virus tails [14,92], as well as, of proteins in sub-micrometric protein mono-layer patches [13]. In all cases, the obtained protein relative dielectric constants in dry air conditions were $\varepsilon_r \sim 3-4$, in good agreement with the values reported from bulk measurements on dry protein powders, $\varepsilon_r \sim 2-5$ [166,167] and with theoretical predictions excluding charged side chains, $\varepsilon_r \sim 4$ [164].

Determining the dielectric constant of proteins is an inherently complex problem, due to its microscopic nature and to its unavoidable interaction with the solvent or environment (e.g., electrolytes or the cell membrane). In fact, measurements performed on protein solutions (e.g., by impedance spectroscopy) reflect both the dielectric properties of the proteins, as well as those of the protein-solvent interface [80]. On the other side, measurements performed on dry crystal powders reflect only partially the structure and dynamics of proteins in physiological conditions [78]. As a result, until today, there is a large uncertainty on the specific value of the dielectric constant of proteins.

6.2.Materials and methods

6.2.1.Bacteria growth and sample preparation

For these experiments, we used *Shewanella oneidensis* MR-1 (ATCC 700550) cultivated first overnight at 30°C in Luria–Bertani (LB) (Scharlab) broth under aerobic conditions. Then, bacteria were resuspended in minimal AB medium [155] supplemented with 100 mM fumarate and 20 mM lactate during two days under anaerobic conditions at 30°C in Hungate tubes. We also used *Pseudomonas aeruginosa* PAO1 (ATCC 15692) grown overnight in LB medium at 37°C under aerobic conditions. The samples for EFM inspection are prepared by taking a drop of the culture solutions, depositing it onto a freshly cleaved HOPG and leaving it to rest for 10 min to promote the adhesion of bacteria on the substrate. Afterwards, the drop sample is rinsed two times, first with PBS and second with mili-Q water to remove any poorly adhered cells or any residual from the sample. Finally, we left the sample to dry under ambient conditions. The HOPG substrate was attached to a 1.5 cm diameter magnet using a carbon double side stick, which was connected to the electrical ground of the atomic force microscope by a small wire.

6.2.2.Scanning dielectric microscopy

We obtained dielectric images by using EFM [113,168] in the amplitude detection mode at constant height, as described in Section 4.3. Data is reported in terms of the capacitance gradient, which is related to the electrostatic force at the 2ω harmonic, $F_{2\omega}$, by eq. (4.7). Capacitance gradient approach curves were recorded on the substrate to determine the tip–substrate distance at which each line has been acquired. To calibrate the tip geometry, we followed the tip calibration procedure explained in Section 4.4.1.

Measurements were performed with a commercial AFM, [169] Cypher S from Asylum Research, using its internal lock-in to apply the ac voltage and to read the amplitude and phase of the electrostatic probe oscillation. Measurements were performed under controlled dry air conditions (RH $< 1\%$) maintained by a N_2 flow. We used platinum silicide conductive probes (PtSi-CONT, Nanosensors) with a spring constant $k \sim 0.2$ N/m (determined by the provider according to the probe dimensions), resonance frequency $f_r \sim 13$ kH, nominal radius $R \sim 20$ nm and half cone angle $\theta \sim 11.5°$. The analysis of the data was carried out using the WSxM software [154] (Nanotec Electrónica S.L.) and a custom-made software developed in Matlab (The Mathworks, Inc.).

Dielectric images were obtained in the SNAP mode of the Cypher S (the built-in line by line constant height mode). All EFM data were obtained with a voltage amplitude $V_{ac} = 3$ V at frequency $f = 2$ kHz (well below the mechanical resonance peak). The capacitance gradient instrumental noise was in the range $\sim 0.7 - 2$ zF/nm depending on the probe used and recording parameters.

6.2.3.Finite-element numerical calculations

We used finite element numerical calculations to simulate theoretical EFM capacitance gradient images and approach curves. These data were used in the quantitative analysis of the experimental EFM measurements. In this chapter, a single angle cone model was used, as in ref. [14], instead of a two-angle cone model that would better reflect the real geometry of the PtSi-CONT tips, since measurements are restricted to very short distances (< 70 nm). In this distance range, single and double cone angle models provide almost identical results, [130] while single angle models largely facilitate its 3D modelling.

The flagellum is modeled as a straight elliptic cylinder with axes w and h for the base ellipse, and length l. The flagellum is assumed to lie on a metallic substrate. Non-straight flagella geometries (e.g., curved elliptic cylinder) have also been considered, producing negligible differences with respect to a straight elliptic cylinder for the actual experimental geometries (see the Supplementary Information of ref. [93] for further details, especially Figure S4.). The straight geometry has been kept for computational efficiency. After an accurate process of optimization, the numerical noise gets to sub-0.1 zF/nm noise accuracy.

Automatic software routines written in Matlab (The MathWorks, Inc.) have been used to compute capacitance gradient images. In the calculations, the tip moves at a constant height with respect to the substrate. In addition, capacitance gradient approach curves have also been recorded by varying the tip–substrate distance.

6.2.4.Probe geometry calibration

The tip geometry has been determined as explained in 4.4.1 by fitting a short range ($15 - 60$ nm) capacitance gradient approach curve recorded over a bare part of the metallic substrate with calculated theoretical capacitance gradient approach curves, with the tip radius and capacitance gradient offset as free parameters. The remaining tip parameters were set to their

nominal values: $\theta = 11.5°$, $H = 12.5$ μm, $L_c = 3$ μm and $W_c = 3$ μm. As we mentioned above, the use of a single cone angle model tip is justified for the sharpened tips used in the present work because only short-range distances are considered in the EFM approach curves used for the tip calibration and in the image acquisition [17].

6.2.5.Flagellum width deconvolution

The flagella width, w, was obtained by fitting the measured topographic profile with the analytical spherical tip-ellipse convolution expression,

$$Z_{conv}(X) = \left(\frac{h}{2} - \frac{w^2}{2h}\right)\sin\big(\alpha(X)\big) + X\frac{w}{h}\tan\big(\alpha(X)\big) - R + \frac{h}{2} \tag{6.1}$$

$$X = \frac{w}{2}\cos\big(\alpha(X)\big) + \frac{R}{\sqrt{1 + \left(\frac{w}{h}\tan\big(\alpha(X)\big)\right)^2}} \tag{6.2}$$

where h is the measured flagella height and R is the calibrated tip radius. Eq.(6.1) and (6.2) and can be used to calculate the tip convoluted profiles if the tangent point between the tip apex and the ellipse is at a height smaller than $R\big(1 - \sin(\theta)\big)$, which was the case for the tips used in the present work. For smaller tip radii, one must also introduce the contribution of the tip cone in the calculation of the tip convolution. A written Matlab (The MathWorks, Inc.) code was written to implement this procedure automatically.

6.2.6.Dielectric constant extraction

The relative dielectric constant of the flagella ε_{flag} was determined as explained in Section 4.4.1 using the experimental capacitance gradient images obtained at different tip-substrate distances and considering the values of the capacitance gradient contrast at the center of the flagella (maximum). These experimental capacitance gradient values were compared with simulated capacitance gradient curves as a function of the flagellum dielectric constant numerically obtained by using the deconvoluted flagellum geometry and the calibrated tip geometry at the given experimental tip-sample distance. The extracted values for ε_{flag} from a given image correspond to the mean and standard deviation of the extracted values for the different tip–substrate distances.

6.3.Results and discussion

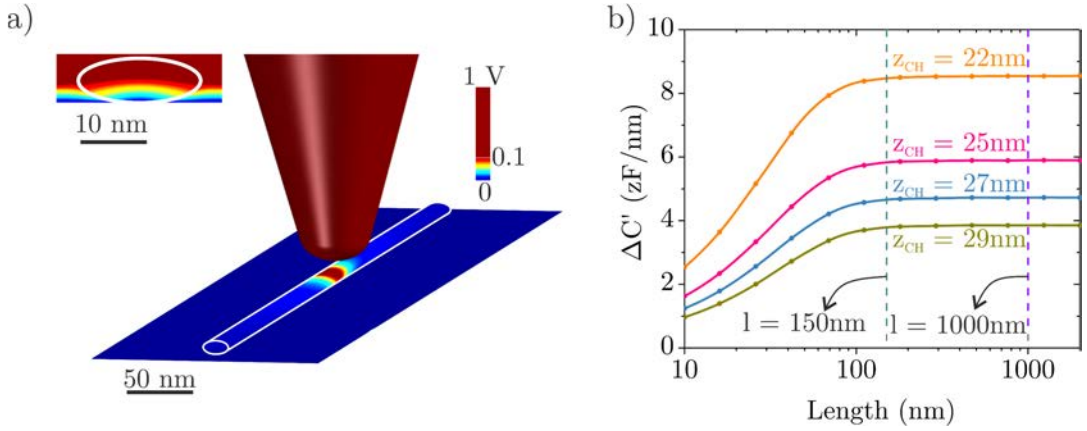

Figure 6.1: a) Example of the electric potential distribution obtained by solving the 3D tip-flagellum electrostatic model by means of finite element numerical calculations. Inset: electric potential distribution of a cross-section cut of the axial plane of the flagellum. b) Calculated capacitance gradient contrast versus flagellum length at different tip-substrate distances.

In this chapter, we measure the dielectric constant of the flagellin proteins in bacterial polar flagella of two different bacterial species, namely, *Shewanella oneidensis* MR-1 and *Pseudomonas aeruginosa* PAO1. Flagella are long thin ($\sim 10-20$ nm diameter) whip like appendages that bacteria use to move towards the nutrients. They are composed of 11 flagellin protein monomers twisting every ~ 5 nm [158]. To measure the dielectric constant, we used Scanning Dielectric Microscopy (SDM) (more details in Section 4.4). Briefly, SDM combines EFM measurements [113,168] and finite element numerical calculations made with realistic geometrical models. For the case of the polar flagella, given its filamentous nature, we need to use 3D electrostatic models. The dielectric constant measured in this way corresponds to a region of the flagellum containing a few hundreds of flagellin protein monomers. This fact can be observed in **Figure 6.1**, which shows the calculated electric potential distribution using the following parameters: cone height $H = 12.5$ μm, cantilever width $W_c = 3000$ nm and length $L_c = 3000$ nm, half cone angle $\theta = 11.5°$, apex radius $R = 24$ nm, tip-substrate distance $z_{CH} = 28$ nm, applied voltage $V = 1$ V, flagellum height $h = 8$ nm, width $w = 18$ nm, length $l = 1$ μm, and relative dielectric constant, $\varepsilon_r = 4$. In addition, the graph presented in **Figure 6.1b**, where the capacitance gradient versus the flagellum length is shown, demonstrates that the capacitance gradient saturates after a flagellum length $l > 150$ nm (green dashed line), and becomes independent from it. This size correspond, approximately, to the region size probed by the tip. The parameters used in the

calculation are: $R = 23.9$ nm, $\theta = 11.5°$, $h = 8.4$ nm, $w = 18$ nm, $\varepsilon_r = 4.1$, $H = 12.5$ μm, $W_c = 3000$ nm and $L_c = 3000$ nm. Flagella in the manuscript were several micrometers long, that we have approximate it to a length $l = 1000$ nm (violet dashed line in **Figure 6.1b**), well beyond any finite size effect.

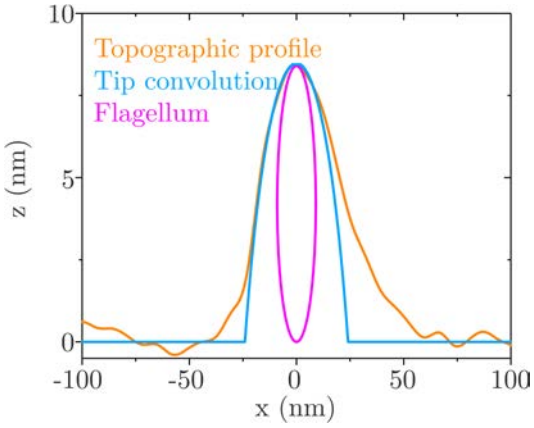

Figure 6.2: Example of a tip deconvolution procedure. The orange line shows the experimental profile, the blue line the calculate profile (using eq. (6.1) and eq. (6.2)) and the purple line shows the cross-section geometry.

Figure 6.3a shows topographic AFM images of two *S. oneidensis* MR-1 and one *P. aeruginosa* PAO1 bacterial cells on a HOPG substrate, illustrating the presence of the polar flagella. **Figure 6.3b** and **Figure 6.3c** show zoom-ins around the respective flagella. In addition, **Figure 6.3d** shows the topographic cross-section profiles taken along the dashed lines in **Figure 6.3b** and **Figure 6.3c**. The dimensions of the *S. oneindensis* flagellum obtained from the topographic images after tip deconvolution (**Figure 6.2**) are: height $h_{So} = 8.8 \pm 0.5$ nm, width $w_{So} = 18 \pm 2$ nm, and length $l_{So} > 1$ μm. For the *P. aeruginosa* flagellum, we obtain $h_{Pa} = 12.8 \pm 0.5$ nm, $w_{Pa} = 27 \pm 2$ nm and $l_{Pa} > 1$ μm, where the error is the standard deviation over five profiles. The measured flagella dimensions are in good agreement with existing experimental data. For instance, ref. [158] reports a near-atomic resolution cryo-Transmission Electron Microscopy (cryo-TEM) structure of flagellar filaments for different bacteria species, especially *P. aeruginosa* flagella. F. wang, *et al.* [158] reports a radius of ~8.5 nm for the *P. aeruginosa* flagella. With the AFM, we have obtained a half-height of ~6.5 nm and a half-width of ~13.5 nm, giving an equivalent circular radius of ~9.5 nm, in excellent agreement with the cryo-TEM measurements. This result indicates that the drying and adsorption process only slightly alters the structure of the flagella, producing a slight flattening at nearly constant area.

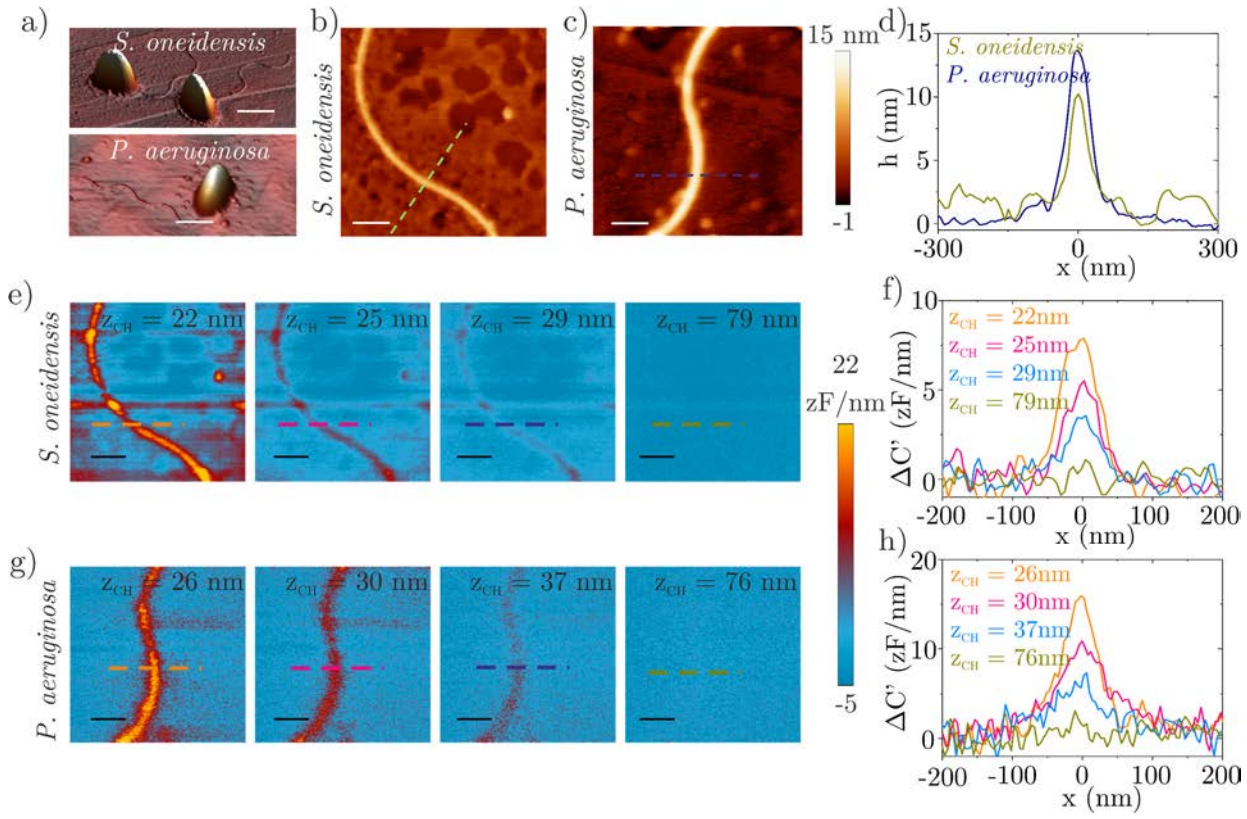

Figure 6.3: a) Topographic AFM images of two *S. oneidensis* MR-1 and one *P. aeruginosa* PAO1 bacterial cells on a HOPG substrate. b) and c) zoom-ins of the images in (a) around the respective flagella. d) Topographical cross-section profiles along the dashed lines in (b) and (c). e) Capacitance gradient EFM contrast images at four different tip-substrate distances of *S. oneidensis* MR-1 flagellum and f) capacitance gradient cross-section profiles along the dashed lines in (e). g) and h) Idem but for *P. aeruginosa* flagellum. The scale bars in the images in (a) correspond to a length of 1.5 μm and in (b) and (c) to 150 nm.

Figure 6.3e and **Figure 6.3g** show two sets of four constant height EFM capacitance gradient images obtained at distances (z_{CH}) ranging from ~20 nm to ~80 nm for the two types of bacterial flagella considered, respectively. The corresponding capacitance gradient cross-section profiles along the dashed lines in the images are shown in **Figure 6.3f** and **Figure 6.3h**. The dielectric EFM images clearly show the presence of the flagellum, especially at the closest tip-substrate distances (< 40 nm), obtaining dielectric contrasts up to $10 - 20$ zF/nm well above the instrumental noise of ~$0.7 - 2$ zF/nm. Note that the dielectric images display regions showing slightly different contrasts. The reason is that the flying tip-substrate distance is set at the ends of each line, and this may slightly change due to the presence of an unavoidable thin layer of residues < 1 nm. However, this issue does not constitute any problem for the analysis, which is done line by line.

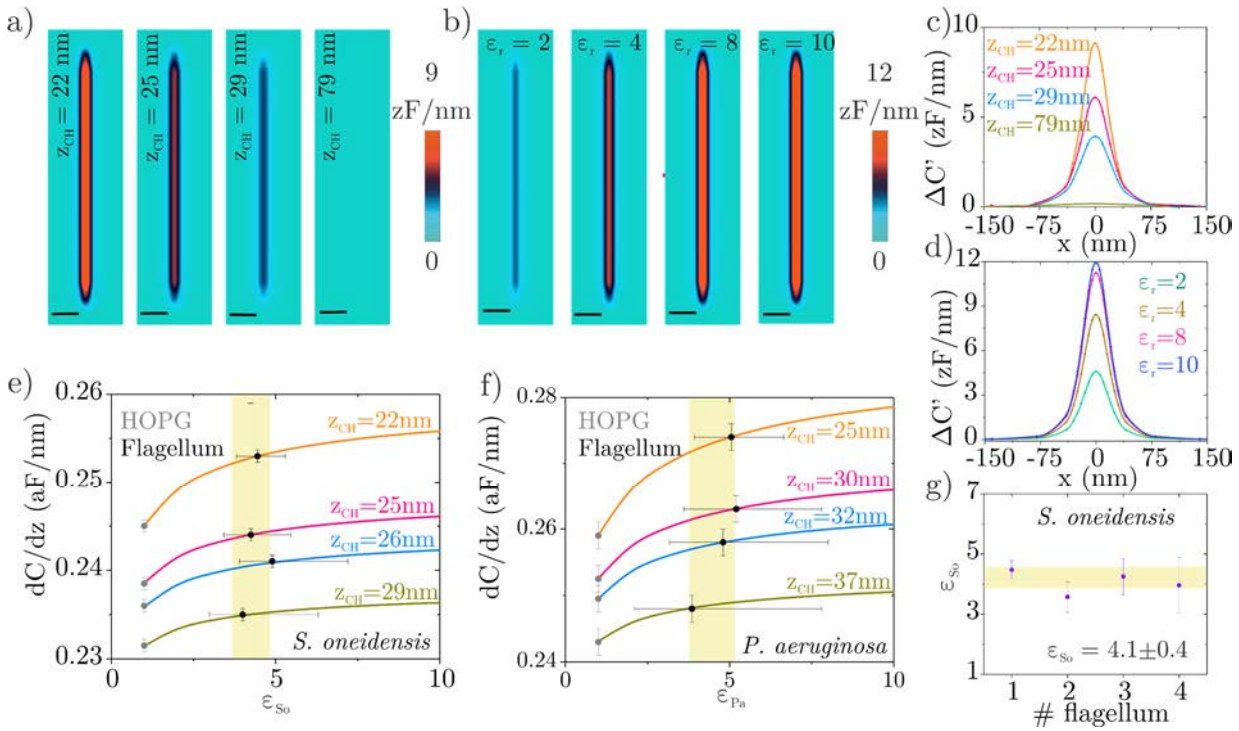

Figure 6.4: a) Examples of calculated capacitance gradient contrast EFM images at four different distances and b) four different dielectric constant for a straight flagellum. c) and d) Corresponding capacitance gradient cross-section profiles along the dashed lines shown in (a) and (b). e) Calculated capacitance gradient profile maxima as a function of the dielectric constant of the *S. oneidensis* MR-1 flagellum for four tip-substrate distances (continuous lines). The black and grey symbols represent, respectively, the experimental capacitance gradient values at the center of the flagellum and on a bare part of the substrate, respectively, obtained from the EFM images in **Figure 6.3**. The average dielectric constant is remarked by the shadowed area. f) Idem for the case of the *P. aeruginosa* PAO1 flagellum. g) Dielectric constant values measured on four different *S. oneidensis* flagella. The overall average dielectric constant value is shown by the shadowed area.

To quantify the dielectric constant of the flagella, we first calibrate the tip geometries following the procedure explained in Section 4.4.1, giving a tip radius $R_{So} = 23.9 \pm 0.5$ nm, half cone angle $\theta_{So} = 11.5°$ and capacitance gradient offset $offset_{So} = 118.5 \pm 0.7$ zF/nm for the tip used in the *S. oneidensis* MR-1 flagellum measurements. For the *P. aeruginosa* PAO1 measurements, the used tip geometry is $R_{Pa} = 30.0 \pm 0.5$ nm, $\theta_{Pa} = 11.5°$, and $offset_{Pa} = 128 \pm 2$ zF/nm. The tip geometries, together with the deconvoluted flagella geometries reported above, are used to calculate numerically theoretical capacitance gradient images. Examples of calculated dielectric images at different tip-substrate distances ($z_{CH} = 22,\ 25,\ 29$ and 79 nm), and setting $\varepsilon_r = 4.3$ constant, are shown in **Figure 6.4a** and **Figure 6.4b**, shows examples of calculated dielectric images with different dielectric constants ($\varepsilon_r = 2,\ 4,\ 8$ and 10) and fixing the tip-substrate

distance $z_{CH} = 22$ nm. The corresponding capacitance gradient cross-section profiles are shown in **Figure 6.4c**. **Figure 6.4d**. For numerical efficiency, we used a straight "short" ($l = 1$ μm) flagellum geometry, instead of the actual long-curved geometry displayed by the flagella (see **Figure 6.3b** and **Figure 6.3c**). This approximation is justified by the locality of the EFM measurements and the moderated curvature of the actual flagella (see **Figure 6.1b** and for more information check the Supplementary Information of ref. [93], especially Figure S4). **Figure 6.4e** and **Figure 6.4f** show the calculated capacitance gradient maxima as a function of the dielectric constant of the *S. oneidensis* and *P. aeruginosa* flagella, respectively, at four tip-substrate distances, z_{CH}, (continuous lines). The calculated curves are compared with the experimentally measured capacitance gradient values at the center of the flagella (black symbols). The intercept gives the dielectric constant. We obtained dielectric constant values of $\varepsilon_{So} = 4.3 \pm 0.6$ for *S. oneidensis* MR-1 and for *P. aeruginosa* PAO1 flagella $\varepsilon_{Pa} = 4.5 \pm 0.7$, where here the error represents the standard deviation of the values obtained at the four tip-substrate distances in each case.

Figure 6.4e and **Figure 6.4f** also show the capacitance gradient values measured on the bare HOPG substrate (grey symbols), which are used to set the tip-substrate distances; and hence matching the dielectric constant to $\varepsilon_r = 1$ by definition. The reliability of the extracted dielectric constant values has been further confirmed by comparing experimental capacitance gradient approach curves measured on top of the flagella with theoretically calculated ones, and by comparing the full experimental capacitance gradient EFM profiles with the calculated ones. This can be seen in **Figure 6.5a** which shows experimental capacitance gradient profiles at four different tip-substrate distances (solid lines) and the simulated profiles taking as a dielectric permittivity the one we obtained earlier ($\varepsilon_r = 4.3$), showing a good matching between experiments and simulations. The parameters used in all these simulations (**Figure 6.4** and **Figure 6.5**) are: $R_{So} = 23.9$ nm , $\theta_{So} = 11.5°$, $h_{So} = 8.4$ nm , $w_{So} = 18$ nm , $l_{So} = 1000$ μm and $offset_{So} = 118.5$ zF/nm for the *S. oneidensis* flagella and $R_{Pa} = 30.0$ nm,$\theta_{Pa} = 11.5°$,$h_{Pa} = 13.0$ nm, $w_{Pa} = 27$ nm, $l_{Pa} = 1000$ μm and $offset_{Pa} = 128.5$ zF/nm for the *P. aeruginosa* flagella. The rest of parameters are: $\varepsilon_r = 4.3$, $H = 12.5$ μm, $W_c = 3000$ nm and $L_c = 3000$ nm.

For additional information, **Figure 6.5b** shows experimental capacitance gradient approach curves over a bare metallic part of the sample (black line) and over a *S. oneidensis* flagellum (blue

line) and they are compared with the values on the image (green and red dots) coinciding images and curves in their respective approach curve (HOPG or flagellum curve). Continuous grey and violet lines represent the theoretical fitted curves for the HOPG and flagellum approach curves, respectively. They are used to calibrate the tip geometry and capacitance gradient offset (tip radius $R_{So} = 23.9 \pm 0.5$ nm and $offset_{So} = 118.5 \pm 0.7$ zF/nm, the cone angle was fixed to $\theta = 11.5°$) and the dielectric constant of the flagellum, ($\varepsilon_{So} = 4.3 \pm 0.6$), respectively. Remarkably, after considering the respective tip and sample geometries, the dielectric constant values obtained for the two types of flagella are almost the same. Also, different ways to obtain the dielectric constant (**Figure 6.4** and **Figure 6.5**) provide similar results among them.

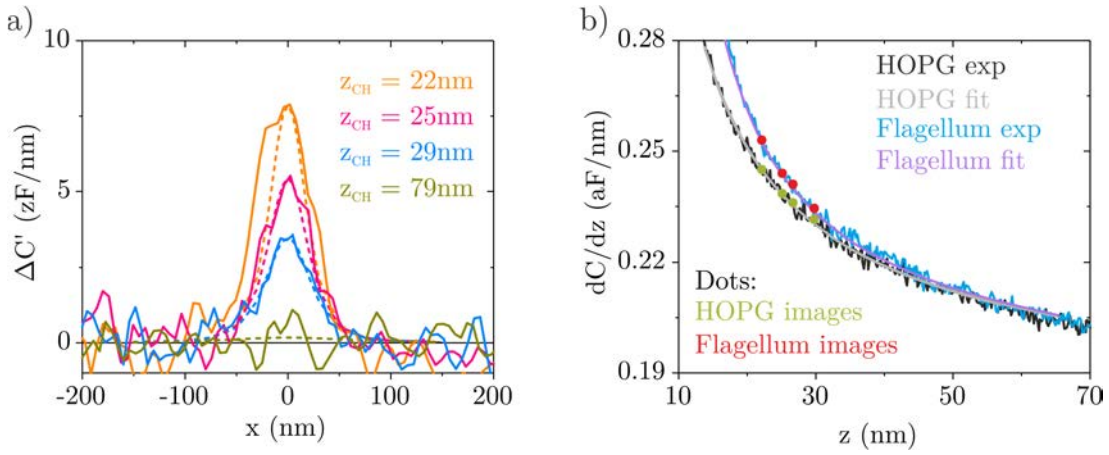

Figure 6.5: a) Experimental capacitance gradient profiles at four different tip-substrate distances (solid lines) and the simulated profiles taking as a dielectric permittivity $\varepsilon_r = 4.3$. b) Experimental capacitance gradient approach curves over a bare metallic part of the sample (black line) and over a *S. oneidensis* flagellum (blue line) and they are compared with the values on the image (green and red dots) coinciding images and curves in their respective approach curve (HOPG or flagellum curve. Theoretical fitted curves for the HOPG and flagellum approach curves (continuous grey and violet lines, respectively).

The same procedure described above was repeated for three different additional flagella of *S. oneidensis*, obtaining in all cases similar values for the extracted dielectric constant (see **Figure 6.4g**). The average value for the relative dielectric constant (N = 4) is $\varepsilon_{So} = 4.1 \pm 0.4$ and individual values are presented in **Table 6.1**.

Determining the dielectric constant of proteins is an inherently complex problem, due to its microscopic nature and to its unavoidable interaction with the solvent or environment (e.g., solution electrolytes or the cell membrane). In fact, measurements performed on protein solutions (e.g., by impedance spectroscopy) reflect both the dielectric properties of the proteins, as well as

those of the protein-solvent interface [80] and interfacial water molecules [89]. On the other side, measurements performed on dry crystal powders reflect only partially the structure and dynamics of proteins in native conditions [78]. SDM enables measuring the dielectric constant in dry conditions, to get rid of solution effects, and on natural protein macromolecular complexes.

# flagellum	Tip radius (nm)	Cone angle (deg)	Height (nm)	Width (nm)	Dielectric constant	Bacteria
Flagellum 1	23.9 ± 0.5	11.5	8.4	18	4.3 ± 0.6	*S. oneidensis*
Flagellum 2	24.5 ± 0.5	11.5	10.8	14	4.5 ± 0.3	*S. oneidensis*
Flagellum 3	26.0 ± 0.5	11.5	10.7	13.8	3.6 ± 0.5	*S. oneidensis*
Flagellum 4	27.8 ± 0.5	11.5	9.4	19	4.0 ± 0.9	*S. oneidensis*
Flagellum 5	30.0 ± 0.5	11.5	13	27	4.5 ± 0.7	*P. aeruginosa*

Table 6.1: Table of parameters of the different flagella analyzed in **Figure 6.4g**, indicating the tip radius, cone angle, flagellum height and width, the dielectric constant, and the type of bacterial cell.

In this chapter, we measured the dielectric constant of the filamentous part of polar flagella, composed of flagellin proteins [170], of two distinct types of bacteria, namely *S. oneidensis* MR-1 and *P. aeruginosa* PAO1. The obtained dielectric constants are within a relatively short range of values ε_r~4− 4.5, well defined by the small uncertainty of the measurements (less than a ~15%, despite the complexity of the measurements and the small size of the flagella). We note that while the amino acid sequences of the terminal regions of flagellin, including about 180 NH_2-terminal and 100 COOH-terminal residues, are known to be well conserved from species to species of bacteria, the central region can be highly variable [171]. In the case of *P. aeruginosa* flagellin protein (FliC) is 122 aminoacids longer at the central region of the protein compared to the *S. oneidensis* flagellin. Despite that, the dielectric response of flagella from *P. aeruginosa* PAO1 and *S. oneidensis* MR- 1 was very similar.

As said in Section 3.3 and **Figure 3.3**, the dielectric constant found for the flagella is similar to the values obtained in other macromolecular protein complexes using the same technique, such as the T7 bacteriophage virus capsid ($\varepsilon_r = 3.5 \pm 0.5$) [14] and virus tail ($\varepsilon_r = 3.4 \pm 0.4$) [92], or submicrometric monolayer patches of bacteriorhodopsin ($\varepsilon_r = 3.3 \pm 0.3$) [13]. However, they differ from those obtained on macromolecular complexes of other cellular components, such as micrometric lipid bilayers patches (DOPC, $\varepsilon_r = 1.9 \pm 0.3$), cholesterol crystals ($\varepsilon_r = 2.1 \pm 0.3$) [13], T7 bacteriphage full viruses ($\varepsilon_r = 6.3 \pm 0.4$) [14] and T7 bacteriophage DNA ($\varepsilon_r = 8.5 \pm 1.4$)

[92]. Thus, present results support the use of dielectric constant values in the range ε_r~$3-4$ for the hydrophobic part of proteins, which is believed to account for electronic polarization and small backbone fluctuations [164]. Whether there is a functional reason for the dielectric constant of proteins to take values in the intermediate range between that of lipids and DNA, or whether there are some proteins showing markedly different dielectric behaviour, still needs to be further investigated.

The SDM dielectric measurements reported here are local and at the nanoscale. The dielectric constant obtained for flagella reflects the dielectric constant of a very small portion of the flagellum. The length of this portion, referred to as dielectric probed length, can be determined as the length of the flagellum starting from which the dielectric contrast reaches a value independent from its length (**Figure 6.1b**). **Figure 6.6** (black symbols, left axis) shows the dependence of the dielectric probed length as a function of the tip radius for the *S. oneidensis* MR-1 flagellum. For the tip radius used in the present study (~25 nm), the probed length of the flagella is ~130 nm, which corresponds to ~250 flagellin protein monomers [162], which is a remarkably small number. Parameters used in the calculations are: $R = 23.9$ nm, $\theta = 1.5°$, $h = 8.4$ nm, $w = 18$ nm, $l = 1000$ nm, $\varepsilon_r = 4.1$ and $z_{CH} = 22$ nm.

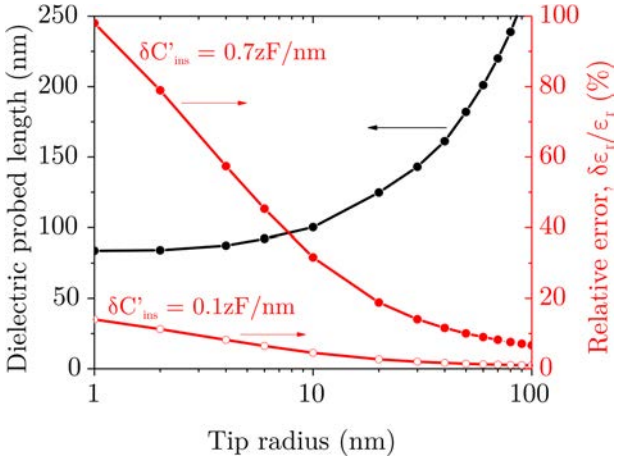

Figure 6.6: (Left axis, black symbols) Numerical calculated length of the flagellum probed using SDM measurements as a function of the tip radius. (Right axis, red symbols) Relative error in the extracted relative dielectric constant as a function of the tip radius for two different instrumental noise levels $\delta C'_{inst} = 0.7$ zF/nm (filled red symbols) and 0.1 zF/nm (empty red symbols). The arrows are guides to the eyes.

Improving the locality of the dielectric measurement on full flagella structures, and, hence, probing a smaller number of protein monomers, is barely possible by using the presented approach.

Further reducing the tip radius and/or the cone angle only moderately improves the locality of the dielectric measurement, as shown in **Figure 6.6** for the smallest radii. Probing a significantly smaller number of flagellin protein monomers using this technique would require considering flagella portions (instead of full flagella), with a length shorter than the dielectric probed length discussed above. Under these conditions and based on previous studies [13], it should be possible to attain the few flagellin monomer limit.

Reducing the tip radius, or the flagella length would increase the uncertainty of the dielectric constant due to a reduction of the signal to noise ratio. We show it in **Figure 6.6** (red symbols, right axis) where we plot the relative error in the dielectric constant extraction as a function of tip radius for the instrumental noise level of the present work, $\delta C'_{\text{inst}} = 0.7$ zF/nm and for the state of the art noise level, $\delta C'_{\text{inst}} = 0.1$ zF/nm [14]. The relative error has been calculated according to the relation

$$\frac{\delta\varepsilon_r}{\varepsilon_r} = \frac{\delta C'_{inst}}{\varepsilon_r \frac{\delta}{\delta\varepsilon_r} \Delta C'(z, \varepsilon_r, R)} \tag{6.3}$$

where ΔC'(z, ε_r, R) is the maximum contrast for a given tip-substrate distance, z, relative dielectric constant of the flagellum, ε_r , and tip radius, R. For the tip radii used in the present work (~25 nm), the relative error in a single measurement is ~15%, which can be reduced below a ~10% by averaging several measurements. However, for smaller tip radii (~5 nm), or for short portions of flagella, the error in the extraction of the dielectric constant would quickly rise to unacceptable values ($> 30\%$), unless the instrumental noise is decreased down to at least ~0.1 zF/nm (empty red symbols in **Figure 6.6**).

On wet samples, the overall dielectric response of proteins might slightly increase due to contributions coming from polar end groups and from eventual tightly adsorbed water molecules. The contribution of the hydrophobic core of the protein, instead, is expected not to be significantly affected. In this respect, the increase could not be so high as expected due to the recent findings on the very low dielectric constant of confined water [89].

Finally, we remark that the present approach should be applicable to most filamentous protein nanostructures present in cells, such as actin or myosin filaments, microtubules or intermediate

filaments, including proteins nanofilaments relevant for some diseases, such as amyloid fibers [162], thus spanning the number of proteins accessible to dielectric quantification significantly.

6.4.Conclusions

In this chapter, we have studied one of the *S. oneidensis* appendages, that is, flagella and we have compared their dielectric properties with *P. aeruginosa* flagella. Therefore, we have used scanning dielectric microscopy to locally measure the dielectric constant of the filamentous part of bacterial polar flagella composed of flagellin proteins. We have obtained dielectric constant values $\varepsilon_{So} = 4.3 \pm 0.6$ and $\varepsilon_{Pa} = 4.5 \pm 0.7$ for *S. oneidensis* MR-1 and *P. aeruginosa* PAO1 flagella, respectively. These values do not depend on the bacterial species and reflect the response of only a few hundred proteins. Similar relative dielectric constant values have been reported for other macromolecular protein complexes using the same technique. Altogether, these results indicate that the relative dielectric constant of proteins under dry conditions show dielectric constant values ($\varepsilon_r \sim 3-5$), like those reported using macroscopic techniques applied to dry protein crystals, and different from the values reported for other cell components such as lipids ($\varepsilon_r \sim 2$) or DNA ($\varepsilon_r \sim 8$). These results may have important implications in the understanding of the relevance of the electrostatic energy contribution to the protein function and structure.

7. Characterization of *Shewanella oneidensis* MR-1 outer membrane vesicles

In this chapter, we propose to study and elucidate the conductance of *S. oneidensis* MR-1 nanowires, or outer membrane vesicles, using Scanning Dielectric Microscopy and the measurement of its dielectric constant. In order to do so, first, we will analyze the topographic properties using Atomic Force Microscopy. Subsequently, the electric properties will be measured using SDM. The bacteria cultivation to produce TSMSs was learned during a short stay at El-Naggar Laboratory, at the University of Southern California (USC), EEUU.

The results presented in this chapter are being collected to prepare an article for publication.

7.1.Introduction

As we mentioned in Chapter 1, gram-negative and, recently discovered, gram-positive bacteria release MVs. They were first discovered to come from controlled blebbing of the outer membrane of gram-negative bacteria and, therefore, they are often called Outer Membrane Vesicles (OMVs). These OMVs have sizes between ~40 to 250 nm in diameter, and they can have diverse functionalities, from communication among themselves or other microorganisms to traffic of molecules [56]. In addition to the OMV, there are other types of MV, especially the TSMSs, of which the simplest version is a chain of OMVs [58]. The TSMSs are tube-like protrusions of the cytoplasmic membrane, that is, a mixture of proteins and lipids and do not contain RNA and chromosomal DNA [58].

Shewanella oneidensis MR-1 is a gram-negative bacterium that produces chains of OMV that can elongate and turn into smooth filaments [49]. These bacteria are electrochemically active, that is, they can exchange electrons with extracellular electron acceptors [6,45,65]. *S. oneidensis* can carry EET out through nanowires that are OME, specifically TSMSs [6,7,46,49–51,65], which act as a conduit of electrons between the cell and distant substrates. Although *S. oneidensis* nanowires are TSMSs, for simplicity and to use the same nomenclature used in the literature, henceforth, we will refer to them as OME.

There is a debate on whether these OMEs are conductive or not. Reguera *et al.*, conclude in their work that *S. oneidensis* nanowires are not conductive [52] while Gorby *et al.* showed the conductive nature of these nanowires [4,66,68]. The different behaviours may be due to the cultivation conditions between both studies, the delicate nature of bacterial pili, and the presence of multiple appendages in *S. oneidensis* MR-1 such as pili, flagella or OMEs which could induce to error when identifying those responsible of EET [45].

7.2.Materials and methods

7.2.1.Bacteria culture and sample preparation

We used *Shewanella oneidensis* MR-1 (ATCC 700550) cultivated first overnight at 30°C in Luria-Bertani (LB) (Scharlab) broth in aerobic conditions, and then in the minimal defined medium [49] supplemented with fumarate overnight at 30°C in Hungate tubes. Then, bacteria are resuspended in the minimal defined medium without fumarate placed in a reactor consisting of a cylinder paste with silicon to a coverslip with evaporated gold or to a cell chamber (more details are explained below, in Section 7.3.1 and in **Figure 7.2**) and let it sit for 3 – 4 hours. After this time, the medium is extracted and the sample is gently rinsed with miliQ. Finally, the sample is left to dry in ambient conditions. Then, the cylinder is removed from the gold coverslip and the last one is attached to a 1.5 cm diameter magnet. Finally, the gold is connected electrically to the magnetic disk using silver paste and this one is connected to the electrical ground of the atomic force microscope by a small wire.

7.2.2.Scanning Electron Microscopy images

We used a FE-SEM JEOL J-7100F from the Centros Cientificos i Tecnológicos de la Universitat de Barcelona (CCiTUB), Spain. Images have been obtained by applying a voltage of

10 kV. SEM samples were prepared using a critical point dry standard protocol. Briefly, bacteria are fixed with paraformaldehyde (PFA). Subsequently, the sample is rinsed with Phosphate Buffer Solution (PBS) and miliQ. Then, the miliQ is changed to a 100% ethanol solution following steps of 40% ethanol, 60% ethanol, 80% ethanol, 95% ethanol and 100% ethanol. Finally, the sample is introduced in a critical point dryer where 100% ethanol is changed with CO_2 liquid and it is raised to the critical point of CO_2. In this way, the morphological properties of the sample are kept intact. In order to see the sample with the SEM, it was coated with a 10 nm carbon layer.

7.2.3.Fluorescence images

Bacteria were stained with N-(3-triethylammoniumpropyl)-4-(6-(4-(diethylamino)phenyl) hexatrienyl)pyridinium dibromide (FM® 4-64FX, Thermo Fisher Scientific) at a concentration of 0.5 µg/ml, according to manufacturer instructions. Fluorescent bacteria were then visualized by a Nikon inverted fluorescent microscope ECLIPSE Ti-S/L100 (Nikon), and images were taken with a DS-Qi2 Nikon camera (Nikon) coupled to the microscope.

7.2.4.Scanning Dielectric Microscopy

EFM images have been obtained with a Cypher S AFM from Oxford Technologies (former Asylum Research) and PtSi-CONT probes with a typical spring constant $k \sim 0.2\,\mathrm{N/m}$ (determined by the provider according to the probe dimensions), resonance frequency $f_r \sim 13\,\mathrm{kHz}$ and nominal tip radius $R \sim 20\,\mathrm{nm}$. We recorded the second harmonic (2ω) of the probe oscillation amplitude, $A_{2\omega}$, by using the system internal lock-ins of the Cypher. EFM data were obtained with a voltage amplitude $V_{\mathrm{ac}} = 5\,\mathrm{V}$ at a frequency $f = 2\,\mathrm{kHz}$ (well below the mechanical resonance peak of the probe). EFM data were reported in terms of the capacitance gradient, which is related to the 2ω oscillation amplitude by eq. (4.7). Further details can be obtained in Section 4.3. EFM measurements were performed in controlled dry air conditions (RH $< 1\%$) maintained by a N_2 flow.

The tip geometry was determined from EFM approach curves measured on a bare part of the metallic substrate. Then, we used finite element numerical calculations to simulate theoretical EFM capacitance gradient approach curves and compared them with experimental curves. The geometrical model and theoretical approach curves are obtained reconstructing the topographical AFM image into a model in COMSOL. Further details are explained in Section 4.4.1. The

following tip parameters were set to their nominal values in the tip geometry calibration: cone height $H = 12.5$ μm, local cantilever $L_c = 3$ μm and cantilever thickness $W_c = 3$ μm.

7.3.Results and discussion

7.3.1.Growth conditions

As said before, the cultivation methods are very important in order to get the maximum cytochrome content in the *Shewanella oneidensis* membrane and their OME, and, eventually, the maximum conductivity [50]. In the present chapter, we used a minimum medium without oxygen [4]. The compounds of the used minimum medium are detailed in **Table 7.1** and were obtained from El-Naggar Laboratory, one of the world leaders about *Shewanella* nanowires, during my stay in their lab at the University of Southern California (USC), California, EEUU.

NW media	g/l	Final concentration
Water	970	N/A
PIPES buffer	9.07	30
Sodium hydroxide	0.3	7.5
Ammonium chloride	1.5	28.04
Potassium chloride	0.1	1.34
Sodium phosphate	0.6	4.35
Sodium chloride	1.75	30
Sodium lactate 98%	6.86	60
Sodium fumarate dibasic	4.8	30
Minerals solution 100X	10 ml	N/A
Amino acid solution 100X	10 ml	N/A
Vitamin solution 100X	10 ml	N/A

Table 7.1: Defined minimum medium used in the obtention of *Shewanella oneidensis* MR-1 nanowires and called *nwmedia*.

The pH of the minimum medium defined in **Table 7.1** is adjusted to pH $=$ 7.2 and autoclave, prior to the addition of the mineral, aminoacid and vitamin solution. The composition of these additional solutions, the mineral solution, vitamin solution and aminoacid solution, are shown in **Table 7.2**. The pH of these solutions is adjusted to pH $=$ 7.2 and they are sterilized by filtering them. In addition to these solutions, we add the subsequent additional minerals: Fe-NTA, $MgCl_2$ and $CaCl_2$. From now on, we will refer to this medium as *nwmedia*.

Mineral solution	Vitamin solution
Nitrilotriacetic acid	Biotin (d-biotin)

Magnesium sulfate heptahydrate	Folic acid
Manganese sulfate monohydrate	Pyridoxine HCl
Sodium chloride	Riboflavin
Ferrous sulfate heptahydrate	Thiamine HCl 1.0 H2O
Calcium chloride dihydrate	Nicotinic acid
Cobalt chloride hexahydrate	D-pantothenic acid
Zinc chloride	B12
Cupric sulfate pentahydrate	P-aminobenzoic acid
Aluminium potassium disulfate dodecahydrate	Thiotic acid
Boric acid	**Aminoacid solution**
Sodium molybdate dihydrate	L-glutamic acid
Nickel chloride hexahydrate	L-arginine
Soidum tungstate	DL-serine
Others	
Fe^{2+} (Iron(II) sulfate heptahydrate)	NTA (Nitrilotriacetic acid trisodium salt)
$MgCl_2$	$CaCl_2$

Table 7.2: Composition of the mineral solution, vitamin solution, aminoacid solution and other minerals added to the *nwmedia* detailed in **Table 7.1**.

As said in the materials and methods (Section 7.2.1), first, we grew bacteria, that previously was on an agar plate for better storage, in LB aerobic medium. Then, these bacteria were transferred to the *nwmedia* supplemented with fumarate at 30°C without O_2 in Hungate tubes. Finally, these bacteria are resuspended in a reactor filled with *nwmedia* without fumarate.

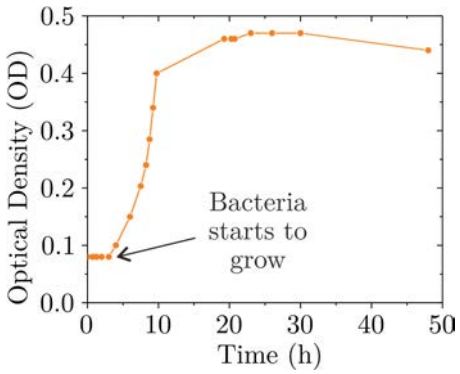

Figure 7.1: Growing rate of *Shewanella oneidensis* MR-1 in the *nwmedia* supplemented with fumarate at 30°C.

Subsequently, we analyzed the growing rate of *Shewanella oneidensis* MR-1 in the anaerobic *nwmedia* supplemented with fumarate. **Figure 7.1** shows that bacteria started to grow after 5 h of being in the medium since the Optical Density (OD) starts to increase. After 20 h, the OD did

not increase anymore because bacteria cannot grow more due to the lack of nutrients. Finally, after 40 h, the OD started to decrease due to cell lysis.

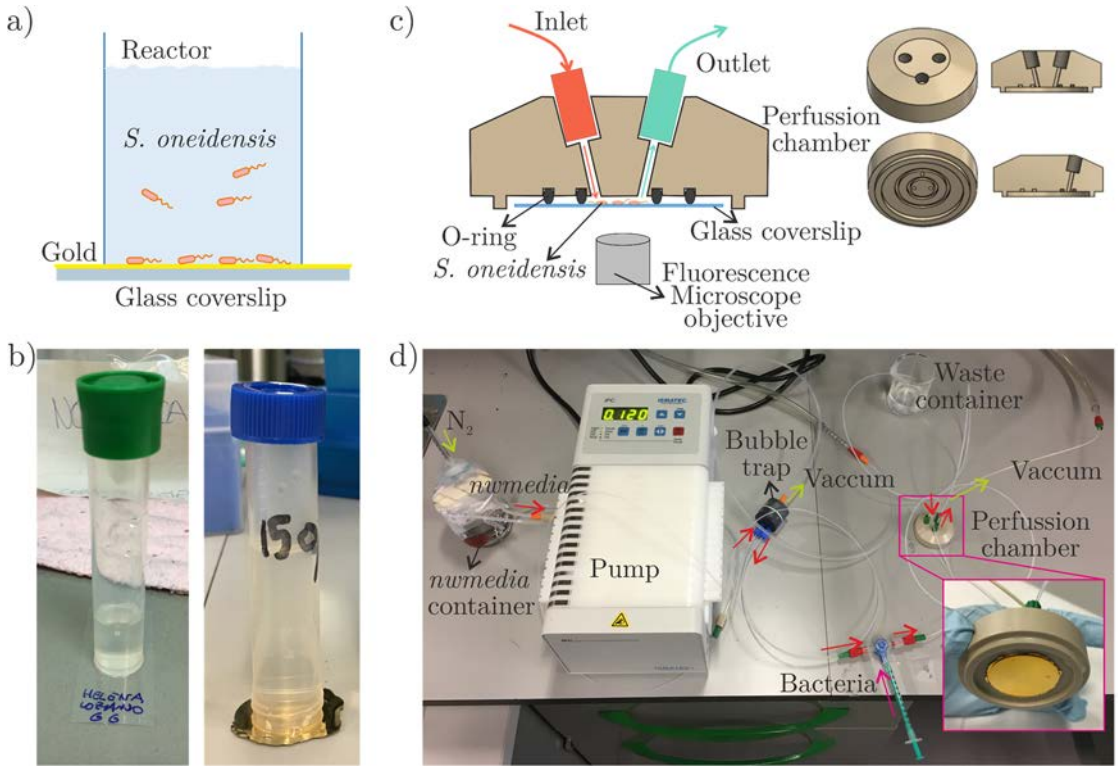

Figure 7.2: a) Schematic representation of the reactor setup. b) Real image of the reactor setup. c) Schematic representation of the perfusion chamber setup. d) Real image of the perfusion chamber setup, the red arrows indicate the flow of the *nwmedia* and the green arrows indicate the flow of vacuum or N_2.

As said before, after the overnight growth in the anaerobic *nwmedia* supplemented with fumarate, bacteria are resuspended in *nwmedia* without fumarate. In this last step, bacteria are left for 3 – 4 h on a surface to allow bacteria to develop the OME. This part can be performed in two different ways. The first one (shown in **Figure 7.2a** and **Figure 7.2b**) takes place in a reactor, it consists of a plastic cylinder and a coverslip attached to one side of the cylinder with silicon, to allow an easy detachment after the 3 – 4 h of the bacteria inoculation. We assume anoxic conditions at the surface of the coverslip since bacteria consume it faster than the diffusion through the system. The coverslip has a thin layer (~80 nm) of evaporated gold to allow further EFM measurements. **Figure 7.2c** and **Figure 7.2d** shows the second method that consists of a cell chamber. In this system, the *nwmedia* without fumarate and without oxygen is pump through the cell chamber, passing through a bubble trap to get rid of air bubbles. Then, the *nwmedia* flow is stopped and bacteria are added to the cell and they are left there for ~15 min to let them

adhere to the surface. Finally, the *nwmedia* flow is started again and it is set like this for 3 – 4 h. After this time, the coverslip under the cell chamber is removed (it was adhered to the cell chamber by a vacuum system), clean and let it dry in ambient conditions for further examination.

7.3.2.Fluorescence analysis

S. Pirbadian, *et al.* [49] claim that *S. oneidensis* nanowires are extensions of the outer membrane and the periplasmic. In order to get this conclusion, they stained the bacteria with a dye that specifically binds to the membrane (FM-464FX) and they saw that after some hours (2 – 3 h), some filaments were going out of the bacteria. These filaments were stained red fluorescent, demonstrating that the nanowires were extensions of the outer membrane. After the fluorescent images, they could observe these filaments on the AFM, showing that they were OME.

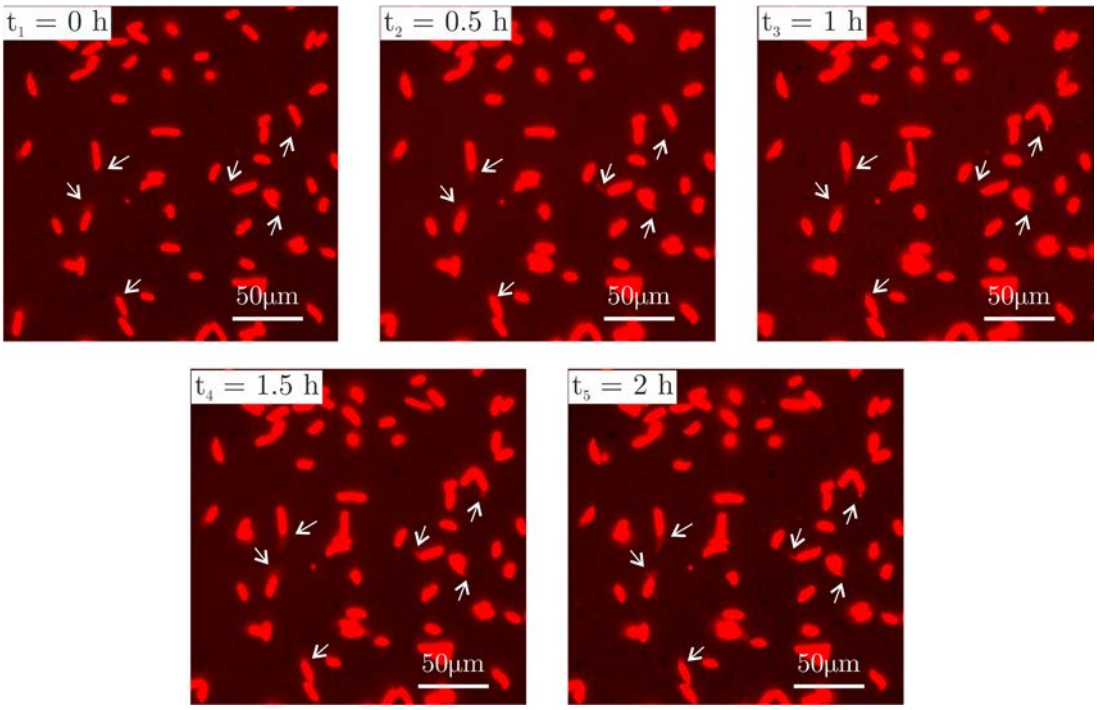

Figure 7.3: Sequence of fluorescence images of *S. oneidensis* bacteria along time. The arrows indicate the OME.

We followed the same procedure in this thesis. First, we characterized the bacteria with fluorescent microscopies using the membrane dye FM-464FX to identify the appendices responsible for the EET. **Figure 7.3** shows a sequence of fluorescent images along time, for $t_1 = 0\ h$, $t_2 = 0.5$ h, $t_3 = 1$ h, $t_4 = 1.5$ h and $t_5 = 2$ h. These extensions started to appear after half an hour of bacteria being on a surface, but it was not until one hour that they developed the

maximum number. As can be seen, we obtained the same extensions that S. Pirbaddian, *et al.* showed in their studies [49,50] claiming their influence in long-range EET.

7.3.3.Topographical characterization

In order to further characterize the shape of the *S. oneidensis* OME, we acquired SEM images. **Figure 7.4** shows two SEM images of *S. oneidensis* bacteria. In those images, the OMEs are clearly present, showing their structures. We can see that the OMEs are formed of subsequently little balls, that is Outer Membrane Vesicles (OMV), forming a tube-shaped membranous structure (TSMS). One can observe that some TSMS parts have smooth into thinner filaments. The OMEs of **Figure 7.4** are ~1 μm long, although it is reported that they can be up to hundreds of microns (see **Figure 7.5** for another example). In addition, in **Figure 7.4a**, bacteria show another kind of appendage, this appendage is called pili and bacteria use it to connect each other and probably exchange molecules or DNA [58].

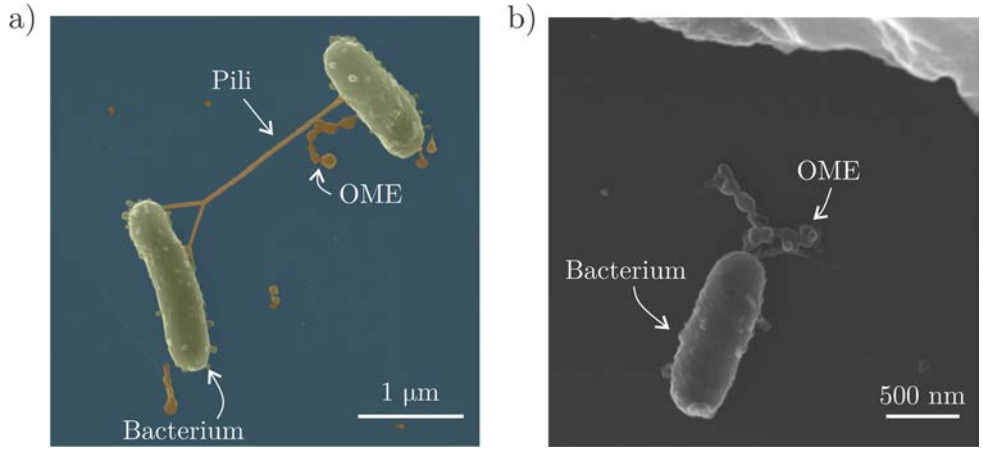

Figure 7.4: a) Artificially coloured Scanning Electron Microscopy (SEM) image of two *S. oneidensis* bacteria, a pilus connecting both of them and the OME extensions. b) SEM image of one *S. oneidensis* bacterium and an OME coming out of the cell body.

Subsequently, **Figure 7.5** shows three selected images of *S. oneidensis* bacterial cells where the OMEs are clearly visible. There are also flagella (~10 nm), but they are not visible with the chosen color scale bar. First, **Figure 7.5a** shows several bacteria and most of them have developed OMEs, this shows that the outer membrane extensions are not an isolated phenomenon of one single bacterium, but most of them extract OMEs.

If we pay attention to one of the OME (**Figure 7.5b**), we can observe that they come out of any part of the bacteria, not like flagella that they emerge only from one extreme of the bacterial

cell (in the case of *S. oneidensis*, see Chapter 6). Also, **Figure 7.5b** shows that the extensions can be several hundred long, especially if they are straight. From these images, we can observe that dry and not fixed *S. oneidensis* bacterial cells are $h = 80 - 120$ nm height, w~0.75 μm width and $l = 1.5 - 2.5$ μm length (these values has been obtained from profiles of these images and similar, not shown). Finally, **Figure 7.5c** shows a zoom-in of one of the *S. oneidensis* nanowires presents in **Figure 7.5b**. This image confirms the presence of chains composed of spherical structures. The obtained height is $h_{OME} = 40 - 60$ nm (this value has been obtained from profiles of these images and similar, not shown). However, these extensions are likely to entangle; as a result, the exact height is difficult to obtain.

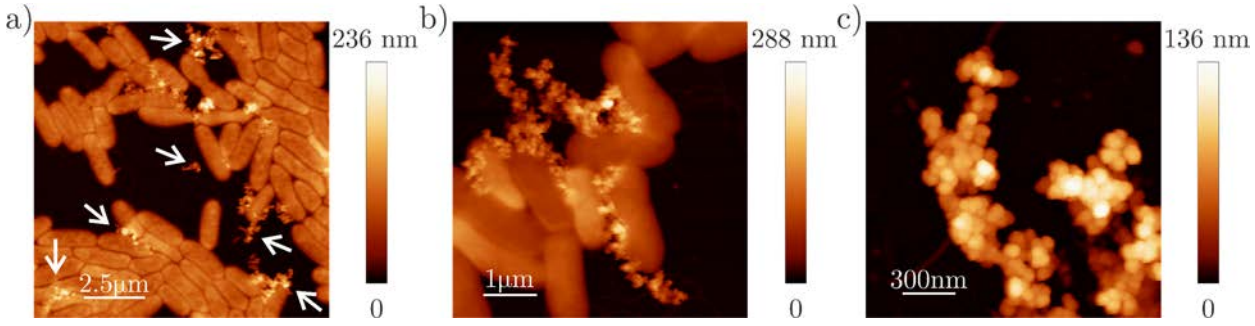

Figure 7.5: Atomic Force Microscopy (AFM) images of *S. oneidensis* bacteria and their OMEs. a) Several bacteria with their hundreds of microns long OMEs pointed with arrows. b) Few bacteria with their hundreds of microns long OMEs. c) Zoom-in of one OME in (b).

To finish with the topographical characterization, a study about the hygroscopic properties of *S. oneidensis* bacteria and their extensions is presented in **Figure 7.6**. In order to do so, first, we measured a region where bacterial cells and OMEs were present in dry conditions (**Figure 7.6a**). Subsequently, miliQ was added (**Figure 7.6b**). With the aim of seeing if bacteria absorb more water over time, images at different times were acquired, taking 40 min from the first image until the last one. Just looking at the topographic images, we can observe that the body of the bacteria increase their height, while the OMEs remain almost unaltered. This is confirmed by the profiles taken along the body of the bacterium (**Figure 7.6c**) and along the OME (**Figure 7.6d**). The profiles show that the height of the bacterial cells is almost tripled when the miliQ is added. Hence, the height of a dry bacterium is h_{dry}~130 nm and after adding the miliQ, it is h_{liq}~300 nm (**Figure 7.6c**). However, once bacteria were soaked in liquid and increased their size, they did not effectively increase it more over time. On the other hand, the OME height does not increase when the miliQ is added or when they are immersed in liquid for more than 40 min.

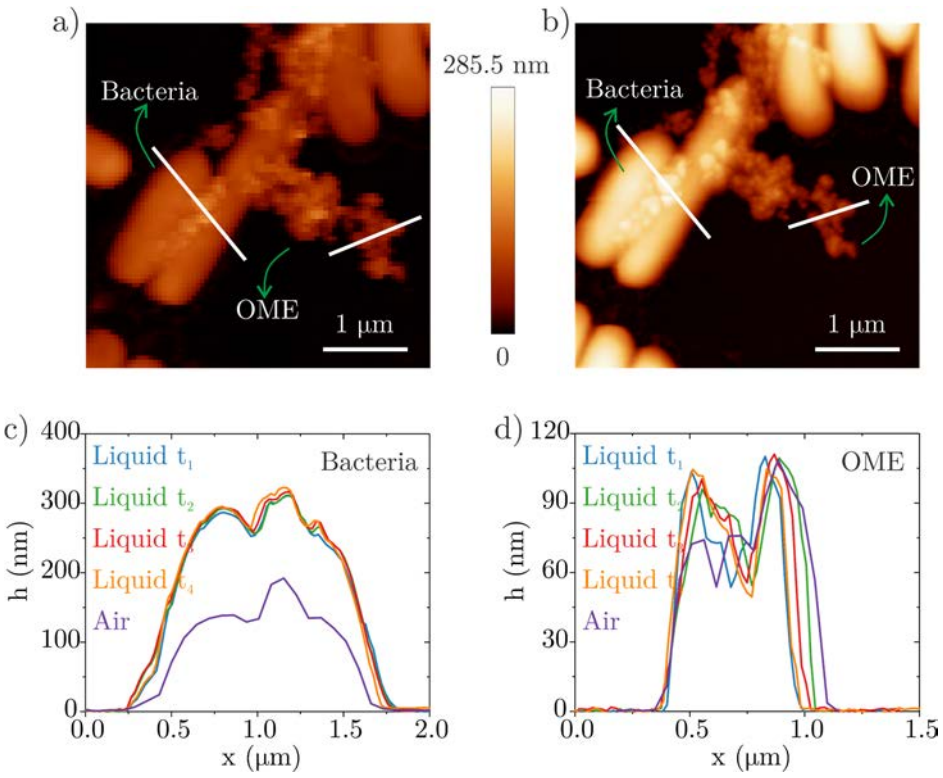

Figure 7.6: a) AFM topographical image of *S. oneidensis* and OMEs in air conditions b) and in liquid conditions. c) Topographical profile of the OMEs d) and the bacterium in air and liquid conditions over the time along the lines in (a) and (b).

7.3.4.Dielectric characterization by SDM

As said before (Chapter 1), *S. oneidensis* MR-1 bacteria is an electrochemically active bacterial cell [6,53]; thus, they can exchange electrons with minerals or electrodes. They develop this behavior under anoxic conditions and it is their way of breathing. In addition, *S. oneidensis* can develop bacterial nanowires to reach further minerals [6,49,53]. These nanowires are OMV chains and are responsible for one of the ways of EET in *S. oneidensis* MR-1.

To measure the dielectric constant of *S. oneidensis* and their extensions, we use Scanning Dielectric Microscopy (SDM), which combines EFM measurements with Finite Element Method (FEM) calculations with realistic geometric models (Section 4.3). In this case, we used the topographic reconstruction since the OME topography is not exactly a wire, but it is spheres one after each other (**Figure 4.6c**, **Figure 4.6d** and **Figure 4.6e**). Using this method, we analyzed the dielectric constant of a nanometric region (~150 nm, Section 6.3, especially **Figure 6.1** and **Figure 6.6**). To do the electrical characterization, first, we acquired a topographical image of the region under study, shown in **Figure 7.7a**. As can be seen, the outer membrane extension is coming out of the cell body. Subsequently, electrical approach curves over a bare metallic part of

the sample (P1), in different points over the OME (P2, P3 and P4) and over the bacteria (P5) were taken. The exact location where the curves were taken is marked in **Figure 7.7a**. These curves are shown in **Figure 7.7b**. To begin with, the capacitance gradient (dC/dz) approach curve over the bare metallic part of the sample (P1 and green line in **Figure 7.7b**) was used to calibrate the tip geometry. For this case, we use a PtSi-CONT tip with an obtained tip radius $R = 23 \pm 2$ nm, a cone angle $\theta = 20 \pm 5°$ and an $offset = 98 \pm 2$ zF/nm. To extract the tip geometry, we used the standard values of cone height $H = 12.5$ µm, local cantilever $L_c = 3$ µm and cantilever thickness $W_c = 3$ µm.

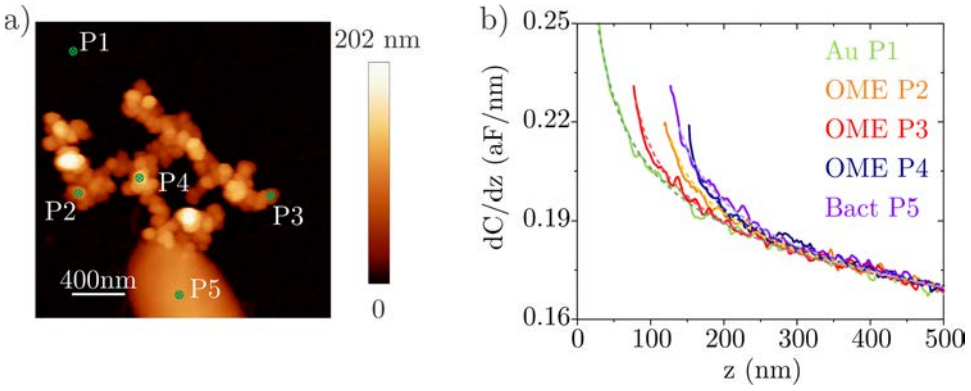

Figure 7.7: a) AFM image of *Shewanella oneidensis* bacteria with an outer membrane extension. b) (Solid lines) Capacitance gradient force curve over the metallic part of the sample (gold) and different points in the OMEs and on the bacteria, and (dashed lines) the corresponding fittings.

Subsequently, capacitance gradient approach curves over three different points of the OME, (P2 green line, P3 red line and P4 blue line in **Figure 7.7**) were taken. Briefly, to extract the dielectric constant of the OMEs, we compare the experimental dC/dz approach curves with simulated ones. For this purpose, we use finite element numerical simulations, using COMSOL Multiphysics®, and simulate electrical curves for a sweep in the electrical permittivity ($\varepsilon_r = 1 - 100$). In this case, the tip geometry was constructed following the parameters obtained from the tip calibration and indicated before ($R = 23.2$ nm, $\theta = 20.3°$, $H = 12.5$ µm, $L_c = 3$ µm and $W_c = 3$ µm). For the sample model, we exported the topographical AFM image to the COMSOL geometry model, and we placed the tip over the point where the experimental approach curve was taken (Section 4.4.1). The dielectric constant obtained is $\varepsilon_{P2} = 3.9 \pm 0.2$ for P2, $\varepsilon_{P3} = 2.6 \pm 0.2$ for P3 and $\varepsilon_{P4} = 3.4 \pm 0.3$ for P4. The average dielectric constant is $\varepsilon_{OME1} = 3.5 \pm 0.8$.

Finally, the same procedure was repeated for the curve over the bacteria (P5 and purple line in **Figure 7.7b**), obtaining a dielectric constant $\varepsilon_{P5} = 3.9 \pm 0.1$. The same procedure was repeated over three different points of different bacterial cells, obtaining a dielectric constant of $\varepsilon_{bact} = 4.3 \pm 0.9$.

This procedure was repeated for over 7 points of three different images, and the overall average dielectric constant was $\varepsilon_{OME} = 3.7 \pm 0.7$. **Figure 7.8** shows the points analyzed correlated with their topographical AFM images.

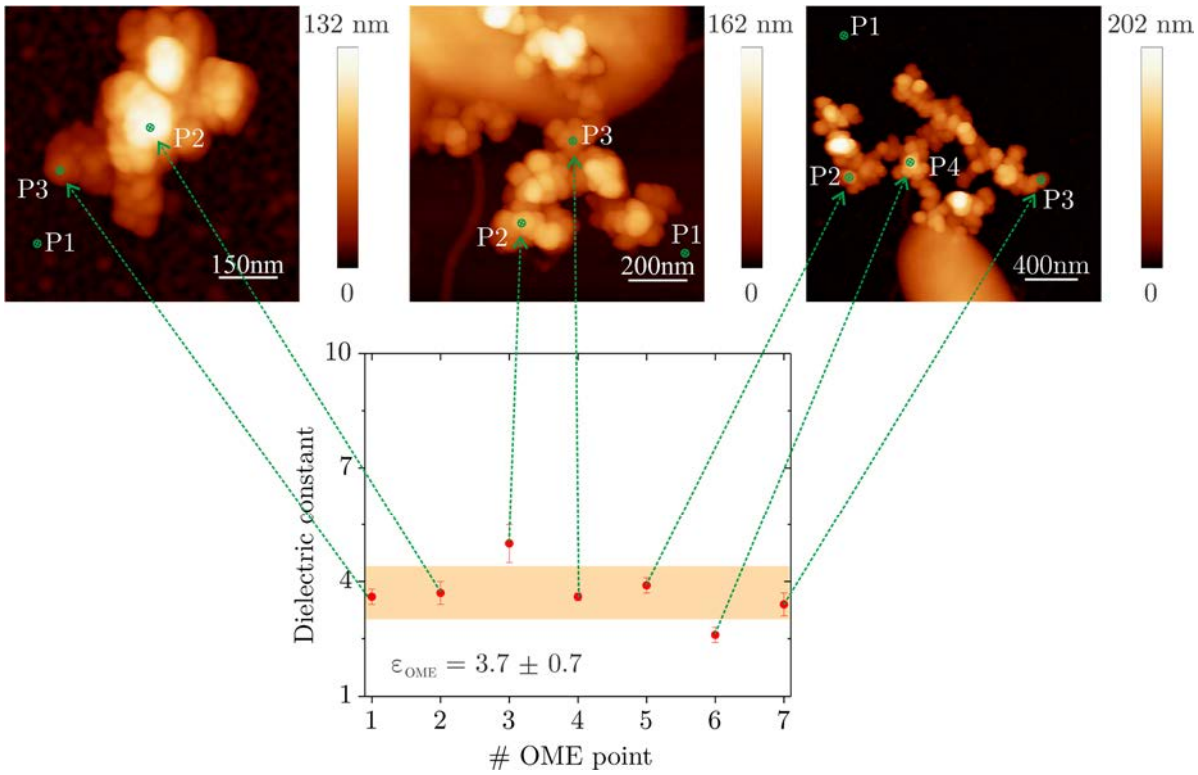

Figure 7.8: Summary of all the OME points analyzed. Notice that each point is correlated with its point in the AFM image.

7.3.5.Discussion

In this chapter, we have analyzed the topographical and electrical properties of *S. oneidensis* MR-1 bacteria and their nanowires, called outer membrane extensions (OMEs). We have first shown the formation of OMEs using fluorescence microscopies, confirming that these appendages are outer membrane extensions [49]. We have also shown that the hygroscopic properties of OMEs and bacterial cells are different. The study showed that OMEs absorb little water, thus, pointing towards an internal composition made of biomolecules (most probably a mixture of lipids and proteins).

Regarding the electrical properties, we have found that *S. oneidensis* OMEs show an average dielectric constant of $\varepsilon_{OME} = 3.7 \pm 0.7$. This value is typical for biomaterials composed of a mixture of lipids (ε_{lipids}~2 [13]) and proteins ($\varepsilon_{proteins}$~4 [14,92,93]) (**Figure 7.9**). This value is slightly lower than the dielectric constant obtained for the bacteria body ($\varepsilon_{bact} = 4.3 \pm 0.9$). This fact is due to its different composition, mainly DNA and periplasmic content [120].

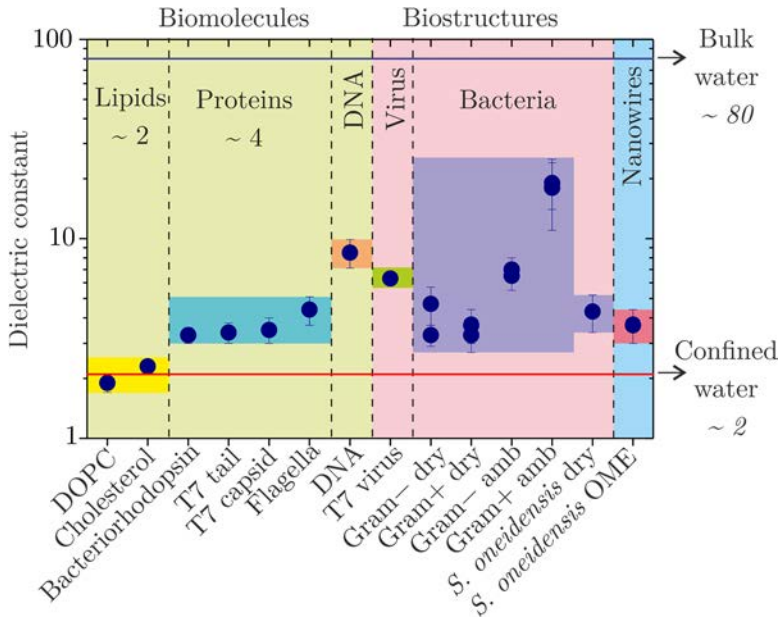

Figure 7.9: Values of the relative dielectric constant of several supramolecular biological micro/nanostructures measured by Electrostatic Force Microscopy. Same as **Figure 3.3** but adding the value of *S. oneidensis* OMEs and bacterial cells. Data from [12–14,92,93].

The obtained dielectric constant of OME is very low if we expect to have a metal-like conductivity through *S. oneidensis* nanowires [66,68]. However, it is claimed that the conduction mechanism is through an electron hopping mechanism, where the electron hops from cytochrome to cytochrome [61,65] (**Figure 2.3a**). The conduction mechanism is, then, different from a metallic-like material, where electrons are delocalized and, once an electric field is applied, they can move to the surface material and screen the electric field. As electrons are no delocalized in electron hopping mechanism, they may not be able to screen the electric field at any moment. Therefore, our results do not contradict the reported conductivity of *S. oneidensis* nanowires.

Since the EET is a biological or chemical behaviour, another reason for this relatively low value is that bacteria are dead and, therefore, they do not have to breathe. In addition, cytochromes are able to migrate around the membrane when bacteria are alive [172,173] approaching when the electron is about to hope and, therefore, allowing it to jump. However, it is not certain that after

dry conditions, these cytochromes can move anymore, producing that cytochromes are too far between each other to allow electron hopping. Besides, the studies about the conduction of *S. oneidensis* nanowires are performed in dry and fixed conditions, producing a shrink in the filaments and approaching the cytochromes [2]. Our measurements are in dry conditions, but the bacteria have not been fixed; thus, the cytochromes could be too far apart between them.

Finally, the cytochrome content in the membrane of the bacteria heavily depends on the growth cultivation. In this work, bacteria have been cultivated first in aerobic conditions, to increase the number of bacteria and their mobility, secondly in anaerobic conditions in the *nwmedia* and, finally, in a reactor where bacteria were left on a surface to allow them to develop the OMV chains. In this process, we assume that on a layer next to the surface, the oxygen level is low because bacteria oxygen consumption is faster than the oxygen diffusion through the medium and reactor. However, this could not be true, and it could induce a reduction in the cytochrome content during the last part of the growing conditions.

7.4.Conclusions

In this chapter, we used SDM to measure, locally, the dielectric constant of *S. oneidensis* OMEs. Using fluorescence microscopy, we have confirmed that these appendages are indeed OMV. We have analyzed the structure and hygroscopic properties of the OMEs. We have observed that the OMEs resemble a chain composed of spherical structures with height h_{OME}~40 nm. Additionally, when dry bacteria are rehydrated, the bacteria height is tripled with respect to the dry height (from h_{dry}~120 nm to h_{liq}~350 nm). However, the height of the OMEs remains the same. Regarding the dielectric constant, we have obtained $\varepsilon_{OME} = 3.7 \pm 0.7$, a value compatible with a lipidic and protein composition. This result is too low to sustain a metal-like conductivity. However, if the nanowires have electron hopping conductivity, with no delocalized electrons, our results would be compatible with a low dielectric constant.

8. Electrical characterization of Cable bacteria

In this chapter, we analyze the electrical properties of another electrochemically active bacteria, the cable bacteria. We observe that the fibers going along the cable bacteria have higher electrostatic response than the rest of the bacteria. Therefore, we also study the electrical properties of the fibers using SDM measurements. In addition, three different models are proposed for the quantification. Cable bacteria have been provided by the Ecosystem Management Research group lead by F. Meysman in Antwerpen, Holland.

These results are being collected to prepare them for a scientific publication.

8.1.Introduction

Long-distance electron transport is a unique strategy followed by some bacteria to cope with the lack of oxygen in the growing environment. During recent years, bacteria species showing exceptionally long-distance ET have been discovered and it has kept the attention of scientists due to its potential in the bioelectronics field.

Cable bacteria [7,54] are multicellular, filamentous bacteria found worldwide in freshwater and marine sediments [55]. They can transport electrons over centimeter distances through fibers all along the cable bacteria [174]. They are formed by bacterial cells, of an average length of 3 μm, that are joined end to end and form a filament that can be over 10 cm long [1]. Each multicellular filament contains several unique ridges located between the cytoplasmic and the outer membrane. It has been demonstrated that these ridges or periplasmic fibers are ~50 nm in diameter, have high conductivity, up to 20 S/cm, and are able to sustain high current densities, up to 1 nA [1], nearly 1000 times more conductive than *S. oneidensis* MR-1 nanowires, for instance.

Although neither the mechanism of the ET nor the biological composition of the fibers is known, the best hypothesis for the conductivity of the cable bacteria is an electronic conduction. This conduction is through a multi-step hopping mechanism along their continuous conductive conduits or periplasmic fibers since some studies showed that an ionic conduction could not be possible [1,70].

The study of the cable bacteria has kept the attention of scientists in the world since several applications could arise from it, like bioremediation or bioenergy.

8.2.Materials and methods

8.2.1.Bacteria culture and sample preparation

The cable bacteria were provided by the group Ecosystem Management Research Group (ECOBE) lead by F. Meysman, from the University of Antwerpen in Belgium. Cable bacteria were cultured from natural sediments collected from Rattekaai salt marsh (The Netherlands). The sediment was sieved, homogenized, repacked in PVC core liner tubes (diameter 40 mm), and incubated in aerated artificial seawater at in situ salinity.

Intact cable bacteria have been handpicked from sediments with a customized glass hook and washed in several droplets of miliQ water on coverslips and transferred to a HOPG substrate. Extracted cable samples were treated with a drop of 1 % (w/w) sodium dodecyl sulphate (SDS) for 10 minutes at room temperature, followed by six miliQ washes, and a second extraction step in a drop of 1 mM sodium ethylenediaminetetraacetate (EDTA), pH 8 and incubated for 10 minutes, followed by six miliQ washes. This extraction procedure removes the cytoplasm and membranes, leaving behind a periplasmic fiber sheath of 60 nm [9].

8.2.2.Scanning Dielectric Microscopy

EFM images have been obtained with a Cypher S AFM from Oxford Technologies (former Asylum Research) and PtSi-CONT probes with a typical spring constant $k \sim 0.2$ N/m (determined by the provider according to the probe dimensions), resonance frequency $f_r \sim 13$ kHz and nominal tip radius $R \sim 20$ nm. We recorded the second harmonic (2ω) of the probe oscillation amplitude, $A_{2\omega}$, by using the system internal lock-ins of the Cypher. EFM data were obtained with a voltage amplitude $V_{\text{ac}} = 3$ V for the full bacteria (**Figure 8.1**), and for the treated bacteria

and the bacteria fibers $V_{ac} = 4$ V, at a frequency $f = 2$ kHz (well below the mechanical resonance peak of the probe). EFM data were reported in terms of the capacitance gradient, which is related to the 2ω oscillation amplitude by eq. (4.7). Further details can be obtained in Section 4.3. EFM measurements were performed in controlled dry air conditions (RH $< 1\%$) maintained by a N_2 flow.

The tip geometry was determined from EFM approach curves measured on a bare part of the metallic substrate. Then, we used finite element numerical calculations using the electric currents module of COMSOL to simulate theoretical EFM capacitance gradient approach curves and compared them with experimental curves. The geometrical model and theoretical approach curves are obtained reconstructing the topographical AFM image into a model in COMSOL for the full bacteria, treated bacteria and the electrostatic image reconstruction of the fiber. For the analysis of the fiber, a wire model similar to the one used in Chapter 6 was used. For further details, check Section 4.4.1. The following tip parameters were set to their nominal values in the tip geometry calibration: cone height $H = 12.5$ µm, local cantilever $L_c = 3$ µm and cantilever thickness $W_c = 3\ \mu m$.

8.3.Results and discussion

In order to study the electrical properties of cable bacteria, we took images of the full bacteria, treated bacteria, where only a thin sheath connection and the fibers remained intact, and a single fiber.

8.3.1.Intact full bacteria

In order to characterize the cable bacteria, first, we took a topographical image. **Figure 8.1a** shows a topographical image of part of the cable bacteria. Some ridges all over the body of the cell can be observed all along the filament. These ridges are more visible in the AFM error image, shown in **Figure 8.1b**. The ridges are barely seen in the topographical profile (**Figure 8.1e** purple line) but they can be appreciated in the zoom-in (inset 1 of **Figure 8.1e**). We can notice, especially in the zoom-in of the profile, that the ridges are separated a distance $d = 127.5 \pm 5.0$ nm.

When an electrical image at constant plane between the tip and the substrate was acquired, $z_{CP} = 183 \pm 14$ nm, the ridges that are along the cable bacteria showed a strong response. The dC/dz is shown in **Figure 8.1c**, while the electrical phase is shown in **Figure 8.1d**, which is constant. The electrical image seems to have a smaller bacterium than the topographical one; that is because the EFM image was taken at constant plane (inset 2 of **Figure 8.1e**), and hence, only the upper part gives a measurable contrast.The red line of **Figure 8.1e** shows the dC/dz profile along the white line in the electrical image (**Figure 8.1c**) and a high electrical signal is recorded on the ridges. A variation of ~ 3.7 nm in the topography gives a variation of ~ 14.5 zF/nm of electrical signal, which is relatively high. Therefore, these ridges seem to be the proposed conductive fibers.

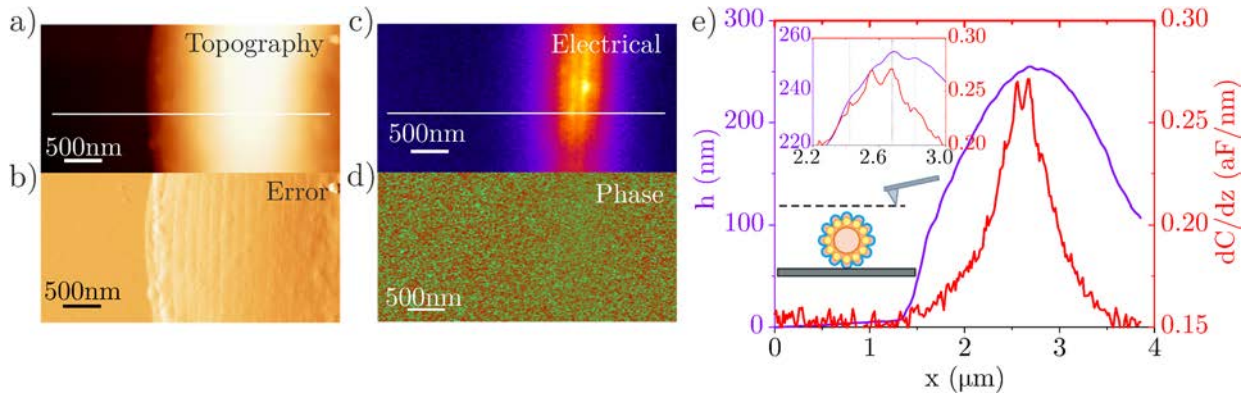

Figure 8.1: a) Topographical, b) error, c) electrical amplitude and d) electrical phase image of the cable bacteria. e) Topographical and electrical profile along the line in (a) and (c), inset 1: zoom-in of the central part of the profile, the dash lines indicate the matching between the ridges in the topographical and the electrical profile. Inset 2: Schematic representation of the cable bacteria on a substrate and the tip flying in constant height.

8.3.2.Treated bacteria

Subsequently, we checked the properties of the cell envelope and fiber structure of cable bacteria. In this case, a special SDS+EDTA treatment allows removing the cytoplasm and membranes, while the periplasmic sheath structure with the conductive fibers remains (see Section 8.2.1). **Figure 8.2a** shows a topographic AFM image of the treated bacteria and the inset shows the schematic representation of what remains after the SDS+EDTA treatment. A zoom-in image is shown in **Figure 8.2b**, which presents a topographic AFM image of the bacteria fiber sheet where the ridges and the joint of the different individual bacteria are clearly visible. The electrical image of the same region, acquired at a tip-substrate distance $z_{CH} = 155 \pm 8$ nm, is presented in

Figure 8.2c. The tip-sample distance is obtained from an acquired dC/dz curve over a bare metallic part of the substrate (not shown) (Section 4.4.1).

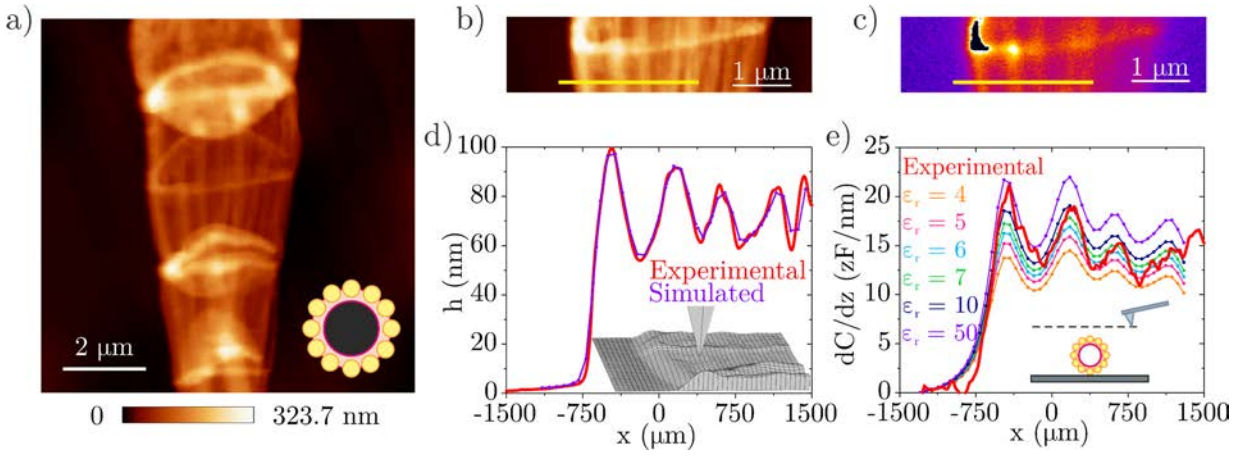

Figure 8.2: a) Topographical image of a treated bacterium. Inset: schematic representation of the treated bacteria. b) Zoom-in image of (a). c) Electrical image of the cable bacteria membrane and d) simulated (purple line) and experimental (red line) topographical profile along the yellow line in (b). Inset: COMSOL geometrical model. e) Experimental (red line) and simulated experimental profiles with different dielectric constant along the yellow line in (c).

We quantitatively analyzed the EFM image in order to determine whether the bacteria sheet shows uniform dielectric properties or not. The electrical analysis of this bacterium was performed by the topographical reconstruction method, where the AFM image is exported to the COMSOL geometrical model (inset **Figure 8.2d**). **Figure 8.2d** displays a topographical profile of the cable bacteria membrane (red line) along the yellow line in **Figure 8.2b** and the topographical profile obtained from the COMSOL model used to measure the electrical properties (purple line). The good matching between both profiles shows the correct topography reconstruction. Afterward, we obtained simulated electrical profiles for different uniform dielectric constants. Following the SDM procedure (Section 4.4), the tip radius was obtained from a capacitance gradient approach curve on a bare metallic part of the sample, getting $R = 26 \pm 2$ nm and $\theta = 22 \pm 3°$. The main parameters used in the simulations are: $R = 25.5$ nm , $\theta = 22°$ and $z_{CH} = 155.4$ nm . The experimental (red line) and the simulated profiles are presented in **Figure 8.2e**. We can observe that the fibers seem to have a high dielectric constant, matching with the profiles of $\varepsilon_r = 10 - 50$. However, the valleys of the topography seem to match better with a lower electrical permittivity $\varepsilon_r = 5 - 6$. We should consider that in the simulation we give the same dielectric constant to the

full bacteria, including valleys and ridges, that is why the profile do not match completely with one value of ε_r.

8.3.3.Fiber

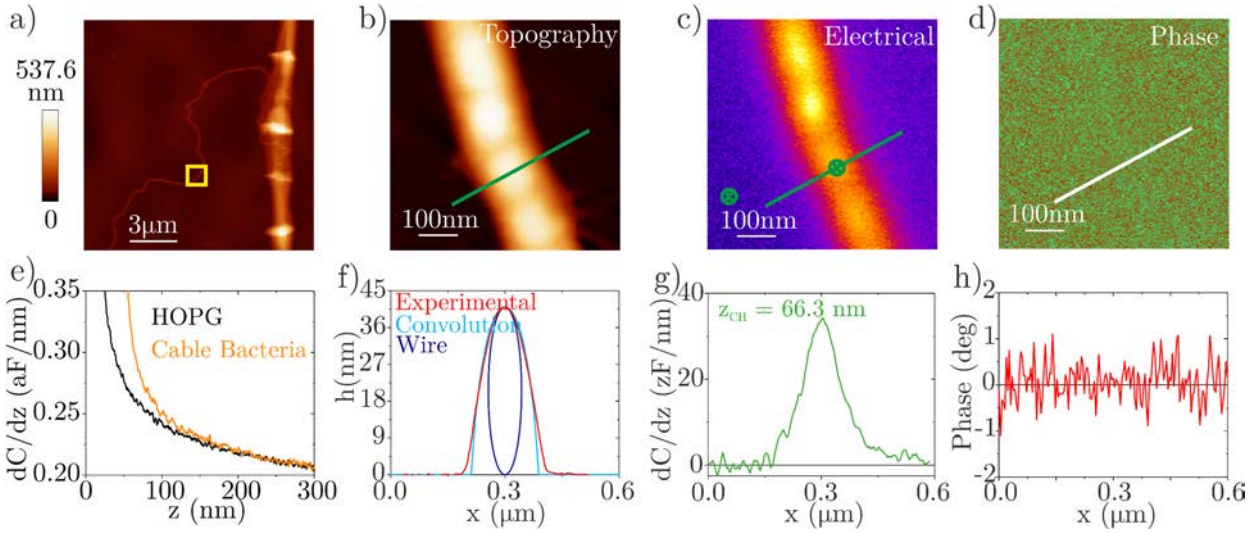

Figure 8.3: a) Topographical image of the treated bacteria with one fiber going out of the bacterium. b) Zoom-in of the fiber in (a). c) Electrical and d) electrical phase image of the fiber in (b). e) Capacitance gradient approach curve over a bare metallic part of the sample (black line) and over the cable (orange line), the points where the curves were taken are indicated in (c). f) Topographical profile along the line in (b) (red line) and the deconvoluted profile (blue line). g) Capacitance gradient profile along the line in (c) and h) phase profile along the line in (d).

Finally, we have analyzed the electrical properties of a single fiber. **Figure 8.3a** shows a topographic image of a treated bacterium, including an isolated fiber going out from the bacterium sheath. In order to perform the analysis, we did a zoom-in on the fiber and performed a topographical and EFM image on it. **Figure 8.3b** presents the topographical image of the fiber. **Figure 8.3c** shows the electrical image and **Figure 8.3d** displays the electrical phase image. The first two images (topography and electrical) show the bumpy nature of the fiber. The electrical phase image does not show any contrast. In addition, **Figure 8.3f**, **Figure 8.3g** and **Figure 8.3h** show topographical, electrical and electrical phase profiles along the line in **Figure 8.3b-d**, respectively. To analyze the electrical properties, first, we obtained the tip geometry using a capacitance gradient approach curve on a bare metallic part of the sample (black line in **Figure 8.3e**). In this case, we obtained a tip radius of $R = 55 \pm 2$ nm and a cone angle $\theta = 22 \pm 3°$. Subsequently, we extracted the fiber dimensions from the topography using the deconvolution process explained in Section 5.2.7. The dimensions of the profile shown in **Figure 8.3f** are $h =$

41 ± 1 nm and width $w = 87 \pm 2$ nm. With the same dC/dz approach curve used to calibrate the tip geometry, the tip-substrate distance, at which the electrical image was acquired, was determined, in this case $z_{CH} = 66 \pm 5$ nm. Finally, notice that the phase image is constant all over it. In addition, we acquired a dC/dz curve over the fiber, orange line in **Figure 8.3e**.

To analyze the electrical properties of the fiber, we followed three different models since just one of them did not explain the measurements completely. These three models correspond to: (i) a pure dielectric fiber, (ii) a dielectric-conductive fiber and (iii) a core-shell fiber model. The models are explained in the following sections.

Pure dielectric model

In this model, we considered that the full fiber has the same dielectric permittivity, then we followed the quantification method explain in Section 4.4.1 to obtain the dielectric constant value. Briefly, once we know the tip geometry, theoretical dC/dz curves with a sweep in the dielectric constant are simulated using COMSOL Multiphysics and they are compared to the experimental dC/dz approach curve obtained on the fiber. In this case, we used a nanowire model with dimensions $h = 41$ nm and width $w = 87.4$ nm and a tip geometry with $R = 54.5$ nm and $\theta = 22°$. By comparing the simulated curves with the experimental ones, we found the electrical permittivity of the fiber, being $\varepsilon_r = 7 \pm 1$, as can be seen in **Figure 8.4a**. This result is also in good agreement with the dC/dz profiles obtained from EFM images (**Figure 8.4b**).

In order to see if all the fiber has uniform dielectric properties, we simulated a portion of the experimental image using the topographic reconstruction model (Inset **Figure 8.4d**). **Figure 8.4c** shows the experimental electrical image (at $z_{CH} = 66 \pm 5$ nm) and **Figure 8.4d** the simulated electrical image (at $z_{CH} = 66$ nm), using the same color scale bar. **Figure 8.4f** and **Figure 8.4g** show the experimental (solid red line) and the simulated (blue dashed line) profiles over the hill and over the valley along the black and red line of **Figure 8.4c** and **Figure 8.4d**, respectively.

The hills seem to have higher dielectric contrast than the valleys, as shown in **Figure 8.4f-g**. Notice that the higher parts of the fiber show higher contrast since, in these parts, the tip was flying closer. Also, the experimental image shows a slightly larger contrast than the theoretical one in the higher parts of the fiber. That is because in the experimental image, the tip bends

towards the fiber, decreasing the tip-sample distance (which was not considered in the simulations) and, hence, increasing the dielectric response. Finally, this procedure was repeated at different tip-substrate distance, always showing a good match between the experimental and the simulated profiles, as shown in **Figure 8.4e**. Therefore, it does not seem to have a uniform dielectric response all over the fiber. This could indicate that the conductive properties of the fibers are condensed in groups all over the fiber. The parameters used in the simulations are: $R = 54.5$ nm, $\theta = 22°$, $h = 41$ nm, $w = 87.4$ nm and $\varepsilon_r = 7.3$.

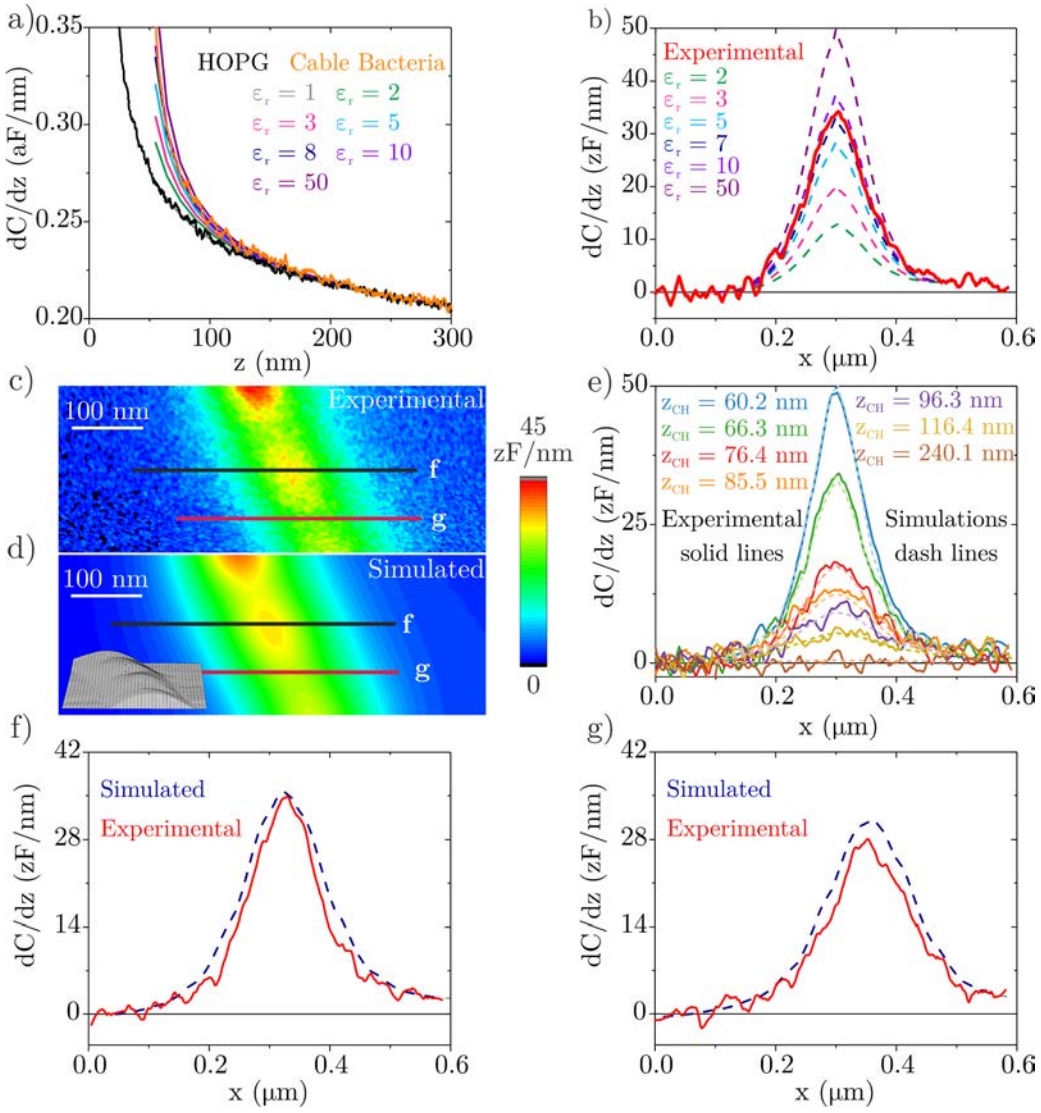

Figure 8.4: a) Capacitance gradient approach curve over a bare metallic part of the sample (black line) and over the fiber (orange curve) and simulated dC/dz curves with different dielectric constant. b) Experimental ($z_{CH} = 66.3$ nm, red line) and simulated (dash line) electrical profiles with different dielectric constant. c) Experimental and d) simulated electrical image of the fiber. Inset: COMSOL geometrical model of the fiber. e) Experimental (solid line) and simulated (dash line) electrical profiles at different tip-substrate distance. f) Simulated

(dashed blue line) and experimental (solid red line) profile across the black line in (c) and (d), and g) across the red line in (c) and (d).

Dielectric-conductor model

The pure dielectric model does not exactly take into account the possible conductivity of the fibers reported in the literature [1,7]. Therefore, we introduced a conductivity to the fiber using the electric currents module of COMSOL Multiphysics. In this thesis, the EFM measurements are performed at 2 kHz; therefore, we studied how the electric force is acting on the tip when flying over a conductive nanowire change with the frequency.

Figure 8.5a shows that with a pure dielectric nanowire, the modulus of the electric force increases when the dielectric constant increases, but it does not depend on the frequency. However, when the nanowire also has conductivity (together with a dielectric constant), the modulus of the electric force changes with the frequency. In the frequency dependence, the minimum value of the modulus of the electric force corresponds to a dielectric model with the value of the ε_{NW}, and the maximum value corresponds to a dielectric model with $\varepsilon_r \gg 100$. **Figure 8.5b** shows the dependency of the phase of the electrical force (ϕ) with the frequency. In the pure dielectric case, the phase is constant ($\phi = 0$), since the system shows a pure capacitance behaviour. However, if conductivity is added, there is a change in the phase for given conductivities. The EFM measurements of this thesis are performed at $f = 2$ kHz (highlighted with a brown dash line in **Figure 8.5**).

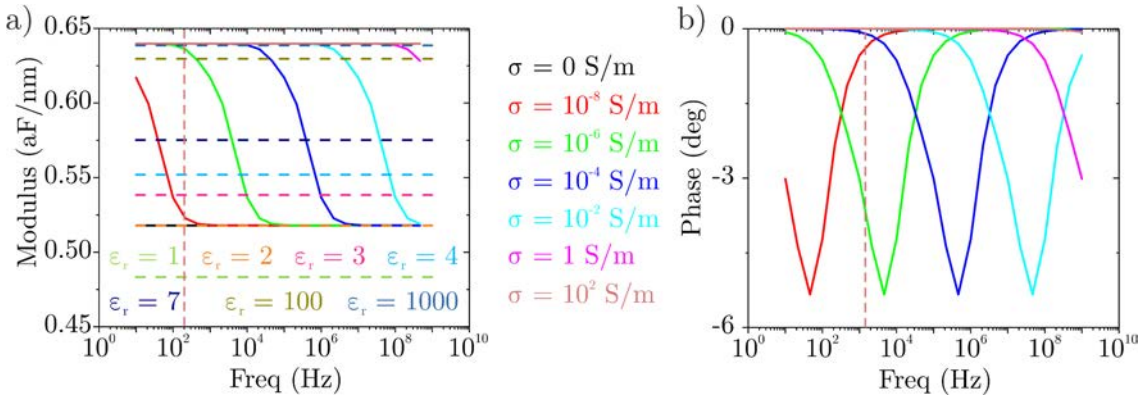

Figure 8.5: a) Modulus of the electrical force for different conductivities and fixed dielectric constant (solid lines, $\varepsilon_r = 2$) and for different dielectric constant and fixed conductivity (dash lines, $\sigma = 0$ S/m) for a sweep in frequencies. b) Phase of the electrical force for different conductivities and fixed dielectric constant ($\varepsilon_r = 2$) for a sweep in frequencies. In both cases, the frequency $f = 2$ kHz at which the EFM measurements are performed are highlighted with a brown dash line.

The experimental dC/dz measurements were compared with simulated profiles of a nanowire with different conductivities. **Figure 8.6a** and **Figure 8.6b** shows the modulus and the phase of the electric force, respectively, for a nanowire with $\varepsilon_r = 2$ and different conductivities. The same analysis but with a nanowire with $\varepsilon_r = 3$ is presented in **Figure 8.6c** and **Figure 8.6d**. Considering the dC/dz profiles, a big jump between low conductivities ($\sigma < 10^{-7}$) and high conductivities ($\sigma > 10^{-6}$) is observed, almost independent from the dielectric constant, which only influences the low conductivity profiles. This jump occurs in a narrow window of conductivities, giving a kind of a discrete behaviour between being conductive or not. Considering the phase profiles, a change in the phase is observed for intermediate conductivities ($10^{-7} < \sigma < 10^{-6}$ S/m) and for the rest of conductivities, the phase is almost constant ($\phi = 0$). Similar conclusions arise from the both cases shown ($\varepsilon_r = 2$ and $\varepsilon_r = 3$).

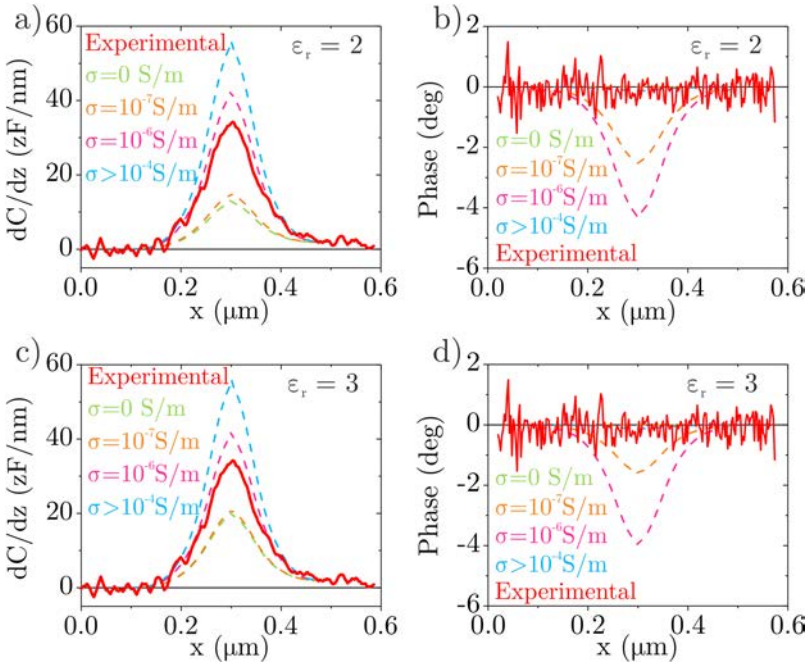

Figure 8.6: a) dC/dz experimental (red solid line) and simulated profiles for different fiber conductivities (dash lines). b) Experimental (red line) and simulated electrical phase profiles for different fiber conductivities (dash lines) for $\varepsilon_r = 2$. c) and d) same with $\varepsilon_r = 3$.

From **Figure 8.6**, we can see that according to the modulus measurements (dC/dz), the conductivity of the fiber has to be intermediate, $10^{-7} < \sigma < 10^{-6}$ S/m. On the other hand, according to the phase measurements, the conductivity of the fiber must be low, $\sigma < 10^{-7}$ S/m, or high, $\sigma > 10^{-4}$ S/m. Thus, an incongruence is obtained, meaning that this simple conductive model does not explain the experimental results.

The parameters used in all the simulations are: $R = 54.5$ nm, $\theta = 22°$, $h = 41$ nm, $w = 87.4$ nm and $f = 2$ kHz.

Core-shell model

In the core-shell model, we considered a nanowire, with a given ε_r, whose core has high conductivity ($\sigma_c = 2000$ S/m) and whose shell does not have conductivity ($\sigma_s = 0$ S/m). The value of σ_c has been obtained from the recent study performed by F. J. R. Meysman, *et al.* which studied the conductivity of cable bacteria [1]. A schematic representation of the model is shown in **Figure 8.7a**. Using this model, we analyzed the dimensions, size of the shell and the core of the nanowire, which best explained our EFM measurements, taking both, the phase and the modulus. To this end, we simulated different profiles changing the dielectric constant and the shell size (d_s), always maintaining a conductive core of the nanowire. The fiber will have a metallic core of dimensions given by eq. (8.1).

$$h_c = h_{NW} - 2d_s \tag{8.1}$$

where h_{NW} is the height of the fiber, d_s the shell size and h_c the core size.

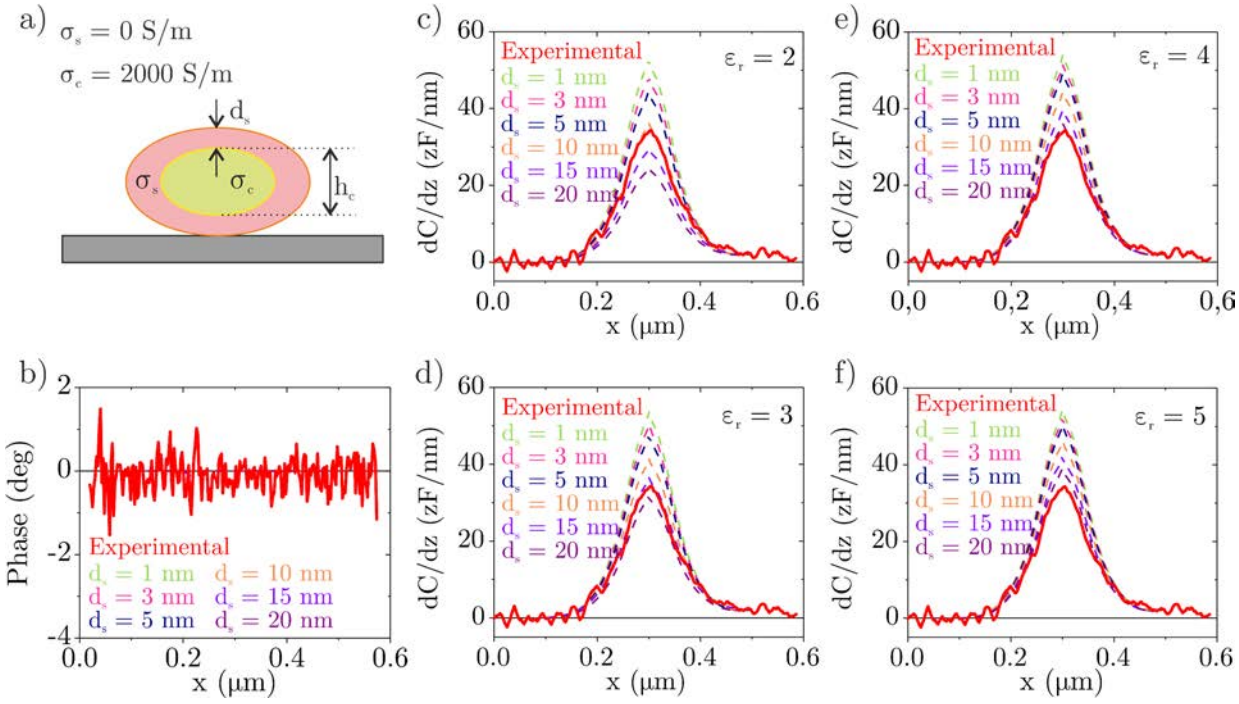

Figure 8.7: a) Schematic representation of the core-shell model. b) Experimental electrical phase profile (solid red line) and simulated for different core sizes (dash lines) c) Capacitance gradient experimental profile (solid red line) and simulated for different core sizes (dash lines) for $\varepsilon_r = 2$, d) $\varepsilon_r = 3$, e) $\varepsilon_r = 4$ and f) $\varepsilon_r = 5$.

Figure 8.7b shows the calculated phase for $\varepsilon_r = 3$ and core thickness (d_c) changing from 1 nm to 20 nm, although for all the dielectric constant analyzed, the phase was the same (not shown). In the figure, it can be observed that the simulated phase profiles are $\phi \cong 0$, in good agreement with the experiments. **Figure 8.7c-f** shows the dC/dz profiles for a sweep in the shell size and for $\varepsilon_r = 2$, $\varepsilon_r = 3$, $\varepsilon_r = 4$ and $\varepsilon_r = 5$, respectively. As can be seen in **Figure 8.7c**, for $\varepsilon_r = 2$, a core-shell model with $d_s = 10$ nm matches, within the experimental error, with the experimental profile. Since $d_s = 10$ nm, the fiber would have a conductive core of $h_c = 21$ nm (eq. (8.1)). For the case of $\varepsilon_r = 3$, a shell of $d_s = 15$ nm and a metallic core of $h_c = 11$ nm is obtained (**Figure 8.7d**). **Figure 8.7e** shows that for $\varepsilon_r = 4$, a core-shell of dimensions $d_s = 20$ nm and $h_c = 1$ nm is found. Finally, for $\varepsilon_r \geq 5$ (**Figure 8.7f** for $\varepsilon_r = 5$), there is no shell size that matches with the experimental profile.

The parameters used in all the simulations are: $R = 54.5$ nm, $\theta = 22°$, $h_{NW} = 41$ nm, $w = 87.4$ nm, $\sigma_c = 2000$ S/m, $\sigma_s = 0$ S/m and $f = 2$kHz.

8.3.4.Discussion

In this chapter, we have analyzed the electrical properties of bacteria. We have seen that cable bacteria is a multicellular organism with some fibers going along the cells. We have observed that these fibers have higher electrostatic interaction than the rest of the cell body. Therefore, we have studied these fibers carefully.

From the pure dielectric point of view, the dielectric constant obtained for the cable bacteria fibers are $\varepsilon_r = 7 \pm 1$. If we take into account the electrical permittivity of biological materials, we can see that this value is close to the value obtained for the DNA (**Figure 8.8**) [92]. In this study, A. Cuervo, *et al.* [92] claim that this relatively high value is due to the sugar-phosphate backbone that gives a high contribution to the dielectric response. Recent studies, based on SEM-EDX measurements, claim a high concentration of phosphate (P), which could explain our relatively high value for the dielectric constant [174].

Other recent studies claim a high conductivity for cable bacteria, being up to $\sigma = 2000$ S/m [1]. However, if this conductivity is added to simulations of a uniform dielectric wire, they do not match with the experimental data, giving incongruences between the electrical phase and the

electrical modulus measurements since simulations cannot match both, the experimental phase and the modulus, simultaneously.

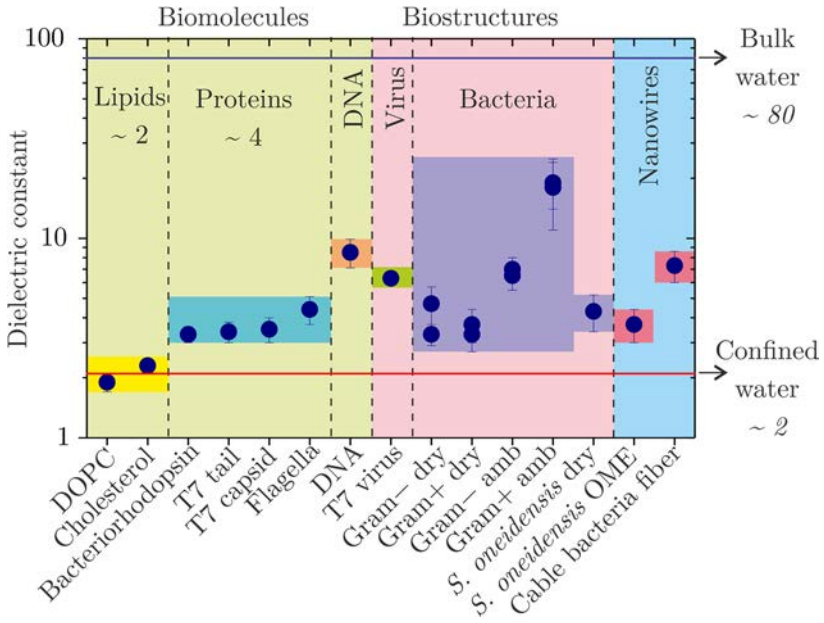

Figure 8.8: Values of the relative dielectric constant of several supramolecular biological micro/nanostructures measured by Electrostatic Force Microscopy. Same as **Figure 7.9** but adding the value of cable bacteria fiber. Data from [12–14,92,93]

Therefore, a core-shell model was built, where the core is a conductor and the shell is a dielectric. In this case, depending on the electric permittivity given to the fiber, different core-shell sizes were obtained (**Figure 8.7**). However, checking the dielectric constant of biological materials (**Figure 8.8**), if one considers that the conductive fiber is covered with a membrane composed of a mixture of lipids and proteins, a dielectric value for the shell would be around ε_r~$2-3$. In this case, a metallic core of h_c~$10-20$ nm would be obtained.

8.4.Conclusions

We have analyzed the cable bacteria with Scanning Dielectric Microscopy to obtain the electric properties of the bacteria and the fibers that go along the bacteria filament. We have obtained higher electric polarizability for the fiber than for the body of the bacteria. Considering a pure dielectric material, the dielectric constant obtained for the fibers was $\varepsilon_r = 7 \pm 1$, which could be related to the high content of phosphate in the cable bacteria. However, the dielectric behaviour did not explain the conduction properties, which are only consistent with a core-shell model. With this model, a conductive core of the fiber with dimensions h_c~$10-20$ nm has been obtained.

9. Electrical measurements in living bacteria using EFM

In this chapter, I continue the electrical characterization of *S. oneidensis* performing electrical measurements of them in liquid and living conditions at the nanoscale. Therefore, I present an analysis of rehydrated bacteria and their appendages and of living bacteria, using EFM measurements. However, all measurements presented in this chapter are qualitative since the quantitative analysis is still under study.

9.1.Introduction to EFM in liquid

As said before, one of the main advantages of SPM is its ability to work under liquid conditions. This is especially important for biological systems, which allows the characterization of them in physiological conditions, and therefore, living organisms in their natural environment. However, when moving to liquid, everything is more complicated. In particular, electrical measurements since when a voltage is applied to the tip, some interactions with the medium, especially the Electrostatic Double Layer (EDL) formation, can mask partially o totally the electrostatic force, needed for EFM.

Additionally, the accumulation of charges induces surface stress bending of the tip due to the change in the energy landscape of the probe surface. Finally, the charge accumulation also produces a diffusive osmotic force that tends to homogenize the ion concentration everywhere at the surface.

To overcome these problems, our group developed some years ago a strategy [105,175,176]. To avoid stress surface, osmotic pressure and EDL formation, high frequency electric excitation needs to be applied. The frequency needed to avoid the EDL formation is higher than the dielectric relaxation frequency of the electrolyte (several hundreds of kHz to tens of MHz), although its value is concentration-dependent (higher the concentration, higher the frequency). However,

commercially available probes due not mechanically oscillate at such high frequencies. The trick implemented in our group consisted of the application of a high frequency wave modulated by a low frequency signal (**Figure 9.1a**). Therefore, the voltage applied to the tip is defined by eq. (9.1)

$$V(t) = V_0\big(1 + \cos(\omega_m t)\big)\cos(\omega_{el} t) \tag{9.1}$$

where ω_m is the low frequency signal and ω_{el} the high frequency wave.

If we take into account the quadratic dependence of the electrostatic force with respect to the voltage and eq. (4.3), there appear eight force harmonics (**Figure 9.1b**). Of these eight harmonics, five are located in the high frequency range, unaccessible to the oscillation tip, and three are in the low frequency range. These three harmonics are the $F_{dc,liq}$, $F_{\omega_m,liq}$ and $F_{2\omega_m,liq}$ and are defined in eq. (9.2), (9.3) and (9.4). As observed from these equations, the three harmonics provide information about dC/dz. But as observed in **Figure 9.1b**, the $F_{\omega_m,liq}$ provides the higher signal to noise ratio.

$$F_{dc,liq} = \frac{3V_0^2}{8}\frac{dC}{dz} \tag{9.2}$$

$$F_{\omega_m,liq} = \frac{V_0^2}{4}\frac{dC}{dz}\cos(\omega_m t) \tag{9.3}$$

$$F_{2\omega_m,liq} = \frac{V_0^2}{8}\frac{dC}{dz}\cos(2\omega_m t) \tag{9.4}$$

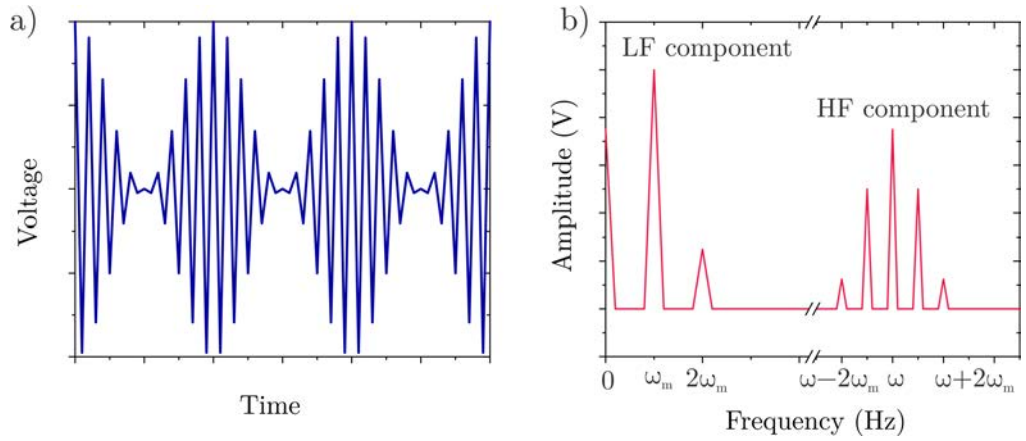

Figure 9.1: a) Schematic diagram of the time evolution voltage wave applied to the tip. b) Fourier transform of the squared voltage in (a), showing the different force harmonics that appear.

To use the high frequency modulated voltages, a different experimental setup is needed [176]. A schematic illustration of the experimental setup is shown in **Figure 9.2**, where a function

generator is used to apply the high frequency voltage signal to the tip. The lock-in amplifier delivers the output signal as the modulation input signal of the function generator, which sends the voltage wave to the tip. The cantilever deflection is recorded and set as input for the lock-in amplifier, which is able to detect the different harmonics.

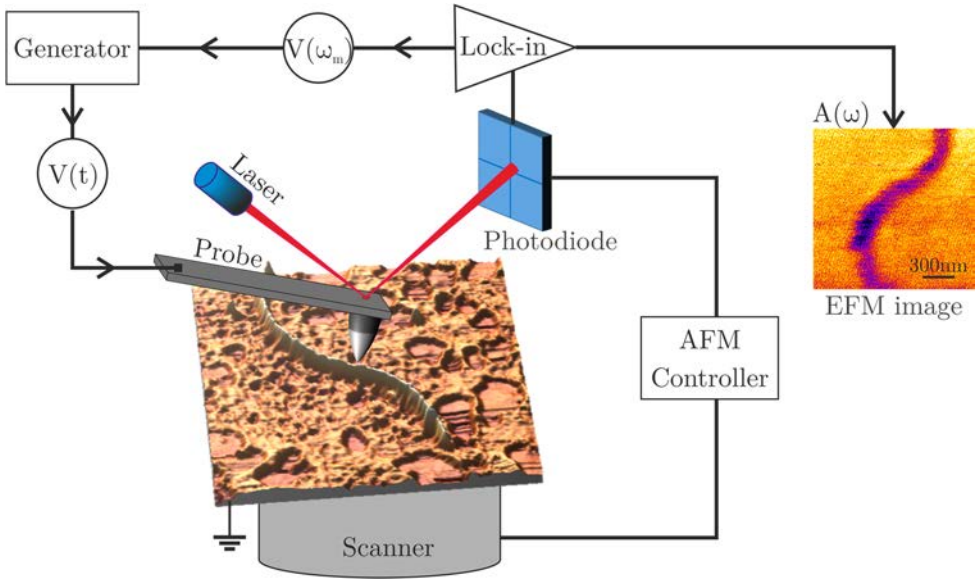

Figure 9.2: Schematic illustration of the liquid EFM experimental setup.

9.2.Electrical properties in a liquid environment

9.2.1.Rehydrated biological samples

Some preliminary results have been obtained in two rehydrated biological systems, namely *S. oneidensis* flagella and *S. oneidensis* outer membrane extensions. The samples have been prepared as explained previously (Section 6.2.1 and Section 7.2.1), but after the drying step, they have been rehydrated with miliQ.

For the first time, electrical measurements of bacterial flagella in liquid media have been performed, and they are shown in **Figure 9.3**. Although the topography image does not have good resolution, in the EFM images, the flagellum is clearly visible. In addition, as the tip-substrate distance increases, the electrostatic contrast decreases, **Figure 9.3a**. Furthermore, the contrast in liquid EFM images is negative, as shown in **Figure 9.3b**. This is due to the electrical permittivity of water, ε_{H_2O}~80, which is higher than the electrical permittivity of flagella, ε_{flag}~4. **Figure 9.3c** shows a topographic image and an EFM image of a bunch of flagella. Here we can

notice that EFM measurements have a good spatial resolution as the different flagella are clearly visible.

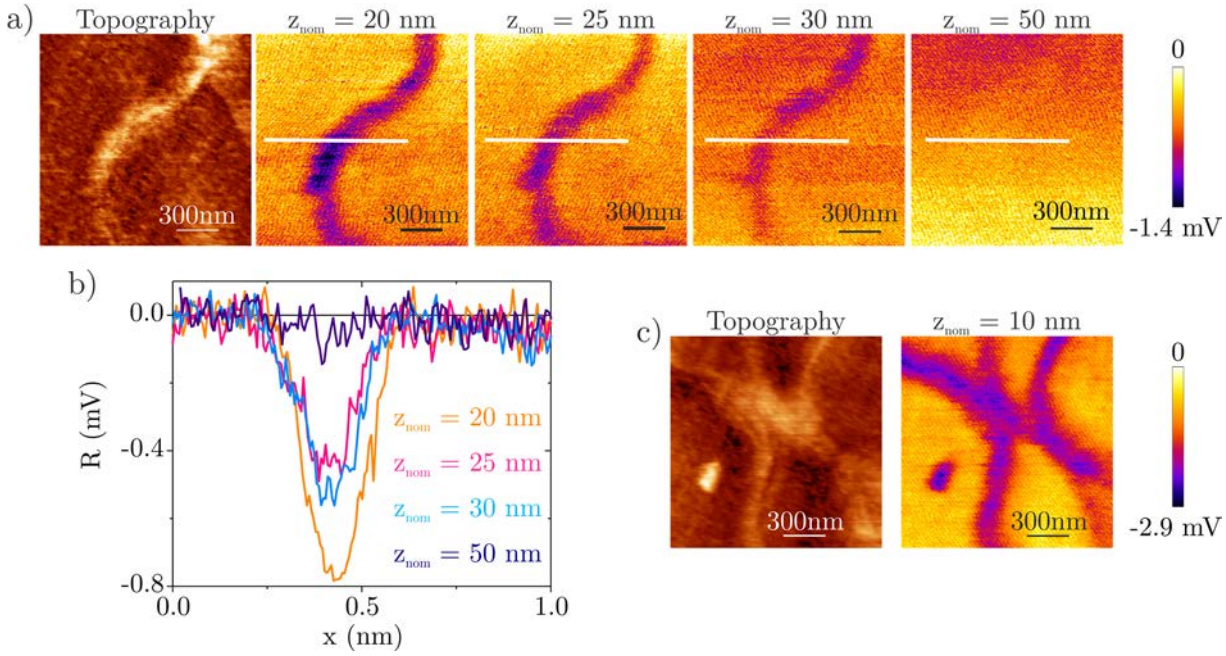

Figure 9.3: a) AFM topographic image and raw EFM in liquid images of *S. oneidensis* flagellum at different tip-sample distances. b) Electrical raw profiles along the lines in (b). c) AFM topographic image and raw EFM in liquid image of a bunch *S. oneidensis* flagella.

However, the quantification of the EFM images in liquid is still under study due to the presence of ions that makes quantification more difficult.

In addition, EFM measurements on rehydrated *S. oneidensis* bacteria and their OMEs have been done. Some of these measurements are shown in **Figure 9.4**. **Figure 9.4a-b** and **Figure 9.4c-d** show similar studies but in two different regions. **Figure 9.4a** presents rehydrated *S. oneidensis* next to an OME that has been detached from the body. dC/dz curves were performed over the body of the bacteria and over the OME and are shown in **Figure 9.4b**. In this case, we can observe a clear difference between the curve on the metal (green line) and the curves over the OME (yellow and pink lines). The two curves over the OME are almost identical, as both of them have been taken over the same material and the height of the OME is similar in both points. Also, the curves over the OME are different from the curve on the bacteria (blue line). This could be because bacterial cells are thicker than the OMEs, therefore, they give lower contrast.

Figure 9.4c shows a nice image of *S. oneidensis* bacterial cells and OMEs coming out of bacteria. In this case, several curves were done over different points of the sample. These curves are presented in **Figure 9.4d**. Similar results were obtained. However, in this experiment, the curves that are over the OME and close to bacteria, that is P4 (brown curve) and P5 (purple curve), are similar to the curve over the bacterium, P6 (red curve). This could be, again, due to the thickness of the object under study, which is the OMEs and bacteria.

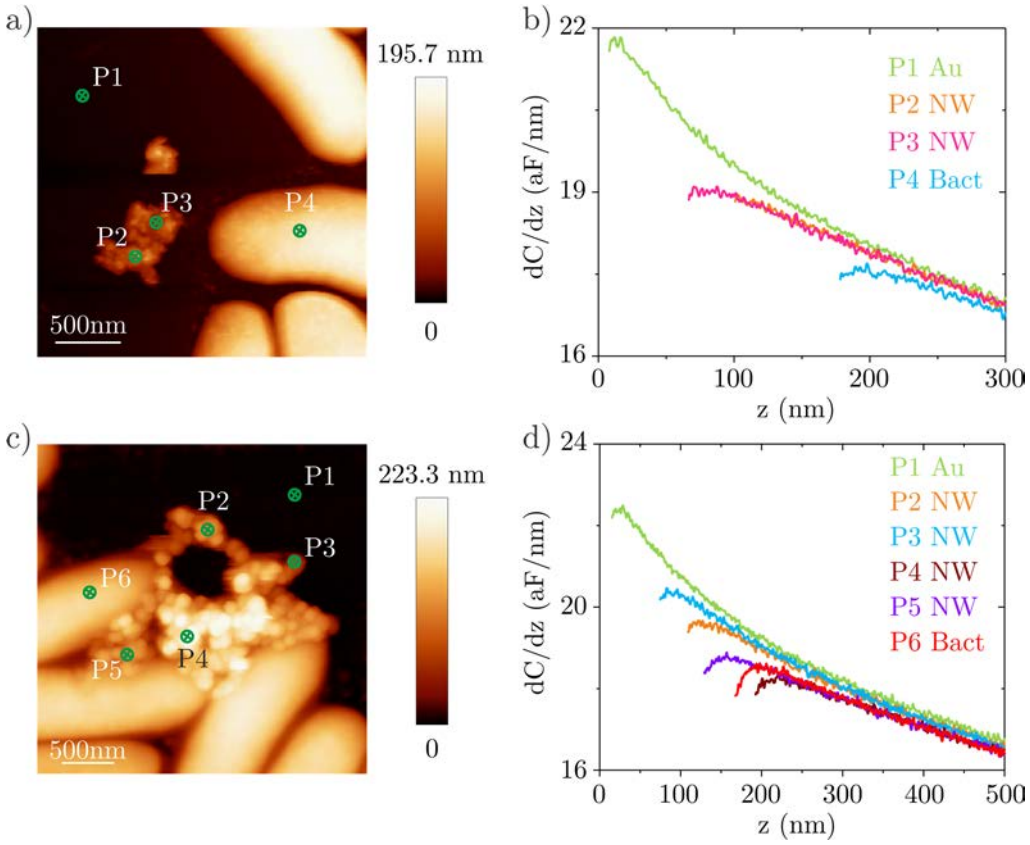

Figure 9.4: a) Topographic image of *S. oneidensis* bacterial cells and an OME. b) Capacitance gradient approach curve over the points marked in (b). c) and d) the same but in another region.

The measurements of **Figure 9.4**, **Figure 9.5** and **Figure 9.6** have been obtained with a tip HQ:NSC19/Cr-Au of spring constant $k = 1.5$ N/m and a voltage of 1.8 V with a frequency of 10 MHz modulated at 2 kHz have been applied. However, as said before, the quantification is still under study.

9.2.2.Living bacteria

Finally, electrical measurements on living bacteria have been attempted. In order to do that, bacteria first needed to be immobilized [177]. Therefore, a HOPG substrate was covered with a

layer of poly-L-lysine. Subsequently, bacteria were deposited onto the HOPG with poly-L-lysine and was left there for 30 min to promote the adhesion. Finally, images were performed in miliQ.

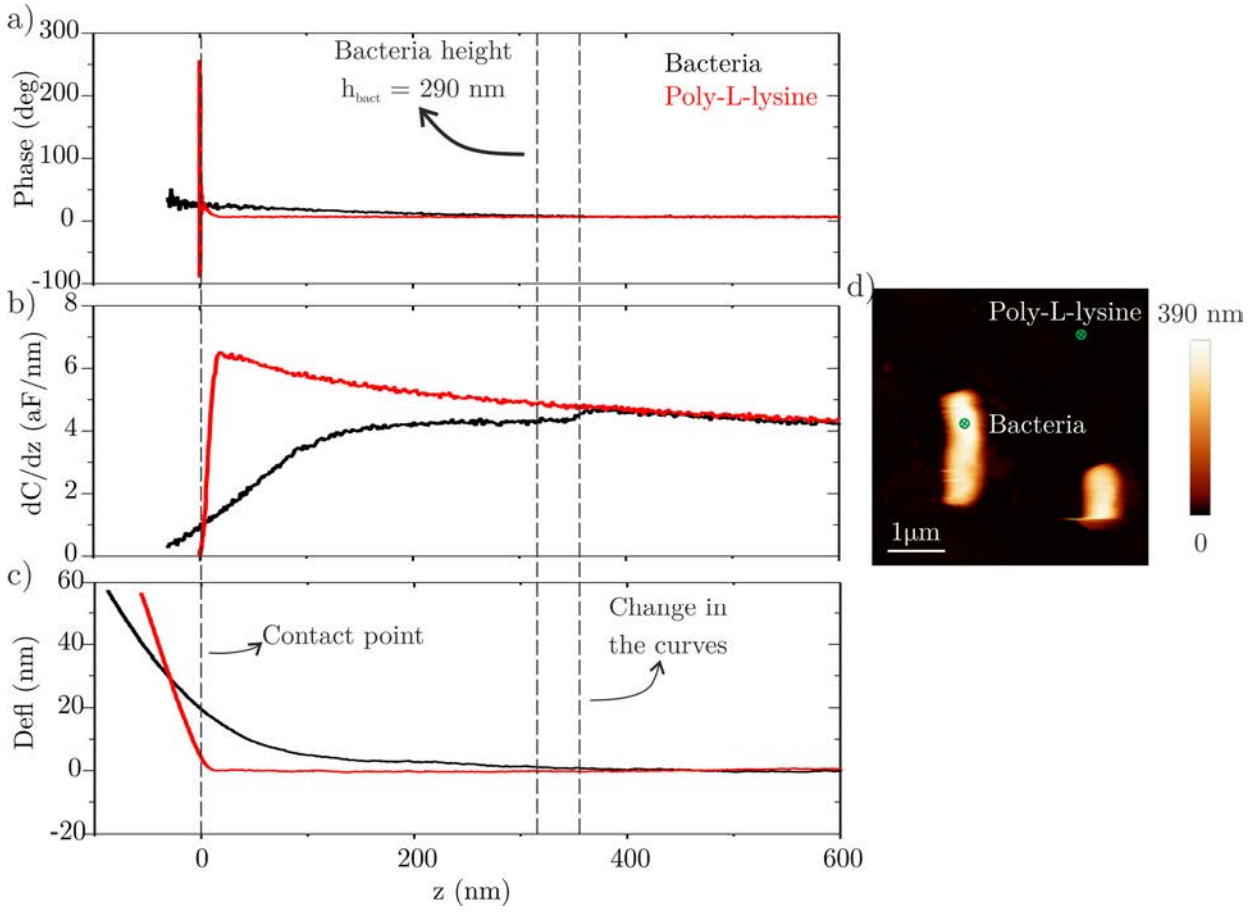

Figure 9.5: a) Electrical phase, b) capacitance gradient and c) deflection approach curves over the points on (d). d) AFM topographic image of two living bacteria.

Figure 9.5 shows the electrical analysis of a living *S. oneidensis* bacterium. In this experiment, approach curves over the substrate (poly-L-lysine), red curve, and over the bacterium, black curve, were obtained. The electrical phase, the dC/dz and the deflection approach curves over the points in **Figure 9.5d** are presented in **Figure 9.5a**, **Figure 9.5b** and **Figure 9.5c**, respectively. In these curves, there are three tip-substrate distances marked, the first one is the contact point, when the tip touches the poly-L-lysine. The second one is the height of the bacteria (h_{bact} = 290 nm). And the third one, when an abrupt change in the bacterium dC/dz curve occur. As can be observed, there is a difference between the point where the bacterium curve changes and the bacterium height. Also, the phase starts to change. A possible explanation for this behaviour is that the dC/dz curve over the bacterium changes when the conductivity of the medium changes. This change of conductivity is due to the ion cloud around the bacterium due to respiration and

exchange of ions. This explanation has to be proven, but it is in good agreement with the simulations of the electrical phase image profiles with conductivity, shown in Section 8.3.3.

Similar results are shown in **Figure 9.6**. In this case, electrical images at constant height were performed. The topographical, electrical, electrical phase and the deflection image (**Figure 9.6a-d** respectively) with profiles along the line marked in the image (**Figure 9.6e-h** respectively) are shown. In this case, we can see an electrical contrast in the image (**Figure 9.6b**), but also an electrical phase contrast (**Figure 9.6c**).

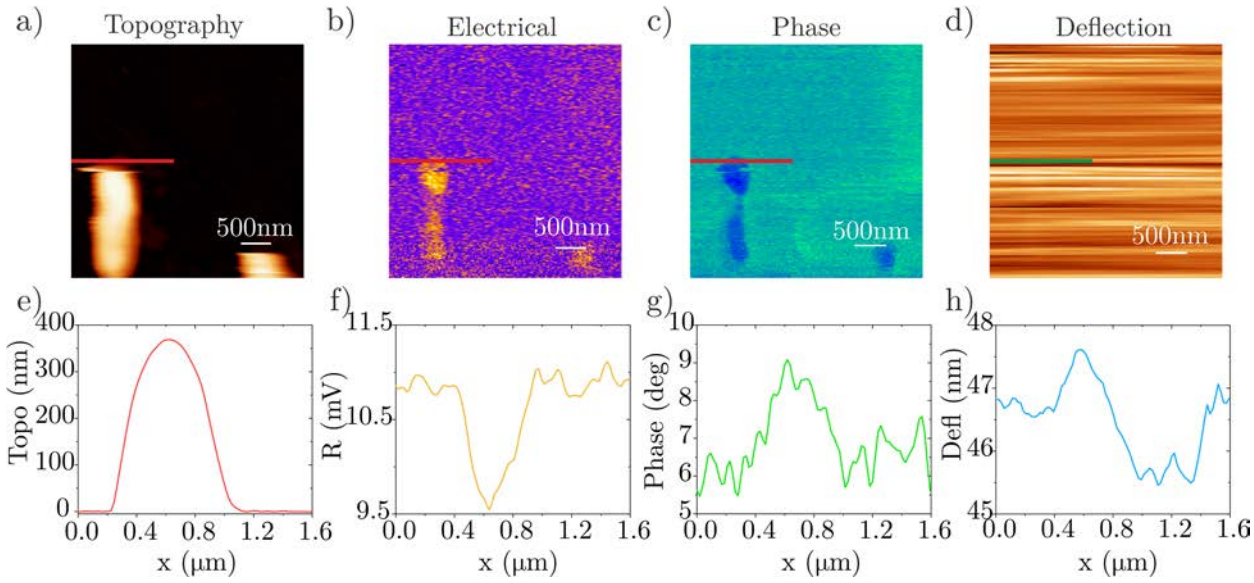

Figure 9.6: a) Topographical, c) raw electrical, electrical phase and d) deflection images of *S. oneidensis*. e) Topographical profile along the line in image (a). f) Raw electrical profile along the line in image (b). g) Electrical phase profile along the line in image (c). h) Deflection profile along the line in image (d).

9.3.Conclusions

In this chapter, we have studied the electrical and topographical properties of rehydrated electrochemically active bacteria in liquid conditions. Qualitative results have been presented, showing an electrostatic contrast, related to the dielectric properties. In addition, some images of living bacteria in liquid conditions are presented. This chapter presents some qualitative data of living bacteria at the nanoscale. However, the quantification of these measurements is still under study since more complex theoretical models are needed to quantify the EFM data in liquid conditions than in dry conditions.

10. Impedance measurements of living bacteria on a chip

This chapter explains the work realized in the Denmark Technical University (DTU) in Copenhagen, performed during a four-months secondment, in the NaBIS group under the supervision of Prof. Winnie E. Svendsen. This chapter explains the design and fabrication of a chip for impedance measurements of living bacteria.

In this chapter, this technique will be used to study the electrical properties of *S. oneidensis* MR-1. The aim is to extract the dielectric properties from impedance measurements in living bacteria at the macroscale. Therefore, they will complement the EFM measurements at the nanoscale on dry bacteria.

10.1.Introduction

One of the methods to electrically characterize bacteria is through impedance measurements, especially through Electrochemical Impedance Spectroscopy (EIS). EIS is a technique that has been used for over a century for many applications like material surface characterization, corrosion analysis or to perform bacteria analysis, such as monitoring the growth conditions, test antibiotics or monitor the functioning of batteries and fuel cells, among many other applications. During the last years, an effort on the development of biosensors based on impedimetric transducers has been made since EIS gives information on the interfacial phenomena occurring on the surface of the device, or close to it. The EIS measurements can be combined with microfluidic sensors, allowing the study of living microorganisms in their natural environment [178,179].

The impedance of a system is usually determined by applying a voltage perturbation of a sinusoidal wave, generally of small amplitude, and detecting the resulting current response. The current response will change upon different system parameters, like the electrode coverage.

Therefore, impedance measurements have been widely used to study layer deposition [180], testing antibiotics [181], to study the viability of the cells [182] or bacterial metabolism [183].

Impedance measurements have been used to study EET processes. For example, in a recent study, a correlation between the EET and the cell surface polarizability was demonstrated using dielectrophoresis measurements [184]. Another study used impedance spectroscopy to characterize the role of flavins, a shuttle molecule of some electrochemically active bacteria [185].

10.1.1.Brief introduction of the theory of impedance spectroscopy measurements

One of the most difficult parts of the EIS is the proper interpretation of the data. For this reason, first, I would like to give an overview of the interpretation of the impedance measurements in a two-electrode system and in flow cytometry systems.

Two-electrode impedance measurements

The typical graph obtained in two-electrodes impedance measurements is the bode plot, and it is shown in **Figure 10.1**. In this plot, the modulus of the impedance ($|Z|$) in a logarithmic scale and of the phase versus the frequency are presented.

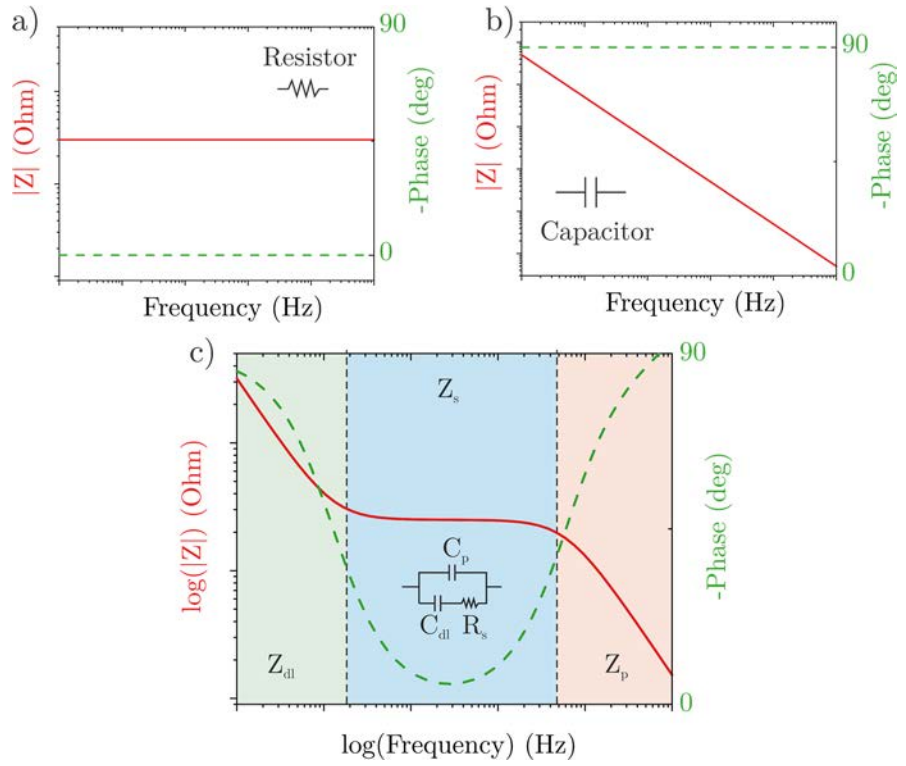

Figure 10.1: a) Bode plot for a resistor. b) Bode plot for a capacitor. c) Bode plot for a resistor-capacitor mixed system. The green part corresponds to the double layer capacity, the blue part to the medium resistance and the orange part to the parasitic capacitance.

For a pure resistor system, the current through a resistor remains in phase with the voltage ($\phi = 0°$). Then, the impedance is independent of the frequency and it does not have an imaginary component, see **Figure 10.1a**. On the other hand, for a pure capacitor system, the current through the capacitor is shifted -90° with respect to the voltage ($\phi = 90°$). In this case, the impedance of the system decreases as the frequency increases, see **Figure 10.1b**.

However, if an AC excitation is applied between two electrodes in an electrolyte, we do not have a pure resistor behaviour nor a capacitor system, but we will have a combination of both. The equivalent circuit for such system is shown in the inset of **Figure 10.1c**, where Z_{dl} is the impedance of the interface; Z_p is the parasitic contribution; and Z_s is the impedance of the sample fluid, assuming that it is governed by its resistive part. The typical bode plot of such system is presented in **Figure 10.1c**.

The individual impedance contribution of the medium is the resistance of the liquid between the electrode, eq. (10.1).

$$Z_s = R_s \tag{10.1}$$

The parasitic impedance will always occur in an electrical system. It arises from the electrical components such as interconnections and general wiring, and their proximity to each other. This impedance is given by eq. (10.2)

$$Z_p = \frac{1}{i\omega C_p} \tag{10.2}$$

where C_p is the parasitic capacitance, also called stray capacitance, ω is the frequency and i is the imaginary number.

Finally, the double layer impedance appears when the electrostatic double layer (EDL) is created. The EDL is formed when a charged electrode comes into contact with an electrolyte in water; it is a layer of opposite polarity at the interface. The EDL can be divided into three sub-layers, the inner Helmholtz plane (IHP), which consists of a hydration sheath of oriented water dipoles. The outer Helmholtz plane (OHP), just beyond the IHP and it is formed by a layer of hydrated ions. The capacitance induced by the IHP and the OHP is called the Helmoltz capacitance (C_H) and it is described by eq. (10.3).

$$C_H = \frac{\varepsilon_0 \varepsilon_r}{d_{OHP}} \tag{10.3}$$

where d_{OHP} is the distance from the electrode to the OHP.

Finally, beyond the OHP, there is a diluted and thick layer of ions and molecules that electrically screens the surface charge of the electrode, producing an exponential decay of the potential. The Debye length (λ_D) is the characteristic length of such exponential decay and it is well defined in the literature. λ_D is mainly dependent on the electrolyte concentration as can be seen in eq. (10.4).

$$\lambda_D = \sqrt{\frac{k_B T \varepsilon_0 \varepsilon_r}{2 Z^2 e^2 n_0}} \tag{10.4}$$

where k_B is the Boltzmann constant, T is the temperature, Z is the number of charges per ion, e is the elementary charge and n_0 the ionic concentration.

The capacitance induced by the diffused layer is called the Gouy-Chapman capacitance (C_G) and it is described by eq. (10.5).

$$C_G = \frac{\varepsilon_0 \varepsilon_r}{\lambda_D} \cosh\left(\frac{z V_0}{2 V_t}\right) \tag{10.5}$$

where V_0 is the potential at the electrode surface.

Hence, the total double layer capacitance (C_{dl}) is described by eq. (10.6) and the double layer impedance will be described by eq. (10.7). However, Z_{dl} does not include factors like surface roughness, non-uniform current and potential distribution, or electrode porosity. Therefore, in order to take these factors into account and fit experimental data more accurately, a phenomenological model with two free constants is used. In this way, the double layer impedance can be modelled by using a constant phase element (CPE) which expression is shown in eq. (10.8).

$$\frac{1}{C_{dl}} = \frac{1}{C_H} + \frac{1}{C_G} \tag{10.6}$$

$$Z_{dl} = \frac{1}{i\omega C_{dl}} \tag{10.7}$$

$$Z_{CPE} = \frac{1}{i\omega^{\alpha} Q} \;;\; 0 < \alpha > 1 \tag{10.8}$$

where Q and α are to parameters to be adjusted and usually α~$0.8 - 1$.

As mentioned before, **Figure 10.1c** shows a typical bode plot for an electrode immersed in a solution. As can be seen, at low frequencies, the double layer impedance is dominating. At high frequencies, the parasitic impedance is dominating. In both cases, a capacitive behaviour is obtained, then a phase close to $\phi = 90°$ and an impedance dependent with the frequency appears. Nevertheless, at intermediate frequencies, the solution impedance and the resistive behaviour is dominating; thus, there is a phase close to $\phi = 0°$ and the impedance is independent of the frequency and a plateau in the Bode plot is obtained. It is desirable to experimentally measure in this zone since the fluid resistance is visible and all the changes in this region are due to changes in the medium. However, if the double layer capacitance or the parasitic capacitance is too large, the bode plot will be almost like a pure capacitor plot (**Figure 10.1b**), and the resistive part of the system will be masked, difficulting the obtainment of the sample properties.

Flow cytometry impedance measurements

Flow cytometry impedance measurements measure the impedance of a particle suspension using an ac excitation signal and a flow of particles. The current passing through the system as a function of frequency is measured to obtain the electrical properties of such particles. In this technique, a large number of cells at high speed are evaluated, but only one cell at a time.

In these measurements, two pair of facing electrodes inserted in a channel are used and the current difference between the two pairs are measured. A schematic drawing of the electrodes and their working principle is shown in **Figure 10.2**. When the particle is not between neither of the two electrodes, it does not influence either electric field generated by the electrodes and the differential signal between both is zero. As the particle travels in the channel, it will only disturb the field of one set of electrodes at a time, which will produce a differential signal. Once the particle has left the channel, a transition looking like a sinusoidal signal will have been recorded, showing the transition of one particle.

Low frequency electric field (100 – 1000 kHz) will not be able to penetrate the bacteria due to the isolating nature of the membrane. Thus, the bacteria will only move the liquid in the medium and the measured signal will only depend on the volume displacement, i.e., the signal depends on the bacteria size. However, at high frequencies (1 MHz – 10 MHz), the electric field is able to penetrate the bacterial membrane, and consequently, the signal will be related to the membrane

and cytoplasmic properties. For this reason, the measurements are carried out at two frequencies simultaneously; a low frequency of $f_{LF} = 200$ kHz and a high frequency of $f_{HF} = 7$ MHz [182,186].

Using this method, the impedance changes are related to both size and membrane or cytoplasmic properties. Therefore, it could be possible to study *S. oneidensis* bacteria and their electrical properties.

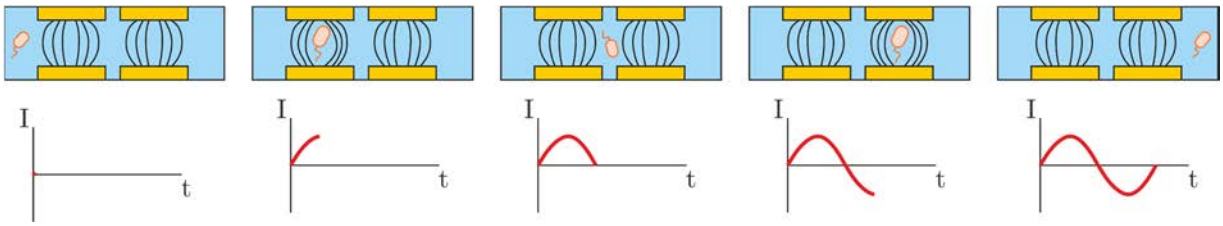

Figure 10.2: Schematic drawing of the detection principle.

10.2.Design of the chip

In order to measure the impedance properties of *S. oneidensis* MR-1 bacteria and their nanowires, a set of chips with different electrode configurations were designed. In order to design the chip, we used CleWin5, a layout editor. The purpose is to measure the *S. oneidensis* nanowires or the full bacteria, since nanowires are OMEs, between two electrodes. For this reason, electrodes separated 1 μm of different widths were proposed.

Figure 10.3a shows the full wafer design. In this design, the chip is repeated twelve times over the 10-inch wafer. Also, a pattern test (**Figure 10.3d**) and a label to identify the wafer were included. A zoom-in of one of the chips is presented in **Figure 10.3b**. In the chip, one can see the microfluidic channel in blue, a frame of the chip in pink and the gold electrodes, and the inverted pattern that will be exposed, in yellow. As can be seen, the pins are separated 4 mm to avoid any short-circuit between one pin and the next one. Also, the pins have a size of 2 mm diameter in order to facilitate future connections. In addition, a counter electrode of 0.8×0.6 mm and a reference electrode of 50×50 μm are included in the design. A zoom-in of the electrodes is shown in **Figure 10.3c**. There are seven pair of electrodes with different electrode width, ranging from 0.8 μm to 10 μm. The distance is also varied, ranging from 0.5 μm to 5 μm. As will be

explained later, a laser direct writer exposure machine was used in the fabrication process, allowing to change the design from one exposure to the next one.

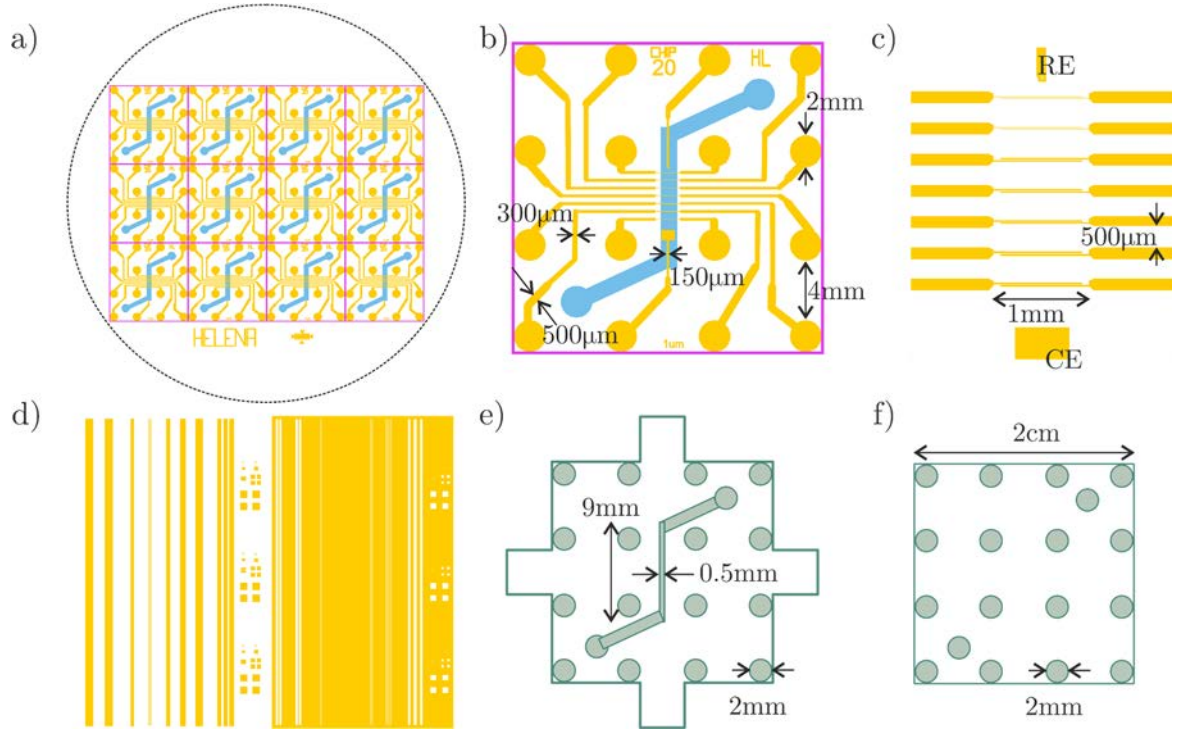

Figure 10.3: a) Full wafer design. b) Zoom-in of one chip of (a). c) Zoom-in of the electrodes zone in (b). d) Pattern test design. e) Microfluidic channel design and f) cap design.

The microfluidic channel was also designed using CleWin5. The channel design is presented in **Figure 10.3e**, where the circles correspond to the gold connections. The designed channel was 9 mm long and 0.5 mm thick, although it increased to ~ 0.8 mm thick due to the laser-cut. In addition, the holes for the inlet and outlet were designed. For the cap, the holes for the gold connections and the holes for the inlet and outlet were created (**Figure 10.3f**). Subsequently, they were laser cut in double-sided tape and poly(methyl methacrylate) (PMMA), respectively. The final dimensions of the chip were $20 \times 20 \times 2.3$ mm.

10.3.Fabrication of the chip

10.3.1.Cleanroom fabrication

In order to fabricate the chips, a standard photolithography method was followed. **Figure 10.4** shows a schematic representation of the cleanroom fabrication process. The steps needed to fabricate the chip are going to be explained in the following sections.

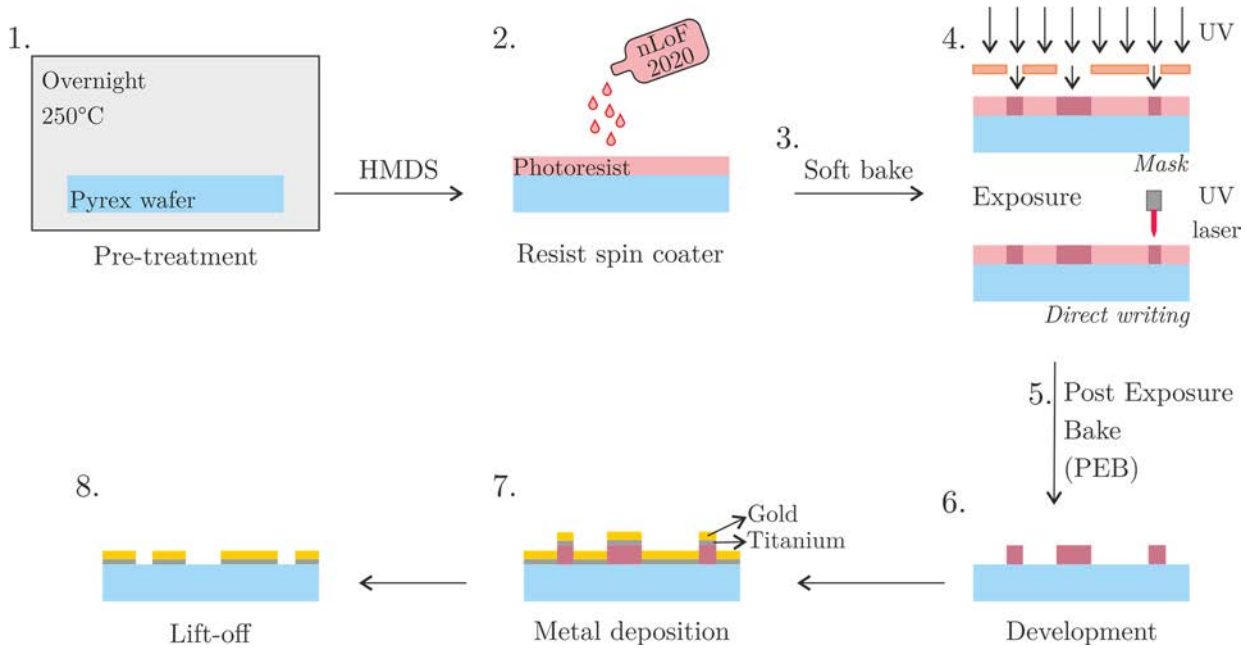

Figure 10.4: Schematic representation of the chip fabrication process, using a negative photoresist.

1. **Pre-treatment:** first, the bare pyrex wafer is treated to promote the adhesion of the photoresist. Therefore, the wafers pass from being hydrophilic to be hydrophobic. We followed two pre-treatment steps:
    - **Oven**: it dehydrates the surface and promotes the resist adhesion. The wafers are introduced in the oven and left them overnight. Afterward, the resist coating is performed as soon as possible.

      Technique: we put the wafers in the oven at 250℃ overnight.
    - **HMDS**: in this step, the substrate is heated in vacuum to dehydrate and subsequently is exposed to hexamethyldisilazane (HMDS) vapor. It is a chemical treatment that promotes the adhesion since it leaves a monolayer of HMDS; therefore, the surface dehydrates and lowers the surface tension.

      Technique: it was performed using the standard recipe of the spin coater from Süss MicroTec, model Gamma 2M.
2. **Resist:** the photoresist is deposited onto the pyrex wafer for the subsequent exposure. *Technique*: we used a spin coater LabSpin 6 from Süss MicroTec. We deposited the negative photoresist AZ nLoF 2020. In order to improve the electrode resolution, we deposited 500 nm resist thickness and, we diluted the resist with the developer mr-Dev

600 in a [1:1] ratio. Later, it was spin-coated at 3000 rpm, during 60 s and accelerating at 1000 rpm/s.

3. **Soft bake (SB)**: after spin coating, the solvent in the resist has to be evaporated to solidify the resist. This step improves the mechanical stability of the resist, and it prevents the sticking of the resist to the mask. The soft bake can be carried out as a contact bake or a proximity bake. In a contact bake, the wafer is maintained in close contact with the hotplate surface. In a proximity bake, the wafer is first moved into proximity, e.g., 1 mm, of the hotplate surface, then it is kept there (on the lift pins) for the duration of the bake.

   Technique: we used contact bake, using a hot plate at 110℃ during 60 s.

4. **Exposure**: in this process, the part of the resist that is exposed to the UV light is polymerized (for a negative photoresist), fixing the exposed zones to the wafer and becoming insoluble to the photoresist developer. For a positive photoresist, the zones that are exposed to the UV light becomes soluble to the photoresist developer. In this step, we obtain the desired pattern in the wafer. This process can be made using a mask, which blocks the UV light following a pattern. Or using a direct laser writer. This last method does not need a mask, facilitating changes in chip design from one chip to another and improving the resolution, since there is no diffraction with the mask.

   Technique: the exposition of the resist was made with a Maskless aligner MLA 150 from Heidelberg Instruments GmbH, a direct laser writer machine using a wavelength of $\lambda = 375\ nm$. First, a dose and defocus test was performed to obtain the optimal parameters of the exposition process, raging the defocus from -10 to 10 and sweeping the dose from 400 mJ/cm^2 to 1000 mJ/cm^2 (**Figure 10.5a** and **Figure 10.5b**). The optimal parameters used to obtain the final chips were a focus of 550 mJ/cm^2 and a defocus of -6. The total time exposure was 40 min. Some pictures of the resist pattern are shown in **Figure 10.5c** and **Figure 10.5d**.

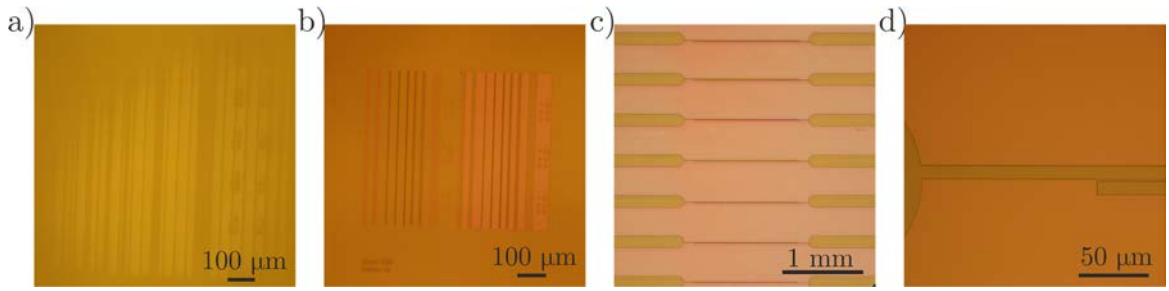

Figure 10.5: a) Pattern test using a low dose (dose = 235 mJ/cm^2 and defoc = -6). b) Pattern test using the chosen dose (dose = 550 mJ/cm^2 and defoc = -6). c) Resist electrodes (dose = 550 mJ/cm^2 and defoc = -6) and d) zoom-in of (d).

5. **Post Exposure Bake (PEB)**: in some resists, the photochemistry is a catalytic process. Thus, this process is activated/assisted thermally in the PEB step.

   Technique: we used the spin coater Gamma 2M from Süss MicroTec, which performs a PEB at 110℃ during 60 s.

6. **Development**: in the exposure step, the light activates the photoactive compound, which changes the solubility of the resist. In this step, the soluble parts are removed via three ways: submersion (the wafer is submerged in a developer bath), spray (the developer is sprayed onto the surface) and puddle (the developer is dispensed onto the surface of the substrate and held there by surface tension).

   Technique: it was performed using the spin coater Gamma 2M from Süss MicroTec, which, instead of depositing resist, it dispenses the developer. The development was performed during 60 s using single puddling and tetramethylammonium hydroxide (TMAH) developer. Lastly, the wafer was rinsed with miliQ.

7. **Metal deposition**: in order to obtain the gold paths of the chip, metal deposition is needed. The metal deposition can be done using different techniques like evaporation using heat or electrons or sputtering, among others.

   Technique: 10 nm Titanium at a rate of 2 Å/s were deposited to promote the gold adhesion to the pyrex wafer. Afterward, 100 nm at a rate of 10 Å/s was deposited using the electron beam evaporator Temescal from Ferrotec.

8. **Lift-off**: the metal evaporation is performed in the full wafer, depositing the Ti/Au onto the pyrex wafer and onto the resist. However, it is desirable to have it only onto the pyrex wafer. Thus, in this process, the photoresist is removed using a resist developer.

Technique: the wafer was introduced into a remover 1165 bath at 40℃ and it was left there during 3h. Subsequently, the ultrasound (US) was applied for 14 min at power 5. Subsequently, the wafer was rinsed in an IPA bath with US power 5 for 5 min. Lastly, the wafer was rinsed with miliQ. Pictures of the resulting electrodes are shown in **Figure 10.6a**, **Figure 10.6b** and **Figure 10.6c**.

9. **Dicing**: finally, the wafer is cut in small pieces to form the chip.

   Technique: the wafer was cut using an automatic dicing saw, model DAD 321, from DISCO. The wafer was cut five times in the horizontal direction and four times in the vertical direction at 3 mm/s, all separated 20 mm using a HUBless Blade B1A862. The final wafer and the diced chip are shown in **Figure 10.6d**.

In the cleanroom process, the maximum resolution obtained was electrodes of 1 μm wide and separated 0.5 μm, surprisingly good for UV lithography. This is shown in **Figure 10.6c**.

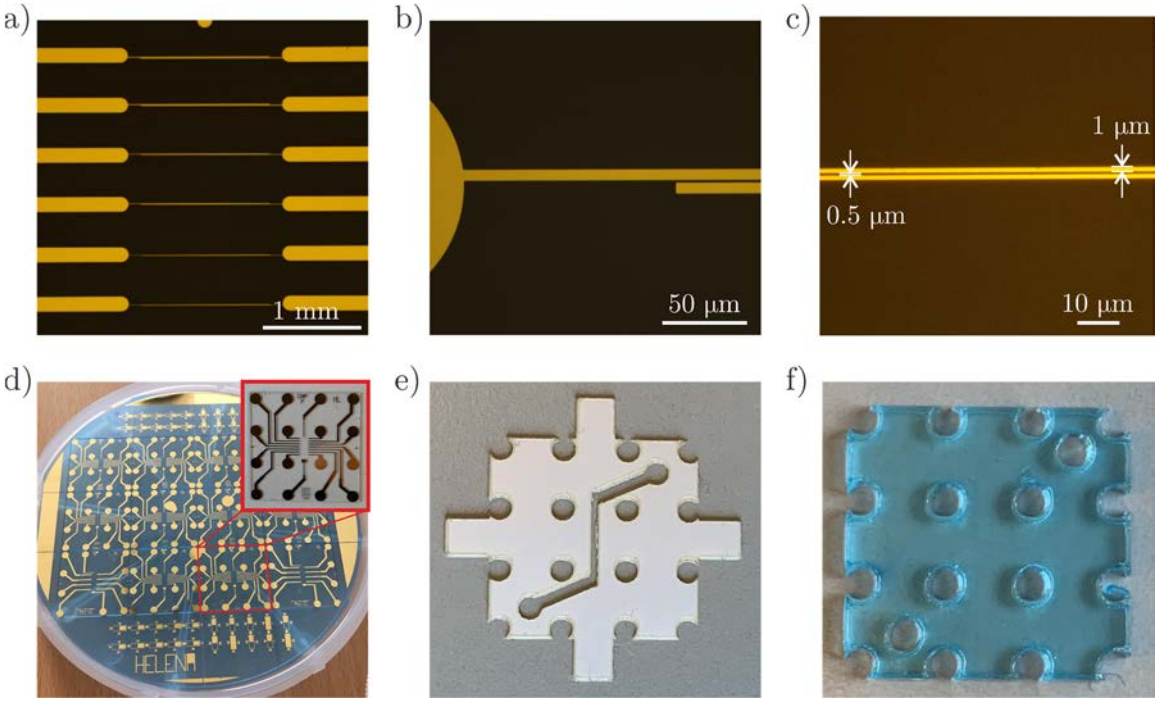

Figure 10.6: a) Picture of the gold electrodes b) zoom-in of (a). c) Picture of two electrodes of 1 μm width separated 0.5 μm. d) Picture of the fully processed wafer, inset: zoom-in of one chip. e) Picture of the cut double-sided tape. f) Picture of the cut PMMA forming the cap.

10.3.2.Microfluidic channel fabrication

In order to build the microfluidic channel, an Epilog Engaver laser cut, from Epilog Laser, was used. In this step, first, the channel was built cutting the design of the gold pinholes and the

channel (**Figure 10.3e**) on double-sided tape of ~80 μm thick, which will be the height of the channel. To cut the double-sided tape, a power of the 25% and a 50% speed was used, the cut was repeated two times. Subsequently, the cap was built cutting on PMMA the gold pin holes design (**Figure 10.3f**), using a 25% power and 5% speed and repeating the cut five times. The final pieces are shown in **Figure 10.6e** and **Figure 10.6f**, respectively.

Lastly, all the pieces were put together. **Figure 10.7** shows the sequence of the full assembly process. As can be seen, first, the double-sided tape was pasted on the chip, and the tabs were used to hold the chip to the table and avoid undesired movements. Subsequently, the PMMA piece was pasted on the chip with the double side tape. Finally, the tabs were cut, and the microfluidic chip was assembled.

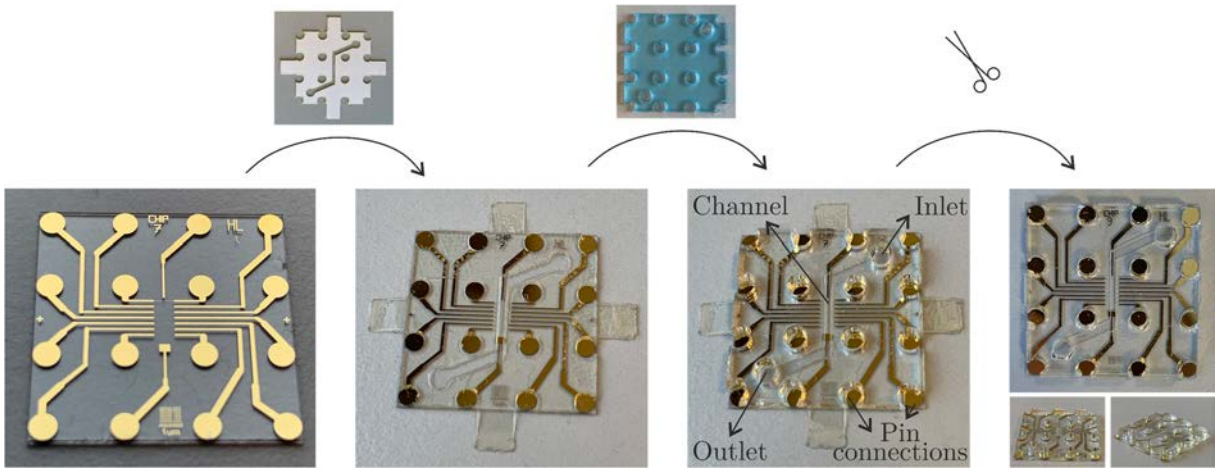

Figure 10.7: Process of the microfluidic chip assembly.

10.4.Impedance characterization of the chip

After the fabrication, an impedance characterization process of the chip was performed. To do so, diverse mediums and buffers were used for different electrode configurations. An Autolab Nova potentiostat from Metrohm was used to perform the measurements. We performed two-electrode measurements applying a DC voltage of 0.5 V and an AC 100 mV rms amplitude. Subsequently, a sweep of frequencies between 10 Hz and 1 MHz was performed while recording the impedance.

Figure 10.8a shows the characterization for one of the electrodes tested. In this case, the electrode width is 2 μm separated 1.5 μm. As said before, the ideal case corresponds to have a

visible resistive part in the impedance spectra, which corresponds to a phase close to $\phi = 0°$ and a plateau in the impedance plot, since in that region electrical properties of the medium can be extracted. Therefore, we analyzed with different mediums the impedance bode plot. We can see that the resistive part is only visible at high frequencies (f~$10^5 - 10^6$ Hz) for miliQ water, which has the lowest conductivity among all the mediums tested. For tap water, PBS 1X and *nwmedia*, only the capacitive behaviour is visible. In addition, for the ferro/ferricyanide, a resistive part is visible at low frequencies (f~$10^1 - 10^2$ Hz), this is due to redox species present in the solution, which allow the exchange of electrons with the electrode.

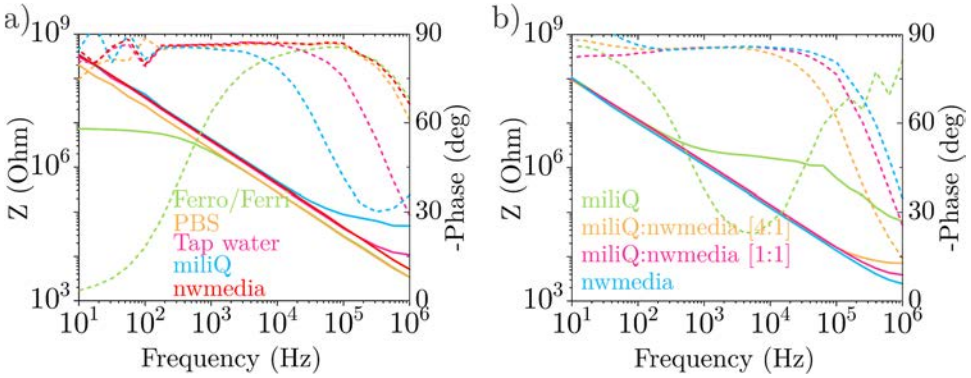

Figure 10.8: a) Bode plot for a chip of 2 μm width electrode separated 1.5 μm using five different mediums, ferro/ferricyanide solution 5 mM, PBS 1x, tap water, miliQ and *nwmedia*. b) Bode plot for a chip of 10 μm width electrodes separated 2 μm for four different concentrations of *nwmedia*.

The reason for not seeing the resistive behaviour in the bode plot is due to the high double layer capacity present in the system since the parasitic capacitance is relatively low, C_p~3.3 pF. In order to decrease the double layer capacity, two strategies can be followed. One is reducing the conductivity of the medium, however, bacteria have to live during several hours in the chip for the planned bacteria experiments; thus, the *nwmedia* would be the ideal solution to work with. Another strategy would be to increase the width of the electrode, thus reducing the double layer.

In order to decrease the high double layer capacity, the chip design was changed to include electrodes between 5 μm and 10 μm width. In addition, since our interesting solution is the *nwmedia*, we tested four different dilutions with miliQ water. **Figure 10.8b** shows the bode plot for 10 μm width electrodes separated 2 μm for four solutions: miliQ, miliQ:*nwmedia* [4:1], miliQ:*nwmedia* [1:1] and *nwmedia*. However, only with pure miliQ water, the resistive part is visible in the range f~$10^3 - 10^4$ Hz. As shown, a 25% dilution of the *nwmedia* starts to show a

resistive part in f~10^6 Hz, frequencies close to the potentiostat operation limit. However, we did not dilute further the medium since higher concentrations of miliQ would kill the bacteria and would not be fruitful for the planned bacteria experiment.

10.5.Impedance measurements of bacterial cells

Some preliminary results using flow cytometry impedance measurements and two-electrodes impedance measurements with bacterial cells have been obtained. In all bacteria measurements, first, bacteria were grown aerobically in Tryptic Soy Broth (TSB) overnight at 30°C. Subsequently, for bacteria grown anaerobically in TSB, bacteria were transferred to TSB media without O_2. For bacteria grown with *nwmedia*, they were transferred to such *nwmedia*, supplemented with fumarate, with or without O_2 (as stated) overnight at 30°C. Finally, for bacteria being in *nwmedia* without fumarate, bacteria were transferred to such *nwmedia* without fumarate, with or without O_2 (as stated), for 5 h.

10.5.1.Flow cytometry impedance measurements

In order to perform an electrical characterization of *S. oneidensis* MR-1 bacterial cells and their nanowires, first, we performed flow cytometry impedance measurements with living cells. To perform the measurements, we used the BactoBox, a flow cytometry equipment from SBT instruments, Denmark.

Figure 10.9 and **Figure 10.10** show the phase impedance in high frequency measurements versus low frequency measurements, and each dot corresponds to one bacterial cell event. Also, they show the opacity versus the impedance modulus at low frequency for different growth conditions. The opacity (O) is the modulus of the HF impedance divided by the modulus of the LF impedance ($O = |HF|/|LF|$) and it is useful because it removes a large part of the particle size influence and thus, mainly provides information about the membrane capacitance.

As can be seen from **Figure 10.9**, a significant difference can be found between bacteria grown in TSB medium with oxygen (O_2) overnight and bacteria grown in *nwmedia* without fumarate and without O_2 (following the same conditions as in Section 7.3.1). However, these differences can be due to bacteria size, since bacteria increase more the size when they grow in rich media, like

TSB, and with oxygen, than when they grow in minimum medium without oxygen, or due to a change in bacterial conductivity.

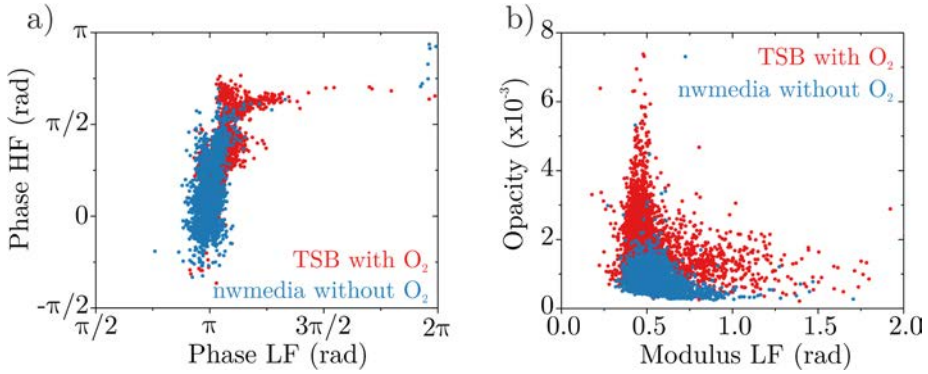

Figure 10.9: a) Phase impedance in high frequency (HF) versus low frequency (LF) for *S. oneidensis* bacteria grown in TSB and with oxygen (red data) and grown in *nwmedia* and without oxygen (blue data) b) Opacity versus the LF modulus of the impedance for the same bacteria analyzed in (a).

In order to investigate further the differences observed, six different growth conditions were tested, being:

1. TSB medium with O_2
2. TSB medium without O_2
3. *Nwmedia* supplemented with fumarate and with O_2
4. *Nwmedia* supplemented with fumarate and without O_2
5. *Nwmedia* without fumarate and with O_2
6. *Nwmedia* without fumarate and without O_2

The results of the measurements were shown in **Figure 10.10**. In this study, no significant differences are observed between bacteria grown aerobically or anaerobically using the same medium. Thus, we conclude that the differences observed in **Figure 10.9** are due to the bacteria size.

Since the EET is performed via electron hopping, which does not induce a change in the dielectric constant (Chapter 7), these results could be in good agreement with the literature. In addition, bacteria develop the nanowires when they are settled on a surface and flow cytometry measurements are performed in suspension.

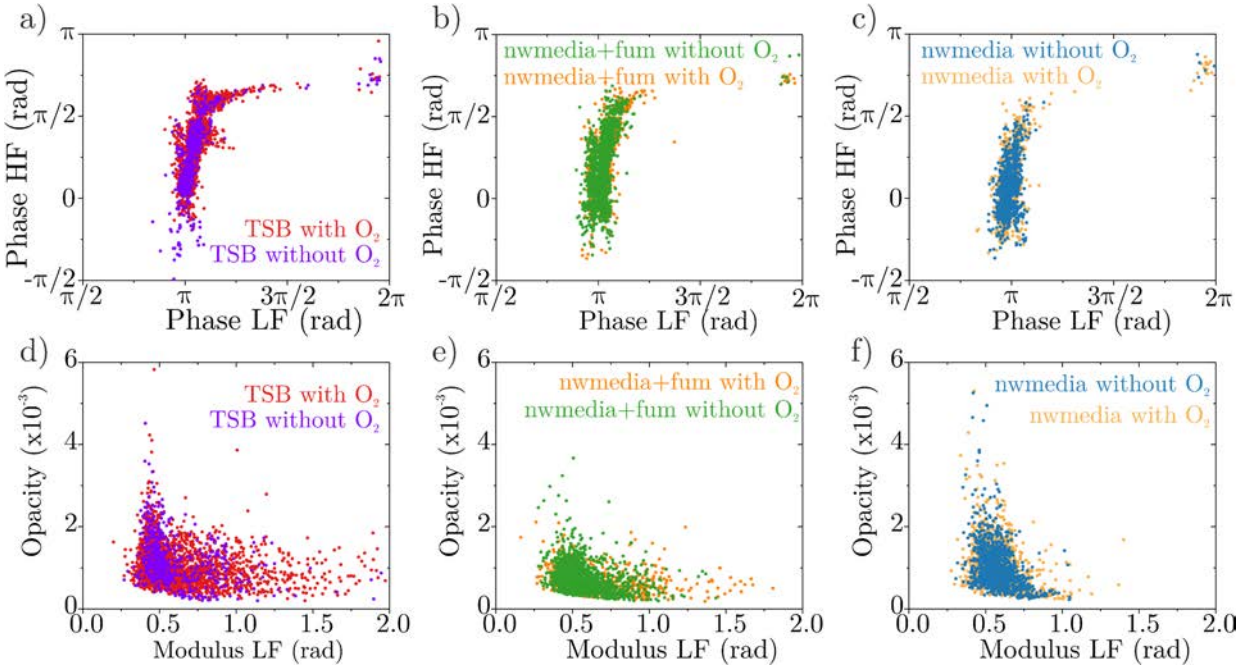

Figure 10.10: a) Phase impedance in high frequency (HF) versus low frequency (LF) for *S. oneidensis* bacteria grown in TSB with and without oxygen, b) in *nwmedia* supplemented with fumarate and c) in *nwmedia* without fumarate. d), e) and f) Opacity versus the LF modulus of the impedance for the same growth conditions as in (a), (b) and (c), respectively.

10.5.2.Two-electrodes impedance measurements

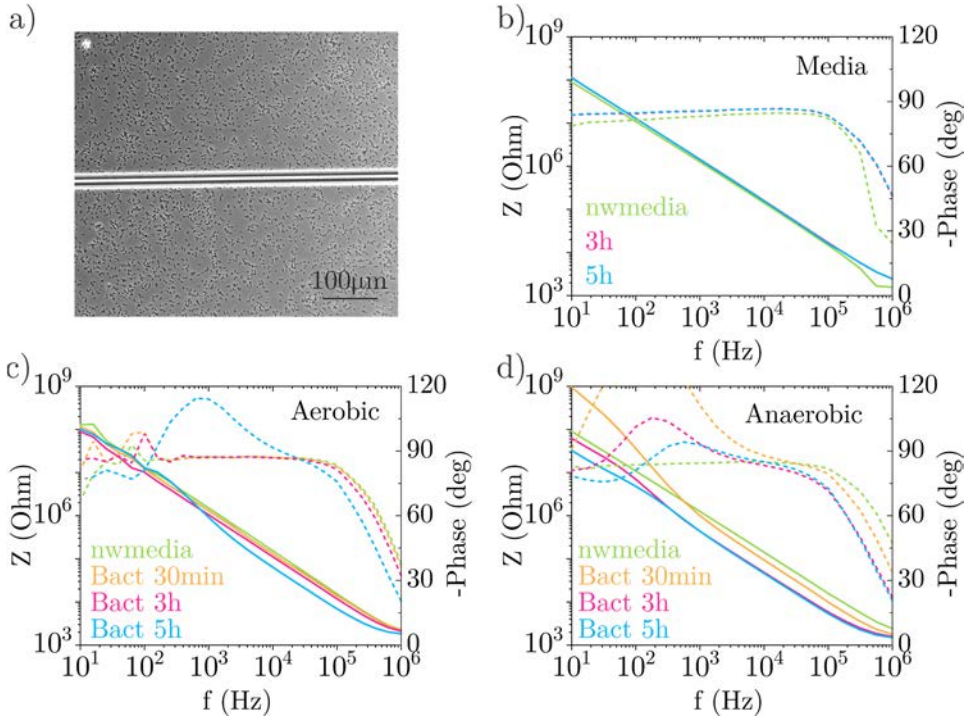

Figure 10.11: a) Phase contrast image of the bacteria coverage in the impedance measurements. b) Impedance measurements with fresh *nwmedia* (green line), after 3 h of bacterial inoculation (pink line) and after 5 h (blue line). c) Impedance measurement of fresh

nwmedia (green line), after 30 min of bacterial-grown-aerobically inoculation (yellow line), after 3 h (pink line) and after 5 h (blue line). d) same as (c) but with bacteria grown anaerobically.

Finally, two-electrodes impedance measurements using an Autolab Nova potentiostat over the fabricated chips were performed. To do the measurements, a DC voltage of 0.5 V and an AC 100 mV rms amplitude were applied. Subsequently, a sweep in frequencies between 1 Hz and 1 MHz was carried out.

We performed impedance measurements testing three chips, of 10 μm width separated 1 μm, at the same time. One of the chips only contained *nwmedia*, and the other two contained bacteria, one grown aerobically and the other one anaerobically. The level of bacteria coverage of the electrodes is illustrated in **Figure 10.11a**. The impedance measurements are explained below:

1. **Media chip**: this served as the control. In this chip, the *nwmedia* was inserted in the microfluidic channel, and impedance measurements were performed immediately after the insertion and after 3 h and 5 h. **Figure 10.11b** shows the measurements of this chip, in which no significant differences are observed.
2. **Aerobic chip**: in this chip, first, the *nwmedia* flowed through the chip, and impedance measurements were performed. Subsequently, *S. oneidensis* bacteria grown aerobically in *nwmedia* was inoculated. We left bacteria on the surface and electrodes of the chip. After 30 min, we flowed *nwmedia* to remove poorly adhered cells. At that time, impedance measurements were performed. Later, impedance measurements after 3 h and 5 h of bacterial inoculation were performed. In this case, we could observe that the bode plot for the *nwmedia* was similar to the control one. In addition, no significant differences were obtained when bacteria were added or after 3 h of bacterial inoculation. However, when bacteria stayed more than 3 h on the chip, a peak over 90° in the phase and an abrupt slope change in the impedance curve appeared at f~10^3 Hz. This is presented in **Figure 10.11c**. This performance could correspond to diffusion effects, which could be caused by the segregation of flavins or exchange of electrons with the electrodes from *S. oneidensis*. After some time of bacteria being in the system, we approached near an anaerobic environment, as the oxygen consumption at the surface is higher than the oxygen diffusion through the PMMA and the medium.

3. **Anaerobic chip**: in this chip, we performed similar measurements than in the aerobic chip, but inoculating bacteria grown anaerobically in *nwmedia*. This case is presented in **Figure 10.11d**, and we can observe that the impedance measurements of only *nwmedia* are like the control one. However, when the anaerobic bacteria were inoculated, a peak over 90° in the phase and an abrupt slope change in the impedance appears for f~$10^2 - 10^3$ Hz, and it continues appearing after 3 h and 5 h of bacterial inoculation. The same phenomenon as in the aerobic chip could happen in the anaerobic chip.

These experiments were repeated three times showing similar results, although the understanding of them is still not clear. More studies need to be done.

10.6.Conclusions

A microfluidic biosensor has been designed and fabricated using a layout editor and cleanroom tools. Electrodes of 10 μm width and separated 1 μm were used to perform two-electrodes impedance measurements with bacterial cells. In these measurements, a peak over 90° in the phase and an abrupt slope change in the impedance appeared for f~$10^2 - 10^3$ Hz, and it was observed when anaerobic bacteria were added to the chip. In addition, this phenomenon was also observed when bacteria stayed on the chip for ~5 h. Besides, flow cytometry measurements did not show significant differences between bacteria being grown aerobically and bacteria being grown anaerobically. This could be due to the fact that the EET is performed via electron hopping, which does not induce a change in the dielectric constant of the bacterial membrane. Additionally, bacteria develop the nanowires when they are settled on a surface; however, flow cytometry measurements are performed in suspension. The understanding of the two-electrodes impedance results is still under development, although some diffusion phenomena could be involved. However, further research is necessary.

11. Conclusions and future perspectives

In this thesis, we have analyzed the topographical and electrical properties of two electrochemically active bacteria, *Shewanella oneidensis* MR-1 and cable bacteria, from the *Desulfobulbaceae* family, and their appendages.

To do so, first, we have proposed a method to obtain the dimensions of nanoscale objects, without damaging the sample, avoiding any physical contact. It was based on the measurement of its electrical polarization by using Electrostatic Force Microscopy measurements combined with a multiparameter quantification extraction algorithm. First, we validated the method using silver nanowires of ~ 50 nm diameter and obtained similar width and height values, compared to the ones obtained from (deconvoluted) AFM topographic imaging and TEM imaging, with just a slightly smaller accuracy. Secondly, we applied the technique to one of the *S. oneidensis* appendages, the flagella. Flagella, with ~10 nm diameter, could be considered as a fragile and low polarizable nano-object. In this case, we again obtained a good agreement with AFM topographic data. The main advantage of the proposed method is that it can be applied to soft and poorly adhered samples, as it is based on the measurement of the long-range electric polarization forces, which does not require contact with the sample at any moment. This fact opens interesting possibilities in the determination of the physical dimensions of nano-objects made of soft materials like biological materials, polymers, gels, biomolecules, liquids, etc., for which an accurate determination has remained elusive for SPM methods until now.

Secondly, we have analyzed the electrical properties of the above mentioned *S. oneidensis* flagella. And we have compared the properties obtained with *P. aeruginosa* PAO1 flagella. We have used AFM to obtain the topographical properties, and we have found that the dimensions of *S. oneidensis* flagella are $h_{So} = 8.8 \pm 0.5$ nm, and $w_{So} = 18 \pm 2$ nm. However, the dimensions of *P. aeruginosa* are slightly bigger, $h_{Pa} = 12.8 \pm 0.5$ nm and $w_{Pa} = 27 \pm 2$ nm. The dimensions

of *P. aeruginosa* flagella are similar to the ones obtained through cryo-TEM studies [158]. Concerning the electrical properties, using SDM, we have obtained the dielectric constant values of $\varepsilon_{So} = 4.3 \pm 0.6$ and $\varepsilon_{Pa} = 4.5 \pm 0.7$, for *S. oneidensis* MR-1 and *P. aeruginosa* PAO1 flagella, respectively. These values do not depend on the bacterial species; and, since flagella are filamentous structures composed of flagellin proteins monomers, these dielectric values correspond to the dielectric constant of a few hundred protein monomers. Similar relative dielectric constant values have been reported for other macromolecular protein complexes using the same technique. Altogether, these results indicate that the relative dielectric constant of proteins under dry conditions show dielectric constant values ($\sim 3-5$), like those reported using macroscopic techniques applied to dry protein crystals, and different from the values reported for other cell components such as lipids (~ 2) or DNA (~ 8). These results may have important implications in the understanding of the relevance of the electrostatic energy contribution to the protein function and structure.

Thirdly, we have analyzed the topographical and electrical properties of another *S. oneidensis* appendages, the Outer Membrane Extensions (OMEs), also called bacterial nanowires. We have observed that the OMEs resemble a chain composed of spherical structures with a height h_{OME}~40 nm. Additionally, when dry bacteria are rehydrated, the height is tripled with respect to the dry height (from h_{dry}~120 nm to h_{liq}~350 nm), but the OMEs height remains the same. Also, we have found, through fluorescence images, that these OMEs start to appear after bacteria left on a surface for, at least, 30 min. Regarding the dielectric constant, we have obtained $\varepsilon_{OME} = 3.7 \pm 0.7$, a low value if those nanowires have a metal-like conductivity. However, the nanowires have electron hopping conductivity, with no delocalized electrons. Therefore, our results are compatible with a low dielectric constant.

Subsequently, the electrical properties of another electrochemically active bacteria, the cable bacteria, have been studied. Cable bacteria are formed by a chain of bacteria forming a filament, and along this filament, there are fibers. These fibers are proposed to be responsible for electrical conduction, connecting the oxygen reduction at the surface sediment with sulfide oxidation in the subsurface of the sediments. These filaments can be several centimeters thick, generating electric currents through it. The mechanism for electron conduction is still unclear, but we have tried to shed some light on these questions. We have analyzed the cable bacteria with Scanning Dielectric

Microscopy to obtain the electrical properties of the bacteria and the fibers. We have obtained higher electric polarizability for the fibers than the body of the bacteria. Considering a pure dielectric material, the dielectric constant obtained for the fibers is $\varepsilon_r = 7 \pm 1$, which could be related to the high content of phosphate in the cable bacteria. However, the dielectric behaviour does not explain the conduction properties, which are only consistent with a core-shell model. With this model, we have obtained a core-shell structure for the fiber with a high conductive core ($\sigma = 2000$ S/m) with dimensions h_c~$10 - 20$ nm.

In addition, we have studied the electrical and topographical properties of rehydrated electrochemically active bacteria in liquid conditions. Also, the same study has been performed in living bacteria in liquid conditions. Qualitative results have been presented, showing an electrostatic contrast, related to the dielectric properties. However, the quantification of these measurements is still under study since more complex theoretical models are needed to quantify the EFM data in liquid conditions than in dry conditions.

Finally, the electrical properties of *S. oneidensis* bacteria and their nanowires have been analyzed using impedance measurements. With this aim, a microfluidic biosensor has been designed and fabricated using a layout editor and nanofabrication equipment. After some characterization tests, electrodes of 10 μm width and separated 1 μm were used to perform two-electrode impedance measurements on the bacteria. In these measurements, a peak over 90° in the phase and an abrupt slope change in the impedance appears for f~$10^2 - 10^3$ Hz. This phenomenon is observed when anaerobic bacteria are added to the chip. In addition, this phenomenon is also observed when bacteria stayed on the chip for more than 3 h. Besides, flow cytometry measurements have been performed, but they do not show significant differences between bacteria grown aerobically and bacteria grown anaerobically. This could be due to the fact that the EET is performed via electron hopping, which does not induce a change in the dielectric constant of the bacterial membrane. Additionally, bacteria develop the nanowires when they are settled on a surface; however, flow cytometry measurements are performed in suspension. The understanding of the results is still under development, although some diffusion phenomena could be involved. Further research is necessary to understand this.

The first future perspective of this thesis is to perform the quantitative analysis of the EFM measurements in liquid conditions. Then, the next step would be to study the electrical properties of *S. oneidensis* MR-1 and cable bacteria in living and physiological conditions. In addition, topographical and electrical images of the OMEs using AFM and EFM, respectively, should be done in living conditions.

Regarding the conductive properties of these biological samples, a future proposed experiment would be the realization of EFM measurements at different frequencies (f) of the ac voltage applied between the tip and the sample. Therefore, we could define better the conduction properties of these kind of bacterial nanowires.

Finally, regarding the impedance measurements, additional experiments should be performed to clarify the anomalous phase behaviour.

Appendix

List of publications and congress presentations

The list of publications and congress presentations derived from this thesis are presented here:

Publications

H. Lozano, R. Fábregas, N. Blanco-Cabra, R. Millán-Solsona, E. Torrents, L. Fumagalli and G. Gomila, Dielectric constant of flagellin proteins measured by scanning dielectric microscopy, *Nanoscale*, 10, 19188–19194, (2018).

H. Lozano, R. Millán-Solsona, R. Fábregas and G. Gomila, Sizing single nanoscale objects from polarization forces, *Scientific Reports,* 9, (1), 1414, (2019).

M. Van Der Hofstadt, R. Fábregas, **H. Lozano**, R. Millán-Solsona, N. Vellas, Ch. Gaquiere, L. Fumagalli and G. Gomila, Subsurface Imaging of Buried Micro/Nanostructures in Thin Dielectric Films by Electrostatic Force Microscopy: a Quantitative Analysis, *in preparation*

H. Lozano, R. Millán-Solsona, R. Fábregas, N. Blanco, E. Torrents and G. Gomila, Electrical study of Shewanella oneidensis MR-1 nanowires, *in preparation*

H. Lozano, R. Millán-Solsona, S. Hidalgo, R. Thiruvallur, F. Meysman and G. Gomila, Quantitative analysis of the electrical properties of cable bacteria fibers, *in preparation*

Congress presentations

Oral

H. Lozano, *Atomic Force Microscopy (AFM)*, Bioengineering workshop, Barcelona, España, 24th February 2017. **Oral presentation**, invited talk

H. Lozano, R. Millán-Solsona, R. Fábregas, N. Blanco-Cabra, E. Torrents and G. Gomila, *Electrical and morphological characterization of bacterial polar flagella*, AFM BioMed Conference Krakow 2017, Cracovia, Polonia, 4th -8th September 2017. **Oral presentation**. This talk was awarded by the best talk prize.

H. Lozano, R. Millán-Solsona, R. Fábregas, N. Blanco-Cabra, E. Torrents and G. Gomila, *Bacterial polar flagella characterized electrically*, 2nd Biomed PhD Day, Barcelona, España, 12nd December 2017. **Oral presentation**

H. Lozano, *Electrical and morphological characterization of bacterial polar flagella*, PhD Discussion, Barcelona, España, 29th June 2018, **Oral presentation**

Poster:

H. Lozano, R. Millán-Solsona, P. Astola, E. Torrents and G. Gomila, *Topographic characterization of microbial nanowires by atomic force microscopy*, 9th IBEC Symposium on Bioengineering for Active Ageing, Barcelona, España, 29th June 2016. **Poster**

H. Lozano, R. Millán-Solsona, P. Astola, E. Torrents and G. Gomila, *Electrical and morphological characterization of bacterial polar flagella*, XX. Linz Winterworkshop Advances in Single-Molecule Research for Biology & Nanoscience, Linz, Austria, 2nd-5th February 2017. **Poster**.

H. Lozano , R. Millán-Solsona, R. Fábregas, N. Blanco-Cabra, E. Torrents and G. Gomila, *Electrical and morphological characterization of bacterial polar flagella*, 10th IBEC Symposium - Bioengineering for Future Medicine, Barcelona, España, 6th -7th June 2017. **Poster**

H. Lozano, R. Millán-Solsona, R. Fábregas, N. Blanco-Cabra, E. Torrents and G. Gomila, *Implementation of the Electrostatic Force Microscopy to characterize bacterial polar flagella*, Extracellular Electron Transfer: Mechanisms and Opportunities, Norwich, UK, 21st-23rd August 2017. **Poster**. This poster was awarded by the best poster prize.

H. Lozano, R. Millán-Solsona, R. Fábregas, N. Blanco-Cabra, E. Torrents and G. Gomila, *Electric polarization properties of bacterial polar flagella measured by electrostatic force microscopy*, 7th Multifrequency AFM Conference, Madrid, España, 18th – 20th April 2018. **Poster**

H. Lozano, R. Millán-Solsona, R. Fábregas and G. Gomila, *Sizing single nanoscale objects from polarization forces*, 12th IBEC Symposium on Active Ageing, Barcelona, España, 17th July 2019. **Poster**

R. Millán-Solsona, M. Checa, **H. Lozano**, and G. Gomila, *Reconstrucción topográfica aplicada al Microscopio de Fuerzas Electrostáticas (EFM)*, Conferencia de COMSOL Multiphysicsb2019, Málaga, España, 28th June 2019. **Poster**

List of acronyms and abbreviations

AC	Alternating current
AFM	Atomic Force Microscopy
AgNW	Silver Nanowire
DC	Direct Current
DMRB	Disimilatrory Metal Reducend Bacteria
EDTA	Ethylenediaminetetraacetate
EET	Extracellular Electron Transfer
EFM	Electrostatic Force Microscopy
EIS	Electrochemical Impedance Spectroscopy
ET	Electron Transfer
FWHM	Full Width at Half Maximum
HF	High Frequency
HMDS	Hexamethyldisilazane
HOPG	Highly Oriented Pyrolytic Graphite
IPA	Isopropanol
LF	Low Frequency
MV	Membrane Vesicle
NW	Nanowire
OME	Outer Membrane Extension
OMV	Outer Membrane Vesicles
PBS	Phosphate Buffer Solution

PEB	Post Exposure Bake
PMMA	Poly(methyl methacrylate)
SDM	Scanning Dielectric Microscopy
SDS	Sodium Dodecyl Sulphate
SEM	Scanning Electron Microscopy
SPM	Scanning Probe Microscopy
TEM	Transmission Electron Microscopy
TSMS	Tube Shape Membrane Structure
US	Ultrasound
UV	Ultraviolet

References

[1] Meysman F J R, Cornelissen R, Trashin S, Bonné R, Martinez S H, van der Veen J, Blom C J, Karman C, Hou J L, Eachambadi R T, Geelhoed J S, Wael K De, Beaumont H J E, Cleuren B, Valcke R, van der Zant H S J, Boschker H T S and Manca J V. 2019 A highly conductive fibre network enables centimetre-scale electron transport in multicellular cable bacteria *Nat. Commun.* **10** 1–8

[2] Lovley D R 2017 e-Biologics: Fabrication of Sustainable Electronics with "Green" Biological Materials *MBio* **8** 1–7

[3] Malvankar N S, Yalcin S E, Tuominen M T and Lovley D R 2014 Visualization of charge propagation along individual pili proteins using ambient electrostatic force microscopy. *Nat. Nanotechnol.* **9** 1012–7

[4] Gorby Y A Y, Yanina S, McLean J S, Rosso K M, Moyles D, Dohnalkova A, Beveridge T J, Chang I S, Kim B H, Kim K S, Culley D E, Reed S B, Romine M F, Saffarini D A, Hill E A, Shi L, Elias D A, Kennedy D W, Pinchuk G, Watanabe K, Ishii S, Logan B, Nealson K H and Fredrickson J K 2006 Electrically conductive bacterial nanowires produced by *Shewanella oneidensis* strain MR-1 and other microorganisms *Proc. Natl. Acad. Sci. U. S. A.* **103** 11358–63

[5] Malvankar N S, Vargas M, Nevin K P, Franks A E, Leang C, Kim B C, Inoue K, Mester T, Covalla S F, Johnson J P, Rotello V M, Tuominen M T and Lovley D R 2011 Tunable metallic-like conductivity in microbial nanowire networks *Nat. Nanotechnol.* **6** 573–9

[6] Lovley D R 2012 Electromicrobiology *Annu. Rev. Microbiol.* **66** 391–409

[7] Pfeffer C, Larsen S, Song J, Dong M, Besenbacher F, Meyer R L, Kjeldsen K U, Schreiber L, Gorby Y a., El-Naggar M Y, Leung K M, Schramm A, Risgaard-Petersen N and Nielsen L P 2012 Filamentous bacteria transport electrons over centimetre distances *Nature* **491** 10–3

References

[8] Nielsen L P, Risgaard-Petersen N, Fossing H, Christensen P B and Sayama M 2010 Electric currents couple spatially separated biogeochemical processes in marine sediment *Nature* **463** 1071–4

[9] Cornelissen R, Bøggild A, Thiruvallur Eachambadi R, Koning R I, Kremer A, Hidalgo-Martinez S, Zetsche E-M, Damgaard L R, Bonné R, Drijkoningen J, Geelhoed J S, Boesen T, Boschker H T S, Valcke R, Nielsen L P, D'Haen J, Manca J V. and Meysman F J R 2018 The Cell Envelope Structure of Cable Bacteria *Front. Microbiol.* **9** 3044

[10] Casuso I, Fumagalli L, Samitier J, Padrós E, Reggiani L, Akimov V and Gomila G 2007 Electron transport through supported biomembranes at the nanoscale by conductive atomic force microscopy. *Nanotechnology* **18** 465503

[11] Fumagalli L, Ferrari G, Sampietro M and Gomila G 2009 Quantitative Nanoscale Dielectric Microscopy of Single-Layer Supported Biomembranes *Nano Lett.* **9** 1604–8

[12] Esteban-Ferrer D, Edwards M A, Fumagalli L, Juárez A and Gomila G 2014 Electric polarization properties of single bacteria measured with electrostatic force microscopy *ACS Nano* **8** 9843–9

[13] Dols-Perez A, Gramse G, Calò A, Gomila G and Fumagalli L 2015 Nanoscale electric polarizability of ultrathin biolayers on insulating substrates by electrostatic force microscopy *Nanoscale* **7** 18327–36

[14] Fumagalli L, Esteban-Ferrer D, Cuervo A, Carrascosa J L and Gomila G 2012 Label-free identification of single dielectric nanoparticles and viruses with ultraweak polarization forces *Nat. Mater.* **11** 808–16

[15] Biagi M C, Fabregas R, Gramse G, Van Der Hofstadt M, Juárez A, Kienberger F, Fumagalli L and Gomila G 2016 Nanoscale electric permittivity of single bacterial cells at gigahertz frequencies by scanning microwave microscopy *ACS Nano* **10** 280–8

[16] Gomila G, Esteban-Ferrer D and Fumagalli L 2013 Quantification of the dielectric constant of single non-spherical nanoparticles from polarization forces: Eccentricity effects *Nanotechnology* **24** 505713

[17] Fumagalli L, Edwards M A and Gomila G 2014 Quantitative electrostatic force microscopy with sharp silicon tips *Nanotechnology* **25** 495701

[18] Hou Y, Jaffrezic-Renault N, Martelet C, Zhang A, Minic-Vidic J, Gorojankina T, Persuy M A, Pajot-Augy E, Salesse R, Akimov V, Reggiani L, Pennetta C, Alfinito E, Ruiz O, Gomila G, Samitier J and Errachid A 2007 A novel detection strategy for odorant molecules based on controlled bioengineering of rat olfactory receptor I7 *Biosens. Bioelectron.* **22** 1550–5

[19] Rodriguez-Trujillo R, Castillo-Fernandez O, Garrido M, Arundell M, Valencia A and Gomila G 2008 High-speed particle detection in a micro-Coulter counter with two-dimensional adjustable aperture *Biosens. Bioelectron.* **24** 290–6

[20] Ing N L, El-Naggar M Y and Hochbaum A I 2018 Going the Distance: Long-Range Conductivity in Protein and Peptide Bioelectronic Materials *J. Phys. Chem. B* **122** 10403–23

[21] Lovley D R 2017 Electrically conductive pili: Biological function and potential applications in electronics *Curr. Opin. Electrochem.* **4** 190–8

[22] Marcus R A and Sutin N 1985 Electron transfers in chemistry and biology *Biochim. Biophys. Acta* **811** 265–322

[23] Hernandez M E and Newman D K 2001 Extracellular electron transfer *Cell. Mol. Life Sci.* **58** 1562–71

[24] Florkin M 1991 The discovery of adenosine triphosphate and the establishment of its structure *J. Hist. Biol.* **24** 145–54

[25] Logan B E and Regan J M 2006 Microbial fuel cells - Challenges and applications *Environ. Sci. Technol.* **40** 5172–80

[26] Shi L, Dong H, Reguera G, Beyenal H, Lu A, Liu J, Yu H-Q and Fredrickson J K 2016 Extracellular electron transfer mechanisms between microorganisms and minerals *Nat. Publ. Gr.* **14** 651–62

[27] Lovley D R 2006 Bug juice: harvesting electricity with microorganisms. *Nat. Rev.*

Microbiol. **4** 497–508

[28] Fredrickson J K and Zachara J M 2008 Electron transfer at the microbe-mineral interface: A grand challenge in biogeochemistry *Geobiology* **6** 245–53

[29] Rabaey K and Verstraete W 2005 Microbial fuel cells: Novel biotechnology for energy generation *Trends Biotechnol.* **23** 291–8

[30] Busalmen J P, Esteve-Nuñez A, Berná A and Feliu J M 2010 ATR-SEIRAs characterization of surface redox processes in G. sulfurreducens *Bioelectrochemistry* **78** 25–9

[31] Busalmen J P, Esteve-Núñez A, Berná A and Feliu J M 2008 C-type cytochromes wire electricity-producing bacteria to electrodes *Angew. Chemie - Int. Ed.* **47** 4874–7

[32] Wrighton K C, Agbo P, Warnecke F, Weber K A, Brodie E L, DeSantis T Z, Hugenholtz P, Andersen G L and Coates J D 2008 A novel ecological role of the *Firmicutes* identified in thermophilic microbial fuel cells *ISME J.* **2** 1146–56

[33] Marshall C W and May H D 2009 Electrochemical evidence of direct electrode reduction by a thermophilic Gram-positive bacterium, *Thermincola ferriacetica Energy Environ. Sci.* **2** 699–705

[34] Bond D R and Lovley D R 2003 Electricity Production by *Geobacter sulfurreducens* Attached to Electrodes *Appl. Environ. Microbiol.* **69** 1548–55

[35] Clarke T A, Edwards M J, Gates A J, Hall A, White G F, Bradley J, Reardon C L, Shi L, Beliaev A S, Marshall M J, Wang Z, Watmough N J, Fredrickson J K, Zachara J M, Butt J N and Richardson D J 2011 Structure of a bacterial cell surface decaheme electron conduit *Proc. Natl. Acad. Sci. U. S. A.* **108** 9384–9

[36] Holmes D E, Bond D R and Lovley D R 2004 Electron Transfer by Desulfobulbus propionicus to Fe(III) and Graphite Electrodes *Appl. Environ. Microbiol.* **70** 1234–7

[37] Pham C A, Jung S J, Phung N T, Lee J, Chang I S, Kim B H, Yi H and Chun J 2003 A novel electrochemically active and Fe(III)-reducing bacterium phylogenetically related to *Aeromonas hydrophila*, isolated from a microbial fuel cell *FEMS Microbiol. Lett.* **223** 129–

34

[38] Wrighton K C, Thrash J C, Melnyk R A, Bigi J P, Byrne-Bailey K G, Remis J P, Schichnes D, Auer M, Chang C J and Coates J D 2011 Evidence for direct electron transfer by a gram-positive bacterium isolated from a microbial fuel cell *Appl. Environ. Microbiol.* **77** 7633–9

[39] Rabaey K, Rodríguez J, Blackall L L, Keller J, Gross P, Batstone D, Verstraete W and Nealson K H 2007 Microbial ecology meets electrochemistry: Electricity-driven and driving communities *ISME J.* **1** 9–18

[40] Nevin K P and Lovley D R 2002 Mechanisms for Fe(III) oxide reduction in sedimentary environments *Geomicrobiol. J.* **19** 141–59

[41] Nevin K P and Lovley D R 2002 Mechanisms for accessing insoluble Fe(III) oxide during dissimilatory Fe(III) reduction by *Geothrix fermentans Appl. Environ. Microbiol.* **68** 2294–9

[42] Kotloski N J and Gralnick J A 2013 Flavin electron shuttles dominate extracellular electron transfer by *Shewanella oneidensis MBio* **4** 10–3

[43] Marsili E, Baron D B, Shikhare I D, Coursolle D, Gralnick J a and Bond D R 2008 *Shewanella* secretes flavins that mediate extracellular electron transfer. *Proc. Natl. Acad. Sci. U. S. A.* **105** 3968–73

[44] Lies D P, Hernandez M E, Kappler A, Mielke R E, Gralnick J A and Newman D K 2005 *Shewanella oneidensis* MR-1 uses overlapping pathways for iron reduction at a distance and by direct contact under conditions relevant for biofilms *Appl. Environ. Microbiol.* **71** 4414–26

[45] Sure S, Ackland M L, Torriero A A J, Adholeya A and Kochar M 2016 Microbial nanowires: An electrifying tale *Microbiology* **162** 2017–28

[46] Lovley D R and Malvankar N S 2015 Seeing is believing: Novel imaging techniques help clarify microbial nanowire structure and function *Environ. Microbiol.* **17** 2209–15

[47] Wang F, Gu Y, O'Brien J P, Yi S M, Yalcin S E, Srikanth V, Shen C, Vu D, Ing N L,

Hochbaum A I, Egelman E H and Malvankar N S 2019 Structure of Microbial Nanowires Reveals Stacked Hemes that Transport Electrons over Micrometers *Cell* **177** 361-369.e10

[48] Bouhenni R A, Vora G J, Biffinger J C, Shirodkar S, Brockman K, Ray R, Wu P, Johnson B J, Biddle E M, Marshall M J, Fitzgerald L A, Little B J, Fredrickson J K, Beliaev A S, Ringeisen B R and Saffarini D A 2010 The Role of *Shewanella oneidensis* MR-1 Outer Surface Structures in Extracellular Electron Transfer *Electroanalysis* **22** 856–64

[49] Pirbadian S, Barchinger S E, Leung K M, Byun H S, Jangir Y, Bouhenni R A, Reed S B, Romine M F, Saffarini D A, Shi L, Gorby Y A, Golbeck J H, El-Naggar M Y, Man K, Suk H, Jangir Y, Bouhenni R A, Leung K M, Byun H S, Jangir Y, Bouhenni R A, Reed S B, Romine M F, Saffarini D A, Shi L, Gorby Y A, Golbeck J H and El-Naggar M Y 2014 *Shewanella oneidensis* MR-1 nanowires are outer membrane and periplasmic extensions of the extracellular electron transport components. *Proc. Natl. Acad. Sci. U. S. A.* **111** 12883–8

[50] Subramanian P, Pirbadian S, El-naggar M Y and Jensen G J 2018 Ultrastructure of *Shewanella oneidensis* MR-1 nanowires revealed by electron cryotomography *Proc. Natl. Acad. Sci.* **115** E3246–55

[51] Jiang X, Hu J, Fitzgerald L A, Biffinger J C, Xie P, Ringeisen B R and Lieber C M 2010 Probing electron transfer mechanisms in *Shewanella oneidensis* MR-1 using a nanoelectrode platform and single-cell imaging *Proc. Natl. Acad. Sci.* **107** 16806–10

[52] Reguera G, McCarthy K D, Mehta T, Nicoll J S, Tuominen M T and Lovley D R 2005 Extracellular electron transfer via microbial nanowires. *Nature* **435** 1098–101

[53] Strycharz-Glaven S M, Snider R M, Guiseppi-Elie A and Tender L M 2011 On the electrical conductivity of microbial nanowires and biofilms *Energy Environ. Sci.* **4** 4366

[54] Teske A 2019 Cable bacteria, living electrical conduits in the microbial world *Proc. Natl. Acad. Sci. U. S. A.* **116** 18759–61

[55] Risgaard-petersen N, Kristiansen M, Frederiksen R B, Dittmer L, Bjerg T, Trojan D, Schreiber L, Damgaard R, Schramm A and Nielsen P 2015 Cable Bacteria in Freshwater Sediments *Appl. Environ. Microbiol.* **81** 6003–11

[56] Anand D and Chaudhuri A 2016 Bacterial outer membrane vesicles: New insights and applications *Mol. Membr. Biol.* **33** 125–37

[57] Jan A T 2017 Outer Membrane Vesicles (OMVs) of gram-negative bacteria: A perspective update *Front. Microbiol.* **8** 1–11

[58] Toyofuku M, Nomura N and Eberl L 2019 Types and origins of bacterial membrane vesicles *Nat. Rev. Microbiol.* **17** 13–24

[59] Filman D J, Marino S F, Ward J E, Yang L, Mester Z, Bullitt E, Lovley D R and Strauss M 2019 Cryo-EM reveals the structural basis of long-range electron transport in a cytochrome-based bacterial nanowire *Commun. Biol.* **2** 19–24

[60] Adhikari R Y, Malvankar N S, Tuominen M T and Lovley D R 2016 Conductivity of individual *Geobacter* pili *RSC Adv.* **6** 8354–7

[61] Malvankar N S and Lovley D R 2014 Microbial nanowires for bioenergy applications *Curr. Opin. Biotechnol.* **27** 88–95

[62] Nevin K P, Richter H, Covalla S F, Johnson J P, Woodard T L, Orloff A L, Jia H, Zhang M and Lovley D R 2008 Power output and columbic efficiencies from biofilms of *Geobacter sulfurreducens* comparable to mixed community microbial fuel cells *Environ. Microbiol.* **10** 2505–14

[63] Brutinel E D and Gralnick J A 2012 Shuttling happens: Soluble flavin mediators of extracellular electron transfer in *Shewanella Appl. Microbiol. Biotechnol.* **93** 41–8

[64] Li F, Li Y X, Cao Y X, Wang L, Liu C G, Shi L and Song H 2018 Modular engineering to increase intracellular NAD(H/+) promotes rate of extracellular electron transfer of *Shewanella oneidensis Nat. Commun.* **9** 1–13

[65] Pirbadian S and El-Naggar M Y 2012 Multistep hopping and extracellular charge transfer in microbial redox chains. *Phys. Chem. Chem. Phys.* **14** 13802–8

[66] El-Naggar M Y, Wanger G, Leung K M, Yuzvinsky T D, Southam G, Yang J, Lau W M, Nealson K H and Gorby Y a 2010 Electrical transport along bacterial nanowires from *Shewanella oneidensis* MR-1. *Proc. Natl. Acad. Sci. U. S. A.* **107** 18127–31

[67] El-Naggar M Y, Gorby Y a, Xia W and Nealson K H 2008 The molecular density of states in bacterial nanowires. *Biophys. J.* **95** L10–2

[68] Leung K M, Wanger G, El-Naggar M Y, Gorby Y, Southam G, Lau W M and Yang J 2013 *Shewanella oneidensis* MR-1 bacterial nanowires exhibit p-type, tunable electronic behavior *Nano Lett.* **13** 2407–11

[69] Jiang Z, Zhang S, Klausen L H, Song J, Li Q, Wang Z, Stokke B T, Huang Y, Besenbacher F, Nielsen L P and Dong M 2018 In vitro single-cell dissection revealing the interior structure of cable bacteria *Proc. Natl. Acad. Sci. U. S. A.* **115** 8517–22

[70] Meysman F J R, Risgaard-Petersen N, Malkin S Y and Nielsen L P 2015 The geochemical fingerprint of microbial long-distance electron transport in the seafloor *Geochim. Cosmochim. Acta* **152** 122–42

[71] Esteve-Núñez A, Sosnik J, Visconti P and Lovley D R 2008 Fluorescent properties of c-type cytochromes reveal their potential role as an extracytoplasmic electron sink in *Geobacter sulfurreducens Environ. Microbiol.* **10** 497–505

[72] Fredrickson J K, Romine M F, Beliaev A S, Auchtung J M, Driscoll M E, Gardner T S, Nealson K H, Osterman A L, Pinchuk G, Reed J L, Rodionov D A, Rodrigues J L M, Saffarini D A, Serres M H, Spormann A M, Zhulin I B and Tiedje J M 2008 Towards environmental systems biology of *Shewanella Nat. Rev. Microbiol.* **6** 592–603

[73] Malvankar N S, Mester T, Tuominen M T and Lovley D R 2012 Supercapacitors based on c-type cytochromes using conductive nanostructured networks of living bacteria *ChemPhysChem* **13** 463–8

[74] Chen A Y, Deng Z, Billings A N, Seker U O S, Lu M Y, Citorik R J, Zakeri B and Lu T K 2014 Synthesis and patterning of tunable multiscale materials with engineered cells *Nat. Mater.* **13** 515–23

[75] Liu X, Gao H, Ward J E, Liu X, Yin B, Fu T, Chen J, Lovley D R and Yao J 2020 Power generation from ambient humidity using protein nanowires *Nature* 1–5

[76] Honig B and Nicholls A 1995 Classical electrostatics in biology and chemistry *Science* **268**

1144–9

[77] Sharp K A and Honig B 1990 ELECTROSTATIC INTERACTIONS IN MACROMOLECULES : Theory and Applications *Annu. Rev. Biophys. Biophys. Chem.* **19** 301–32

[78] Simonson T 2003 Electrostatics and dynamics of proteins *Reports Prog. Phys.* **66** 737–87

[79] M.F.Perutz 1978 Electrostatic effects in proteins *Science* **201** 1187–91

[80] Pethig R 1992 Protein-Water Interactions Determined by Dielectric Methods *Annu. Rev. Phys. Chem.* **43** 177–205

[81] Li L, Li C, Zhang Z and Alexov E 2013 On the dielectric "constant" of proteins: Smooth dielectric function for macromolecular modeling and its implementation in DelPhi *J. Chem. Theory Comput.* **9** 2126–36

[82] Raabe G and Sadus R J 2011 Molecular dynamics simulation of the dielectric constant of water: The effect of bond flexibility *J. Chem. Phys.* **134** 234501

[83] Paul R, Tusynski J A and Chatterjee R 1984 Dielectric constant of biological systems *Phys. Rev. A* **30** 2676–85

[84] Sun J and Lucyszyn S 2018 Extracting Complex Dielectric Properties from Reflection-Transmission Mode Spectroscopy *IEEE Access* **6** 8302–21

[85] Janezic M D and Williams D F 1997 Permittivity characterization from transmission-line measurement *IEEE MTT-S Int. Microw. Symp. Dig.* **3** 1343–6

[86] Afsar M N, Afsar M N, Birch J R, Clarke R N and Chantry G W 1986 The Measurement of the Properties of Materials *Proc. IEEE* **74** 183–99

[87] Jacob M V., Mazierska J, Leong K and Krupka J 2002 Microwave properties of low-loss polymers at cryogenic temperatures *IEEE Trans. Microw. Theory Tech.* **50** 474–80

[88] Hakki B W and Coleman P D 1960 A Dielectric ductive Resonator Method of Measuring Capacities in the Millimeter Range *IRE Trans. Microw. Theory Tech.* **8** 402–10

[89] Fumagalli L, Esfandiar A, Fabregas R, Hu S, Ares P, Janardanan A, Yang Q, Radha B,

Taniguchi T, Watanabe K, Gomila G, Novoselov K S and Geim A K 2018 Anomalously low dielectric constant of confined water *Science* **360** 1339–42

[90] Hess C M, Riley E A, Palos-Chávez J and Reid P J 2013 Measuring the spatial distribution of dielectric constants in polymers through quasi-single molecule microscopy *J. Phys. Chem. B* **117** 7106–12

[91] Signore G, Abbandonato G, Storti B, Stöckl M, Subramaniam V and Bizzarri R 2013 Imaging the static dielectric constant in vitro and in living cells by a bioconjugable GFP chromophore analog *Chem. Commun.* **49** 1723–5

[92] Cuervo A, Dans P D, Carrascosa J L, Orozco M, Gomila G, Fumagalli L, Carrascosa J L, Orozco M, Gomila G and Fumagalli L 2014 Direct measurement of the dielectric polarization properties of DNA *Proc. Natl. Acad. Sci.* **111** E3624–30

[93] Lozano H, Fabregas R, Blanco-Cabra N, Millán-solsona R, Torrents E, Fumagalli L and Gomila G 2018 Dielectric constant of flagellin proteins measured by scanning dielectric microscopy *Nanoscale* **10** 19188–94

[94] G. Binnig, C. F. Quote C G and E W 1982 Surface Studies by Scanning Tunneling Microscopy *Phys. Rev. Lett.* **49** 57–61

[95] G. Binning, C.F.Quate and Ch. Gerber 1986 Atomic Force Microscopy *Phys. Rev. Lett.* **56** 930–3

[96] Martin Y, Williams C C and Wickramasinghe H K 1987 Atomic force microscope-force mapping and profiling on a sub 100-Å scale *J. Appl. Phys.* **61** 4723–9

[97] Albrecht T R, Grütter P, Horne D and Rugar D 1991 Frequency modulation detection using high-Q cantilevers for enhanced force microscope sensitivity *J. Appl. Phys.* **69** 668–73

[98] Giessibl F J 1995 Atomic resolution of the silicon (111)-(7x7) surface by atomic force microscopy *Science* **267** 68–71

[99] Jang J, Schatz G C and Ratner M A 2004 Capillary force in atomic force microscopy *J. Chem. Phys.* **120** 1157–60

[100] Kawai S, Foster A S, Björkman T, Nowakowska S, Björk J, Canova F F, Gade L H, Jung T A and Meyer E 2016 Van der Waals interactions and the limits of isolated atom models at interfaces *Nat. Commun.* **7** 1–7

[101] Oesterhelt F, Oesterhelt D, Pfeiffer M, Engel A, Gaub H E and Müller D J 2000 Unfolding pathways of individual bacteriorhodopsins *Science* **288** 143–6

[102] Hinterdorfer P, Baumgartner W, Gruber H J, Schilcher K and Schindler H 1996 Detection and localization of individual antibody-antigen recognition events by atomic force microscopy *Proc. Natl. Acad. Sci. U. S. A.* **93** 3477–81

[103] Müller D J and Dufrêne Y F 2011 Atomic force microscopy: A nanoscopic window on the cell surface *Trends Cell Biol.* **21** 461–9

[104] Müller D J and Dufrêne Y F 2009 Atomic force microscopy as a multifunctional molecular toolbox in nanobiotechnology *Nanosci. Technol. A Collect. Rev. from Nat. Journals* **3** 269–77

[105] Gramse G, Dols-Perez A, Edwards M A, Fumagalli L and Gomila G 2013 Nanoscale measurement of the dielectric constant of supported lipid bilayers in aqueous solutions with electrostatic force microscopy *Biophys. J.* **104** 1257–62

[106] Rugar D, Mamin H J, Guethner P, Lambert S E, Stern J E, McFadyen I and Yogi T 1990 Magnetic force microscopy: General principles and application to longitudinal recording media *J. Appl. Phys.* **68** 1169–83

[107] Li H, Qi X, Wu J, Zeng Z, Wei J and Zhang H 2013 Investigation of MoS_2 and graphene nanosheets by magnetic force microscopy *ACS Nano* **7** 2842–9

[108] Gruverman A and Kalinin S V. 2006 Piezoresponse force microscopy and recent advances in nanoscale studies of ferroelectrics *J. Mater. Sci.* **41** 107–16

[109] Zhao M H, Wang Z L and Mao S X 2004 Piezoelectric characterization individual zinc oxide nanobelt probed by piezoresponse force microscope *Nano Lett.* **4** 587–90

[110] Jesse S, Baddorf A P and Kalinin S V. 2006 Switching spectroscopy piezoresponse force microscopy of ferroelectric materials *Appl. Phys. Lett.* **88** 1–4

[111] Melitz W, Shen J, Kummel A C and Lee S 2011 Kelvin probe force microscopy and its application *Surf. Sci. Rep.* **66** 1–27

[112] Palermo V, Palma M and Samori P 2006 Electronic characterization of organic thin films by Kelvin probe force microscopy *Adv. Mater.* **18** 145–64

[113] Girard P 2001 Electrostatic force microscopy: Principles and some applications to semiconductors *Nanotechnology* **12** 485–90

[114] Fumagalli L and Gomila G 2018 Probing the Dielectric Constant at the Nanoscale with Scanning Probe Microscopy *Capacitance Spectroscopy of Semiconductors* ed J V. Li and G Ferrari (Pan Standford Publishing Pte. Ltd) p 33

[115] Lu W, Wang D and Chen L 2007 Near-static dielectric polarization of individual carbon nanotubes *Nano Lett.* **7** 2729–33

[116] Lu W, Xiong Y and Chen L 2009 Length-dependent dielectric polarization in metallic single-walled carbon nanotubes *J. Phys. Chem. C* **113** 10337–40

[117] Gramse G, Casuso I, Toset J, Fumagalli L and Gomila G 2009 Quantitative dielectric constant measurement of thin films by DC electrostatic force microscopy *Nanotechnology* **20** 395702

[118] García R and Pérez R 2002 Dynamic atomic force microscopy methods *Surf. Sci. Rep.* **47** 197–301

[119] Hofstadt M Van Der, Fabregas R, Biagi M C, Fumagalli L and Gomila G Nanoscale dielectric microscopy of non- planar samples by lift-mode electrostatic force microscopy *Nanotechnology* **27** 1–13

[120] Checa M, Millan-Solsona R, Blanco N, Torrents E, Fabregas R and Gomila G 2019 Mapping the dielectric constant of a single bacterial cell at the nanoscale with scanning dielectric force volume microscopy *Nanoscale* **11** 20809–19

[121] Fumagalli L, Gramse G, Esteban-Ferrer D, Edwards M A and Gomila G 2010 Quantifying the dielectric constant of thick insulators using electrostatic force microscopy *Appl. Phys. Lett.* **96** 2008–11

[122] Hudlet S, Saint Jean M, Guthmann C and Berger J 1998 Evaluation of the capacitive force between an atomic force microscopy tip and a metallic surface *Eur. Phys. J. B* **2** 5–10

[123] Gomila G, Gramse G and Fumagalli L 2014 Finite-size effects and analytical modeling of electrostatic force microscopy applied to dielectric fi lms *Nanotechnology* **25** 255702

[124] Villarrubia J S 1994 Morphological estimation of tip geometry for scanned probe microscopy *Surf. Sci.* **321** 287–300

[125] Markiewicz P and Goh M C 1994 Atomic Force Microscopy Probe Tip Visualization and Improvement of Images Using a Simple Deconvolution Procedure *Langmuir* **10** 5–7

[126] Xu S and Arnsdorf M F 1994 Calibration of the scanning (atomic) force microscope with gold particles *J. Microsc.* **173** 199–210

[127] Ramirez-Aguilar K A and Rowlen K L 1998 Tip characterization from AFM images of nanometric spherical particles *Langmuir* **14** 2562–6

[128] Itoh H, Fujimoto T and Ichimura S 2006 Tip characterizer for atomic force microscopy *Rev. Sci. Instrum.* **77** 103704

[129] Tian F, Qian X and Villarrubia J S 2008 Blind estimation of general tip shape in AFM imaging *Ultramicroscopy* **109** 44–53

[130] Van Der Hofstadt M, Fabregas R, Millan-Solsona R, Juarez A, Fumagalli L and Gomila G 2016 Internal Hydration Properties of Single Bacterial Endospores Probed by Electrostatic Force Microscopy *ACS Nano* **10** 11327–36

[131] Lozano H, Millán-Solsona R, Fabregas R and Gomila G 2019 Sizing single nanoscale objects from polarization forces *Sci. Rep.* **9** 74799

[132] Roldan Cuenya B and Behafarid F 2015 Nanocatalysis: Size- and shape-dependent chemisorption and catalytic reactivity *Surf. Sci. Rep.* **70** 135–87

[133] Perini G, Salvatori F, Ochsenbein D R, Mazzotti M and Vetter T 2019 Filterability prediction of needle-like crystals based on particle size and shape distribution data *Sep. Purif. Technol.* **211** 768–81

[134] Hussain S M, Braydich-Stolle L K, Schrand A M, Murdock R C, Yu K O, Mattie D M and Schlager J J 2009 Toxicity evaluation for safe use of nanomaterials: Recent achievements and technical challenges *Adv. Mater.* **21** 1549–59

[135] Samuel R 2011 Nano rules fall foul of data gap. *Nature* **480** 160–1

[136] Schrurs F and Lison D 2012 Focusing the research efforts *Nat. Nanotechnol.* **7** 546–8

[137] Fadeel B, Fornara A, Toprak M S and Bhattacharya K 2015 Keeping it real: The importance of material characterization in nanotoxicology *Biochem. Biophys. Res. Commun.* **468** 498–503

[138] Allen T 2003 *Powder Sampling and Particle Size Determination* (Elsevier Science)

[139] Mourdikoudis S, Pallares R M and Thanh N T K 2018 Characterization techniques for nanoparticles: Comparison and complementarity upon studying nanoparticle properties *Nanoscale* **10** 12871–934

[140] R. Pecora 2000 Dynamic Light Scattering Measurement of Nanometer Particles in Liquids *J. Nanoparticle Res.* **2** 123–31

[141] Filipe V, Hawe A and Jiskoot W 2010 Critical evaluation of nanoparticle tracking analysis (NTA) by NanoSight for the measurement of nanoparticles and protein aggregates *Pharm. Res.* **27** 796–810

[142] Pyrz W D and Buttrey D J 2008 Particle size determination using TEM: A discussion of image acquisition and analysis for the novice microscopist *Langmuir* **24** 11350–60

[143] Hoo C M, Starostin N, West P and Mecartney M L 2008 A comparison of atomic force microscopy (AFM) and dynamic light scattering (DLS) methods to characterize nanoparticle size distributions *J. Nanoparticle Res.* **10** 89–96

[144] Delvallée A, Feltin N, Ducourtieux S, Trabelsi M and Hochepied J F 2015 Direct comparison of AFM and SEM measurements on the same set of nanoparticles *Meas. Sci. Technol.* **26** 85601

[145] Boyd R D and Cuenat A 2011 New analysis procedure for fast and reliable size measurement of nanoparticles from atomic force microscopy images *J. Nanoparticle Res.*

13 105–13

[146] Eaton P, Quaresma P, Soares C, Neves C, de Almeida M P, Pereira E and West P 2017 A direct comparison of experimental methods to measure dimensions of synthetic nanoparticles *Ultramicroscopy* **182** 179–90

[147] Klapetek P, Valtr M, Nečas D, Salyk O and Dzik P 2011 Atomic force microscopy analysis of nanoparticles in non-ideal conditions *Nanoscale Res. Lett.* **6** 1–9

[148] Petr Klapeterk 2013 *Quantitative Data Processing in Scanning Probe Microscopy* ed W A Amsterdam (Elsevier, William Andrew)

[149] Attota R K and Liu E C 2016 Volume determination of irregularly-shaped quasi-spherical nanoparticles *Anal. Bioanal. Chem.* **408** 7897–903

[150] Baur C, Bugacov A, Koel B E, Madhukar A, Montoya N, Ramachandran T R, Requicha A A G, Resch R and Will P 1998 Nanoparticle manipulation by mechanical pushing: Underlying phenomena and real-time monitoring *Nanotechnology* **9** 360–4

[151] Junno T, Deppert K, Montelius L and Samuelson L 1995 Controlled manipulation of nanoparticles with an atomic force microscope *Appl. Phys. Lett.* **66** 3627–9

[152] Radmacher M, Fritz M and Hansma P K 1995 Imaging soft samples with the atomic force microscope: gelatin in water and propanol *Biophys. J.* **69** 264–70

[153] Knoll A, Magerle R and Krausch G 2001 Tapping Mode Atomic Force Microscopy on Polymers: Where Is the True Sample Surface? *Macromolecules* **34** 4159–65

[154] Horcas I, Fernández R, Gómez-Rodríguez J M, Colchero J, Gómez-Herrero J and Baro A M 2007 WSXM: A software for scanning probe microscopy and a tool for nanotechnology *Rev. Sci. Instrum.* **78** 013705

[155] Uría N, Muñoz Berbel X, Sánchez O, Muñoz F X, Mas J, Mu X, Olga S, Mu F X and Mas J 2011 Transient storage of electrical charge in biofilms of *Shewanella oneidensis* MR-1 growing in a microbial fuel cell *Environ. Sci. Technol.* **45** 10250–6

[156] Julius A S 1941 *Electromagnetic Theory* (Mcgraw Hill Book Company)

[157] Fabregas R and Gomila G 2020 Dielectric nanotomography Based on Electrostatic Force Microscopy: a Numerical Analysis *J. Appl. Phys.* **127** 024301

[158] Wang F, Burrage A M, Postel S, Clark R E, Orlova A, Sundberg E J, Kearns D B and Egelman E H 2017 A structural model of flagellar filament switching across multiple bacterial species *Nat. Commun.* **8** 960

[159] Bockrath M, Markovic N, Shepard A, Tinkham M, Gurevich L, Kouwenhoven L P, Wu M W and Sohn L L 2002 Scanned Conductance Microscopy of Carbon Nanotubes and λ-DNA *Nano Lett.* **2** 187–90

[160] Lu W, Xiong Y, Hassanien A, Zhao W, Zheng M and Chen L 2009 A scanning probe microscopy based assay for single-walled carbon nanotube metallicity *Nano Lett.* **9** 1668–72

[161] Yang Y, Guo W, Wang X, Wang Z, Qi J and Zhang Y 2012 Size dependence of dielectric constant in a single pencil-like ZnO nanowire *Nano Lett.* **12** 1919–22

[162] Knowles T P J, Vendruscolo M and Dobson C M 2014 The amyloid state and its association with protein misfolding diseases *Nat. Rev. Mol. Cell Biol.* **15** 384–96

[163] Gilson M K and Honig B H 1986 The dielectric constant of a folded protein *Biopolymers* **25** 2097–119

[164] Simonson T and Brooks C L 1996 Charge screening and the dieletric constant of proteins: Insights from molecular dynamics *J. Am. Chem. Soc.* **118** 8452–8

[165] Schutz C N and Warshel A 2001 What are the dielectric "constants" of proteins and how to validate electrostatic models? *Proteins Struct. Funct. Genet.* **44** 400–17

[166] S.T.Bayley 1951 The dielectric properties of various solid crystalline proteins, amino acids and peptides *Trans. Faraday Soc.* **47** 509–17

[167] Takashima S and Schwan H P 1965 Dielectric dispersion of crystalline powders of amino acids, peptides, and proteins. *J. Phys. Chem.* **69** 4176–82

[168] Martin Y, Abraham D W and Wickramasinghe H K 1988 High-resolution capacitance measurement and potentiometry by force microscopy *Appl. Phys. Lett.* **52** 1103–5

[169] Eaton P and West P 2010 *Atomic Force Microscopy* (Oxford University Press)

[170] Fujii T, Kato T, Hiraoka K D, Miyata T, Minamino T, Chevance F F V, Hughes K T and Namba K 2017 Identical folds used for distinct mechanical functions of the bacterial flagellar rod and hook *Nat. Commun.* **8** 1–10

[171] Wilson D R and Beveridge T J 1993 Bacterial flagellar filaments and their component flagellins *Can. J. Microbiol.* **39** 451–72

[172] Pérez-Mejías G, Guerra-Castellano A, Díaz-Quintana A, De la Rosa M A and Díaz-Moreno I 2019 Cytochrome c: Surfing Off of the Mitochondrial Membrane on the Tops of Complexes III and IV *Comput. Struct. Biotechnol. J.* **17** 654–60

[173] Myers C R and Myers J M 1992 Localization of cytochromes to the outer membrane of anaerobically grown *Shewanella putrefaciens* MR-1 *J. Bacteriol.* **174** 3429–38

[174] Kjeldsen K U, Schreiber L, Thorup C A, Boesen T, Bjerg J T, Yang T, Dueholm M S, Larsen S, Risgaard-Petersen N, Nierychlo M, Schmid M, Bøggild A, de Vossenberg J van, Geelhoed J S, Meysman F J R, Wagner M, Nielsen P H, Nielsen L P and Schramm A 2019 On the evolution and physiology of cable bacteria *Proc. Natl. Acad. Sci. U. S. A.* **116** 19116–25

[175] Gramse G, Edwards M A, Fumagalli L and Gomila G 2013 Theory of amplitude modulated electrostatic force microscopy for dielectric measurements in liquids at MHz frequencies *Nanotechnology* **24** 415709

[176] Gramse G, Edwards M A, Fumagalli L and Gomila G 2012 Dynamic electrostatic force microscopy in liquid media *Appl. Phys. Lett.* **101** 213108

[177] Van Der Hofstadt M, Hüttener M, Juárez A and Gomila G 2015 Nanoscale imaging of the growth and division of bacterial cells on planar substrates with the atomic force microscope *Ultramicroscopy* **154** 29–36

[178] Randviir E P and Banks C E 2013 Electrochemical impedance spectroscopy: An overview of bioanalytical applications *Anal. Methods* **5** 1098–115

[179] Dimaki M, Vergani M, Heiskanen A, Kwasny D, Sasso L, Carminati M, Gerrard J A,

Emneus J and Svendsen W E 2014 A compact microelectrode array chip with multiple measuring sites for electrochemical applications *Sensors (Switzerland)* **14** 9505–21

[180] Marchesi L F, Jacumasso S C, Quintanilha R C, Winnischofer H and Vidotti M 2015 The electrochemical impedance spectroscopy behavior of poly(aniline) nanocomposite electrodes modified by Layer-by-Layer deposition *Electrochim. Acta* **174** 864–70

[181] Brosel-Oliu S, Mergel O, Uria N, Abramova N, Van Rijn P and Bratov A 2019 3D impedimetric sensors as a tool for monitoring bacterial response to antibiotics *Lab Chip* **19** 1436–47

[182] Clausen C H, Dimaki M, Bertelsen C V, Skands G E, Rodriguez-Trujillo R, Thomsen J D, Svendsen W E, Hyttel C, Vinther C, Erik G, Dahl J and Edith W 2018 Bacteria detection and differentiation using impedance flow cytometry *Sensors (Switzerland)* **18** 1–12

[183] Gómez-Sjöberg R, Morisette D T and Bashir R 2005 Impedance microbiology-on-a-chip: Microfluidic bioprocessor for rapid detection of bacterial metabolism *J. Microelectromechanical Syst.* **14** 829–38

[184] Wang Q, Jones A A D, Gralnick J A, Lin L and Buie C R 2019 Microfluidic dielectrophoresis illuminates the relationship between microbial cell envelope polarizability and electrochemical activity *Hist. da Historiogr.* **11** 1–12

[185] Ramasamy R P, Gadhamshetty V, Nadeau L J and Johnson G R 2009 Impedance spectroscopy as a tool for non-intrusive detection of extracellular mediators in microbial fuel cells *Biotechnol. Bioeng.* **104** 882–91

[186] Morgan H, Sun T, Holmes D, Gawad S and Green N G 2007 Single cell dielectric spectroscopy *J. Phys. D. Appl. Phys.* **40** 61–70